ABSTRACT

Title of dissertation: CONTRIBUTIONS TO THE DYNAMICS OF HELICOPTERS WITH ACTIVE ROTOR CONTROL

Carlos A. Malpica
Doctor of Philosophy, 2008

Dissertation directed by: Professor Roberto Celi
Department of Aerospace Engineering

This dissertation presents an aeromechanical closed loop stability and response analysis of a hingeless rotor helicopter with a Higher Harmonic Control (HHC) system for vibration reduction. The analysis includes the rigid body dynamics of the helicopter and blade flexibility. The gain matrix is assumed to be fixed and computed off-line. The discrete elements of the HHC control loop are rigorously modeled, including the presence of two different time scales in the loop. By also formulating the coupled rotor-fuselage dynamics in discrete form, the entire coupled helicopter-HHC system could be rigorously modeled as a discrete system. The effect of the periodicity of the equations of motion is rigorously taken into account by converting the system into an equivalent system with constant coefficients and identical stability properties using a time lifting technique. The most important conclusion of the present study is that the discrete elements in the HHC loop must be modeled in any HHC analysis. Not doing so is unconservative. For the helicopter configuration and HHC structure used in this study, an approximate continuous modeling of the HHC system indicates that the closed loop, coupled helicopter-HHC sys-

tem remains stable for optimal feedback control configurations which the more rigorous discrete analysis shows can result in closed loop instabilities. The HHC gains must be reduced to account for the loss of gain margin brought about by the discrete elements. Other conclusions of the study are: (i) the HHC is effective in quickly reducing vibrations, at least at its design condition, although the time constants associated with the closed loop transient response indicate closed loop bandwidth to be 1 rad/sec on average, thus overlapping with FCS or pilot bandwidths, and raising the issue of potential interactions; (ii) a linearized model of helicopter dynamics is adequate for HHC design, as long as the periodicity of the system is correctly taken into account, i.e., periodicity is more important than nonlinearity, at least for the mathematical model used in this study; and (iii) when discrete and continuous systems are both stable, and quasisteady conditions can be guaranteed, the predicted HHC control harmonics are in good agreement. Quantitative assessment of the results needs to be tempered with the natural limitations of the nonlinear analytical helicopter model at hand to accurately predict vibration.

CONTRIBUTIONS TO THE DYNAMICS OF HELICOPTERS WITH ACTIVE ROTOR CONTROLS

by

Carlos A. Malpica

Dissertation submitted to the Faculty of the Graduate School of the
University of Maryland, College Park in partial fulfillment
of the requirements for the degree of
Doctor of Philosophy
2008

Advisory Committee:
Professor Roberto Celi, Chair/Advisor
Professor Inderjit Chopra
Professor J. Gordon Leishman
Professor Norman Wereley
Professor Balakumar Balachandran, Dean's Representative

To my wife Lizzette

Acknowledgements

The support of the U.S. Army Research Office, under the project number 41569-EG, "Control of Systems With Periodic Coefficients With Application to Active Rotor Control," Technical Monitor Gary Anderson, is gratefully acknowledged.

The research was carried out in close collaboration with Prof. Patrizio Colaneri and Prof. Marco Lovera, of the Dipartimento di Elettronica e Informazione of the Politecnico di Milano, Milan, Italy, who provided invaluable help with the development of the control algorithms and, in general, with the properties of continuous and discrete systems with periodic coefficients. Additionally, Prof. Lovera kindly shared with me his T-matrix calculation codes.

I must also thank my advisor Dr. Roberto Celi who probably believed in me more than I did myself, and who patiently put up with me for all these years without going completely insane. He provided every possible means of support I needed to successfully complete my degree.

I feel I should also express my deepest and most sincere gratitude towards the members of my dissertation committee, Drs. Inderjit Chopra, J. Gordon Leishman, Norman Wereley and Balakumar Balachandran, for their unconditional support and advice.

I must also thank my colleagues and friends from the Rotorcraft Center, both past and present, for the lively discussions or simple chitchat which I will always remember fondly. Especially Maria Ribera, who always seemed to there for me. The many years of shared experiences made our relationship transcend the level of coworker into true friendship. Rendy Cheng and Dario Fusato helped me settle in at the beginning and for

this I am indebted. My “paisano” Felipe Bohorquez I have to thank for the constant moral support and the fun times.

Finally, the acknowledgements would not be complete without thanking my family and friends here in Maryland, as well as those from afar. But above all I thank my wife, Lizzette, for all her unconditional love and encouragement.

Table of Contents

List of Tables

List of Figures

Nomenclature

$A(t)$	Open loop state matrix
A_0	Open loop state matrix (constant approximation)
$B(t)$	Input (or control) matrix
B	Number of blocks in the Harmonic Transfer Function
$C(t)$	Output (or measurement) matrix
C_T	Rotor thrust coefficient
$D(t)$	Direct input/output matrix
g	Acceleration due to gravity
J	Vibration performance function or index
K	SISO HHC controller feedback gain
$\mathbf{K}$	MIMO HHC controller feedback gain
k	Discrete-time variable associated with T (1/rev dynamics)
M	Mach number
m	Number of control inputs
N	Number of rotor blades
n	Number of output channels with acceleration measurements
n_s	System order; number of acceleration (output) samples per revolution, $n_s = T/P$
P	Acceleration (output) sampling interval, $P = T/n_s$
p	Total number of outputs, $p = 2n$; aircraft roll rate
Q	Output weighting matrix in HHC performance index
q	Aircraft pitch rate
R	Control weighting matrix in HHC performance index
r	Tuning parameter in HHC performance index; aircraft yaw rate
T	Rotor revolution period, $T = 2\pi/\Omega$, or SISO transfer matrix
$\mathbf{T}$	MIMO steady, frequency-domain vibration reponse transfer matrix
t	Time (continuous)
u	SISO HHC input vector; aircraft forward velocity component
$\mathbf{u}$	System input vector
$\mathbf{u}_{FCS}$	pilot or flight control system input
$\mathbf{u}_{HHC}$	HHC input
V	Aircraft flight speed
v	Aircraft lateral velocity component
w	Aircraft vertical velocity component
$\mathbf{x}, \mathbf{y}$	State and output vectors
y	SISO output vector
y^i_{Nc}, y^i_{Ns}	N/rev cosine and sine harmonic of i-th acceleration measurement (output)

Greek symbols

α_F	Aircraft angle of attack
α_Y	Blade section angle of attack
β_F	Fuselage sideslip angle

η	Discrete-time variable associated with P (acceleration sampling)
θ	Aircraft pitch attitude angle; blade pitch angle
θ_{kc}, θ_{ks}	k/rev cosine and sine harmonic of pitch control input
κ	Proportinal feedback gain coefficient
σ	Rotor solidity; Matrix singular value
$\Phi(t, \tau)$	State Transition Matrix
ϕ	Aircraft roll attitude angle
ψ	Azimuth angle of reference blade, $\psi = \Omega t$; aircraft yaw attitude angle
Ω	Rotor angular velocity

Subscripts and Superscripts

$()_C$	Quantity in the controller model
$()_F$	Quantity in the harmonic analyzer model
$()_H$	Quantity in the helicopter dynamic model
$()_{lift}$	Time-lifted quantity
$()_Z$	Quantity in the zero-order-hold model
$\tilde{()}$	Discrete-time counterpart of continuous-time signal

Abbreviations

ARCS	Active Rotor Control System
CG	Center of mass of the helicopter
FCS	Flight Control System
HHC	Higher Harmonic Control
HTF	Harmonic Transfer Function
IBC	Individual Blade Control
LTI	Linear Time Invariant (or constant-coefficient) model
LTP	Linear Time Periodic (or periodic-coefficient) model
MIMO	Multi-Input Multi-Output system
PHHC	Periodic Higher Harmonic Control
SISO	Single-Input Single-Output system

Chapter 1

Introduction

1.1 Motivation

The motivating force behind the present study is prompted by recent advances in different areas of research in active rotor control, both from a control theory perspective and from a point of view of the evolution of actuator technologies, in combination with the recognition that active rotor control systems are essential for the development of future rotorcraft concepts aiming to expand current state-of-the-art payload, range and speed envelopes. Efforts in these areas vary largely, from analytical studies, to wind-tunnel and flight test initiatives. However, research on active rotor control has rarely considered the possible interactions with the entire helicopter coupled fuselage-rotor dynamics from a control engineering stability perspective. Encouraging efforts to move research away from the laboratory into prototype systems and full-fledged flight testing activities have also surfaced recently. Consequently, awareness for the fact that rotor and fuselage dynamics are not isolated, but rather strongly coupled, is one of the chief concerns in this study. With these issues as a backdrop, research presented in this study intends to investigate the importance of often neglected helicopter and control system dynamics on the aeromechanical stability of helicopters with closed loop higher harmonic control (HHC) systems;

first, that of the inherent periodicity in both the helicopter dynamics and control feedback gain and second, that of discrete-time delays involved in the controller implementation.

1.1.1 Background

Ever since the inception of the helicopter people have realized their potential for commercial commuter travel. Rotorcraft, or VTOL aircraft in general, possess the unique ability to carry out runway-independent and point-to-point passenger delivery operations. Exploiting this ability would significantly increase the overall flexibility of the transportation grid system. In the not so distant future, world transport requirements will be dominated by increasingly crowded urban environments. Runway independent aircraft present attractive solutions for this future transportation dilemma. Also, continuous demand for rapid and reliable transport, and requirement for robust military systems are likely to remain constant driving forces for vertical lift flight technology. As of today, commercial use of the helicopter has not yet become a commonplace reality, due in no small part to the failure to achieve a minimum measure of consumer acceptance and economy efficiency [1–4]. References [5, 6] present concise illustrative reviews of the many basic difficulties encountered in helicopter design which have prevented it from competing more favorably against their fixed wing brethren in the commercial transportation market.

Vibration and noise are key elements of community acceptance in as much as they are significant limiting factors of both, comfort and speed. Vibration is not a problem only for occupants (crew and passengers), it is also a leading cause of component fatigue, and related operational costs. Current helicopter designs are normally equipped with a vari-

ety of passive devices that have been developed to reduce fuselage vibration, either by counteracting the vibratory motion or by isolating the rotor vibratory loads from the fuselage. These are usually in the form of mass dampers or shock dampers which come with hefty weight penalties and are insufficient to guarantee the smooth ride flight conditions required for the civilian market in any case.

Leatherwood et al. [7–9] have extensively investigated ride comfort criteria incorporating the effects of both noise and vibration. This exhaustive research program conducted at NASA Langley Research Center produced a mathematical model that accounts for the effects of combined axis vibrations, and includes corrections for the effect of vibration duration and interior noise on helicopter ride quality. The output of the model consists of an estimate of the passenger discomfort produced by a given noise and or vibration environment. Depending on interior noise levels, acceleration vibration levels can be translated to percentages indicating the probability of an individual reporting the overall environment as being uncomfortable.

Current NASA recommendations suggest desirable vibration levels should be under $0.05g$ over the entire flight envelope. This vibration requirement is basically anchored by the mimimum discomfort curve at 5 Hz, as determined by Leatherwood et al. [7–9]. The resonance frequency of the seated human body has been shown to be about 5 Hz according to power absorption measurements (see, e.g., Ref. [10]), explaining the local minima observed in the equal discomfort curves drawn by Leatherwood et al. as functions of vertical vibration acceleration amplitude and frequency.

Considering the combined effect of noise and vibration on the comfort levels of the human body suggests that even a $0.05g$ peak acceleration level might not be sufficiently

conducive to passenger acceptance. A harmonic vibration with a vertical peak acceleration amplitude of $0.05g$ will yield a r.m.s. acceleration level of about $0.035g$. Depending on the noise level, this level of vibration can be translated to a 40% discomfort rating (i.e., a probability of 40% that a subject will feel discomfort when subjected to that environment) at A-weighted noise levels of about 60 dB [9]. Ride discomfort ratings increase substantially, up to about 90%, for noise levels around 87 dB. Limiting the peak acceleration to $0.005g$ in all directions, throughout the flight envelope, would go a long way towards ensuring a "jet-smooth" ride quality and justifying the ambitious long range goal limit of $0.005g$ to be achieved by the year 2022 suggested in Ref. [2].

Even the $0.05g$ target is an ambitious goal and must be defined more clearly. The now obsolete MIL-H-8501A standard established low speed vibration limits of $0.15g$ for frequencies up to 32 Hz, and $0.2g$ for frequencies under 36 Hz for high speed level flight. In Ref. [6] Arnold shows that even these targets were met with difficulty by current helicopter designs over the entire flight envelope, in particular in the high speed range.

Compared to the MIL-H-8501A, which was primarily concerned with the effect vibrations had on the pilot's ability to handle the helicopter, more modern standards such as the International Organization for Standardization (ISO) 2631 and the Aeronautical Design Standard (ADS) 27, provide guidance for evaluating the severity of human whole-body exposure to mechanical vibration and shock. The general philosophy behind these standards is to account for the combined effects of the different whole-body vibration (WBV) exposure variables (i.e. intensity, duration, direction and frequency) which affect the human body. Consequently, ADS-27 and ISO 2631 standards tend to impose more restrictive limits on the vibratory environment applicable to rotary-wing aircraft. Refer-

ence [11] breaks down the strengths and weaknesses of the two based on comparisons of vibration signatures from UH-1 and UH-60 helicopters.

Defined by Crews [12], the Intrusion Index is the fundamental metric used in the ADS-27 specifications to quantify the exposure level to whole body vibration experienced in the helicopter environment. It is defined as the norm of the four largest weighted peak amplitudes along each of the three orthogonal axes on each point where the Index is being computed. Therefore it follows that limiting the four largest components in each of the three orthogonal directions to a peak of $0.05g$ at normal blade passage frequencies (i.e., 16 Hz) or above typically leads to Intrusion Index values of about 0.8–1.4. For frequencies at or below a typical blade passage frequency, such values for the Intrusion Index will tend to push the peak acceleration requirements down to much lower values. The latter situation is probably not representative because the Intrusion Index is dominated primarily by bN/rev harmonics produced by the main rotor loads.

The original motivation for establishing the ADS-27 stems from the failure of the UTTAS and AAH projects to meet their original human factors specifications [12]. These aimed to limit peak vibration in all directions to about $0.05g$ at the blade passage frequency and below, but none came close. Present day helicopters, especially medium to heavy lift models, still face tremendous difficulties in meeting vibration levels as specified by ADS-27, when equipped only with passive vibration damping mechanisms. If only the 25 Hz frequency is considered, a peak $0.05g$ vertical acceleration will result in an Intrusion Index of about 0.4 to 0.5, which amounts to about 1/5 to 1/4 of current AH-64 and UH-60 Intrusion Index values in a worst case level flight [12]. In Ref. [5], Bousman compares Intrusion Index values computed from measurements obtained during the UH-60A

Airloads program with data measurements reported by Crews (see [12]) as well as from data recorded during the acoustics flight testing program detailed in Ref. [13].

Noise categories are differentiated between internal noise, affecting primarily the crew and passengers, and external noise, which carries implications for the communities surrounding aircraft operation centers. Both are equally significant if rotary-wing aircraft are to be successful in the civil transportation market. Although engines and rotors contribute to the overall cabin noise levels, the principal source of internal cabin noise, and the most disturbing, is the high frequency noise generated by the transmission gears. Gear noise is transmitted to the cabin through the structure of the airframe, which suggests the best way to isolate the noise is by actively canceling the vibratory loads directly at the points where the gearbox is mounted to the structure. Active noise control techniques implemented in the Sikorsky S-76 achieved an extraordinary 10–20 dB noise reduction for the main gear mesh frequency [14].

Vibration and cabin noise are not the only significant barriers stunting the potential use of the helicopter in civil transportation. External noise is a very troublesome characteristic, specially as cities and urbanized areas become more and more crowded, and helicopters are increasingly called upon to operate to and from these areas. Regulatory entities such as the FAA and ICAO enforce strict maximum allowable overflight noise limits in order to minimize the strong environmental impact noise has on surrounding communities. Every new helicopter must pass rigorous flyover noise certification tests in different flight conditions.

External noise is mostly governed by rotor noise and is therefore more in tune with the discussion on active rotor control which is the purpose of this study. So-called blade-

vortex interaction (BVI) noise and high speed impulsive (HSI) noise are highly obtrusive and problematic sources of rotor noise, due to their impulsive nature. Most passive solutions involve innovative blade designs aimed at reducing rotor blade tip vortex strength or shock effects, and thus directly attacking impulsive rotor noise at its source. BVI and HSI noise radiation directivity patterns are fairly complex, and are beyond the scope of the present discussion. However they are relevant because they directly affect how noise radiation affects surrounding communities. HSI, for example, propagates forward of the rotor plane. BVI noise propagation tends to propagate mostly forward and downward. Both, BVI and HSI noise radiation are largely dependent on the flight condition (i.e., speed and path angle). Typical peak BVI noise values, forward of the rotor plane, range from 80 to 110 dB, and reductions of 4–14 dB have been reported through the use of advanced blade tip planforms and special airfoil designs [2, 15]. Active rotor control techniques may make it possible to further reduce helicopter acoustic signatures, beyond the limits achievable through passive methods only.

Even though the issues regarding noise and vibration examined in the previous discussion are certainly as relevant today as in the near future, they take on an entirely new significance, considering their adverse impact on the long-term development of future rotary-wing aircraft. Requirements for future generation rotorcraft will see increasing growth in payload, cruise altitude, speed and endurance specifications. A series of studies sponsored by NASA have identified potential requirements for future transport runway independent aircraft for them to be viable from a commercial point of view [2]. In these studies, future technologies are cited as requiring the capability of flying 50–120 passengers in excess of 340 kn.

Motivated by these RIA studies NASA has recently focused on the technologies which will enable a hypothetical civil VTOL transport capable of carrying 120 passengers at a cruise speed of 350 kn at 30,000 ft of altitude and a 1200 nm range [16]. The investigation of several rotary-wing conceptual configurations presented in Ref. [16] identified the tilt-rotor as the best candidate to fulfill the theoretical requirements of a large civil VTOL airliner, in terms of cost efficiency and performance.

Requirements for a heavy lift VTOL military transport have simultaneously motivated the research of similar concepts under the Joint Heavy Lift (JHL) program. Driven by specific military tactical requirements, JHL emphasizes larger payload capacity (16–26 tons) over range (210–500 nm radii) or cruise speed (treated as a design variable). Although these numbers are naturally in flux, overall, such an aircraft would be comparable in size to NASA's Heavy Lift Rotorcraft System, and would be limited by the same technological barriers.

For comparison purposes only, consider the current Mil Mi-26P civil transport version, which is quoted as being capable of carrying 63 passengers at a cruise speed of 137 kn (and a maximum of 160 kn) over a 1,080 nm (1,240 mile) maximum range [17]. The Mi-26 pretty much represents the current state-of-the-art in terms of heavy lift helicopters. Put in these terms, NASA's goal amounts to carrying about twice the number of comfortably seated passengers at speeds over twice those of the current state of the art, as defined by the Mil Mi-26P, over comparable distances.

The Mi-26 is reported to have fairly smooth and quiet ride characteristics (e.g., [18]). Clearly the 8-bladed rotor makes for lower noise and vibration signatures, when compared to other rotors, but pays a heavy price in terms of cruise speed and performance.

This is an inescapable consequence of conventional helicopters which have to drag a rotor sideways through the air, which is why heavy lift rotorcraft will probably not follow in the lines of the conventional helicopter, but will rather take shape in the form of tilt-rotor or compound rotorcraft configurations. These new concepts present their own set of aeromechanical and aeroacoustic challenges, which will in all probability drive the necessary advances in active control technologies.

Driven by the necessity of minimizing induced velocity and of optimizing hover performance, main rotor sizing is largely dependent on the disk loading, which must be held to a minimum. The strength of the rotor wake induced velocity field is of primary concern to the safety of all ground crew and installations serving the aircraft, given the amount of thrust that these rotors have to generate. Disk loading is clearly a factor also in determining the induced power required. The requirement for a low disk loading factor at the given rotor thrust results in very large rotors and consequently low main rotor speeds, due to tip speed constraints. The large civil transport concepts in Ref. [16], for example, have main rotor speeds ranging from 137 to 162 rpm (140 rpm for the LCTR) for hover, from 51 to 75 rpm (75 rpm for LCTR) for cruise, and rotor diameters in the order of 76.7 to 90.5 ft (88.7 ft for LCTR).

An unintended consequence of the low rotor speed and elongated blades is that they result in a lower fundamental blade flapping frequency, bringing it closer to the region where pilots or flight control systems tend to operate. Main rotor frequencies found in the large civil transport study range from 2.28 to 2.70 Hz for hover, and from 0.85 to 1.25 Hz for cruise.

Additionally, the sheer size and large inertia of these aircraft are likely to result

in low frequency flexible structural airframe modes, which in turn may create complex aeromechanical rotor-fuselage couplings. To make matters worse, these heavy lift airliners may have multiple rotor systems, and their position on the aircraft may be inconvenient, if not detrimental, to the overall design of the aircraft. Consider the different tilt-rotor configurations, for example. Outboard placement of engines and rotors on the wing tips make them especially susceptible to low frequency and large amplitude motions.

Reference [16] provides a preliminary analysis of the sizing results on airframe structural modes for all three of the heavy lift airliner configurations detailed in the study. In the particular case of the LCTR, both operating modes put the 4/rev blade passage frequency right on, or very near, the natural frequencies of different structural airframe modes as well as blade modes. The most critical of the two operating points is that for cruise, because the 5.0 Hz blade passage frequency falls well within reach of the natural wing mode frequencies. Airframe structural frequencies range from 2.64 Hz to about 11 Hz. The first six modes are identified to be the symmetric and antisymmetric bending, chord bending, and torsion wing modes, which roughly puts them at about 2.6–5.0 Hz. The lowest frequency wing mode for the LCTR is the symmetric wing beam bending at 2.64 Hz. Blade passage frequency for the hover operating mode is 9.33 Hz. At this frequency, main rotor vibratory loads fall near the highest frequency airframe modes which turn out to be fuselage modes.

In general all three configurations have a low speed rotor operating point, resulting in a blade passage frequency that can potentially excite some of the airframe's natural modes. Also, because these concepts have rotors that operate at two distinct speeds, this brings up questions about the potential effect of fuselage-rotor interactions on the heli-

copter dynamics as the rotor spins up or down, and rotational speed or blade passage frequency pass through the frequency range of fuselage modes. Note that because blade passage frequencies, especially the 5.0 Hz cruise frequency reported for the LCTR, fall right on the frequency range of greatest discomfort for human beings, vibration attenuation becomes a critical design necessity.

Tilt-rotors pose an aggravating noise propagation problem due to the variable orientation of the main rotor tip path planes which causes them to intersect the fuselage when transitioning into cruise flight, thus increasing the impact of main rotor noise on interior cabin. The actual significance of this particular factor depends on the eventual impact of BVI or HSI noise on the interior cabin environment. But the possibility clearly does exist.

1.1.2 Active rotor control

Vibration and noise reduction designs integrating passive elements with fixed characteristics, such as, hydraulic or mass dampers, or even clever mechanical or aerodynamic blade design features, into the rotor system in order to modify its natural dynamic response, typically only operate optimally for a specific flight condition. When passive methods are insufficient for providing adequate noise and vibration qualities, additional reductions may only be possible by means of active control techniques.

Active rotor control is a loose definition that encompasses different control techniques developed over the previous three decades for purposes as varied as helicopter vibration suppression, noise reduction, performance improvement or even rotor blade aeromechanical stability augmentation. Survey papers presented by Friedmann et al. [19,

20] and Teves et al. [21] review many of the different technologies and trends in the fields of rotary-wing active control, mainly that of active rotor control. Passive and active BVI noise abatement methods are reviewed in Ref. [15].

Higher Harmonic Control (HHC) and Individual Blade Control (IBC) are active vibration control technologies designed for the purpose of reducing N/rev (N being the number of blades) vibratory motion in the fuselage. HHC and IBC concepts are oftentimes classified specifically in the literature as active blade *root* control concepts due to the fact that these technologies originated from swashplate-based actuators, where whole blades were necessarily oscillated at the root. Since, promising active twist and trailing-edge flap controlled blade technologies with smart material actuators have emerged, allowing control loads to be applied directly at the region of the blades where they can have the greatest impact on the rotor's aerodynamic loading, and thus avoiding the need to actuate the entire blade. Notional methods involving smart materials and structures that could, hypothetically, actively modify the mechanical properties of the blade root springs have also surfaced in the literature. One example of such methods has been presented in [22], where it was shown that good vibration reduction characteristics can theoretically be achieved by generating multi-cyclic variations of blade root flap and lag stiffness.

One of the main concerns arises from the ability, or inability, of the rotor blade actuators to operate simultaneously in the frequency bands needed for primary control as well as for noise and vibration control. Several recent studies have investigated the theoretical feasibility of employing on-blade elevons, or trailing edge flaps, as a means of providing primary flight control in place of more conventional rotor swashplate mechanisms. These studies have shown the potential of trailing edge flaps to satisfy the primary

control requirements in steady flight conditions. By means of a simplified aeroelastic model, Ormiston [23] examined the fundamental characteristics of a swashplateless rotor with on-blade trailing-edge flaps, or elevons. In particular, Shen et al. [24–29] carried out a comprehensive aeromechanic analysis of the use of trailing-edge flaps on helicopter blades in a swashplateless rotor. A parametric study of various key design parameters was performed, and an effective optimized design of the trailing-edge flap system was determined. Helicopters operate in, or are designed for, a wide array of tasks. In order to measure or qualitatively characterize the usefulness of on-blade trailing-edge flaps for primary control purposes, it is necessary to understand how much control authority can be exerted on the aircraft when maneuvering or performing specific mission task requirements other than flying in a straight and level trajectory. Reference [30] addressed some of these issues by quantifying the small-amplitude attitude change handling qualities of a medium weight articulated rotor helicopter–through bandwidth and phase delay simulation results of the helicopter pitch and roll attitude responses to longitudinal and lateral inputs–in accordance to the Target Acquisition and Tracking metrics specified in the ADS-33 aeronautical design standard performance specification.

On a basic fundamental level, active control is understood to act on a dynamic system through the explicit application of force or moment in response to input or feedback. Accordingly, active blade or rotor control systems usually operate by directly altering the aerodynamic loading on the rotor blades in an attempt to modify its dynamic response. Interference of the active rotor control system with the rotor aerodynamic loading brings up questions about the possibility of active rotor control and flight control requirements acting in contraposition of each other, considering that the rotor provides not only he-

licopter propulsion and lift, but also the primary means of aircraft control available to the pilot. This is a critical question, because if these technologies are ever to be widely employed in production helicopters, rotor induced noise and vibration reduction must be achieved without degrading performance or handling qualities.

Active control techniques for vibration suppression operate on the principle that *interharmonic coupling* due to the periodicity of rotor dynamics in forward flight (see Ref. [31]) can be exploited by adding suitably phased and modulated higher harmonic components, such as, e.g., N, $(N \pm 1)$ and $(N \pm 2)$/rev, to the rotor controls in order to achieve attenuation of N/rev vibratory components in the fuselage. Recognizing that rotor noise and vibration are fundamentally precipitated by the same phenomena, namely, unsteady blade aerodynamic loading and motion in forward flight, has spurred appreciable research on rotor noise reduction techniques, by means of the basic principles normally studied in the context of vibration control [15]. Experience has shown it is generally not possible to suppress rotor low-frequency noise and vibratory loads simultaneously at these frequencies, due to significant phasing discrepancies between independent optimal control requirements for each problem [15,32–38]. Blade control inputs at 2/rev, however, have been shown to be advantageous in effectively reducing low-frequency BVI noise, while at the same time improving performance, without impacting fuselage vibrations [15, 39].

In reference to feedback, active rotor control can be either open or closed loop, without distinction. Feedback control methods may allow for active rotor systems which can adapt to different operating flight conditions. Inevitably, issues about stability crop up when introducing closed loop control concepts, and care is needed to make sure that

feedback gains do not cause the helicopter to become unstable or cause adverse aeromechanical interactions.

Concerns about vibration control interfering adversely with performance or rotor noise characteristics, for example, may translate to the design of closed loop controllers, depending on the closeness of the effective frequency bands for vibration, BVI noise and performance control, as well as flight control, in particular if control inputs are not steady, because of frequency shifting induced by time-modulation of the amplitude of the higher harmonic controls. Risk associated with this particular aeromechanical interaction is amplified in helicopters with lower number of blades (i.e., 3 or 4 blades), while rotors with a higher number of blades (i.e., 6 or higher) may pose a very light coupling risk due to the natural separation of "vibration control frequencies" and "noise and performance control frequencies". In a 6-bladed rotor, for example, "vibration control frequencies" range from 4 through 7 or 8/rev, while "noise and performance control frequencies" are confined to 2 and 3/rev. However, very limited attention has been devoted so far in the literature to the dynamic analysis of vibration attenuation schemes (see, e.g., [40, 41])

Active rotor and flight control methods will play a prime role ensuring that next generation breakthrough concepts overcome current technological barriers which restrict the full potential of rotorcraft for commercial transportation and military systems, with the general idea in mind that noise and vibration should be brought down to levels comparable to those of current fixed-wing subsonic aircraft.

Recognition that, on a fundamental level, helicopter noise and vibration are precipitated by the same phenomena, namely unsteady blade aerodynamic loading and motion, has spurred appreciable research on helicopter rotor noise reduction techniques, through

basic higher harmonic control and individual blade control principles normally studied in the context of vibration control. Remarkable progress in understanding the fundamental physical causes and adequate reduction mechanisms for main rotor noise has taken place over recent decades [15]. Given the complexity of modeling BVI noise analytically, the bulk of the work has been limited to experimental settings. Active blade twist or trailing-edge flaps, as well as conventional blade root HHC and IBC pitch concepts have shown promise for noise reduction, provided actuator power requirements can be met. Although HHC has been shown to be effective in reducing BVI noise, one of the challenges has been to optimize the simultaneous vibration and noise reduction. HHC settings producing minimum noise do not necessarily yield minimum vibration, so optimal solutions normally entail a compromise. While HHC has been proven successful in reducing BVI noise, it has also shown a tendency to increase low frequency noise. On the other hand, IBC tests have shown 2/rev pitch inputs are more adequate for achieving simultaneous reduction of rotor noise and vibratory loads [37]. Since Ref. [15] was published, wind tunnel tests on an active twist rotor have confirmed the difficulty in achieving simultaneous control of BVI and low frequency noise, as well as N/rev vibration, with $(N-1)$, N and $(N+1)$/rev harmonic inputs only [36]. An aeroelastic model suitable for BVI noise simulations presented by Liu et al. [42] has shown a good agreement with experimental results in terms of simultaneous vibration and noise reduction, signaling the possible maturation of analytic computational models. References [43, 44] present further advances in these areas.

Emphasis on active rotor noise control techniques has mostly been limited to open-loop, experimental studies. Few studies have investigated the potential implications of closing the feedback loop. Kube et al. [45, 46] carried out a series of wind tunnel demon-

strations showing the utility of closed loop HHC for simultaneous reduction of BVI impulsive noise and vibration. The difficulty in accurately modeling or predicting BVI noise levels analytically has largely stunted the development of closed loop BVI noise control algorithms. As far as the controller design is concerned, BVI plant dynamics are highly nonlinear. Some advancements have been made recently [47], on the basis of a very specific set of simplifying assumptions.

Eurocopter Germany carried out a series of flight tests demonstrating the use of closed-loop IBC on a MBB BO105 helicopter equipped with on-board microphones [48]. Success of the BO105 tests has spawned further initiatives aimed at expanding the knowledge envelope to include different types of rotor systems and active rotor control concepts, namely the six-bladed articulated rotor on the CH-53G [40, 41], and a BK117-borne ADASYS four-bladed hingeless rotor system equipped with active trailing-edge flaps [49]. Presently, the main thrust of these initiatives has been directed at flight testing closed loop IBC for vibration reduction in the fuselage, with closed loop BVI noise control and rotor performance improvement investigations expected at some point in the future. In particular, flight tests with the BK117-ADASYS rotor system [49] have been designed with an emphasis on the system identification steps necessary for vibration controller design and testing. Additional flight test activities will involve topics such as aeromechanical stability augmentation, stall delay as well as rotor power improvements. Any flight testing program must be linked to to a serious effort in advancing the capabilities of comprehensive analytical prediction tools for active rotor control system developments. A recently closed-loop computational aeroelastic analysis using Actively Controlled Flaps [50] represents a positive step forward in this context.

Summarizing, it should be said that there is definitely fertile ground for the future growth of active rotor control technologies: firstly, so-called comprehensive models have matured to the point where they are beginning to prove useful for analysis and prediction by capturing, at least, the major aerodynamic and aeromechanic phenomena [51]; secondly, prototype active control technologies have been implemented into real-life helicopter testbeds which will allow future flight testing of open and closed loop control algorithms; and finally, the potential evolution of future rotary-wing aircraft concepts is intimately tied to the development of capable active rotor control techniques. Care must be taken, however, when studying these technologies in the context of frequency-domain feedback control, keeping in mind that closing the loop has implications regarding the stability margins of the entire system, and, also, remembering that potential FCS/ARCS interactions can occur due to the coupling of rotor and fuselage dynamics.

1.2 Literature Review

1.2.1 Higher harmonic control

As mentioned in the previous discussion, Higher Harmonic Control (HHC) is an active rotor control technique designed for the purpose of reducing N/rev (N being the number of rotor blades) vibratory components in the fuselage by adding higher harmonic components to the rotor controls. Amplitude and phase of these harmonics are determined on line by a suitable control law. If the higher harmonic inputs are applied in the rotating system, via rotating high frequency actuators, the technique is usually called Individual Blade Control (IBC). IBC and HHC are generally considered as effective techniques for

vibration reduction, but issues of power requirements and reliability have until now prevented widespread application on production helicopters [52].

HHC has been the subject of extensive research over the last three decades. Research previous to 1982 has been reviewed by Johnson [53] as part of an extensive study of several types of HHC algorithms and implementation techniques that remains relevant to this date. More recent survey papers have been written by Friedmann and Millott [19] and Teves et al. [21]. Although HHC is generally studied in the context of rotor control, the basic HHC algorithm has also been successfully used for fuselage-mounted active vibration reduction [54] and gear-mesh noise reduction [14]. Finally, it is worthwhile to point out that while HHC and IBC represent significantly different technologies from the implementation point of view (i.e., choice of actuators and sensors), they are completely equivalent from the control theoretic point of view. In particular, the extension of IBC to the more realistic case of a rotor with dissimilar blades requires only a trivial modification of the control algorithms. The terms HHC or IBC throughout this work will refer to the control logic itself, indistinctly of the blade actuation mechanisms.

Figure 1.1 shows the schematic of a typical HHC system for vibration reduction. While this is not the only possible approach, nor is it necessarily the best, it is important for historical and practical reasons, and has been extensively studied theoretically and experimentally (e.g., [55–57]). Some helicopter outputs, typically N/rev components of fuselage vibrations are extracted through a harmonic analysis, fed to a controller that computes appropriate values of the higher harmonic controls, which are then injected into the rotor controls. Since the controller is designed to deal only with the harmonics of vibration components and controls, it is therefore considered to effectively operate in the

frequency-domain. The notion of a frequency-domain higher harmonic controller which relates the harmonics of the vibration with those of the controls has presented a convenient model for HHC algorithm analysis, and has been widely exploited. Conceptually, this control system is designed to regulate the "envelope" variables that define amplitude of the harmonic vibration signal, rather than the vibration itself. Figure 1.2 portrays a simplified, frequency-domain schematic of the HHC closed-loop algorithm, which is coherent with this notion. Owing to the fact that the purpose of such a feedback configuration is to maintain vibration level at a minimum (ideally at zero), in the presence of external disturbances, it can be fundamentally considered to operate as a classical linear feedback regulator.

The steps necessary to carry out the transformation between the time and frequency domains are not instantaneous, but are carried out over finite time intervals, and therefore cannot be rigorously described by first-order, linear ordinary differential equations (i.e., in state space form). Consider, e.g., the hypothetical timing scheme in Figure 1.3. In this example, the control updating period is equal to one revolution. One quarter of a revolution is allotted for the system to settle to its steady condition. Sampling of vibration takes place during the second quarter of revolution. The remaining time is allotted for inner loop dynamics to take place. The closed loop HHC algorithm is typically defined, not as a continuous system, but rather at specific instants t_k, where $t_k = k\Delta t$. The controls are updated at every t_k, and kept steady during the entire time interval Δt, allowing sufficient time for the system to sample vibration, execute the harmonic analysis, and compute updated control amplitude and phase quantities; while at the same time allowing transient dynamics to dissipate. This modeling problem is the probable reason why, although the

basic characteristics of HHC algorithms have been investigated extensively, the influence of the aeromechanic behavior of the helicopter on the performance and, especially, the stability of the closed loop HHC system has been typically ignored.

The analysis of active vibration control in helicopters is aggravated by the time-varying, or more specifically, time-periodic nature of the helicopter equations of motion. Classical linear control theory stability analysis methods applicable to time-invariant systems do not carry over entirely to the time-varying case. The steady-state, frequency-domain reduction of helicopter dynamics (see Fig. 1.2) represents a natural solution approach to the problem, at the expense of oversimplifying the dynamics of both the helicopter and the HHC controller systems. However, this approach requires that helicopter dynamics be treated as quasisteady, that is to say, that transient dynamics in the response to HHC inputs be considered unimportant, so that closed loop helicopter plant dynamics remain, steady, or approximately steady, under the effect of the HHC controller. The underlying assumption is that HHC controls are updated slowly enough, that transient dynamics have a minimal impact on the closed loop dynamics.

Consequently, the majority of investigations dedicated to open or closed loop HHC performance or stability analysis have, up to date, generally relied on at least one of two fundamental simplifying assumptions [58]:

1. Helicopter response to higher harmonic inputs can be assumed to be quasisteady.

2. Periodic helicopter dynamics are inconsequential, such that helicopter can be modeled as a linear time invariant system.

Quasisteady T-matrix algorithm

Helicopter dynamics have mostly been considered indirectly, through their contribution to the quasisteady, frequency-domain rotor response to higher harmonic controls. The concept of a transfer, or T-, matrix to model the linear, quasisteady, frequency-domain approximation of the helicopter response to rotor control inputs, was first introduced by McCloud and Kretz [59], and has been widely used in the study of HHC algorithm performance. The frequency-domain representation of the helicopter dynamics reflects the periodic nature of the rotor control inputs and the corresponding helicopter response in steady flight. McCloud and Kretz [59] and Shaw [55, 56] present detailed analytical and experimental calculations of the T-matrix.

The entirety of T-matrix-based HHC algorithms are based on one of two possible models of the plant dynamics, as far as the vibration response is concerned. In this sense control laws can be based either on local or on global models of the plant dynamics. The former are based upon a linearization about the current operating condition. The latter assume that the system is linear over the entire range of control. Models differ only in the non-linearities of the plant dynamics. Therefore, the two approaches turn out to be equivalent if the actual helicopter plant is linear. The local response model relates the discrete change in vibration to the step change in the control input between two time samples. This relation can be written generically as

$$\Delta \mathbf{y}_k = T_k \Delta \mathbf{u}_k \tag{1.1}$$

where $\mathbf{u}$ represents generic control inputs, which in the classical HHC sense would be the blade harmomic pitch envelope variables. Comparatively, the global model is based on

the relation

$$\mathbf{y}_k = T_k \mathbf{u}_k + \mathbf{y}_0 \tag{1.2}$$

where $\mathbf{y}_0$ is the baseline, or uncontrolled, vibration; and $\mathbf{y}_k$ is the vibration at time sample t_k. Transfer matrix T_k can, generally, be time-varying, thus the subindex k.

Linearity of the plant dynamics for vibration reduction problem is generally shown to be a good assumption, as long as the amplitude of the control inputs remains small [55, 60]. There are however some instances where experimental results seem to indicate non-linear dependencies of the response on the magnitude of the control [61, 62]. Global T-matrix models are completely independent of the value of the controls. Should there be evidence of non-linear response to control over the required control amplitude range, then control design may require the use of locally linearized models. Molusis [63] presents a complete analytical discussion on some of the issues regarding non-linear phenomena, and how they affect the overall control design and convergence of the regulator to a minimum vibration level. The inability of HHC to completely eliminate vibration in some cases seemed to be explained by the presence of multiple local minima to which the various optimal control laws could converge to.

Feedback control design solutions can be fundamentally categorized according to the knowledge of the plant dynamic system that is available. In this sense, control laws can be either deterministic or stochastic. Deterministic control algorithms are implemented assuming perfect knowledge of the dynamic system is available. Deterministic control is possible, e.g., if perfect measurements of the control variables are available. In reality, only imperfect measurements are attainable due to the presence of Gaussian

noise and measurement error. In practice, performance of a deterministic control law in a stochastic environment is, inevitably, degraded by the random unmodeled dynamics present.

Uncertain quantities can be estimated, or predicted within a reasonable margin of error if the knowledge of the statistics defining these uncertain quantities is available, giving rise to what are known as stochastic control methods. Optimal stochastic control methods, for example, are designed to minimize an expected value of a performance function, rather than the function itself.

In the context of active rotor vibration reduction, deterministic higher harmonic controllers are commonly designed to minimize a weighted quadratic performance function of the vibration, as well as the control inputs and their increments. In general, such performance indicators typically fall into the form

$$J = \mathbf{y}_k^T W_y \mathbf{y}_k + \mathbf{u}_k^T W_u \mathbf{u}_k + \Delta \mathbf{u}_k^T W_{\Delta u} \Delta \mathbf{u}_k \tag{1.3}$$

where W_y, W_u and $W_{\Delta u}$ are the optimal control weighing matrices. The first recorded use of such an approach in the context of helicopter active vibration control can be found in the wind tunnel tests performed by Hammond [64]. Hammond tested a controller designed to minimize a quadratic performance function of the vibration harmonics of the hub moments and vertical shear in a model articulated rotor.

Stochastic minimum-variance controllers operate on the expected value of such quadratic combinations of the vibration and input harmonics, rather than on the quadratic performance index itself. Therefore, performance objective functions for such cases tend

to be expressed, for example, as

$$J = E\left\{\mathbf{y}_k^T W_y \mathbf{y}_k + \mathbf{u}_k^T W_u \mathbf{u}_k + \Delta\mathbf{u}_k^T W_{\Delta u} \Delta\mathbf{u}_k\right\}. \tag{1.4}$$

A special form of stochastic control, cautious control assumes that the control inputs are known and uncertainty is only found in the measured vibrations. The performance function reflecting these conditions then takes the form

$$J = E\left\{\mathbf{y}_k^T W_y \mathbf{y}_k\right\} + \mathbf{u}_k^T W_u \mathbf{u}_k + \Delta\mathbf{u}_k^T W_{\Delta u} \Delta\mathbf{u}_k. \tag{1.5}$$

Molusis, Hammond, and Cline [65] showed, through both analytical studies and wind tunnel tests, that a stochastic controller adapted better to variations of the flight condition (i.e., speed) than a deterministic one. Johnson [53] also touched on the issue of stochastic controllers, showing how the inclusion of information on the stochastic nature of the sensor measurements in the control law design decreases the response to measurement noise and increases the stability range of the controller. These findings were corroborated by Hall and Wereley [58].

Adaptive control and system identification

Identification of the plant dynamics is a fundamental element of HHC algorithm design. Over the years, a great amount of effort has been dedicated to the problem of identifying the rotor (or helicopter) vibratory response, or transfer matrix, to higher harmonic control inputs. Accurate calculation of the rotor, or helicopter, system transfer matrix has been shown to be an essential element of controller gain synthesis, strongly influencing algorithm performance and stability [53, 55, 57, 58, 66], especially in the face of potentially

variable operating flight conditions. System identification requirements vary according to the dynamic model assumed. Local models only require the knowledge of T, while global models require the knowledge of both T and $\mathbf{y}_0$. Consequently, control laws based on local models only require the identification of T. Global controllers can operate on the identification of either the uncontrolled vibration or the transfer matrix, or both. Whenever T is not identified on-line it must be provided some other way.

As far as system identification goes, there exist two fundamental options. Plant dynamics can be identified either off-line, and used in a constant control (i.e., fixed gain) algorithm, or on-line, typically by means of an adaptive recursive estimator.

The most common method for off-line identification of the system transfer, or response, matrix (and the baseline vibration) is through the application of the least-squares fit method to a succession of measurements of the system output, in response to a known input. Nearly all methods of parameter identification, whether off-line or on-line, originate from this technique. Test input signals consist of harmonic functions and are described by their Fourier series. References [55, 57, 58, 66] present some examples of fixed-gain controllers for active reduction of vibration. Off-line techniques are not appropriate for identification of local models, because the latter typically involve time-varying parametric values.

Some studies have retained some level of periodicity for design and analysis, recognizing that control can be improved by introducing information on the LTP dynamics [67–71]. Frequency-domain system identification of LTP systems is slightly more involved, requiring the identification of the multiple components of the harmonic transfer function (HTF) [67, 68]. The steady response matrix T represents only the constant

portion of the HTF. Practical system identification methodologies have been established in order to determine the multicomponent HTF [69–71]. Since the frequency response of LTP systems involves a time-dependent aspect, these techniques which have been proposed must register the time at which the input and output occur, as well as the inputs and outputs themselves. Test signals must include this time-varying element. Parameter identification of LTP systems is made possible by the introduction of a test input signal consisting of sinusoidally modulated Fourier series of a periodic signal [69]. This can be done also through a series of time delayed sine-sweep signals [70]. This methodology is implemented for system identification of the Active Twist Rotor system in wind tunnel tests [71].

Adaptive T-matrix algorithms require the knowledge of the control inputs and the measured vibration outputs at each time step in order to produce estimates of the transfer matrix. Existing methods reflect the stochastic nature of the actual operating conditions. Adaptive filters typically used for on-line identification of the system dynamics generally fall into the following categories: (1) Kalman filters or recursive versions of the least-squares (RLS) method, or (2) stochastic gradient descent methods such as the least-mean-squares (LMS) filter. One of the significant differences between the two approaches is that RLS or Kalman filters operate directly on the signals or measurements themselves (and thus depend on the statistical characteristics of the environment to be provided by the designer as input), rather than on the stochastic characteristics of the signals, as is the case with LMS filters.

Shaw and Albion [60] tested the closed loop feedback control of 3, 4, and 5/rev root flapwise bending moments in a model hingeless rotor. Wind tunnel tests confirmed the

dependency of the T-matrix on the flight condition (i.e., airspeed). A theoretical analysis by Shaw [55] considered the influence of errors in the estimate of T on controller stability, showing that either gain-scheduled feedback gains, or online identification, was required to achieve good vibration rejection performance in the face of varying flight conditions during accelerating flight. Good convergence and stability was demonstrated with the Kalman filter that was tested.

Taylor, Farrar and Miao [62] presented the results from a numerical, time-domain simulation of a closed loop adaptive stochastic higher harmonic control algorithm designed to minimize the expected value of a quadratic performance function of fuselage mounted accelerator signals and control inputs. Performance was evaluated in terms of the quickness of the transient vibration rejection response. Influence of the quadratic performance function weighting coefficients, as well as the amount of sensor noise, on the vibration rejection speed was investigated.

Wind tunnel tests of closed loop deterministic control of an articulated model rotor [65] showed that the identification of baseline vibration, by itself, failed to provide reasonable tracking for the varying airspeed conditions. Deterministic controllers with on-line identification of the T-matrix exhibited better, although erratic behavior. Good performance, defined by a smooth operation and tracking ability, was only possible with the stochastic (cautious) controllers.

These studies motivated the comprehensive review [53], at the time, of the current HHC system identification and control algorithms. Johnson reviews some of the recursive algorithms commonly employed for on-line or adaptive system identification: mainly, the Kalman filter method and various recursive adaptations of the basic least-squares method.

Around the same time, Chopra and McCloud [66, 72] presented a numerical investigation of some of these algorithms, including open and closed loop configurations with both off-line (fixed-gain) and on-line (adaptive) system identification. Chopra and McCloud [66] illustrated for a multi-harmonic HHC configuration how the erroneous modeling of the T-matrix, for any given flight condition, can result in an unstable closed loop.

Although erroneous estimates of T are a primary cause of closed loop instability, adaptation amplifies control response time delays, making it more sluggish, and potentially incapable of reacting to rapidly changing vibration amplitudes. Considering this restriction, it may be advantageous to implement a gain-scheduled, fixed-gain control law to account for the varying operating conditions. This is precisely one of the premises in the work by Hall and Wereley [58]. Wind tunnel testing by Shaw et al. [57] on a dynamically scaled three-bladed CH-47D rotor had previously demonstrated that fixed-gain control, with gain-scheduling, can be effective in achieving multi-component suppression of hub loads. Determination of the baseline vibration was done either by direct measurement or estimated through a Kalman filter. The controller was shown to be able to cancel step changes in vibration amplitude with a time constant of 160 msec. Hall and Wereley [58] showed that the basic T-matrix algorithm is sufficiently robust that specific adaptive techniques may not be necessary. However, the helicopter model may be overly simplistic to be able to make this assessment.

More recently, Jacklin [73] compared the performance of different identification algorithms with respect to the Kalman filter method. The results of this study indicate that all the system identification methods produce similar accuracy, but differ substantially in the complexity of implementation. These differences have an impact on the computational

speed of the different techniques. The speed of the Kalman filter comes from the fact that the algorithm assumes the initial estimate of T, T covariance, measurement-noise covariance, and process-noise covariance are known or can be assumed. Least-mean-squares filters, on the other hand, require no a priori knowledge of the theoretical qualities of the estimates. This makes them slower, but also computationally more robust.

Classical recursive adaptation techniques, such as those mentioned in the previous discussion, bring about unfortunate consequences which complicate the analysis of HHC stability by introducing nonlinear feedback control laws into the regulator loop dynamics. Recursive algorithms for on-line system identification create dependence of the estimated T-matrix (and therefore the feedback gain) on the controls. This is not unexpected, since the adaptive algorithms discussed require the knowledge of the controls in order to estimate T from the measured response. These nonlinearities make the analytical stability evaluation of the coupled, closed loop higher harmonic control system (i.e. regulator) unsuitable for analysis by means of classical control theory. Rather, their analysis is heavily dependent on simulation studies (e.g., Ref. [66]).

In addition to these nonlinearities, feedback adaptation introduces time-varying dynamics into the loop by changing the parameter estimates at each time step. Under these conditions eigenvalues are time-varying and cannot be used to establish global stability conditions, but rather if each individual step will converge or diverge from the previous state. The same is also true, of course, if the plant matrix T is time-varying due to changing flight conditions. A necessary assumption imposed on the analysis is that the system identification filter be allowed to converge to a steady solution before the control is updated for the next iteration (as well as T varying slowly enough that it can be considered

steady during the algorithm cycle) [53, 55].

The problem of system parameter identification and its effects on algorithm performance is thoroughly investigated in Ref. [53]. Since this study, the focus on the HHC algorithm has largely centered on the convergence characteristics of the controller, in the face of model uncertainty. Recently, Chandrasekar et al. [74] consolidate and extend the existing literature into a common framework for algorithm performance analysis. Following this methodology or line of thought, Patt et al. [75] have explored numerical techniques with the purpose of improving the disturbance rejection robustness properties of the HHC algorithm. This so-called relaxation technique introduces a positive and less than one weighing (i.e., relaxation) coefficient that multiplies the optimal control step change at every time step, effectively reducing the magnitude of the feedback gain. This basically has a similar effect as rate limits have on the optimal control gain synthesis, making it less responsive or sensitive to errors in the estimate of the plant dynamics, by slowing down the speed of response of the controller [53, 66].

Alternative control algorithms

Apart from T-matrix based algorithms or control laws which form, by far, the most common approach, a significant number of alternative control methodologies can also be found throughout the literature on active vibration control. Some of these are covered in this Section for the sake of completeness. All of these approaches have dealt, in one way or another, with the periodic dynamics system identification, and control, problems previously discussed. As a general rule, periodic dynamics increase the complexity of

the various control laws proposed. In some instances periodicity has been explicitly neglected, with this having varying degrees of impact on the performance.

An alternative approach to the active vibration control problem was proposed by Gupta and Du Val [76]. A linear time-invariant helicopter model in hover, including both fuselage and simplified rotor dynamics, was coupled to a frequency-tuned state feedback vibration controller designed to target rigid fuselage accelerations at the vibration frequency ($N\Omega$). In essence, the vibration controller was designed to optimize a quadratic cost functional, with frequency shaping of the feedback gain achieved by imposing large penalties on fuselage accelerations at the vibration frequency. The narrow band feedback control law was implemented by passing fuselage accelerations through a set of undamped second-order filters tuned to resonate at the N/rev frequency. The issue of periodicity in the equations was eschewed by limiting the study to a linear helicopter model in hover. Any remaining periodic terms are eliminated from the equations by defining the rotor degrees of freedom in the non-rotating axes via a Multi-Blade Coordinate (MBC) transformation. This alternative method of vibration attenuation belongs to a different class of control systems and it completely omits the effects of the digital implementation of the extraction of output harmonics.

Throughout the 1980s, and early 1990s, Ham and McKillip explored various time-domain, LTP system identification and closed loop control techniques for blade dynamics in the rotating frame, in the context of IBC [77–83]. The methods proposed shied away from LQG optimal control approaches precisely because of their propensity to produce large feedback gains at the control frequencies [79]. Rather, they opted for a model following technique, in the context of time-domain, state-space control, using an array of

accelerometers laid throughout the rotating frame of reference as "kinematic observers" to try to reconstruct unknown states and to accurately identify the system periodic parameters [81–83]. This problem is inherently time-periodic because the signals picked up by the accelerometers involve a description of system dynamics, resulting in periodic output dynamics. This was observed to be an important source of complexity for observer-based techniques and Kalman filter designs.

In a more recent approach, the adaptive potential of neural networks was employed in an IBC system, and was shown to asymptotically cancel vibrations in a rotor system equipped with trailing-edge flaps [84]. Again, system periodicity was shown to increase the complexity of control system algorithms, and LTI algorithms were only able to provide good performance as long as time-varying dynamics remained relatively small.

The problem of periodic control has been treated rigorously from a control theory perspective by several authors [85–89]. The emphasis of these studies has been on finding solutions for the associated periodic Riccati equations or linear matrix inequalities resulting from the formulation of the periodic disturbance rejection problem of a known frequency through modern (optimal or robust) control synthesis techniques. With the focus of these studies centering on the mathematical or theoretical aspects of the control algorithm and the disturbance rejection performance, however, no formal stability analysis has been established.

Arcara et al. [85,86] find a solution inspired by optimal control theory. The resulting differential Riccati equation is solved on the basis of the solution being periodic. Solving the periodic Riccati equation is computation intensive, therefore such an approach is fine for the design of fixed gain controllers but is impractical for purposes of adaptive

techniques. Bittanti and Cuzzola [88, 89] take this a step further by framing the periodic disturbance rejection problem via H_∞ techniques.

Mannchen et al. [90, 91] approach the problem by performing the controller design based on reduced order linear, time-periodic, models of the helicopter dynamics at multiple equally spaced azimuthal positions of the rotor, resulting in a time-scheduled controller with a period equal to one revolution. The added knowledge in the controller design was found to improve the performance in simulations.

1.2.2 Stability Analysis of Closed-Loop Higher Harmonic Control

Arguably, the most significant consequence that results from approaching the subject of closed loop HHC from a quasisteady perspective is that under steady flight conditions, the stability of the closed loop is inferred directly from the stability of the controller. Consequently, stability analyses have mostly focused on the stability, or convergence, of the HHC update algorithm in the face of model uncertainty, with or without on-line identification, not on the closed loop stability of the complete helicopter under the control of the HHC system [53, 55, 66, 75].

Additionally, no studies have formally accounted for the discrete-time dynamics resulting from the digital implementation of the sampling and the harmonic analysis. This is probably because, with the inception of a frequency-domain model for the helicopter all the details of the real-time implementation of the sampling and harmonic analysis discrete dynamics can be integrated into the helicopter model as shown in Fig. 1.2, in order to simplify the HHC controller analysis. However, when operating conditions are not

quasisteady, these elements become relevant and should not be neglected in the analysis. Roughlty equivalent time-continuous approximations, or representations, of the algorithm components have been suggested in order to facilitate the stability analysis [58, 92] of the closed loop system.

Quasisteady sssumption

The interval Δt between control updates is chosen, not only to allow for the real-time implementation of the time to frequency domain transformation, but to let the transient response die out. This last provision is essential to guarantee a quasisteady helicopter response to the HHC inputs. The implication is that system vibration response at time instants t_k correspond to the steady-state, frequency-domain response of the system. Contrary to the general case, under quasisteady flight conditions the discrete-time algorithm response at time instants t_k matches the expected continuous-time response accurately. Since the dynamic response in both cases is equivalent, stability can therefore be inferred from the convergence properties of the resulting algorithm.

Furthermore, after it has been applied, the control input is kept steady during the entire interval in between time samples. The helicopter is assumed to reach its steady state during this interval. Therefore, the helicopter and HHC control system effectively operate together as an open-loop system during every interval Δt. Shaw therefore suggested that closed-loop stability can be inferred from the stability characteristics of the open-loop [55]. The argument can be taken further. If the helicopter is stable, then the stability of the entire vibration control closed loop system is determined only by the stability of

the control algorithm. This goes to show that in the absence of transient dynamics due to the quasisteady restriction, any source of unstable dynamics in the closed loop must be produced by the controller itself [53].

The theoretical investigation by Shaw [55] is the first to relate the convergence rates of the constant, or fixed-gain, closed loop regulator dynamics with the roots of the associated characteristic equation. Based on these simulation studies, the closed loop regulator is shown to take anywhere between 2–5 controller cycles (i.e., approximately 1–2.5 sec), either to converge to its steady state, or to completely eliminate the vibratory components. In certain conditions it was shown that the closed loop system might become unstable when the transfer matrix used for gain synthesis is too far off from the actual steady response of the plant. Control gains in this study were obtained by direct inversion of the assumed T-matrix.

Johnson [53] examined the essential qualities of various possible regulator configurations in light of a thorough discussion of the different control elements: the helicopter model, the system identification and the control problems, including open loop and closed loop feedback. The analysis considers, without loss of generality, a SISO version of the algorithm. Controller dynamics resulting from the different optimal control laws are examined in conjunction with the adaptive filter coupling.

The stability analysis of the various optimal deterministic closed loop control options, and how they affect controller stability is presented in a very general form. In fact, in the particular case when $W_u = W_{\Delta u} = 0$ the analysis presented in Ref. [53] reduces to the same result obtained from the stability analysis of the closed loop controller in the theoretical work by Shaw [55].

Reference [53] provides guidance for the selection of the different design parameters of the optimal control regulators proposed in the literature, such as the optimal control weighing coefficients, the Kalman filter measurement noise variance and parameter variance, and the choice of system identification algorithm. It is shown how W_u and $W_{\Delta u}$ increase the stability range for estimation errors of T (i.e., large $W_{\Delta u}$ reduces the sensitivity of the regulator to errors in the estimate of the transfer matrix T, and to measurement noise.) The problem with control magnitude limits, W_u, is that they curtail the maximum possible higher harmonic control authority. Rate limits $W_{\Delta u}$ are generally preferable because they reduce sensitivity to measurement noise and estimation error [53]. Rate limits are recommended to be as large as possible, as long as the controller response is not too sluggish.

Chopra and McCloud [66] carry out a numerical evaluation, through simulation, of multi-harmonic deterministic versions of the regulator algorithms discussed in Ref. [53]. These analytical results confirm the stabilizing effect optimal control rate limits $W_{\Delta u}$ can have on the closed loop regulator eigenvalues of fixed-gain controllers, when the matrix T estimated off-line differs substantially from the actual value of the plant T-matrix. Increasing sluggishness of these types of vibration controllers is also confirmed by the stability analysis, which shows that several of the eigenvalues converge towards one, in the complex plane.

Stability investigations [53, 55, 66] on the regulator-type closed loop higher harmonic control system configuration which are discussed above are fundamentally limited, however, to the analysis of the controller dynamics induced by the different control laws, and how the system identification filter technique impacts the aforementioned controller

dynamics. This approach is justified by the fact that the control law is the primary source of controller dynamics, whereas the helicopter steady plant model is simply considered part of the regulator loop closure.

Validity of the previous methods is predicated on the control input being updated slowly enough that transient dynamics do not affect the steady response measurements. Note that, if transient dynamics are not allowed to dissipate, the overall closed loop response at the sample times will contain a non-zero spurious component corresponding to the zero-input response of the states, resulting in erroneous control amplitude and phase estimates for the next iteration. This is in fact equivalent to introducing model uncertainty in the estimation of the T-matrix. Continuous, high frequency, periodic excitation of the system transient behavior may result in unstable or unbounded amplitude responses.

Although essentially defined as a discrete-time system, it has been shown that the universal HHC algorithm behaves fundamentally as a narrow band feedback controller centered at the vibration frequency $N\Omega$, achieving the reduction of vibration by ideally imposing an infinitely large feedback gain at this frequency [58]. Controller bandwidth, as an indicator of how fast the control input is updated, is inversely proportional to Δt.

The control update time step is conventionally considered to be at least one revolution of the rotor; on the basis of rotor wake natural settling times being of this order (i.e. damping ratio of 0.5–1/rev). Shorter update time intervals will result in a wider band controller which may excite unwanted or unforeseen helicopter modes causing them to become unstable. Furthermore, since rotor first lag (bending) modes as well as helicopter flight modes have slower transient dynamics, the assumption that rotor wake settling times determine the controller updating frequency may not be the best when the entire helicopter

is considered. A couple of studies [57, 62, 93] have compared, with mixed results, the effects of the frame time between control updates using simulation. Overall performance of the controller in Ref. [62] was not affected, probably due to the addition of stochastic control techniques. However, the potential destabilizing effect was hinted at from the simulations. A controller update rate of 1/4 rev during flight tests [41] was, however, found to be adequate and sufficiently slow that frequency ranges of the rotor dynamics and IBC control activity are well separated.

Broad band control methods

The performance and stability analysis of closed loop active vibration control systems is fundamentally limited by the need to guarantee quasisteady response conditions. Effects of high control bandwidth on helicopter stability cannot be fully assessed under these conditions. Either plant models which have been used were overly simplified, or controller bandwidth was purposely low. A few studies found in the literature approach the stability problem based on linear, time-continuous mathematical representations of the helicopter and the control system dynamics. Such represensentations of the dynamics are not bandwidth limited, allowing the analysis of closed loop stability in the face of a broad band control spectrum.

The stability analysis presented by Gupta and Du Val [76] is easilly one of the few studies to actually compute the stability eigenvalues of the closed loop, coupled helicopter/HHC system, and to look at the effects of fuselage and rotor, state or output feedback on the entire helicopter dynamics. This is made possible because helicopter dy-

namics have been formulated in a state-space LTI mathematical representation. Stability results appeared to indicate a significant effect of rotor state feedback on both fuselage poles and rotor (rigid flapping mode) poles. The procedure avoids, however, to deal with the problems imposed by the periodic dynamics in forward flight. Also, due to the alternative control algorithm definition, the discrete-time nature of the HHC T-matrix algorithm is fully neglected.

Hall and Wereley [58] present an equivalent continuous, linear and time-invariant representation of the classical discrete-time SISO T-matrix HHC algorithm. A stability analysis for a simplified LTI helicopter model is made possible on the basis of classical control theory analysis techniques. Stability margins were predicted to be large enough that control bandwidth could potentially be increased enough to produce a satisfactory vibratory disturbance rejection performance, without running an excessive risk of producing unstable closed loop dynamics.

In a more recent study, Shin et al. [92] relied on multiple SISO T-matrix controllers based on the continuous-time approximation introduced in [58] in order to achieve the multiobjective and multiharmonic control of the 4/rev and 1/rev hub loads of an Active Twist Rotor system. This arrangement avoids the issue of *interharmonic coupling*. Therefore, the individual controllers can be represented as LTI systems. Previous system identification tests [71] had confirmed the periodicity of this rotor system to be virtually negligible, allowing the use of LTI frequency-domain stability analysis techniques.

A generalization of the T-matrix algorithm has been proposed in the literature (see [37]) in order to exploit the *interharmonic coupling*, but no detailed theoretical analysis of that approach has been carried out so far. As the above mentioned generalization of

the T-matrix algorithm turns out to be a linear time-periodic compensator, it was referred to as the Periodic HHC (PHHC) algorithm. Therefore, both the HHC and the PHHC algorithms call for the use of periodic systems theory (see [87]) for closed loop stability and performance analysis. This is true even if helicopter dynamics are approximated by a LTI system of equations, because HHC controller is inherently periodic when frequencies other than N/rev are used.

Also, no study on the potential interactions between an HHC system and a flight control system was available in the literature. These analyses require a mathematical representation in state-space form, preferably with constant coefficients. Some recent studies have addressed this gap. However, they rely to a greater or lesser degree on approximations or assumptions put in place to simplify the issues with the modeling of periodic helicopter dynamics.

Falling short of approaching the subject of potential FCS/HHC interaction, some studies have been limited to the analysis of the interactions of the coupled rotor and fuselage dynamics, instead. Only Gupta and Du Val [76] present the topic from a control engineering perspective. Taylor, Farrar and Miao [62] present one of the few other time-domain analysis that include a full description of helicopter dynamics, although the quasisteady assumption is respected and no stability analysis is included. Friedmann et al. [94] and Papavassiliou et al. [95] present a comprehensive aeroelastic analysis of the effect of coupled rotor/fuselage dynamics on the steady-state performance of active vibration reduction control systems, but the analysis completeley neglects the transient behaviour and its potential impact on aircraft flight dynamics. The linear, time-invariant stability analysis in [76] presented one of the few state-space mathematical representations

of the coupled, helicopter-HHC closed loop system, suitable for this type of investigation.

More recently, Cheng et al. [96] have extracted a linearized, state-space, time-invariant model of the helicopter, and have used it for a study of the interaction between the HHC and the flight control system. Periodic dynamics resulting in forward flight have been removed through a time averaging process. The harmonic analyzer is essentially modeled after an analog filter, continuously extracting the required N/rev vibration harmonics. Computation delays are modeled using Padé approximants and the HHC input is updated continuously. The gain matrix T is fixed.

One important conclusion from these studies is that while the HHC appears to have very little influence on the flight control system and on the handling qualities, the reverse is not true. There is a significant effect of maneuvers on vibration, which leads to higher required crossover frequencies for the HHC loop. This phenomenon was clearly observed in the different IBC flight testing activities in [41], where significant variation in the IBC input amplitude and phase were commanded by the controller in response to the small disturbances created by the pilot as he reacted to counteract the atmospheric disturbances in steady state flight. However, no situations were observed in which the IBC actually increased the vibrations in response to maneuvering flight. The same is also true of earlier flight test initiatives presented in Ref. [97].

Based on these experiences, concern for these potential issues is clearly warranted in the case of heavy lift rotorcraft discussed in Sec. 1.1.1 due to the closeness of the operating frequencies of the pilot/FCS and HHC/IBC systems, as well as the natural frequencies of the structural modes. However, analytical investigation of these issues requires suitable methods and models which capture the mathematical and physical peculiarities of

the problem. Until now, no single analytical investigation on the problem of closed loop stability of helicopter active vibration control systems has presented a comprehensive or unified methodology capable of accounting for all of the issues simultaneously.

Stability Robustness and Performance

Feedback control design has always involved a careful tradeoff between the fundamental necessity to render the system insensitive to external uncertainty (i.e., disturbances) without increasing the sensitivity to internal uncertainty (i.e., modeling error) which can result in the closed loop system becoming unstable. This is particularly true for the HHC vibration control system.

This has motivated the evolution and implementation of adaptive and robust control techniques. The use of adaptive control aims to reduce the sensitivity to error in the estimation of the T-matrix. A complete discussion on commonly employed system identification methods in the context of HHC has already been introduced in Sec. 1.2.1. This also explains the formulation of the problem in robust control frameworks, such as H_∞ techniques, which acccount for the periodicity by considering it a source of uncertainty in the dynamics. Complexity of robust control algorithms is typically higher when time-periodic dynamics are involved. Adaptive filters also generally involve computation times, introducing additional delays into the loop.

Hall and Wereley [58] show that the approach suggested by Gupta and Du Val [76] can be treated as a narrow band feedback control problem, in much the same fashion as the equivalent continuous representation of the classical T-matrix algorithm proposed by

Shaw, and that the HHC vibration attenuation problem is nothing more than the classical narrow band disturbance rejection control problem. Furthermore, disturbance rejection properties are shown to be a result of the integral dynamics intrinsic to the spectral filtering action in the controller, not necessarily of the plant modeling accuracy. Adaptation is shown not to be strictly necessary to improve performance, and therefore, good disturbance rejection performance is theoretically achievable with a fixed gain controller, even in the presence of modeling errors.

Good vibration rejection performance can be obtained by increasing controller bandwidth. This, however, stretches the quasisteady dynamics assumption, and increases the risk of destabilizing the system due to plant uncertainty. While the state space helicopter models employed in Ref. [76] are not subject to the controller bandwidth restrictions related to the quasisteady requirement, they do not, however, address the modeling problems represented by the periodic helicopter dynamics.

Quickness of the closed loop vibration rejection response takes on an added significance, however, when a pilot or flight control system is active within the loop dynamics. The vibration control system should be able to react quickly enough to be able to reject vibratory disturbances generated by the pilot, or the FCS, as they make the necessary adjustments to the flight controls in order to maintain a steady flight condition or to initiate a maneuver. The additional time delay in the response may result in a potentially destabilizing situation. Alternatively, if the vibration control system reacts to vibration at speeds comparable to the frequencies normally associated with the FCS bandwidth, then it may cause he latter to react to the HHC commands. This possibility has been shown to be less likely than the former, however.

As mentioned above, the problem with making the vibration control system bandwidth excessively large is that this may render the closed loop system susceptible to modeling errors or unmodeled dynamics. At the very least this may excite unwanted helicopter natural modes. All of these issues need to be studied with the assistance of an adequate analytic model. Few studies address this issue directly due to the lack of appropriate analytical models. A detailed look at helicopter dynamics modeling issues is warranted, in light of the previous discussion. The previous discussion also justifies taking a closer look at helicopter dynamics issues and their effects on vibration rejection performance and closed loop stability.

1.2.3 Helicopter dynamics

A few experimental and analytical studies in the literature have looked at the response time required by the closed loop control system to completely elimite a step change of the vibration amplitude. This is important because these time constants are a good indicator of closed loop bandwidth. Overall, closed loop control systems have been shown to be able to reject step changes in vibration amplitude within 1–20 sec, resulting in closed loop bandwidth ranging from 0.2 to 6 rad/sec. Closed loop bandwidth is the maximum frequency of an oscillatory vibration amplitude which the control system can suppress satisfactorily. These bandwidths point out to a potential complication in the design of closed loop HHC systems, regarding potential interactions with the flight control system, due to potentially overlapping bandwidths of the two systems. At the very least, the low bandwidths should call into question the capability of the HHC system to eliminate

vibration in full-scale helicopters during maneuvers or when encountering turbulence.

Among the early work in active vibration control, the theoretical analysis by Taylor, Farrar and Miao [62] was original in being the first to address the importance of fuselage dynamics, in particular flexible fuselage modes, on the effectiveness of closed-loop active vibration control systems. This study is significant also because it is among the first to consider the transient behavior of the closed-loop in the time-domain after the controller is turned on. Depending on the location of the sensors, 90–99% reductions of the vibration performance index take place in about 2–2.5 seconds (8–10 revs) after the controller is turned on. These results should result in borderline vibration reduction performance in response to maneuvers or pilot commands due to the closeness of the resulting closed loop bandwidth, to the frequencies at which the pilot normally operates. These settling times are fully in line with those obtained from the simulation studies performed by Shaw [55] for an isolated rotor, in response to a sudden change in the flight condition.

Wind tunnel tests by Hammond [64, 98] were part of a series of steps leading to the eventual flight-testing of a prototypical, higher harmonic, blade pitch, closed loop vibration control system, adapted to a modified OH-6A test-bed helicopter (Wood et al. [99]). Different adaptive control schemes were tried in the series of wind tunnel tests. The control update period in the flight tests by Wood et al. [100, 101] was chosen to be two revolutions and 4 sec vibration rejection times were observed.

Wind tunnel tests in Ref. [57] for a three-bladed, dynamically scaled CH-47D Chinook rotor determined the controller could react to a step change in vibration amplitude with a time constant of 160 msec, suggesting the maximum achievable bandwidth to be 6.25 rad/sec, or about 1 Hz. This bandwidth indicates that the controller was capable of

rejecting oscillatory changes in the vibration amplitude at frequencies lower than 1 Hz. With this bandwidth, the HHC system in this study should suppress environment (i.e., turbulence or gust) or pilot induced vibrations satisfactorily. There are some concerns as to how this performance translates to a full-size rotor or, more importantly, an actual helicopter.

Polychroniades and Achache [97] explore various stochastic and deterministic adaptive algorithms during a series of flight tests performed aboard a three-bladed SA349 Gazelle helicopter. The advantages of stochastic techniques are demonstrated in the improved vibration reduction response times, relative to those observed with deterministic control only. Control response times were generally slower in this series of tests, than those reported in Refs. [100, 101]. Stochastic control laws took about 10–20 seconds to achieve elimination of vibratory disturbances. This at a speed of 170 km/h, or an advance ratio of $\mu = 0.22$, which is not a particularly high speed, but is rather closer to the transitional speed range. Although a slower response time to changes in flight condition generally indicates the existence of lower frequency controller dynamics (e.g., 0.2–0.4 rad/sec in this case), tests in this case showed that higher harmonic control had a very small effect on pilot inputs, aircraft attitude and rotor power (i.e., flight dynamics).

In Ref. [41] a 1/4 update rate was found to be sufficient to guarantee reasonable good disturbance rejection performance, but without stability issues coming into play. System identification capabilities involve Recursive Least Squares (RLS) methods, as well as Kalman filter based system identification methods. Both, local and global T-matrix model identification capabilities were included.

There are also a few studies specific to the BO-105 in the literature. Open loop

IBC wind tunnel tests on a full-scale BO-105 helicopter rotor in the 40- by 80-Foot wind tunnel at the NASA Ames Research Center [102] for transition and cruise speed flight conditions showed that the maximum higher harmonic control amplitudes do not need to exceed 1.0 deg. Results indicated that 85% simultaneous reductions in both BVI and hub loads were possible with multi-harmonic control.

Papavassiliou et al. [95] refute the validity of the assertion that vibration reduction of hub loads translates to reduction of accelerations throughout the fuselage. For this, the coupling of the rotor with the fuselage is modeled, with the rotor represented by a four-bladed hingeless configuration attached to a flexible fuselage model retaining five rigid-body degrees of freedom (no yaw) and six elastic degrees of freedom (two vertical bending modes, two horizontal bending modes, and two torsional modes). The model was loosely based on the MBB BO-105 helicopter.

Simulation models

There are few analytical studies among the early works on higher harmonic control, and those available are not comprehensive enough. The helicopter mathematical models available limited early analytical studies on higher harmonic control. The level of sophistication of the helicopter models used in the numerous theoretical studies up to date varies substantially, from simple, quasi-static, frequency-domain representations, to full-blown non-linear aeroelastic comprehensive simulation programs including flexible fuselage dynamics and rotor-fuselage couplings. Differences may exist also between the model used for controller synthesis or design, and the model used to simulate or verify the closed loop

regulator operation performance.

The majority of adaptive control systems, studied in the framework of the classic T-matrix HHC algorithm, rely on measurements of the vibration and the knowledge of the controls to estimate the vibration transfer matrix and the uncontrolled, or baseline, vibration. Kalman filter estimators may also require an initial estimate of these quantities to begin the identification process. Fixed-gain controllers, on the other hand, require the system T-matrix to be identified or computed off-line. In either case, the analytical simulation of the HHC loop requires some form of plant model representing helicopter, or at least rotor, dynamics.

Plant models in early investigations are generally based on the simplified, linear frequency-domain transfer function representations of the helicopter, and are obtained either from rotor "airloads" programs, or from wind tunnel tests (e.g., Refs. [55,66,73]). In the theoretical investigations by Shaw [55], for example, a fixed hub rotor loads program is used to update the plant transfer matrix representing the vibration harmonic response to higher harmonic blade pitch inputs. Control feedback gains are computed by direct inversion of the system transfer matrix, which is estimated through a Kalman filter. On-line adaptive estimation of the system response matrix is built in to track the changing flight conditions. For their numerical simulation of HHC systems, Chopra and McCloud [66] used a linear, frequency-domain transfer matrix of a Kaman 7.02 m Controllable Twist Rotor obtained experimentally from tests performed in the 40-by-80 foot wind tunnel at the Ames Research Center, to model the helicopter plant. Gaussian noise is artificially introduced in order to model sensor measurement contamination, and to evaluate the efficiency of the Kalman filter to pick up the real system model and uncontrolled vibration.

This is done for both off-line identification of the transfer matrix, as well as for on-line identification techniques used in adaptive regulators. Deterministic optimal controllers were then synthesized using the estimated transfer matrix.

A similar approach is followed by Jacklin [73] in order to evaluate the different system identification algorithms. Accuracy of wake models to capture unsteady aerodynamics (shed wake) is put into question by Jacklin [73]. This study is limited, however, only to the system identification algorithms, and closed loop control is not tested.

Hall and Wereley [58, 103] present an insightful analysis of the periodic disturbance rejection properties of the classical HHC algorithms. However, the helicopter plant model in this study is overly simplistic, and representative of the helicopter dynamics in a very generic sense only. At the least it neglects the effect of the natural helicopter periodic dynamics in forward flight. Hall and Wereley [58] introduce an approximate continuous-time transfer function version of the discrete-time HHC algorithm proposed by Shaw and Albion [60], allowing the analysis of the closed loop system through classical LTI frequency-domain techniques. Controller gains are generated without loss of generality by direct inversion of the T-matrix.

On top of the time-periodic dynamics, the helicopter aeroelasticity problem is inherently characterized by aerodynamic and elastic rotor nonlinearities, and rigid body kinematic fuselage nonlinearities. This raises questions about the validity of the simplistic linear, constant, quasisteady models found in most of the early analytical studies, especially since closed loop controller bandwidth does not necessarily have to be small. Earlier aeroelastic response codes, like the one used in Refs. [62, 63], do not have accurate descriptions of the geometrical nonlinearities due to moderate blade deflections,

nor do they include a suitable time-domain model for calculating the unsteady aerodynamic loads due to high frequency blade pitch. Emergence of so-called comprehensive aeroelastic simulation models suitable for vibration analysis [93–95, 104–110], has enabled the investigation of fundamental issues in HHC, providing physical insight into the vibratory load reduction mechanics. Time-domain unsteady aerodynamics, coupled flap-lag-torsional flexible blade and rotor wake modeling are considered essential elements in comprehensive simulation models. Most importantly, models must account for the coupled aeroelastic response of the rotor.

Various aspects of both, deterministic and minimum-variance (cautious) controllers, for local and global HHC models of a soft-in-plane hingeless rotor aeroelastic simulation model were studied [104]. The fundamental solution method allows for the computation of the steady vibratory response of the helicopter to a steady higher harmonic control input. Thus, the baseline T-matrices are calculated from the linearized vibratory response about the baseline operating conditions. Also, since the control inputs and the vibratory response in a simulation model of this nature are known explicitly, this is equivalent to assuming there is zero process and measurement noise.

The study by Robinson and Friedmann [104] incorporated a finite-state, time-domain model of unsteady aerodynamics suitable for computing circulatory and non-circulatory loads for an airfoil undergoing arbitrary pitch and plunge motion, as well as a model of quasisteady aerodynamics. The influence of blade section aerodynamics modeling on the structure of the T-matrix is investigated. A similar investigation, by Nguyen and Chopra [107], had introduced a more sophisticated, linear, unsteady aerodynamics model (Leishman-Beddoes [111]), including the nonlinear effects of flow separation and dy-

namic stall, as well as a free-wake analysis for the calculation of the induced inflow distribution. The structural model is otherwise similar to that used in Ref. [104].

The HHC vibration control systems simulated in this study are based on both local and global transfer matrix vibration control response models; and are designed to minimize a deterministic quadratic performance index of the harmonics of vibration and control inputs. Only non-adaptive, fixed-gain controllers were employed in Ref. [107]. The global response model is reserved for open loop control. Closed loop control controllers are based on local response models, and are technically not fixed-gain control systems, since the transfer matrix varies at each cycle, and needs updating [112]. The initial matrix T is calculated from the nonlinear equations using a finite-difference approach. The transfer matrix for the local control response model is updated at every algorithm cycle by means of Broydens generalization of the secant method. This is by no means an adaptive algorithm in the same sense that the Kalman filter is. It is, rather, a method for improving estimates on the Jacobian for nonlinear systems.

The use of trailing-edge flaps for vibration control is investigated in Refs. [93, 105, 108,109,113] with the use of similar structural and aerodynamic models as those proposed in Refs. [104, 107]. Models mainly include refinements in the aerodynamics to include flapped airfoil sections.

Invariably, the underlying closed loop control system dedicated to the task of eliminating vibration is based on some variation of the classical T-matrix algorithm, most notably, any of the fixed-gain deterministic versions of the optimal regulator which have been discussed above. Again, whenever fixed-gain controllers are used, the transfer matrix T used for control syntheses is generally obtained initially by numerical linearization

of the nonlinear vibration response about the zero control operating condition.

With the possible exception of Ref. [93], the entirety of these comprehensive aeroelastic analyses involving the closed loop HHC algorithm for vibration control [104, 107, 109, 113] have treated the simulation of the closed loop response dynamics purely as a quasisteady problem. That is to say, the assumption that transient dynamics are allowed to dissipate before the control inputs are updated is fully respected. Neglecting the transient dynamics of the closed loop by treating the helicopter as quasi-static causes the closed loop response problem to devolve into a sequence of trim solution computations. The convergence of the closed loop response can be demonstrated. However, the iteration steps may not necessarily represent actual time steps. Vibration transient response setting times are important indicators of the performance of the controller, especially in the face of pilot induced disturbances. Therefore, steady, or trim based analyses are possibly inadequate for predicting these types of phenomena. This is, of course, a direct consequence of neglecting the information provided by the transient dynamics when treating the closed loop as quasisteady.

Millott and Friedmann [93, 105] investigate, analytically, the validity of the quasisteady assumption by comparing the steady (i.e. trim) solution with the time-domain response obtained by integrating the system of ODEs defining the rotor dynamics. Lower damping available in the blade lag models is shown to produce a sufficiently slow settling time that the quasisteady assumption is invalidated for a control update interval of one revolution.

Solution methods for the calculation of the steady helicopter response in forward flight [104, 105] fundamentally attempt to compute the simultaneous solution of the ve-

hicle trim problem and the rotor vibration response. Vehicle trim solution methods are typically based on one of several variations of the propulsive trim approach, with the differences mainly lying in the degrees of freedom of the hub attitude.

Numerous variations, or degrees of simplification, on the propulsive trim methodology are employed in these studies. These range from wind tunnel to free-flight trim procedures. Yaw and lateral equilibrium equations can be neglected, for example, eliminating the tail rotor pitch setting and the main rotor lateral shaft angle as trim variables [104]. Consequently, the lateral cyclic control is adjusted only to make the rotor rolling moment equal to zero. Wind tunnel trim calculations, on the other hand, basically only require that the cyclic flapping angles be trimmed to zero.

These procedures do not adequately capture fuselage accelerations. Because it is assumed that the main rotor is attached to a fixed hub and a rigid fuselage, all the degrees of freedom that define the fuselage dynamics are neglected, and therefore this type of analysis is capable only of simulating vibratory hub loads. Consequently, the evaluation of the HHC algorithms can only be done on the basis of vibratory hub load reduction. Should the fuselage be considered rigid, but not fixed in space, then HHC reduction of aircraft vibratory motion (i.e., acceleration) and vibratory hub loads would produce equivalent control solutions.

Although so called free-flight trim procedures may include rotor shaft pitch and roll degrees of freedom, this does not necessarily mean that fuselage dynamics are modeled. Such an analytical model requires that the rotor and the fuselage be dynamically coupled, i.e., rotor hub loads are transferred to the fuselage simultaneously as the fuselage or hub motion is transferred to the rotor.

Calculation of the steady rotor vibration response involves finding the steady state solution for the set of ODEs that define the rotor dynamics. The harmonic balance technique allows for the simultaneous solution of the vehicle trim problem and the harmonic vibration response problem in one pass. Most studies consider only the time-average or constant portion of the vehicle trim equations in the harmonic balance. Eliminating the higher harmonic hub loading and fuselage motion renders this trim solution method useless for purposes of evaluating the HHC of vibratory motion. Hanagad et al. [114] demonstrates how the harmonic balance technique is employed to calculate the steady vibration response for a fully coupled, flexible rotor-fuselage system of ODEs. The method is employed by Millott and Friedmann to find the steady response to HHC inputs. Vehicle trim equations in Millott and Friedmann completely neglect the periodic components, however.

On the other hand, closed loop HHC investigations in the context of active control of the structural response, such as Ref. [115], often involve complex fuselage structural models but no rotor dynamics. Vibratory hub loads are considered to be external excitations acting on the fuselage, and representative hub loads obtained from flight test measurements are used for simulation purposes. A recursive-least-squares filter is employed in this study to estimate the transfer matrix throughout the simulation studies. Other studies [116, 117] studies include a very detailed helicopter models, providing a powerful analytical platform to investigate the problem of vibration suppression in the context of ACSR. The control algorithm used in these studies is of a totally different class of control algorithms from the classical T-matrix algorithm, though [118]. Papavassiliou et al. [95] fully account for the coupled rotor-flexible fuselage dynamics for HHC inves-

tigations with a simple fuselage model. Only open loop control is investigated, however. The problem of solving the vibration response in these studies is treated as a trim problem by means of the harmonic balance technique in much the same way as in [93], but the vibratory motion of the fuselage is accounted for by considering also the higher harmonics in the balance technique.

1.3 Current Investigation

Preliminary results for this investigation have been presented in References [119–122]. These preliminary results and procedures have been revised and will be presented here. Additional results will be presented here as well. The closed loop stability of a hingeless rotor helicopter equipped with an HHC system has been studied in Ref [119]. The T-matrix is constant, and the HHC algorithm is written as a linear time-invariant dynamic compensator using the technique developed by Hall and Wereley [58], extended to cover inputs and outputs at different harmonics. This compensator is coupled to a high-order, coupled rotor-fuselage model, and the closed loop stability is studied using Floquet theory and constant coefficient approximations. The feedback gains of the control system are proportionally scaled down. The key results of the study with this low gain controller are that: (i) the HHC system does not degrade the aeromechanic stability, (ii) the time constants of the HHC are such that interactions with a flight control system could occur, and (iii) that the effects of periodic coefficients need to be taken into account.

A gap in the analysis of HHC systems however remains open, because the issues related to the actual discrete-time implementation were not included in Ref. [119] and have

never been studied in detail in the literature. Discrete-time issues are likely to play a major role in determining the closed loop behavior of the system. In fact, the typical update frequency for HHC control inputs is 1/rev, which is comparable with the bandwidth of the dynamics of the open loop, i.e., uncontrolled helicopter rotor. Previous work on this problem (see, e.g., [58, 119]) tried to overcome this difficulty by developing continuous-time, time domain counterparts of the discrete elements. On the other hand, a more complete and rigorous picture of the operation of HHC can be obtained by looking at the entire control loop, including the coupled rotor-fuselage dynamics, in discrete time rather than in continuous time. Preliminary results accounting for the discrete-time analysis of closed loop HHC were shown in [120, 122].

1.4 Objectives

In the light of the preceding discussion, the present investigation has the following objectives:

1. To provide a simple state space derivation for the continuous time form of the SISO HHC compensator, first introduced in [58];

2. To demonstrate how the same approach can be used to work out a state space representation for the SISO PHHC compensator, which is suitable for stability and robustness analysis of this kind of rotor control algorithm;

3. To generalize the above results in order to get to a general approach for the derivation of the state space form for a MIMO HHC controller;

4. To present the results of a numerical investigation into the stability properties of Higher Harmonic Control, based on a simulation study of the coupled rotor-fuselage dynamics of a four bladed hingeless rotor helicopter (see [123, 124]);

5. To describe a typical discrete-time HHC architecture and derive suitable linearized, state-space, discrete models for all the components present in the control loop;

6. To formulate a coupled helicopter-HHC discrete model, and convert it from a periodic, multiple sampling rate model to a constant coefficient, single sampling rate model using time-lifting techniques; and

7. To perform a closed loop, aeromechanic stability and response analysis of the discrete-time, coupled helicopter-HHC model, and compare it with the corresponding results obtained using a continuous-time model.

1.5 Principal Contributions

The most significant contribution to the state-of-the-art in the field of active rotor control algorithms for vibration attenuation by this study is that it constitutes the first closed-loop coupled rotor-fuselage aeroelastic stability analysis of a helicopter equipped with HHC/IBC including the:

1. First rigorous treatment of the "real-life" effects of HHC/IBC algorithm implementation: discrete elements, multiple sampling rates, computation delays. The time-lifting technique allows the reformulation of the discrete LTP systems that make up the regulator system into LTI systems at one common sampling rate.

2. First aeroelastic stability analysis with a fully discrete rotor-fuselage representation which is rigorously equivalent to the continuous form. Stability equivalence of the two forms can be established since stability of continuous LTP systems, as established by Floquet thoery, is identical to the stability for the time-lifted discrete LTI helicopter representation.

3. Although the problem of FCS/HHC interaction has not been studied in depth, the methodology proposed in this study introduces the first mathematical representation of the closed loop, coupled helicopter-HHC systems suited to the analysis of potential FCS/HHC interactions in a control engineering framework that captures the most important dynamics.

1.6 Outline of the Dissertation

Chapter 2 describes the mathematical model of the helicopter, including details of the HHC controller algorithm in continuous and discrete-time. The chapter also illustrates the solution methods for the trim calculation, the extraction of linear systems, and the time integration.

Chapter 3 presents an analytical discussion of the magnitude of the T-matrix SISO and MIMO optimal control feedback gains as a function of the control effort parameter weighing coefficient.

Chapter 4 discusses simulation stability results of the helicopter with a continuous-time representation of Shaw's HHC algorithm. The effects of periodic helicopter dynamics on closed loop stability is one of the fundamental issues addressed in the chapter.

Chapter 5 is devoted to studying the closed loop aeromechanical stability of the helicopter when the discrete-time dynamics of the HHC algorithm are taken into consideration. The analytical approach suggested in the chapter required the transformation of the continuous-time helicopter system into the discrete-time domain, so that the closed loop can be formulated in discrete-time.

Chapter 6 provides the conclusion to the study and recommendations for future work.

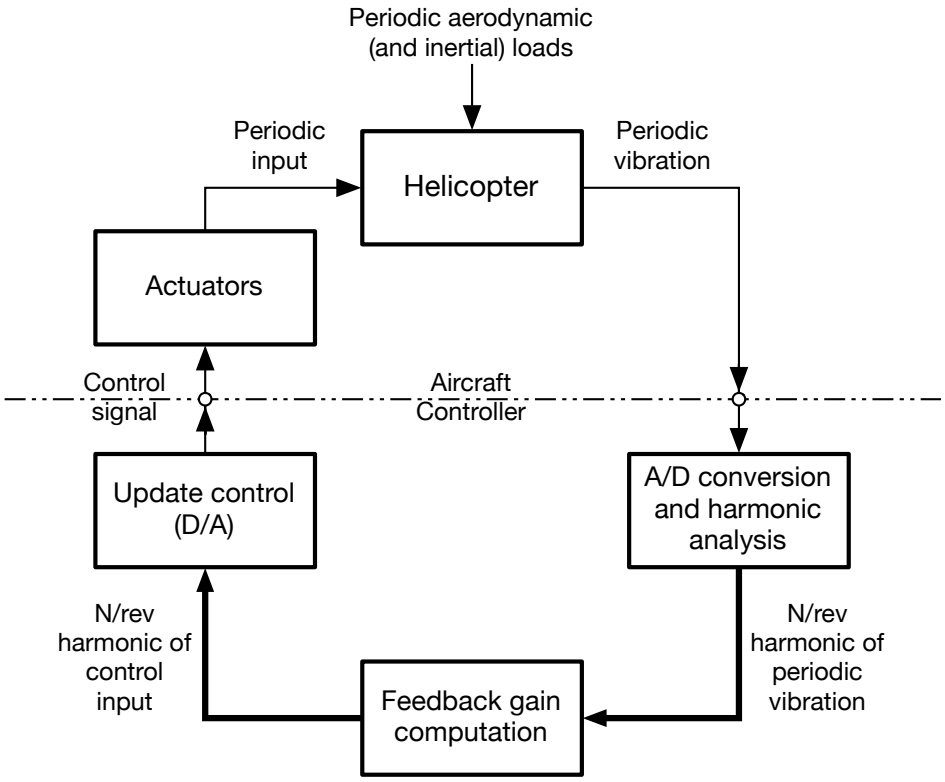

Figure 1.1: Schematic of the HHC system in the time-domain

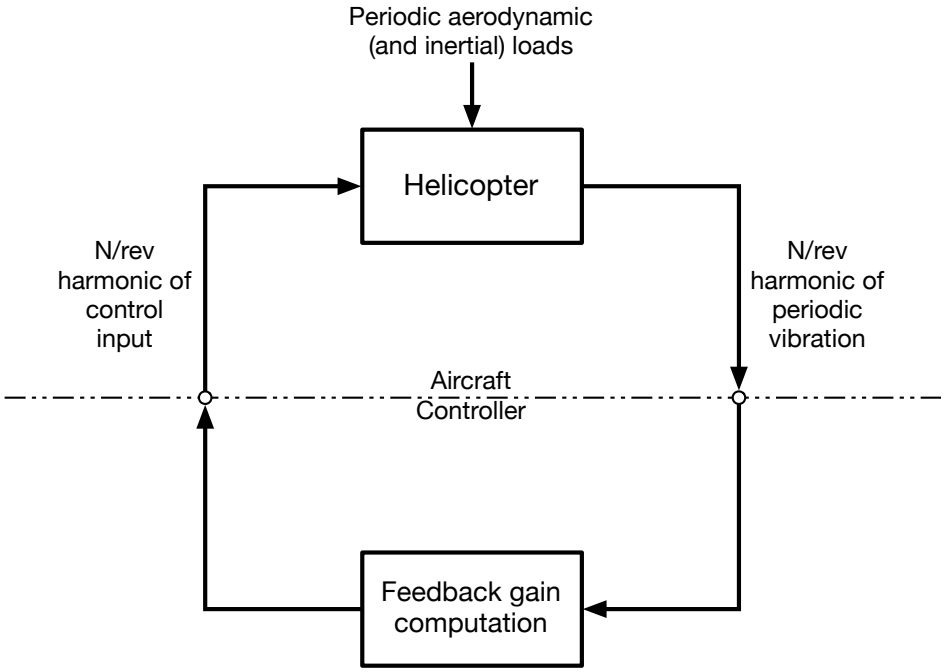

Figure 1.2: Simplified schematic for quasisteady HHC system (frequency-domain)

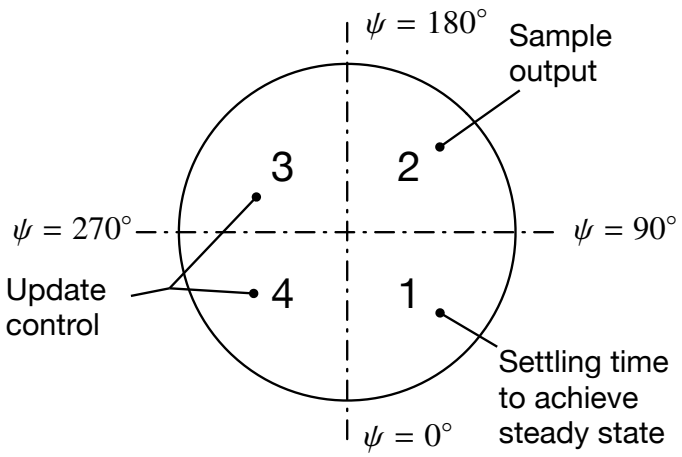

Figure 1.3: HHC system timing example

Chapter 2

Mathematical Model

This Chapter is divided into two main parts. In the first, a brief description of the helicopter mathematical simulation model is presented, including a short description of the two-dimensional aerodynamical models used for the calculation of aerodynamic loads on the blade, and followed by a synopsis of the different solution methods implemented to manipulate the systems of equations; mainly, the computation of helicopter trim state flight conditions, and the extraction of linearized models suitable for stability and control design and analysis. Then in the second part, the Higher Harmonic Control system algorithm design and implementation techniques, as well as the closed loop analysis methodologies are discussed.

2.1 Helicopter governing equations

The baseline simulation model used in this study is a nonreal-time, blade element type, coupled rotor-fuselage simulation model. The model is discussed in detail in Ref. [123, 124], and only a brief description will be provided here. The fuselage is assumed to be rigid and dynamically coupled with the rotor. A total of nine states describe fuselage motion through the nonlinear Euler equations. Fuselage and blade aerodynamics are

described through tables of aerodynamic coefficients, and no small angle assumption is required. A coupled flap-lag-torsion elastic rotor model is used [125, 126]. Blades are modeled as Bernoulli-Euler beams. The rotor is discretized using finite elements, with a modal coordinate transformation to reduce the number of degrees of freedom. The elastic deflections are not required to be small. Blade element theory is used to obtain the aerodynamic characteristics on each blade section. Both quasisteady and unsteady aerodynamics are used, along with a 3-state dynamic inflow wake model.

The complete dynamic system is modeled as a set of nonlinear first order differential equations written in implicit form [127]

$$\mathbf{g}\left(\dot{\mathbf{y}}, \mathbf{y}, \mathbf{u}; t\right) = \mathbf{0} \tag{2.1}$$

where the control vector $\mathbf{u}$ defines the helicopter's control inputs determined by the pilot's control activity and the active vibration controller, and state vector $\mathbf{y}$ consisting of all the variables that completely definine the dynamics of the helicopter model.

2.1.1 Fuselage equations

As discussed in the previous Section, a nonlinear coupled rotor-fuselage flight dynamics model is used in the present study. It models the rigid body dynamics of the helicopter with the nonlinear Euler equations. The three translational velocity components in a body-fixed coordinate system; the angular velocities about these axes; and the roll, pitch and yaw attitude angles with respect to the inertial reference frame are required to describe the helicopter dynamics.

For the forces

$$\begin{Bmatrix} X \\ Y \\ Z \end{Bmatrix} = m \begin{Bmatrix} \dot{u} \\ \dot{v} \\ \dot{w} \end{Bmatrix} + mS(\boldsymbol{\omega}) \begin{Bmatrix} u \\ v \\ w \end{Bmatrix} + m \begin{Bmatrix} g_x \\ -g_y \\ -g_z \end{Bmatrix} \tag{2.2}$$

For the moments

$$\begin{Bmatrix} L \\ M \\ N \end{Bmatrix} = I \cdot \begin{Bmatrix} \dot{p} \\ \dot{q} \\ \dot{r} \end{Bmatrix} + S(\boldsymbol{\omega}) \cdot \left(I \cdot \begin{Bmatrix} p \\ q \\ r \end{Bmatrix} \right) \tag{2.3}$$

where $S\ (\boldsymbol{\omega})$ is the skew symmetric matrix

$$S\ (\boldsymbol{\omega}) = \begin{bmatrix} 0 & -r & q \\ r & 0 & -p \\ -q & p & 0 \end{bmatrix} \tag{2.4}$$

g_x, g_y and g_z are the gravity vector components along the body axes (i.e., a system of coordinate axes that is centered at the helicopter c.g. and is fixed to the helicopter body, with the x, y and z axes pointing forward, sidewards to the right and downwards, respectively); and I is the matrix of moments of inertia about the body axes. The X, Y and Z forces as well as the L, M and N moments contain contributions from the main rotor, the tail rotor, and the fuselage and empennage aerodynamic loads.

Roll, pitch and yaw angular velocities are related to the roll, pitch and yaw attitude rates through the linear rotation transformation

$$\begin{Bmatrix} p \\ q \\ r \end{Bmatrix} = \begin{bmatrix} 1 & 0 & -\sin\theta_F \\ 0 & \cos\phi_F & \sin\phi_F \cos\theta_F \\ 0 & -\sin\phi_F & \cos\phi_F \cos\theta_F \end{bmatrix} \begin{Bmatrix} \dot{\phi}_F \\ \dot{\theta}_F \\ \dot{\psi}_F \end{Bmatrix} \tag{2.5}$$

The aerodynamic characteristics of the fuselage and empennage are included in the form of experimental based look-up tables. Following an approach inherited from GENHEL [128], the main rotor downwash interference effects on the fuselage and empennage are taken into account by introducing a correction factor on the total freestream velocity at the fuselage and empennage aerodynamic reference points. Fuselage interference

components are

$$u_{in_F} = w_0 \nu_{x_{w_F}}(\beta_{1c}, \chi) \tag{2.6}$$

$$v_{in_F} = 0 \tag{2.7}$$

$$w_{in_F} = w_0 \nu_{z_{w_F}}(\beta_{1c}, \chi) \tag{2.8}$$

where w_0 is the main rotor downwash. Non-linear functions $\nu_{x_{w_F}}(\beta_{1c}, \chi)$ and $\nu_{z_{w_F}}(\beta_{1c}, \chi)$ are determined from look-up tables; and are functions of the longitudinal tilt of the tip path plane, β_{1c}, and the rotor wake skew angle, χ. Data for lateral interference velocity components is not known. Interference velocity components on the tail rotor and empennage are treated in a similar fashion; except an additional correction factor is introduced to take into account delayed main rotor wake effects. These interference components result from the product of aircraft forward velocity, exponentially decaying delayed downwash and sidewash coefficients, and a dynamic pressure loss correction factor. Delayed downwash and sidewash coefficients are modeled by first-order differential equations

$$\dot{\nu}_{DW} = \frac{\epsilon_H - \nu_{DW}}{\tau_e} \tag{2.9}$$

$$\dot{\nu}_{SW} = \frac{\epsilon_V - \nu_{SW}}{\tau_e} \tag{2.10}$$

where terms ϵ_H and ϵ_V are empirically determined functions of fuselage angle of attack and sideslip, and τ_e is the freestream time of travel from the main rotor to the tail. See Turnour [129] for specific details.

2.1.2 Rotor equations

The dynamics of the rotor blades are modeled with a coupled flap, lag and torsion, finite element discretization and a modal coordinate transformation to reduce the number of degrees of freedom. Matrix V_m is the modal coordinate transformation matrix and $\mathbf{q}$ the vector of modal coefficients, where the columns of V_m contain the normal mode shape vectors of the blade. Thus the vector of finite element nodal degrees of freedom $\mathbf{y}_n$ can be related to $\mathbf{q}$ through the linear transformation

$$\mathbf{y}_n = V_m \mathbf{q} \tag{2.11}$$

Vector $\mathbf{q}$ is taken to be the vector of generalized coordinates which describe rotor bending dynamics. This is possible because blade bending can be entirely described by the modal coefficients, provided that natural mode shapes are known.

Induced inflow is modeled with a linear dynamic inflow approach, with three variables defining the state of the inflow distribution; the uniform distribution, λ_0, and linear lateral and longitudinal distributions, λ_s and λ_c. This approach is based on the dynamic inflow model introduced by Peters and He [130, 131].

Two-dimensional sectional blade unsteady aerodynamics can be included in the mathematical analysis model as well. This is based on the Leishman-Nguyen state space unsteady aerodynamics model [132], which accounts for the shed wake effects caused by blade motion. The unsteady aerodynamics model can be used in conjunction with a simple three state dynamic inflow wake model, because the latter only accounts for the effects of the trailing vorticity, and not the shed vorticity. The two-dimensional unsteady aerodynamics on an airfoil is defined by an 8-th order linear state space system of equa-

tions. The states define the different circulatory and non-circulatory components of the unsteady lift and pitching moments based on thin airfoil theory, and empirically account for the effects of compressibility in subsonic flow. Unsteady aerodynamics loads must be computed over sufficient points on the blade in order to obtain an accurate resolution of the unsteady aerodynamics loads over the entire blade span. In the present study 5 points per blade were considered, and a different set of states define the aerodynamic loadsfor each point. Therefore a total of 160 states are required to define the aerodynamic forces and moments over the rotor disk.

Finally, as mentioned above, the equations of motion for the helicopter model are expressed as a system of nonlinear, time-varying, first-order differential equations in the implicit form

$$\mathbf{g}\left(\dot{\mathbf{y}}, \mathbf{y}, \mathbf{u}; t\right) = \mathbf{0} \tag{2.12}$$

where the control vector $\mathbf{u}$ contains the helicopter control inputs. Vector u contains both, the pilot control and the higher harmonic control inputs. The former are defined by the lateral cyclic, longitudinal cyclic and collective blade pitch harmonics, and the tail rotor collective pitch. The higher harmonic controls are defined by the Fourier coefficients of the higher harmonics of the blade input in the rotating frame. Therefore control input vector is defined as

$$\mathbf{u} = \begin{Bmatrix} \mathbf{u}_P \\ \mathbf{u}_{HHC} \end{Bmatrix} \tag{2.13}$$

where $\mathbf{u}_P$ is the vector of pilot controls, and $\mathbf{u}_{HHC}$ is a vector containing the HHC inputs, such that

$$\mathbf{u}_P^T = \begin{Bmatrix} \theta_{1c} & \theta_{1s} & \theta_0 & \theta_t \end{Bmatrix} \tag{2.14}$$

and

$$\mathbf{u}_{HHC}^{T} = \left\{\theta_{2c} \quad \theta_{2s} \quad \theta_{3c} \quad \theta_{3s} \quad \theta_{4c} \quad \theta_{4s} \quad \theta_{5c} \quad \theta_{5s} \quad \theta_{6c} \quad \theta_{6s}\right\} \tag{2.15}$$

and the state vector $\mathbf{y}$ contains all the body states, main rotor states, main and tail rotor inflow states, empennage aerodynamic interaction states, and unsteady aerodynamic states, if included, necessary to define the helicopter dynamics at a given instant t.

$$\mathbf{y} = \begin{Bmatrix} \mathbf{y}_F \\ \mathbf{y}_R \\ \mathbf{y}_I \\ \mathbf{x}_u \end{Bmatrix} \tag{2.16}$$

where the rigid-body or fuselage states are

$$\mathbf{y}_F^{T} = \left\{u \quad v \quad w \quad p \quad q \quad r \quad \phi_F \quad \theta_F \quad \psi_F\right\} \tag{2.17}$$

Blade mode coefficients and rates for each mode and each blade define the main rotor states. Rates are necessary to completely describe rotor flexible dynamics in a system of first-order differential equations. The complete main rotor state vector contains the modal coefficients for each mode

$$\mathbf{y}_R = \begin{Bmatrix} \mathbf{y}_{q_1} \\ \mathbf{y}_{q_2} \\ \vdots \\ \mathbf{y}_{q_{N_m}} \end{Bmatrix} \tag{2.18}$$

where N_m is the number of modes that have been retained for use in the model. For a 4-bladed rotor, the m-th mode main rotor states are defined as

$$\mathbf{y}_{q_m} = \begin{Bmatrix} \dot{q}_1^m \\ \dot{q}_2^m \\ \dot{q}_3^m \\ \dot{q}_4^m \\ q_1^m \\ q_2^m \\ q_3^m \\ q_4^m \end{Bmatrix} \tag{2.19}$$

The vector $\mathbf{y}_I$ contains the main rotor and tail rotor inflow states and the rotor downwash aerodynamic interaction coefficient states

$$\mathbf{y}_I = \begin{Bmatrix} \lambda_0 & \lambda_c & \lambda_s & \lambda_t & \nu_{DW} & \nu_{SW} \end{Bmatrix}' \tag{2.20}$$

Finally, let $\mathbf{z}_i^j$ be the unsteady aerodynamics states for the j-th collocation point on the i-th blade. Assuming n_p collocation points per blade are selected, the complete state vector is

$$\mathbf{x}_u = \begin{Bmatrix} \mathbf{z}_1^1 \\ \vdots \\ \mathbf{z}_1^{n_p} \\ \mathbf{z}_2^1 \\ \vdots \\ \mathbf{z}_2^{n_p} \\ \mathbf{z}_3^1 \\ \vdots \\ \mathbf{z}_3^{n_p} \\ \mathbf{z}_4^1 \\ \vdots \\ \mathbf{z}_4^{n_p} \end{Bmatrix} \tag{2.21}$$

There are 8 states used to define the blade bending motion for each blade mode in a 4-blade rotor (Eq. 2.19). These consist of one modal coefficient and the corresponding time derivative for each blade. The unsteady aerodynamics at each collocation point requires of 8 states to completely define the aerodynamic loads. Counting the 9 rigid-body of fuselage states, plus the 6 states defining the induced inflow and downwash aerodynamic interactions, the model requires a total of $15 + 8N_m + 48n_p$ states for a 4-bladed rotor, when unsteady aerodynamics are used. With 5 retained modes and 5 unsteady aerodynamics collocation points per blade, the total number of states is 215. If unsteady aerodynamics are removed, then the system reduces the size of the system to 55 states.

2.2 Blade section aerodynamic models

The main element required for the calculation of aerodynamic forces and moments is the absolute velocity of an arbitrary point on the elastic axis of the blade. The total velocity can be expressed in terms of the airflow velocity components in the blade sectional aerodynamics coordinate system (see Ref. [133]).

$$\boldsymbol{V}_A = U_T \mathbf{e}_T + U_P \mathbf{e}_P + U_R \mathbf{e}_R \tag{2.22}$$

where $\boldsymbol{V}_A$ is the resultant velocity of the airflow at the 1/4-chord location, and U_T, U_P and U_R are the tangential, perpendicular and radial components of the airflow at this location on the blade.

Presence of a radial velocity component implies airflow over the blade section at a point on the blade is skewed by an angle γ_I with respect to the blade, such that the true aerodynamic angle of attack of this yawed airfoil is defined as

$$\alpha_Y = \tan^{-1}\left[\frac{(U_T \tan\theta_G + U_P)\cos\gamma_I}{U_T - U_P \tan\theta_G \cos^2\gamma_I}\right] \tag{2.23}$$

where the airflow skew, or yaw, angle γ_I of the flow over the blade section is defined such that

$$\cos\gamma_I = \frac{|U_T|}{\sqrt{U_T^2 + U_R^2}} \tag{2.24}$$

and the geometric pitch angle θ_G is

$$\theta_G = \theta_0 + \theta_{1c}\cos(\psi + \Delta_{SP}) + \theta_{1s}\sin(\psi + \Delta_{SP}) + \theta_{TW} + \theta_n + \phi \tag{2.25}$$

where $\Delta_{SP} = -10^\circ$ is the swashplate phasing angle, ϕ is the elastic rotation of the blade

section about the elastic axis and θ_n is the higher harmonic input defined by

$$\theta_n(\psi) = \sum_{k=N-1}^{N+1} (\theta_{kc} \cos k\psi + \theta_{ks} \sin k\psi) \tag{2.26}$$

The blade section steady lift, drag and moment coefficients are obtained from data look-up tables as a function of the local angle of attack and Mach number,

$$C_L = C_L(\alpha_Y, M) \tag{2.27}$$

$$C_D = C_D(\alpha_Y, M) \tag{2.28}$$

$$C_M = C_M(\alpha_Y, M) \tag{2.29}$$

2.2.1 Quasisteady aerodynamics

Blade sectional aerodynamic loads are calculated on the basis of a two-dimensional quasi-steady aerodynamics model [134] which takes into account the shed wake effects associated with variations in the aerodynamic loads with respect to time. Simplified expressions for the distributed lift L, drag D and pitching moment M are obtained by neglecting the acceleration terms $\ddot{h}$ and $\ddot{\alpha}$, related to non-circulatory or apparent mass loads, in the basic equations [134]. Therefore the lift L is given by

$$L = L_Q + \frac{1}{8} a \rho V_0 c^2 \dot{\alpha} \tag{2.30}$$

where L_Q is the quasisteady lift and is given by

$$L_Q = \frac{1}{2} \rho V_0^2 c \left[C_L + \frac{a\dot{\alpha}}{V_0} \left(\frac{c}{2} - x_A \right) \right] \tag{2.31}$$

the aerodynamic drag is given by

$$D = C_D \frac{1}{2} \rho V_0^2 c \tag{2.32}$$

and, finally the pitching moment M is

$$M = M_S + M_Q + M_{\dot{\alpha}} \tag{2.33}$$

where the total aerodynamic pitching moment is determined by the components

$$M_S = \frac{1}{2} C_M \rho V_0^2 c^2 \tag{2.34}$$

$$M_Q = F_P \frac{L_Q}{L} x_A \cos\theta_G + F_T \frac{L_Q}{L} x_A \sin\theta_G \tag{2.35}$$

$$M_{\dot{\alpha}} = -\frac{1}{8} a \rho V_0 c^2 \dot{\alpha} \left(\frac{c}{2} - x_A \right) \tag{2.36}$$

and where a is the lift-curve slope, ρ is the air density, c is the non-dimensional chord length, α is the total pitch angle of the blade section, V_0 is the oncoming freestream flow velocity, x_A is the blade cross-sectional aerodynamic center offset from the elastic axis (positive for aerodynamic center forward of the elastic axis), and $\dot{\alpha}$ is the time rate of change of the total blade pitch angle and is approximated by

$$\dot{\alpha} = \dot{\theta}_G = -\theta_{1c} \Omega \sin(\psi + \Delta_{SP}) + \theta_{1s} \Omega \cos(\psi + \Delta_{SP}) + \dot{\theta}_n + \dot{\phi} \tag{2.37}$$

2.2.2 Unsteady aerodynamics

Quasisteady aerodynamics may be inadequate for higher harmonic control applications due to the higher reduced frequency values associated with the application of $N - 1$, N and $N + 1$/rev blade pitch harmonics. Therefore, the Leishman-Nguyen state space representation of the unsteady aerodynamics on an airfoil [132] is also considered in the present study to account for the effects of the shed wake associated with the high frequency variations in the aerodynamic loads with respect to time. The basic equations for the normal force and the 1/4-chord pitching moment coefficient response to an arbitrary

$\alpha(t)$ and $q(t)$ time history are given in generic state space form

$$\dot{\boldsymbol{x}}_u = A_u \boldsymbol{x}_u + B_u \begin{Bmatrix} \alpha \\ q \end{Bmatrix} \tag{2.38}$$

$$\begin{Bmatrix} C_N^u \\ C_M^u \end{Bmatrix} = C_u \boldsymbol{x}_u + D_u \begin{Bmatrix} \alpha \\ q \end{Bmatrix} \tag{2.39}$$

where $q = \dot{\alpha} c / V_0$ represents the non-dimensional pitch rate about the 1/4-chord. The total value of the normal force and pitching moment coefficients is

$$C_N = C_N^u + C_{N_0} \tag{2.40}$$

$$C_M = C_M^u + C_{M_0} + \left(\frac{c}{4} - x_{ac} \right) C_{N_0} \tag{2.41}$$

where C_{N_0} and C_{M_0} are the steady values of the lift coefficient at zero angle of attack and the zero-lift pitching moment coefficient, which must be added to the unsteady aerodynamic coefficients, and x_{ac} is the location of the aerodynamic center measured from the leading edge. These quantities are all obtained from data look-up tables for the airfoil. Finally, in addition to the expression for the pitching moment coefficient, lift and drag coefficients are obtained by resolving the normal and axial suction force coefficients about the angle of attack, α

$$C_L = C_N \left(\cos\alpha + \eta \tan(a_0) \sin\alpha \right) \tag{2.42}$$

$$C_D = C_N \left(\sin\alpha - \eta \tan(a_0) \cos\alpha \right) + C_{D_0} \tag{2.43}$$

where the leading-edge suction recovery factor, η, is determined empirically and accounts for the effects of viscosity on an airfoil of finite thickness, and C_{D_0} is the drag coefficient at zero angle of attack.

In practice, the approximation for $\dot{\alpha}_Y$ in Eq. 2.37 was shown to be inadequate, and

leads to inaccurate calculations of the unsteady aerodynamic loads. Instead, a more accurate analytical expression for the first derivative of α_Y is obtained from

$$\left(1 + \tan^2\alpha_Y\right)\dot{\alpha}_Y = \frac{d}{dt}\tan\alpha_Y \tag{2.44}$$

where $\tan\alpha_Y$, from Eq. 2.23, is

$$\tan\alpha_Y = \frac{(U_T\tan\theta_G + U_P)\cos\gamma_I}{U_T - U_P\tan\theta_G\cos^2\gamma_I} \tag{2.45}$$

Therefore the derivative of α_Y can be expressed as

$$\dot{\alpha}_Y = \frac{G\dot{F} - F\dot{G}}{F^2 + G^2} \tag{2.46}$$

where F and G are defined as

$$F = (U_T\tan\theta_G - U_P)\cos\gamma_I \tag{2.47}$$

$$G = U_T + U_P\tan\theta_G\cos^2\gamma_I \tag{2.48}$$

and

$$\dot{F} = \left[\dot{U}_T\tan\theta_G + U_T\left(1 + \tan^2\theta_G\right)\dot{\theta}_G - \dot{U}_P\right]\cos\gamma_I + (U_T\tan\theta_G - U_P)\frac{d}{dt}\cos\gamma_I \tag{2.49}$$

$$\dot{G} = \dot{U}_T + \dot{U}_P\tan\theta_G\cos^2\gamma_I + U_P\left(1 + \tan^2\theta_G\right)\dot{\theta}_G\cos^2\gamma_I + U_P\tan\theta_G\frac{d}{dt}\cos^2\gamma_I \tag{2.50}$$

with

$$\frac{d}{dt}\cos^2\gamma_I = 2\cos\gamma_I\frac{d}{dt}\cos\gamma_I \tag{2.51}$$

and

$$\frac{d}{dt}\cos\gamma_I = \frac{U_R^2U_T\dot{U}_T - U_T^2U_R\dot{U}_R}{\cos\gamma_I\left(U_T^2 + U_R^2\right)^2} \tag{2.52}$$

2.3 Solution methods

2.3.1 Trim state solution

Fundamentally, trim is defined as the problem of computing a steady state solution of the governing equations of motion for the helicopter dynamics. The solution of the steady state condition is determined by converting the system of coupled ordinary differential equations in Eq. 2.1 to a system of nonlinear algebraic equations. The periodicity of the helicopter response must be satisfied in a steady state condition. The helicopter trim flight condition is calculated in a coordinated, steady, helical turn [135] defined by the

1. velocity along the flight path trajectory, V
2. turn rate about the z_B body axis, $\dot{\psi}_F$
3. flight path climb angle, γ

Straight and level flight is a special case where $\dot{\psi}_F = \gamma = 0$. Hover is a special case of straight and level flight where $V = 0$.

The trim procedure is the same as in Ref. [136]. The rotor equations of motion are transformed into a system of nonlinear algebraic equations using a Galerkin method. The algebraic equations enforcing force and moment equilibrium, the Euler kinematic equations, the inflow equations and the rotor equations are combined in a single coupled system. The solution yields the harmonics of a Fourier expansion of the rotor degrees of freedom, the pitch control settings, trim attitudes and rates of the entire helicopter, and main and tail rotor inflow.

With this in mind trim equations are now defined. Aircraft velocity components in the body axes are expressed in terms of the absolute velocity, V; and the angles of attack, α_F, and sideslip, β_F, which define the orientation of the fuselage relative to the flight path

$$u = V \cos\alpha_F \cos\beta_F \tag{2.53}$$

$$v = V \sin\beta_F \tag{2.54}$$

$$w = V \sin\alpha_F \cos\beta_F \tag{2.55}$$

In a steady turn the bank angle, ϕ_F, and the pitch angle, θ_F, remain constant, such that $\dot{\phi}_F$ and $\dot{\theta}_F$ are equal to zero. Therefore, the aircraft turn rates are based entirely on the yaw turn rate $\dot{\psi}_F$

$$p = -\dot{\psi}_F \sin\theta_F \tag{2.56}$$

$$q = \dot{\psi}_F \sin\phi_F \cos\theta_F \tag{2.57}$$

$$r = \dot{\psi}_F \cos\phi_F \cos\theta_F \tag{2.58}$$

Fuselage trim equations

Aircraft trim motion is completely determined by the prescribed values V and $\dot{\psi}_F$ and the unknown quantities α_F, β_F, ϕ_F and θ_F. Implicit in the definition of steady flight is the fact that accelerations, both linear and angular, in the body axes coordinate system are equal to zero. The four fixed-stick inputs (i,e, collective, lateral, longitudinal, and rudder) complete the set of unknowns for the fuselage system of equations defining the trim problem. The following equilibrium conditions for the fuselage are established:

- *Force and moment equilibrium equations.*

Force equilibrium in the body axes

$$\begin{Bmatrix} X \\ Y \\ Z \end{Bmatrix} - mS\,(\boldsymbol{\omega}) \begin{Bmatrix} u \\ v \\ w \end{Bmatrix} + m \begin{Bmatrix} -g_x \\ g_y \\ g_z \end{Bmatrix} = 0 \tag{2.59}$$

Moment equilibrium in the body axes

$$\begin{Bmatrix} L \\ M \\ N \end{Bmatrix} - S\,(\boldsymbol{\omega}) \cdot \left(I \cdot \begin{Bmatrix} p \\ q \\ r \end{Bmatrix} \right) = 0 \tag{2.60}$$

where linear and angular velocities are determined by Eqs. 2.53–2.58.

- *Turn coordination equation.* Accounts for the inertial terms resulting from the rotation of the body axes with respect to the inertial, or gravitational, coordinate system. If the turn is coordinated then $Y = 0$, resulting in the equilibrium equation

$$g_y - (ur - wp) = 0 \tag{2.61}$$

substituting Eqs. 2.53–2.58 results in

$$\sin\phi_F - \frac{\dot{\psi}_F V}{g}(\cos\alpha_F \cos\phi_F + \sin\alpha_F \tan\theta_F)\cos\beta_F = 0 \tag{2.62}$$

In straight and level flight $\dot{\psi}_F = 0$ and the equation simplifies to

$$\sin\phi_F = 0 \tag{2.63}$$

This is a reasonable equilibrium condition for straight and level flight at advance ratios above $\mu = 0.1$. This implies the helicopter is trimmed to zero roll angle. For advance ratios below $\mu = 0.1$ zero sideslip trim condition is directly enforced by the constraint

$$\beta_F = 0 \tag{2.64}$$

- *Steady climb constraint*. This equation establishes a kinematic relation between the flight path angle and the attack, sideslip, roll and pitch angles. This relation is based on the condition that the resultant velocity vector component along the vertical direction in the gravitational reference frame be steady.

$$\sin(-\gamma) = \mathbf{e}_T \cdot \mathbf{k}_G \tag{2.65}$$

where $\mathbf{e}_T$ is the unit vector tangent to the trajectory. Expanding the unit vector product results in the relation

$$-\sin\gamma = (\sin\alpha_F \cos\beta_F \cos\phi_F + \sin\beta_F \sin\phi_F)\cos\theta_F - \cos\alpha_F \cos\beta_F \sin\theta_F \tag{2.66}$$

Main rotor loads are harmonic in nature and introduce small amplitude oscillations on the fuselage motion. Consequently, in practice it is impossible to satisfy the trim definition for every instant in time. Rather, these equations are considered in a average sense, over one rotor revolution. Therefore, the left hand side expressions in Eqs. 2.59, 2.60, 2.62 and 2.66 are assembled in vector $\boldsymbol{\epsilon}(\bar{\mathbf{x}})$ such that the trim problem system of equations is defined as

$$\mathbf{F}(\bar{\mathbf{x}}) = \int_0^{2\pi} \boldsymbol{\epsilon}(\bar{\mathbf{x}})\, d\psi = \mathbf{0} \tag{2.67}$$

The assumption of steady inflow distribution implies the main rotor and tail rotor inflow trim state derivatives must satisfy the conditions:

$$\int_0^{2\pi} \dot{\lambda}_0 d\psi = 0 \tag{2.68}$$

$$\int_0^{2\pi} \dot{\lambda}_c d\psi = 0 \tag{2.69}$$

$$\int_0^{2\pi} \dot{\lambda}_s d\psi = 0 \tag{2.70}$$

for the main rotor coefficients, and

$$\int_0^{2\pi} \dot{\lambda}_t d\psi = 0 \tag{2.71}$$

for the tail rotor.

Similar conditions are imposed on the downwash aerodynamic interaction coefficients, enforcing the time average of the rate of change of the coefficients to be zero over one revolution.

Treatment of blade trim equations

The approach for calculating the blade mode trim states assumes that blade motion is periodic such that the k-th generalized blade coordinate can be approximated by a Fourier series [136, 137]. The generalized coordinates and their first and second derivatives are given by

$$q^k(\psi) \approx q_0^k + \sum_{j=1}^{N_h} \left(q_{jc}^k \cos j\psi + q_{js}^k \sin j\psi \right) \tag{2.72}$$

$$\dot{q}^k(\psi) \approx \Omega \sum_{j=1}^{N_h} j \left(-q_{jc}^k \sin j\psi + q_{js}^k \cos j\psi \right) \tag{2.73}$$

$$\ddot{q}^k(\psi) \approx -\Omega^2 \sum_{j=1}^{N_h} j^2 \left(q_{jc}^k \cos j\psi + q_{js}^k \sin j\psi \right) \tag{2.74}$$

where the coefficients q_0^k, q_{1c}^k, q_{1s}^k, $\cdots$, $q_{N_hc}^k$ and $q_{N_hs}^k$ are unknown.

All blade mode generalized coordinates are assembled in vector $\mathbf{q}$; and the governing blade bending ordinary differential equations are written in the general form

$$\ddot{\mathbf{q}} - \mathbf{f}(\dot{\mathbf{q}}, \mathbf{q}) = 0 \tag{2.75}$$

The solution for the set of unknown coefficients must satisfy the set of equations

$$\int_0^{2\pi} (\ddot{\mathbf{q}} - \mathbf{f}(\dot{\mathbf{q}}, \mathbf{q}))\, d\psi = \mathbf{0} \tag{2.76}$$

$$\int_0^{2\pi} (\ddot{\mathbf{q}} - \mathbf{f}(\dot{\mathbf{q}}, \mathbf{q})) \cos j\psi\, d\psi = \mathbf{0}, \qquad j = 1, \cdots, N_h \tag{2.77}$$

$$\int_0^{2\pi} (\ddot{\mathbf{q}} - \mathbf{f}(\dot{\mathbf{q}}, \mathbf{q})) \sin j\psi\, d\psi = \mathbf{0}, \qquad j = 1, \cdots, N_h \tag{2.78}$$

which are appended to the system of non-linear algebraic equations. The unknown coefficients are solved for simultaneously along with the fuselage and inflow unknowns.

Unsteady aerodynamics

Solution of the blade unsteady aerodynamics states is also time-periodic and can therefore be approximated by a Fourier series in the same way it is done for the blade modal coefficients. The solution of the k-th unsteady aerodynamics state is approximated by

$$z_k(\psi) \approx z_{k_0} + \sum_{j=1}^{N_h} \left(z_{k_{jc}} \cos j\psi + z_{k_{js}} \sin j\psi \right) \tag{2.79}$$

While the solution for the unsteady aerodynamic unknown harmonic coefficients can be obtained following the same general solution method as for the main rotor coefficients, this is not made practical by the size of the system of equations. As mentioned above, the number of states per unsteady aerodynamics collocation point is 8. Assuming N_h harmonics are used in the approximation of the steady state solution for each state, then the number of variables increases by $8n_p(2N_h + 1)$.

The problem can be simplified substantially because the unsteady aerodynamics states are independent of each other. The governing equations for each state are simple first-order, linear, non-homgeneous time-periodic differential equations with the general

form of

$$\dot{z}_k(t) = a_{f_k}(t) z_k(t) + f_k(t) \tag{2.80}$$

where $f_k(t)$ is a function of the angle of attack motion and the airflow velocity at the given point on the blade; both of which are harmonic functions in trim flight. The steady solution for the unsteady aerodynamics coefficients can be fully determined provided the periodic motion of the point on the blade relative to the air mass is known and well determined.

The fact that the equations governing the unsteady aerodynamics are linear simplifies the calculation of the trim state because the steady state solution for a periodic input is readily available [67]. It can be shown that the harmonic coefficients of the periodic solution are related to the harmonics of the forcing function $f_k(t)$ by a linear algebraic system with an infinite number of equations. If the solution is approximated by the truncated series in Eq. 2.79, and only N_h harmonics are retained, then the $2N_h + 1$ unknown coefficients can be solved for by solving the linear system

$$(C - \mathcal{A}) \begin{Bmatrix} z_{k_0} \\ z_{k_{1c}} \\ z_{k_{1s}} \\ \vdots \\ z_{k_{N_h c}} \\ z_{k_{N_h s}} \end{Bmatrix} = \begin{Bmatrix} f_{k_0} \\ f_{k_{1c}} \\ f_{k_{1s}} \\ \vdots \\ f_{k_{N_h c}} \\ f_{k_{N_h s}} \end{Bmatrix} \tag{2.81}$$

The matrix $\mathcal{A}$ is related to the harmonics of the coefficient $a_{f_k}(t)$ from Eq. 2.80.

$$\mathcal{A} = \begin{bmatrix} a_{k_0} & \frac{1}{2}a_{k_{1c}} & \frac{1}{2}a_{k_{1s}} & \cdots & \frac{1}{2}a_{k_{jc}} & \frac{1}{2}a_{k_{js}} \\ a_{k_{1c}} & & \mathcal{A}_{11} & \cdots & & \mathcal{A}_{1j} \\ a_{k_{1s}} & & & & & \\ \vdots & & \vdots & \ddots & & \\ a_{k_{ic}} & & \mathcal{A}_{i1} & & & \mathcal{A}_{ij} \\ a_{k_{is}} & & & & & \end{bmatrix} \tag{2.82}$$

where the $\mathcal{A}_{ij}$ block matrices are 2×2 matrices whose elements are defined by

$$a_{11}^{ij} = \frac{1}{\pi} \int_0^{2\pi} a_{f_k}(\cdot) \cos i\psi \cos j\psi \, d\psi$$

$$a_{21}^{ij} = \frac{1}{\pi} \int_0^{2\pi} a_{f_k}(\cdot) \sin i\psi \cos j\psi \, d\psi$$

$$a_{12}^{ij} = \frac{1}{\pi} \int_0^{2\pi} a_{f_k}(\cdot) \cos i\psi \sin j\psi \, d\psi$$

$$a_{22}^{ij} = \frac{1}{\pi} \int_0^{2\pi} a_{f_k}(\cdot) \sin i\psi \sin j\psi \, d\psi$$

The matrix C is block diagonal

$$C = \begin{bmatrix} 0 & & & \\ & C_1 & & \\ & & \ddots & \\ & & & C_{N_h} \end{bmatrix} \tag{2.83}$$

and the block for the j-th harmonic is

$$C_j = \Omega \begin{bmatrix} 0 & -j \\ j & 0 \end{bmatrix} \tag{2.84}$$

2.3.2 Linearization

Systems of linear equations can be extracted via a first-order Taylor series expansion of the full set of non-linear equations of motion. Dropping the higher order terms in the expansion and assuming $\mathbf{g}(\dot{\mathbf{y}}_0, \mathbf{y}_0, \mathbf{u}_0; t) = \mathbf{0}$, where the 0 subindex indicates trim values, Eq. 2.1 is reduced to

$$\left[\frac{\partial \mathbf{g}}{\partial \dot{\mathbf{y}}}\right]_0 \cdot \delta\dot{\mathbf{y}} + \left[\frac{\partial \mathbf{g}}{\partial \mathbf{y}}\right]_0 \cdot \delta\mathbf{y} + \left[\frac{\partial \mathbf{g}}{\partial \mathbf{u}}\right]_0 \cdot \delta\mathbf{u} \approx \mathbf{0} \tag{2.85}$$

where the partial derivative matrices are defined as

$$C(\psi) = \left[\frac{\partial \mathbf{g}}{\partial \dot{\mathbf{y}}}\right]_0 \tag{2.86}$$

$$D(\psi) = \left[\frac{\partial \mathbf{g}}{\partial \mathbf{y}}\right]_0 \tag{2.87}$$

$$E(\psi) = \left[\frac{\partial \mathbf{g}}{\partial \mathbf{u}}\right]_0 \tag{2.88}$$

Linearized models are extracted numerically, by perturbing rotor, fuselage, inflow states, unsteady aerodynamics states and control inputs about a trimmed equilibrium position. Because blade dynamics and unsteady aerodynamics are used, the trim state vector $\mathbf{y}_0$ contains time-periodic coefficients in the rotating reference frame. This is true even in hover, where small amounts of longitudinal and lateral cyclic inputs are required to maintain the trim flight condition. As a consequence of this, the matrices of partial derivatives are time-periodic. The resulting first-order linear equations are given in the state-space form

$$\dot{\mathbf{x}} = A(\psi)\mathbf{x} + B(\psi)\mathbf{u} \tag{2.89}$$

where

$$A(\psi) = -C^{-1}(\psi)D(\psi) \tag{2.90}$$

$$B(\psi) = -C^{-1}(\psi)E(\psi) \tag{2.91}$$

and vectors $\mathbf{x}$ and $\mathbf{u}$ represent the perturbation state and control vectors.

The linearized systems are extracted for several rotor azimuth locations over one revolution, and transformed into the non-rotating frame by means of the Multibody Coordinate Transformation which is presented in Appendix A. Since the equations of the coupled rotor/fuselage dynamics are now written in the fixed, or non-rotating, frame of

reference, the linearized models turn out to be time-periodic with period T/N, where N is the number of rotor blades and T is the period of one rotor revolution. The matrices of the linearized model can then be generated as Fourier series. For example, the state matrix $A(\psi)$ is given as:

$$A(\psi) = A_0 + \sum_{k=1}^{K} \left(A_{kc} \cos(kN\psi) + A_{ks} \sin(kN\psi)\right) \tag{2.92}$$

where the matrices A_0, A_{kc}, and A_{ks} are constant, and only A_0 is retained for constant coefficient approximations.

2.4 Higher Harmonic Control

The HHC controller used in the present study is based on a linear, steady state, frequency domain representation of the dynamics of the helicopter. The vector $\tilde{\mathbf{u}}_{HHC}(k)$ of the harmonics of the rotor controls computed by the HHC system is defined as

$$\tilde{\mathbf{u}}_{HHC}(k) = \left[\theta_{3c}(k) \;\; \theta_{3s}(k) \;\; \theta_{4c}(k) \;\; \theta_{4s}(k) \;\; \theta_{5c}(k) \;\; \theta_{5s}(k)\right]^T \tag{2.93}$$

where k is the discrete-time index associated with the sample time at which the control loop operates (i.e., 1/rev). The vector $\tilde{\mathbf{y}}_{HHC}(k)$ contains the N/rev cosine and sine harmonics of the fuselage accelerations, and is defined as

$$\tilde{\mathbf{y}}_{HHC}(k) = \left[\tilde{y}^1_{Nc}(k) \;\; \tilde{y}^2_{Nc}(k) \;\; \ldots \;\; \tilde{y}^n_{Nc}(k) \;\; \tilde{y}^1_{Ns}(k) \;\; \tilde{y}^2_{Ns}(k) \;\; \ldots \;\; \tilde{y}^n_{Ns}(k)\right]^T \tag{2.94}$$

where $\tilde{y}^i_{Nc}(k)$ and $\tilde{y}^i_{Ns}(k)$, $i = 1, \ldots, n$ are, respectively, the cosine and sine components of the i-th N/rev output $\tilde{y}^i(k)$, each defined as

$$\tilde{y}^i_{Nc}(k) = \frac{1}{\pi} \int_{k\pi}^{(k+1)\pi} y^i_H(\psi) \cos N\psi \, d\psi \tag{2.95}$$

$$\tilde{y}^i_{Ns}(k) = \frac{1}{\pi} \int_{k\pi}^{(k+1)\pi} y^i_H(\psi) \sin N\psi \, d\psi \tag{2.96}$$

The generic output $\tilde{y}^i(k)$ can be one of the linear or angular components of the accelerations, which in turn can be measured at one or more locations. In general, there will be n such measurements, and therefore the measurement vector will have $p = 2n$ elements. Finally, $\tilde{\mathbf{z}}$ is the vector of N/rev disturbance components corresponding to $\tilde{\mathbf{y}}_{HHC}(k)$.

Then, assuming that the accelerations are linearly related to the HHC harmonics, the variables defined above can be related by

$$\tilde{\mathbf{y}}_{HHC}(k) = \mathbf{T}\tilde{\mathbf{u}}_{HHC}(k) + \tilde{\mathbf{z}}(k) \tag{2.97}$$

where $\mathbf{T}$ is a real, constant coefficient matrix that links the harmonics of the HHC inputs to those of the acceleration response (see Ref. [119] for details). The matrix $\mathbf{T}$ can be either estimated from measured data using on-line or off-line identification algorithms, or computed on the basis of a mathematical model of the helicopter, as done in the present study. In general, $\mathbf{T}$ is a function of the flight condition. At each discrete time step the HHC controller selects the value of the input harmonics $\tilde{\mathbf{u}}_{HHC}$ to reduce the effect of $\tilde{\mathbf{z}}$ on $\tilde{\mathbf{y}}_{HHC}$. Assuming that the baseline acceleration vector $\tilde{\mathbf{z}}$ is constant over the time step, the optimal open loop solution is given by

$$\tilde{\mathbf{u}}_{HHC}(k) = -\mathbf{T}^{\dagger}\tilde{\mathbf{z}}(k) \tag{2.98}$$

where $\mathbf{T}^{\dagger}$ is the pseudoinverse of the $\mathbf{T}$ matrix (which is not necessarily square). Since in general $\tilde{\mathbf{z}}$ cannot be measured directly, the same result can be obtained by using a discrete-time integral control law in closed loop, i.e., based on the measurements of $\tilde{\mathbf{y}}_{HHC}$:

$$\tilde{\mathbf{u}}_{HHC}(k+1) = \tilde{\mathbf{u}}_{HHC}(k) - \mathbf{T}^{\dagger}\ \tilde{\mathbf{y}}_{HHC}(k) \tag{2.99}$$

The HHC control algorithm used in the present study is defined in terms of the

minimization of a quadratic cost function J of the form [115]

$$J = \tilde{\mathbf{y}}_{HHC}^T \, Q \, \tilde{\mathbf{y}}_{HHC} + \Delta\tilde{\mathbf{u}}_{HHC}^T \, R \, \Delta\tilde{\mathbf{u}}_{HHC} \tag{2.100}$$

where $Q = Q^T \geq 0$ and $R = R^T > 0$ are matrices that allow different weighting of acceleration outputs and $\Delta\tilde{\mathbf{u}}_{HHC}$ is the increment of $\tilde{\mathbf{u}}_{HHC}$ from one iteration to the next:

$$\Delta\tilde{\mathbf{u}}_{HHC}(k+1) = \tilde{\mathbf{u}}_{HHC}(k+1) - \tilde{\mathbf{u}}_{HHC}(k) \tag{2.101}$$

The minimization of J, Eq. (2.100) leads to the control law

$$\Delta\tilde{\mathbf{u}}_{HHC}(k+1) = -(\mathbf{T}^T Q \, \mathbf{T} + R)^{-1} \, \mathbf{T}^T Q \, \tilde{\mathbf{y}}_{HHC}(k) \tag{2.102}$$

The $\mathbf{T}$ matrix links the N/rev harmonics of the output to the harmonics of the HHC input vector $\tilde{\mathbf{u}}_{HHC}$. The matrix is fixed, and is obtained from the linearized model of the complete helicopter using a methodology based on the harmonic transfer function. The derivation is presented in detail in Ref. [119].

2.5 Architecture of the HHC System

The present study focuses on the simulation of the HHC architecture shown in general form in Fig. 2.2. The operation of the system consists of the following three steps, which are performed at every rotor revolution: (i) the determination of the N/rev acceleration output vector $\tilde{\mathbf{y}}_{HHC}(k)$; (ii) the update $\tilde{\mathbf{u}}_{HHC}(k+1)$ of the control input using Eq. (2.102); and (iii) the actual application of $\tilde{\mathbf{u}}_{HHC}(k+1)$ via a simple zero-order-hold.

Two different sampling rates are used. The first, and faster, corresponds to the sampling of the acceleration signals required to reconstruct the N/rev harmonics. The

second, and slower, is that corresponding to the 1/rev update of the HHC inputs. The portions of the block diagram where each sampling rate is used are shown in Fig. 2.2.

2.6 State space formulation of higher harmonic controllers

This section presents the state space formulation of HHC controllers of increasing complexity. First, some background on the T-matrix algorithm is given, and a continuous-time, state space analysis is presented for the case of a SISO HHC system in which input and output are at the same harmonic (N/rev, i.e. N times the rotor speed) of rotor speed. Next, the analysis is extended to the case in which input and output are at different harmonics and the case of a MIMO HHC system with inputs and outputs at arbitrary harmonics is considered, by combining the results of the two previous cases. More precisely the following three cases, corresponding to three different selections for the control input vector u, will be dealt with:

- Control input given by a single harmonic at the blade passing frequency, i.e.,

$$u = u_N = \begin{bmatrix} \theta_{Nc} & \theta_{Ns} \end{bmatrix}^T .$$

- Control input u given by a single harmonic at a frequency different from the blade passing one, i.e.,

$$u = u_M = \begin{bmatrix} \theta_{Mc} & \theta_{Ms} \end{bmatrix}^T ,$$

  with $M \neq N$, like, e.g., $M = N - 1$ or $M = N + 1$.

- Control input u given by the superposition of a number of different harmonics:

$$\mathbf{u}^T = \begin{bmatrix} \theta_{N_1 c} & \theta_{N_1 s} & \theta_{N_2 c} & \theta_{N_2 s} & \dots & \theta_{N_m c} & \theta_{N_m s} \end{bmatrix},$$

with N_i, $i = 1, \ldots, m$ multiples of the rotor angular frequency. For example, one might consider in practice the choice of u given by

$$u = \begin{bmatrix} \theta_{(N-1)c} & \theta_{(N-1)s} & \theta_{Nc} & \theta_{Ns} & \theta_{(N+1)c} & \theta_{(N+1)s} \end{bmatrix}^T . \tag{2.103}$$

As will be made clear in the following, assuming as control variables the harmonics of the rotating frame pitch control greatly simplifies the task of the state space realization of the HHC compensators.

2.6.1 SISO with input and output at the same frequency

A typical non-adaptive HHC system is based on a discrete time mathematical model describing the response of the helicopter to higher harmonic inputs, of the form

$$\mathbf{y}_N(k) = T_{N,N}\mathbf{u}_N(k) + \mathbf{z}_N(k) \tag{2.104}$$

where k is the rotor revolution index, $\mathbf{y}_N$ is a vector of N/rev harmonics of measured outputs (e.g., hub loads or accelerations at some point of the fuselage), $\mathbf{u}_N$ is a vector of control inputs, and $T_{N,N}$ is a 2 by 2 constant matrix. The vector $\mathbf{y}_N(k)$ is defined as

$$\mathbf{y}_N(k) = \begin{bmatrix} y_{Nc}(k) \\ y_{Ns}(k) \end{bmatrix} = \begin{bmatrix} \frac{1}{\pi}\int_{k\pi}^{(k+1)\pi} y(\psi)\cos(N\psi)d\psi \\ \frac{1}{\pi}\int_{k\pi}^{(k+1)\pi} y(\psi)\sin(N\psi)d\psi \end{bmatrix} \tag{2.105}$$

The vector $\mathbf{z}_N$ contains the N/rev harmonics of the "baseline" vibrations, i.e., the vibrations in the absence of HHC. The control input vector is similarly defined as:

$$\mathbf{u}_N = \begin{bmatrix} \theta_{Nc} \\ \theta_{Ns} \end{bmatrix} \tag{2.106}$$

where θ_{Nc} and θ_{Ns} are, respectively, the cosine and sine components of the N/rev pitch control input, applied in the rotating system.

The HHC inputs are generally updated at discrete time intervals, for example, once per rotor revolution. The conventional HHC control law is derived by minimizing at each discrete time step k the cost function

$$J(k) = y_N(k)^T Q y_N(k) + \Delta u_N(k)^T R \Delta u_N(k) \tag{2.107}$$

where $Q = Q^T \geq 0$, $R > 0$ and $\Delta u_N(k)$ is the increment of the control variable at time k, i.e.,

$$\Delta u_N(k) = u_N(k) - u_N(k-1). \tag{2.108}$$

Differentiating (2.107) with respect to $\Delta u_N(k)$ yields the control law

$$\mathbf{u}_N(k+1) = \mathbf{u}_N(k) - K_{N,N}\mathbf{y}_N(k). \tag{2.109}$$

where $K_{N,N} = (T_{N,N}^T Q T_{N,N} + R)^{-1} T_{N,N}^T Q$. Equation (2.109) is well known in the literature as the "T-matrix" algorithm. It can be seen from Eqs. (2.104) and (2.109) that this control algorithm introduces a discrete time integral action which ensures that $y_N \to 0$ as $k \to \infty$. Actually, with $Q = I_{2,2}$ and $R = 0$ deadbeat control (i.e., the output goes to zero after one discrete-time step) could in principle be achieved if exact knowledge of the $T_{N,N}$ matrix was available, and if the static model, Eq. (2.104), was an accurate representation of rotor dynamics. However, these two assumptions are generally not satisfied, as $T_{N,N}$ can only be estimated up to some accuracy level and Eq. (2.104) clearly does not hold if the helicopter is not operating in steady state. Note, also, that if in the cost function (2.107) one chooses $R = 0$ and Q proportional to the identity matrix, the control law (2.109) reduces to

$$\mathbf{u}_N(k+1) = \mathbf{u}_N(k) - T_{N,N}^{-1}\mathbf{y}_N(k), \tag{2.110}$$

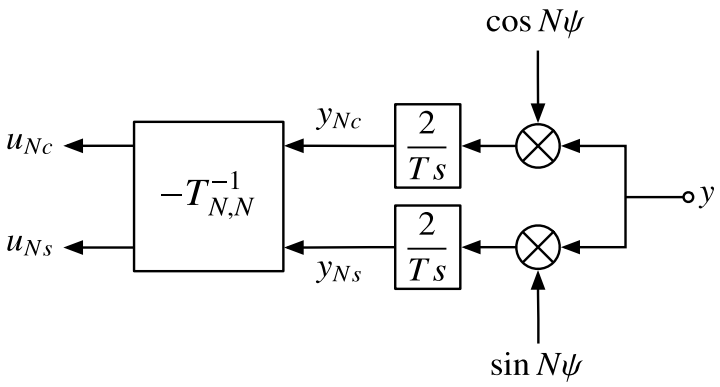

Figure 2.1: Block diagram of the continuous time SISO HHC algorithm.

which can be given a minimum variance interpretation, in the sense that this control law guarantees at each time step the closed loop minimization of the cost function

$$J(k) = \mathbf{y}_N(k)^T \mathbf{y}_N(k). \tag{2.111}$$

Neglecting the effects of the sample and hold scheme of the digital implementation in the T-matrix algorithm, the overall control algorithm can be represented by the block diagram given in Figure 2.1.

Now, following [58], choose y_{Nc} and y_{Ns} as state variables for the controller in Fig. 2.1. Then, the following state space model for the HHC compensator is obtained:

$$\dot{\mathbf{y}}_N = A_c \mathbf{y}_N + B_c(\psi)\mathbf{y} \tag{2.112}$$

$$u = C_c \mathbf{y}_N \tag{2.113}$$

where

$$A_c = \begin{bmatrix} 0 & 0 \\ 0 & 0 \end{bmatrix} \tag{2.114}$$

$$B_c(\psi) = K_{N,N} \begin{bmatrix} \cos(N\psi) \\ \sin(N\psi) \end{bmatrix} \tag{2.115}$$

$$C_c = -\frac{2}{T} I_{2,2}.$$

2.6.2 SISO with input and output at different frequencies

The HHC input in the rotating system is usually not limited to the same N/rev frequency of the vibrations to be attenuated. Typically, inputs at $N-1$/rev and $N+1$/rev are also applied (recall that N/rev inputs of collective, longitudinal, and lateral cyclic pitch in the fixed system result in $N-1$, N, and $N+1$/rev pitch inputsin the rotating system).

In this case, the steady state model relating the N/rev harmonic of the output $y(t)$ to the M/rev harmonic of the pitch input $u(t)$, with $M \neq N$, can be written in the form

$$\mathbf{y}_N(k) = T_{N,M}\mathbf{u}_M(k) + \mathbf{z}_N(k) \tag{2.116}$$

where $\mathbf{u}_M$ is defined as in Eq. (2.106), but for an M/rev harmonic, and where the (constant) matrix $T_{N,M}$ relates the amplitude of the M/rev control input u to the corresponding steady state amplitude of the N/rev component of the output y. The control scheme for the attenuation of N/rev vibrations using an M/rev input can then be derived along the lines of the previous case, and is represented by the equation

$$\mathbf{u}_M(k+1) = \mathbf{u}_M(k) - K_{N,M}\mathbf{y}_N(k). \tag{2.117}$$

where $K_{N,M} = (T_{N,M}^T Q T_{N,M} + R)^{-1} T_{N,M}^T Q$. As shown in the following Section, the matrix $T_{N,M}$ can be related to the Harmonic Transfer Function (HTF) of the controlled system,

which is an extension to periodic systems of the frequency response function of a time-invariant system [67, 138]. In addition, as in the case of HHC with input and output at the same frequency N/rev, the discrete control law, Eq. (2.117) guarantees that $y_N \to 0$ as $k \to \infty$, provided that the system can be modeled as in Eq. (2.116).

Similarly to the $M = N$ case, the state space model for the case $N \neq M$ is given by

$$\dot{\mathbf{y}}_N = A_c \mathbf{y}_N + B_c(\psi)\mathbf{y} \tag{2.118}$$

$$u = C_c \mathbf{y}_N \tag{2.119}$$

where

$$A_c = \begin{bmatrix} 0 & 0 \\ 0 & 0 \end{bmatrix} \tag{2.120}$$

$$B_c(\psi) = K_{N,M} \begin{bmatrix} \cos(N\psi) \\ \sin(N\psi) \end{bmatrix} \tag{2.121}$$

$$C_c = -\frac{2}{T} I_{2,2}. \tag{2.122}$$

This discussion shows that a coupled rotor-fuselage system with even a simple SISO HHC controller is intrinsically a system with periodic coefficients if the HHC output and the vibration to be attenuated are at two different multiples of the rotor frequency. This happens even if the rotor-fuselage system is modeled as a system with constant coefficients. Therefore, stability, performance and robustness analyses of an HHC system can only be carried out using the tools of periodic systems theory.

2.6.3 MIMO with input and output at arbitrary harmonics

In typical implementations of HHC, multi-harmonic signals are frequently used to attenuate several components of the vibratory loads. For example, inputs at $N - 1$, N and

$N+1$/rev, sine and cosine (for a total of 6 inputs), could be used simultaneously to control six components of the N/rev vibratory hub forces and moments. Therefore, this section extends the previous SISO discussion to a MIMO HHC system. We will consider a general configuration in which output measurements of N/rev vibration are available at n different locations, while a number m of harmonics at frequencies N_i, $i = 1, \ldots, m$ is applied on the control input u. In this case, the measurement vector has $2n$ elements and is defined as:

$$\mathbf{y}_N^T = \begin{bmatrix} y_{Nc}^1 & \ldots & y_{Nc}^n & y_{Ns}^1 & \ldots & y_{Ns}^n \end{bmatrix} \tag{2.123}$$

where y_{Nc}^i and y_{Ns}^i, $i = 1, \ldots, n$ are, respectively, the cosine and sine components of the i-th N/rev output, which can be, for example, a force or moment component, or a component of the acceleration at one or more points of the fuselage.

On the other hand, the HHC input vector $\mathbf{u}$ has $2m$ elements and is defined as

$$\mathbf{u}^T = \begin{bmatrix} u_{N_1 c} & u_{N_1 s} & u_{N_2 c} & u_{N_2 s} & \ldots & u_{N_m c} & u_{N_m s} \end{bmatrix}. \tag{2.124}$$

where $u_{N_i c}$, $i = 1, \ldots, m$ and $u_{N_i s}$, $i = 1, \ldots, m$ are the cosine and sine component of the HHC input, at desired harmonics not necessarily equal to N.

Assume now, as in the SISO case, that input and output harmonics are related by the linear equation

$$\mathbf{y}_N(k) = \mathbf{T}\mathbf{u}(k) + \mathbf{z}_N(k) \tag{2.125}$$

where $\mathbf{T}$ is a $2n \times 2m$ constant coefficient matrix, which is again related to the HTF of the time periodic linearized model of the helicopter. Then, the "T-matrix algorithm" is given by

$$\mathbf{u}(k+1) = \mathbf{u}(k) - \mathbf{K}\mathbf{y}_N(k). \tag{2.126}$$

where $\mathbf{K} = (\mathbf{T}^T Q \mathbf{T} + R)^{-1} \mathbf{T}^T Q$, where $Q = Q^T \geq 0$ and $R = R^T > 0$ are cost weighting matrices of suitable dimensions.

In the MIMO case, the operation of the HHC control law differs considerably depending on the relationship between the number of control inputs and measured variables which are available. In order to illustrate this, we now consider the formulation of the "T-matrix algorithm" in the MIMO case with $Q = I_{n,n}$ and $R = 0$, by treating separately the cases of $n = m$ and $n > m$[1].

In the case of a "square" control problem, i.e., when $n = m$, the SISO algorithm can be readily extended to

$$\mathbf{u}(k+1) = \mathbf{u}(k) - \mathbf{T}^{-1} \mathbf{y}_N(k). \tag{2.127}$$

On the other hand, if $n > m$ matrix $\mathbf{T}$ is not square anymore and the discrete time control algorithm must be written as

$$\mathbf{u}(k+1) = \mathbf{u}(k) - \mathbf{T}^{\dagger} \mathbf{y}_N(k), \tag{2.128}$$

where $\mathbf{T}^{\dagger} = (\mathbf{T}^T \mathbf{T})^{-1} \mathbf{T}^T$ is the pseudoinverse of $\mathbf{T}$. In particular, the minimum of the cost function equals zero only in the $n = m$ case, i.e., unless one considers (at least) the square case, it is not possible to guarantee that the vibratory disturbance will be zeroed on all output channels.

The equivalent continuous time formulation for the MIMO HHC compensator, described in discrete form by Eq. (2.126), can be obtained by applying the previously described SISO results.

Therefore, considering first the case of a control system with as many inputs as

[1]The case of $n < m$ is hardly relevant from a practical point of view.

outputs, the state-space formulation is given by the order $2n$ system:

$$\dot{\mathbf{y}}_N = A_c \mathbf{y}_N + B_c(\psi)\mathbf{y} \tag{2.129}$$

$$u = C_c \mathbf{y}_N \tag{2.130}$$

where A_c is the $2n \times 2n$ matrix

$$A_c = \begin{bmatrix} 0 & 0 & \dots & 0 \\ 0 & 0 & \dots & 0 \\ \vdots & \vdots & & \vdots \\ 0 & 0 & \dots & 0 \end{bmatrix}, \tag{2.131}$$

$B_c(\psi)$ is the $2n \times n$ matrix

$$B_c(\psi) = \mathbf{K} \begin{bmatrix} \cos(N\psi) I_{n,n} \\ \sin(N\psi) I_{n,n} \end{bmatrix} \tag{2.132}$$

and

$$C_c = -\frac{2}{T} I_{2n \times 2n}. \tag{2.133}$$

For example, consider the case of a control system relying on the application of (N-1), N and (N+1)/rev inputs in the rotating frame in order to attenuate vibratory accelerations in $n = 3$ different locations in the fuselage, so that $m = 3$, $N_1 = N - 1$, $N_2 = N$ and $N_3 = N + 1$ and

$$u^T = \begin{bmatrix} \theta_{(N-1)c} & \theta_{(N-1)s} & \theta_{Nc} & \theta_{Ns} & \theta_{(N+1)c} & \theta_{(N+1)s} \end{bmatrix} \tag{2.134}$$

$$y^T = \begin{bmatrix} y_1 & y_2 & y_3 \end{bmatrix}. \tag{2.135}$$

Then, the state space model for the controller is given by

$$A_c = 0_{6\times 6} \tag{2.136}$$

$$B_c(\psi) = \mathbf{K}\begin{bmatrix} \cos(N\psi) & 0 & 0 \\ 0 & \cos(N\psi) & 0 \\ 0 & 0 & \cos(N\psi) \\ \sin(N\psi) & 0 & 0 \\ 0 & \sin(N\psi) & 0 \\ 0 & 0 & \sin(N\psi) \end{bmatrix}. \tag{2.137}$$

As in the SISO case, since the control inputs are directly given by the higher harmonics of θ, there is no need for a "modulation" term in matrix C_c which therefore turns out to be constant:

$$C_c = -\frac{2}{T} I_{6\times 6}. \tag{2.138}$$

Similar expressions can be worked out in the case of a control system with more outputs than inputs.

2.7 Definition of the T-matrix in terms of the helicopter models

The control laws discussed in the previous Section call for the availability of input/outout models for the helicopter response to higher harmonic control inputs. The aim of this Section is to provide the necessary background on the frequency response of time-periodic systems and use such analytical tools in order to derive explicit expressions for the T-matrix.

2.7.1 Development of the Harmonic Transfer Function

This Section summarizes the main aspects of the development of the Harmonic Transfer Function (HTF) [67]. Consider a continuous-time linear periodic system:

$$\begin{aligned} \dot{\mathbf{x}}(t) &= A(t)\mathbf{x}(t) + B(t)\mathbf{u}(t) \\ \mathbf{y}(t) &= C(t)\mathbf{x}(t) + D(t)\mathbf{u}(t) \end{aligned} \tag{2.139}$$

Each matrix can be expanded in a complex Fourier series

$$A(t) = \sum_{m=-\infty}^{\infty} A_m e^{jm\Omega t} \tag{2.140}$$

and similarly for $B(t)$, $C(t)$ and $D(t)$. The system can be analyzed in the frequency domain as follows. Introduce the class of *Exponentially Modulated Periodic* (EMP) signals [67]. The (complex) signal $u(t)$ is said to be EMP of period T and modulation s if

$$u(t) = \sum_{k=-\infty}^{\infty} u_k e^{s_k t} = e^{st} \sum_{k=-\infty}^{\infty} u_k e^{jk\Omega t} \tag{2.141}$$

where $t \geq 0$, $s_k = s + jk\Omega$, and s is a complex scalar.

The class of EMP signals is a generalization of the class of T-periodic signals, i.e., of signals with period T: in fact, an EMP signal with $s = 0$ is just an ordinary time-periodic signal.

In much the same way as a time invariant system subject to a (complex) exponential input has an exponential steady-state response, a periodic system subject to an EMP input has an EMP steady-state response. In such a response, all signals of interest (x, $\dot{x}$, y) can be expanded as EMP signals. By deriving Fourier expansions for $A(t)$, $B(t)$, $C(t)$ and $D(t)$, it is possible to prove that the EMP steady-state response of the system can be expressed as the infinite dimensional matrix equation with *constant* elements [67]

$$\begin{aligned} s\mathcal{X} &= (\mathcal{A} - \mathcal{N})\mathcal{X} + \mathcal{B}\mathcal{U} \\ \mathcal{Y} &= \mathcal{C}\mathcal{X} + \mathcal{D}\mathcal{U} \end{aligned} \tag{2.142}$$

where $\mathcal{X}$, $\mathcal{U}$ and $\mathcal{Y}$ are doubly infinite vectors formed with the harmonics of $\mathbf{x}$, $\mathbf{u}$ and $\mathbf{y}$ respectively, organized in the following fashion:

$$\mathcal{X}^T = \begin{bmatrix} \cdots & \mathbf{x}_{-2}^T & \mathbf{x}_{-1}^T & \mathbf{x}_0^T & \mathbf{x}_1^T & \mathbf{x}_2^T & \cdots \end{bmatrix}, \tag{2.143}$$

and similarly for $\mathcal{U}$ and $\mathcal{Y}$. $\mathcal{A}$, $\mathcal{B}$, $\mathcal{C}$ and $\mathcal{D}$ are doubly infinite Toeplitz matrices formed with the harmonics of $A(\cdot)$, $B(\cdot)$, $C(\cdot)$ and $D(\cdot)$ respectively as follows

$$\mathcal{A} = \begin{bmatrix} \ddots & \vdots & \vdots & \vdots & \vdots & \vdots & \\ \cdots & A_0 & A_{-1} & A_{-2} & A_{-3} & A_{-4} & \cdots \\ \cdots & A_1 & A_0 & A_{-1} & A_{-2} & A_{-3} & \cdots \\ \cdots & A_2 & A_1 & A_0 & A_{-1} & A_{-2} & \cdots \\ \cdots & A_3 & A_2 & A_1 & A_0 & A_{-1} & \cdots \\ \cdots & A_4 & A_3 & A_2 & A_1 & A_0 & \cdots \\ & \vdots & \vdots & \vdots & \vdots & \vdots & \ddots \end{bmatrix} \tag{2.144}$$

(and similarly for $\mathcal{B}$, $\mathcal{C}$ and $\mathcal{D}$), where the submatrices A_n in Eq. (2.144) are the coefficients of the Fourier expansion of matrix $A(t)$, given in Eq. (2.140). Note that the expansions of the state space matrices can be also expressed in trigonometric form (see Eq. 2.160), recalling that[2]

$$A_k = \frac{1}{2}(A_{kc} - jA_{ks}) \qquad A_{-k} = \frac{1}{2}(A_{kc} + jA_{ks}) \qquad k = 1, 2, \ldots \tag{2.145}$$

with A_0 identical in both Eq. (2.144) and Eq. (2.160). Similar relations hold for the harmonics of B, C, and D.

[2]Recall that the Fourier series can be rewritten in complex exponential form, i.e., $a(t) = a_0 + \sum_{k=1}^{\infty}(a_{nc}\cos n\omega t + a_{ns}\sin n\omega t) = \sum_{k=-\infty}^{\infty} a_k e^{jk\omega t}$, with $a_k = (a_{kc} - ja_{ks})/2$, and $a_{-k} = (a_{kc} + ja_{ks})/2, k = 1, 2, \ldots$

Matrix $\mathcal{N}$ is a block diagonal complex-valued matrix given by

$$\mathcal{N} = \text{blkdiag}\{jn\Omega I\} = j\Omega \begin{bmatrix} \ddots & \vdots & \vdots & \vdots & \vdots & \vdots & \\ \cdots & -2I & 0 & 0 & 0 & 0 & \cdots \\ \cdots & 0 & -I & 0 & 0 & 0 & \cdots \\ \cdots & 0 & 0 & 0 & 0 & 0 & \cdots \\ \cdots & 0 & 0 & 0 & I & 0 & \cdots \\ \cdots & 0 & 0 & 0 & 0 & 2I & \cdots \\ & \vdots & \vdots & \vdots & \vdots & \vdots & \ddots \end{bmatrix} \tag{2.146}$$

where I is the identity matrix, of size equal to the number of states.

From Eq. (2.142), one can define the HTF as the operator:

$$\mathcal{G}(s) = C[s\mathcal{I} - (\mathcal{A} - \mathcal{N})]^{-1}\mathcal{B} + \mathcal{D}. \tag{2.147}$$

which relates the input harmonics and the output harmonics (contained in the infinite vectors $\mathcal{U}$ and $\mathcal{Y}$ respectively). Eq. (2.147) is the extension to the case of periodic systems of the corresponding constant coefficient expression for the transfer function

$$G(s) = C\left[sI - A\right]^{-1} B + D. \tag{2.148}$$

In particular, if $s = 0$, which, in the helicopter case, corresponds to the steady-state response of the system to a periodic input of basic frequency N/rev, the appropriate input/output operator for periodic systems becomes

$$\mathcal{G}(0) = C[\mathcal{N} - \mathcal{A}]^{-1}\mathcal{B} + \mathcal{D}. \tag{2.149}$$

2.7.2 Definition of the T-matrix

The $T_{N,N}$, $T_{N,M}$ and $\mathbf{T}$ matrices used in the formulation of the HHC and PHHC algorithms can be related to the elements of the HTF of the linearized helicopter model, as follows.

First of all recall that the T-matrix, by definition, relates the steady state response of the helicopter to a proper steady state higher harmonic input. This implies that in order to define the T-matrix for the helicopter we only have to study the response of the periodic helicopter models to a EMP input with $s = 0$, i.e., we only have to compute the input/output operator $\hat{\mathcal{G}}(0)$. Also, note that according to the definition of the control input vector u which has been adopted, the rotor will be subject to a proper, steady state higher harmonic control input whenever the control vector u is *constant*. For example, consider the linear time-periodic system (2.139) and the constant input $u(t) = u_0$. The vector $\mathcal{U}$ corresponding to $u(t) = u_0$ is clearly given by

$$\mathcal{U}^T = \begin{bmatrix} \cdots & 0 & 0 & \mathbf{u}_0^T & 0 & 0 & \cdots \end{bmatrix}, \tag{2.150}$$

and the steady state response $\mathcal{Y}$ of the periodic system is given by

$$\mathcal{Y} = \mathcal{G}(0)\mathcal{U} \tag{2.151}$$

which can be equivalently written as

$$\begin{bmatrix} \vdots \\ y_{-2N} \\ y_{-N} \\ y_0 \\ y_N \\ y_{2N} \\ \vdots \end{bmatrix} = \begin{bmatrix} \ddots & \vdots & \vdots & \vdots & \vdots & \vdots & \\ \cdots & G_{-2N,-2N} & G_{-2N,-N} & G_{-2N,0} & G_{-2N,N} & G_{-2N,2N} & \cdots \\ \cdots & G_{-N,-2N} & G_{-N,-N} & G_{-N,0} & G_{-N,N} & G_{-N,2N} & \cdots \\ \cdots & G_{0,-2N} & G_{0,-N} & G_{0,0} & G_{0,N} & G_{0,2N} & \cdots \\ \cdots & G_{N,-2N} & G_{N,-N} & G_{N,0} & G_{N,N} & G_{N,2N} & \cdots \\ \cdots & G_{2N,-2N} & G_{2N,-N} & G_{2N,0} & G_{2N,N} & G_{2N,2N} & \cdots \\ & \vdots & \vdots & \vdots & \vdots & \vdots & \ddots \end{bmatrix} \begin{bmatrix} \vdots \\ 0 \\ 0 \\ u_0 \\ 0 \\ 0 \\ \vdots \end{bmatrix}. \tag{2.152}$$

From equation (2.152) we have that

$$\begin{bmatrix} y_{-N} \\ y_N \end{bmatrix} = \begin{bmatrix} G_{-N,0} \\ G_{N,0} \end{bmatrix} u_0 \tag{2.153}$$

and converting the N/rev harmonics of the output from exponential to trigonometric form we have that[3]

$$\begin{bmatrix} y_{Nc} \\ y_{Ns} \end{bmatrix} = 2 \begin{bmatrix} \text{Real}[G_{N,0}] \\ \text{Imag}[G_{N,0}] \end{bmatrix} u_0, \tag{2.154}$$

so that the T-matrix is given by

$$\mathbf{T} = 2 \begin{bmatrix} \text{Real}[G_{N,0}] \\ \text{Imag}[G_{N,0}] \end{bmatrix}. \tag{2.155}$$

2.7.3 Construction of the T-matrix

From a practical point of view, the above theoretical analysis of the frequency response of periodic system, and the corresponding definitions for the T-matrix relating selected input-output frequencies only, rely on the use of infinite dimensional matrices. When it comes to the numerical construction of the T-matrix, however, one has to resort to finite dimensional approximations of the system matrices $\mathcal{A}$, $\mathcal{B}$, C, and $\mathcal{D}$. Consider, for example, the problem of constructing the T-matrix, as defined in equation (2.155) for a periodic system of the form (2.139) with n outputs, m inputs and n_s states. First of all, one chooses the dimension of the expansions $\mathcal{A}$, $\mathcal{B}$, $\mathcal{C}$, and $\mathcal{D}$ for the state space matrices A, B, C, and D, in terms of the number of block rows one wants to take into account in $\mathcal{A}$. For example, we choose to include a number $B = 5$ of blocks in each row of the expansion of the system matrices, then $\mathcal{A}$ has dimension $n_s B \times n_s B$ and is given by

$$\mathcal{A} = \begin{bmatrix} A_0 & A_{-1} & A_{-2} & A_{-3} & A_{-4} \\ A_1 & A_0 & A_{-1} & A_{-2} & A_{-3} \\ A_2 & A_1 & A_0 & A_{-1} & A_{-2} \\ A_3 & A_2 & A_1 & A_0 & A_{-1} \\ A_4 & A_3 & A_2 & A_1 & A_0 \end{bmatrix}, \tag{2.156}$$

[3]Note that $G_{-N,0}$ and $G_{N,0}$ are complex conjugates.

and similarly for $\mathcal{B}$, C, and $\mathcal{D}$. Therefore, the HTF is given by the $2nB \times mB$ matrix, as follows

$$\begin{bmatrix} y_{-2N} \\ y_{-N} \\ y_0 \\ y_N \\ y_{2N} \end{bmatrix} = \mathcal{G}(0)\mathcal{U} = \begin{bmatrix} G_{-2N,-2N} & G_{-2N,-N} & G_{-2N,0} & G_{-2N,N} & G_{-2N,2N} \\ G_{-N,-2N} & G_{-N,-N} & G_{-N,0} & G_{-N,N} & G_{-N,2N} \\ G_{0,-2N} & G_{0,-N} & G_{0,0} & G_{0,N} & G_{0,2N} \\ G_{N,-2N} & G_{N,-N} & G_{N,0} & G_{N,N} & G_{N,2N} \\ G_{2N,-2N} & G_{2N,-N} & G_{2N,0} & G_{2N,N} & G_{2N,2N} \end{bmatrix} \begin{bmatrix} 0 \\ 0 \\ u_0 \\ 0 \\ 0 \end{bmatrix}. \tag{2.157}$$

Using a Matlab-like notation, the blocks $G_{-N,0}$, $G_{N,0}$ can be extracted from $\mathcal{G}(0)$ as the submatrices $\mathcal{G}(0)(2n+1:3n, 2m+1:3m)$ and $\mathcal{G}(0)(4n+1:5n, 2m+1:3m)$. respectively. Clearly, the choice of the number of block rows B will affect the accuracy of the numerical construction (see also [139] for an analysis of the effect of truncation in the study of frequency response operators), so as general rule B should be chosen sufficiently large in order to ensure that the T-matrix constructed from the truncated HTF gives a good approximation of the actual T-matrix.

2.8 Helicopter models for control design

Linear models are extracted numerically, as described in Sec. 2.3.2, by perturbing rotor, fuselage, and inflow states about a trimmed equilibrium position. The resulting continuous-time, linearized, time periodic model of the helicopter is in the form

$$\dot{\mathbf{x}}_H(t) = A_H(t)\mathbf{x}_H(t) + B_{FCS}(t)\mathbf{u}_{FCS}(t) + B_{HHC}(t)\mathbf{u}_{HHC}(t) \tag{2.158}$$

$$\mathbf{y}_H(t) = C_H(t)\mathbf{x}_H(t) + D_{FCS}(t)\mathbf{u}_{FCS}(t) + D_{HHC}(t)\mathbf{u}_{HHC}(t) \tag{2.159}$$

where all the matrices are periodic, with period corresponding to N/rev; the control vectors $\mathbf{u}_{FCS}(t)$ and $\mathbf{u}_{HHC}(t)$ are defined as in Eqs. (2.162) and (2.163), later in this section, while the outputs are the body frame accelerations measured by the control system.

The matrices of the linearized model are generated as Fourier series as in Eq. 2.160. For example, the state matrix $A_H(\psi)$ is given as:

$$A_H(\psi) = A_{H0} + \sum_{\ell=1}^{L} (A_{H\ell c} \cos \ell N\psi + A_{H\ell s} \sin \ell N\psi) \tag{2.160}$$

with $\psi = \Omega t$, and where the matrices A_{H0}, $A_{H\ell c}$, and $A_{H\ell s}$ are constant.

The control matrices $B_{FCS}(\psi)$ and $B_{HHC}(\psi)$ are obtained in the same Fourier series form as $A_H(\psi)$, Eq. (2.160), by assuming that the pitch control angle of the i-th blade is given by

$$\begin{aligned} \theta_i(\psi) = \theta_0 &+ \theta_{1c} \cos\psi + \theta_{1s} \sin\psi \\ &+ \theta_{3c} \cos 3\psi + \theta_{3s} \sin 3\psi \\ &+ \theta_{4c} \cos 4\psi + \theta_{4s} \sin 4\psi \\ &+ \theta_{5c} \cos 5\psi + \theta_{5s} \sin 5\psi \end{aligned} \tag{2.161}$$

where $\psi_i = \psi + 2\pi i/N$ for $i = 0, \ldots, N-1$ is the azimuth angle, and the number of blades $N = 4$. Therefore, the input harmonics are defined in the rotating system, but they are identical for each blade. This arrangement will be defined as HHC, although it could also fall under some definitions of IBC. Note that the HHC inputs are assumed to be applied through active pitch links, and using acceleration sensors in the fixed system (hub or fuselage), however, the theoretical development that follows is essentially independent of the specific configuration for actuators and sensors.

The vector $\mathbf{u}_{FCS}(t)$ contains the controls that would be applied by the pilot or the flight control system. For the derivations of the paper $\mathbf{u}_{FCS}(t)$ is defined as

$$\mathbf{u}_{FCS}(t) = [\theta_0(t) \;\; \theta_{1c}(t) \;\; \theta_{1s}(t)]^T \tag{2.162}$$

The input vector $\mathbf{u}_{FCS}(t)$ actually used in the simulations also includes the tail rotor collective pitch $\theta_t(t)$. The partition $\mathbf{u}_{HHC}(t)$ contains the harmonics of the HHC system, that is

$$\mathbf{u}_{HHC}(t) = [\theta_{3c}(t) \;\; \theta_{3s}(t) \;\; \theta_{4c}(t) \;\; \theta_{4s}(t) \;\; \theta_{5c}(t) \;\; \theta_{5s}(t)]^T \tag{2.163}$$

The development that follows only addresses the HHC control loops. In fact, the primary meaning of the words "closed loop" is that the HHC vibration control loops are closed. Although small amounts of pitch and roll attitude and rate feedback were added to stabilize the flight dynamic modes, such a simple flight control system architecture is not realistic enough to allow reliable studies of HHC-flight control system interaction. The HHC analysis holds, under linearity assumptions, regardless of whether the FCS loops are open or closed. This is not necessarily true for the effects on the full nonlinear dynamics of the helicopter.

The output vector $\mathbf{y}_H(t)$ can be formed with any of the three linear and three angular components of the accelerations, measured at one or more points of the airframe (the dimensions of $\mathbf{u}(t)$ and $\mathbf{y}(t)$ need not be the same). The output matrices $C_H(t)$, $D_{FCS}(t)$ and $D_{HHC}(t)$ in Eq. (2.158) therefore depend on the specific form of the output vector $\mathbf{y}_H(t)$ (i.e., on the specific arrangement of sensors), and will be provided later in the paper.

2.9 Discrete-time stability analysis

The closed-loop analysis of the helicopter with the HHC system is carried out as follows:

1. Discrete-time models are obtained for each of the components of the control loop, including the block representing the dynamics of the helicopter;

2. A complete model is obtained for the series connection of hold circuit, helicopter, and harmonic analyzer: this model will prove to be time-periodic;

3. A time-invariant reformulation of the complete model is obtained using the theory of time-lifting of periodic systems, using the slower sampling rate (i.e., that of the controller);

4. The overall closed-loop stability analysis is carried out in discrete-time.

2.9.1 Discrete Models of the Loop Components

In this section, discrete-time models of all the elements in the closed loop scheme of Fig. 2.2 are derived. They include: (i) the helicopter model, (ii) the harmonic analyzer, (iii) the controller, and (iv) the zero-order-hold.

According to the architecture defined in the previous section, the HHC inputs are updated at 1/rev, while the outputs are sampled at a higher frequency to allow the reconstruction of the N/rev component of the accelerations of interest.

Discrete helicopter model

The discrete-time helicopter dynamic model is obtained from the linearized continuous-time model of Eq. (2.158). The sampling frequency is the faster of the two in the system, i.e., that required to allow the reconstruction of the N/rev component of the accelerations of interest.

Writing the state and output equations, Eq. (2.158), for the helicopter model over a sampling interval P, under the usual assumption of constant input in the interval, one can

write the analytical solution for the continuous state vector $\mathbf{x}_H(t)$ at time $t = \eta P + P$ as

$$\begin{aligned}\mathbf{x}_H(\eta P + P) &= \Phi_H(\eta P + P, \eta P)\mathbf{x}_H(\eta P) \\ &\quad + \int_{\eta P}^{\eta P + P} \Phi_H(\eta P + P, \tau) B_H(\tau)\mathbf{u}_{HHC}(\tau) d\tau \qquad (2.164)\\ \mathbf{y}_H(\eta P) &= C_H(\eta P)\mathbf{x}_H(\eta P) + D_H(\eta P)\mathbf{u}_{HHC}(\eta P) \qquad (2.165)\end{aligned}$$

where Φ_H is the state transition matrix associated with the state matrix A_H. Defining the discrete-time state vector $\tilde{\mathbf{x}}_H$ as $\tilde{\mathbf{x}}_H(\eta) = \mathbf{x}_H(\eta P)$ (similarly for the control vector $\mathbf{u}_{HHC}$ and the output vector $\mathbf{y}_H$) results in the following discrete-time, state-space linearized model of the helicopter

$$\begin{aligned}\tilde{\mathbf{x}}_H(\eta + 1) &= \tilde{A}_H(\eta)\tilde{\mathbf{x}}_H(\eta) + \tilde{B}_H(\eta)\tilde{\mathbf{u}}_{HHC}(\eta) \\ \tilde{\mathbf{y}}_H(\eta) &= \tilde{C}_H(\eta)\tilde{\mathbf{x}}_H(\eta) + \tilde{D}_H(\eta)\tilde{\mathbf{u}}_{HHC}(\eta)\end{aligned} \qquad (2.166)$$

where the system matrices are defined as

$$\tilde{A}_H(\eta) = \Phi_H(\eta P + P, \eta P) \qquad (2.167)$$

$$\tilde{B}_H(\eta) = \int_0^P \Phi_H(\eta P + P, \tau' + \eta P) B_H(\tau' + \eta P) d\tau' \qquad (2.168)$$

$$\tilde{C}_H(\eta) = C_H(\eta P) \qquad (2.169)$$

$$\tilde{D}_H(\eta) = D_H(\eta P) \qquad (2.170)$$

The system matrices are periodic, with a common period equal to n_s samples. The vector $\tilde{\mathbf{y}}_H(\eta)$ is the vector y in Fig. 2.2.

Harmonic Analysis

To implement the HHC control algorithm, the N/rev components $\tilde{\mathbf{y}}_{HHC}$ of the output accelerations must be extracted from their time domain measurements $\tilde{\mathbf{y}}_H$. In each period, the information about $\mathbf{y}_H$ is available starting from $\eta = n_s/2 - 1 + Kn_s$, $K = 1, 2, \ldots$ but is

provided as output only at $\eta = (K+1)n_s$. The operation of the harmonic analyzer can be described mathematically by a linear time-periodic (LTP) model with discrete time η and period n_s:

$$\begin{aligned} \tilde{\mathbf{x}}_F(\eta+1) &= \tilde{A}_F(\eta)\tilde{\mathbf{x}}_F(\eta) + \tilde{B}_F(\eta)\tilde{\mathbf{y}}_H(\eta) \\ \tilde{\mathbf{y}}_{HHC}(\eta) &= \tilde{C}_F(\eta)\tilde{\mathbf{x}}_F(\eta) \end{aligned} \tag{2.171}$$

The matrices $\tilde{A}_F(\eta)$, $\tilde{B}_F(\eta)$ and $\tilde{C}_F(\eta)$ are defined in a way that reflects the various phases of the harmonic analysis that occur over one rotor revolution. The vector $\tilde{\mathbf{y}}_{HHC}(\eta)$ is the vector $Y\tilde{}$ in Fig. 2.2. For the four-bladed rotor of this study there are three distinct phases, defined as follows (see also Figure **??**):

1. *During the first quarter of the period*, $\eta = 1, 2, \ldots, n_s/4$, the output signal $\mathbf{y}_H$ is allowed to reach steady state following the update of the control input $\mathbf{u}_{HHC}$ at the end of the previous rotor revolution. During this time, the output of the harmonic analyzer is set to zero and the vectors $\mathbf{y}_H$ measured are not accumulated in the integrals, Eqs. (2.95) and (2.96). Therefore the state space matrices of the harmonic analyzer are given by

$$\tilde{A}_F(\eta) = I \quad \tilde{B}_F(\eta) = 0 \quad \tilde{C}_F(\eta) = 0 \tag{2.172}$$

2. *During the second quarter of the period*, $\eta = n_s/4+1, n_s/4+2, \ldots, n_s/2$, the outputs $\mathbf{y}_H$ are actually sampled and the integrals, Eqs. (2.95) and (2.96), computed, but the output of the analyzer is kept to zero while these computations are done. Note that the state of the harmonic analyzer must be reset to zero at the beginning of the

second quarter of the period, so the state space matrices will be defined as:

$$\tilde{A}_F(\eta) = \begin{cases} 0 & \eta = \dfrac{n_s}{4} \\ I & \text{elsewhere} \end{cases} \tag{2.173}$$

$$\tilde{B}_F(\eta) = \text{blkdiag}\left\{\begin{bmatrix} \cos\left(\dfrac{2N\pi}{n_s}\eta\right) \\ \\ \sin\left(\dfrac{2N\pi}{n_s}\eta\right) \end{bmatrix}\right\} \tag{2.174}$$

$$\tilde{C}_F(\eta) = 0 \tag{2.175}$$

3. *During the remaining half period*, $\eta = n_s/2 + 1, n_s/2 + 2, \ldots, n_s$ the new value of the control input $\tilde{\mathbf{u}}_{HHC}$ is computed from the recently updated value of $\tilde{\mathbf{y}}_{HHC}$, and applied to the rotor; therefore the operation of the analyzer is stopped and the computed value for the N/rev harmonic of $\mathbf{y}_H$ is made available to the controller:

$$\tilde{A}_F(\eta) = I \tag{2.176}$$

$$\tilde{B}_F(\eta) = 0 \tag{2.177}$$

$$\tilde{C}_F(\eta) = \begin{cases} \dfrac{8}{n_s} I & \eta = n_s \\ \\ 0 & \text{elsewhere} \end{cases} \tag{2.178}$$

The entire sequence of operations described above can be summarized in the following expressions for the state space matrices of the harmonic analyzer, which hold for a

generic value of the 1/rev discrete time index k (i.e., for the generic, k-th rotor revolution):

$$\tilde{A}_F(\eta) = \begin{cases} 0 & \eta = kn_s + \dfrac{n_s}{4} \\ I & \text{elsewhere} \end{cases} \tag{2.179}$$

$$\beta_F(\eta) = \begin{cases} 1 & kn_s + \dfrac{n_s}{4} \le \eta < kn_s + \dfrac{n_s}{2} \\ 0 & \text{elsewhere} \end{cases} \tag{2.180}$$

$$\tilde{B}_F(\eta) = \beta_F(\eta)\text{blkdiag}\left\{\begin{bmatrix} \cos\left(\dfrac{2N\pi}{n_s}\eta\right) \\ \sin\left(\dfrac{2N\pi}{n_s}\eta\right) \end{bmatrix}\right\} \tag{2.181}$$

$$\tilde{C}_F(\eta) = \begin{cases} \dfrac{8}{n_s}I & \eta = kn_s + n_s \\ 0 & \text{elsewhere} \end{cases} \tag{2.182}$$

Therefore, the output of the above model is nonzero only for $\eta = 0, n_s, 2n_s, \ldots$.

Controller

The control law given by Eq. (2.102) can be written in state-space form as a linear time-invariant system

$$\tilde{\mathbf{x}}_C(k+1) = \tilde{A}_C\tilde{\mathbf{x}}_C(k) + \tilde{B}_C\tilde{\mathbf{y}}_{HHC}(k) \tag{2.183}$$

$$\tilde{\mathbf{u}}_{HHC}(k) = \tilde{C}_C\tilde{\mathbf{x}}_C(k) \tag{2.184}$$

where

$$\tilde{A}_C = I \tag{2.185}$$

$$\tilde{B}_C = -\left(\mathbf{T}^T Q\mathbf{T} + R\right)^{-1}\mathbf{T}^T Q \tag{2.186}$$

$$\tilde{C}_C = I \tag{2.187}$$

The vectors $\tilde{\mathbf{u}}_{HHC}(k)$ and $\tilde{\mathbf{y}}_{HHC}(k)$ are indicated in Fig. 2.2.

Zero-Order-Hold circuit

The hold circuit is the interface between the controller and the helicopter. Since the controller operates at the discrete-time k (i.e., once per revolution) while the helicopter model has been obtained at the discrete-time η (i.e., once per sample needed to extract the N/rev harmonics), the controller provides a new value of the control variables only at $\eta = kn_s$, $k = 1, 2, \ldots$, and this output must be kept constant for the intervening samples $kn_s \leq \eta < (k+1)n_s$. Therefore, the model of the hold circuit is linear, discrete-time periodic, with discrete time η and period n_s, and is given by

$$\tilde{\mathbf{x}}_Z(\eta+1) = \tilde{A}_Z(\eta)\tilde{\mathbf{x}}_Z(\eta) + \tilde{B}_Z(\eta)\tilde{\mathbf{u}}_{HHC}(\eta) \tag{2.188}$$

$$\mathbf{u}_{HHC}(\eta) = \tilde{C}_Z(\eta)\tilde{\mathbf{x}}_Z(\eta) + \tilde{D}_Z(\eta)\tilde{\mathbf{u}}_{HHC}(\eta) \tag{2.189}$$

where

$$\tilde{A}_Z(\eta) = \delta(\eta) \tag{2.190}$$

$$\tilde{B}_Z(\eta) = I - \delta(\eta) \tag{2.191}$$

$$\tilde{C}_Z(\eta) = \delta(\eta) \tag{2.192}$$

$$\tilde{D}_Z(\eta) = I - \delta(\eta) \tag{2.193}$$

and

$$\delta(\eta) = \begin{cases} 0 & \eta = kn_s, \quad k = 1, 2, \ldots \\ I & \text{elsewhere} \end{cases} \tag{2.194}$$

The vector $\tilde{\mathbf{u}}_{HHC}(\eta)$ is the vector U in Fig. 2.2.

2.9.2 Series connection of closed loop components

The overall discrete HHC model, which relates the harmonics of the HHC input $\tilde{\mathbf{u}}_{HHC}$ to the harmonics of the acceleration output $\tilde{\mathbf{y}}_{HHC}$ can be obtained by connecting in series the harmonic analyzer, Eq. (2.171), the discrete model for the response of the helicopter to HHC inputs, Eq. (2.164), and that of the zero order hold, Eq. (2.188). The model, with discrete-time η, is given by

$$\tilde{\mathbf{x}}_Z(\eta+1) = \tilde{A}_Z\tilde{\mathbf{x}}_Z(\eta) + \tilde{B}_Z\tilde{\mathbf{u}}_{HHC}(\eta) \tag{2.195}$$

$$\tilde{\mathbf{x}}_H(\eta+1) = \tilde{A}_H\tilde{\mathbf{x}}_H(\eta) + \tilde{B}_H\tilde{C}_Z\tilde{\mathbf{x}}_Z(\eta) + \tilde{B}_H\tilde{D}_Z\tilde{\mathbf{u}}_{HHC}(\eta) \tag{2.196}$$

$$\begin{aligned}\tilde{\mathbf{x}}_F(\eta+1) = {} & \tilde{A}_F\tilde{\mathbf{x}}_F(\eta) + \tilde{B}_F\tilde{C}_H\tilde{\mathbf{x}}_H(\eta) + \\ & + \tilde{B}_F\tilde{D}_H\tilde{C}_Z\tilde{\mathbf{x}}_Z(\eta) + \tilde{B}_F\tilde{D}_H\tilde{D}_Z\tilde{\mathbf{u}}_{HHC}(\eta)\end{aligned} \tag{2.197}$$

$$\tilde{\mathbf{y}}_{HHC}(\eta) = \tilde{C}_F\tilde{\mathbf{x}}_F(\eta) \tag{2.198}$$

(the argument η in the matrices has been omitted for simplicity). This model cannot be connected directly to the HHC controller because its sampling rate is still different from that of the discrete HHC control law (n_s/rev vs. 1/rev). A combined model at the same sampling rate as the HHC controller can be obtained using the theory of time-invariant reformulations of linear time-periodic systems and, more precisely, through a time-lifted reformulation.

2.10 Time-lifted Formulation of the Closed Loop System

A closed-loop stability analysis requires a single sampling period for the entire system. Therefore, the model will be reformulated using the shorter sampling period $P = T/n_S$

as the common period. The implicit assumption that the longer sampling period T, corresponding to one rotor revolution, is an integer multiple of the acceleration sampling period P is clearly quite reasonable. This reformulation is carried out using time lifting, and results in a discrete model with overall sampling period T and time index k. Time lifting is described in detail in Ref. [140] and is summarized in Ref. [141], which also contains numerical examples of the application to a flapping rigid rotor blade. A useful byproduct of the use of a lifted reformulation is that the resulting model has constant coefficients, which simplifies the closed loop stability analysis.

2.10.1 Time lifting of periodic systems

Time lifting is based on the idea that the knowledge of the state vector at time k and of the inputs between time k and $k+1$ is sufficient to determine the value of the state at time $k+1$ and the value of the outputs between k and $k+1$. The key steps of time lifting will be briefly outlined here.

Consider the linear, discrete-time periodic system with a period equal to n_s samples, and with m inputs and p outputs

$$\begin{aligned} \tilde{\mathbf{x}}(\nu+1) &= A(\nu)\tilde{\mathbf{x}}(\nu) + B(\nu)\tilde{\mathbf{u}}(\nu) \\ \tilde{\mathbf{y}}(\nu) &= C(\nu)\tilde{\mathbf{x}}(\nu) + D(\nu)\tilde{\mathbf{u}}(\nu) \end{aligned} \tag{2.199}$$

where $\nu = 0, 1, 2, \ldots, n_s - 1$. Then, the state vector at time $\nu > \tau$ is given by the discrete-time Lagrange formula [142]

$$\tilde{\mathbf{x}}(\nu) = \Psi(\nu,\tau)\tilde{\mathbf{x}}(\tau) + \sum_{j=\tau+1}^{\nu} \Psi(\nu, j)B(j-1)\tilde{\mathbf{u}}(j-1) \tag{2.200}$$

where $\Psi(\nu,\tau) = A(\nu-1)A(\nu-2)\cdots A(\tau)$ is the transition matrix from time τ (also an integer between 0 and n_s-1) to time ν for the state equation, Eq. (2.199). Equation (2.200)

can be used to build an equivalent (i.e., with the same output given the same input) time-invariant system by sampling the state vector at a frequency of n_s, and packing the input and output vectors for each sample into larger input and output vectors. This results in the "lifted" reformulation [140, 141]

$$\begin{aligned} \tilde{\mathbf{x}}(k+1) &= F\tilde{\mathbf{x}}(k) + G\mathbf{u}_{lift}(k) \\ \mathbf{y}_{lift}(k) &= H\tilde{\mathbf{x}}(k) + E\mathbf{u}_{lift}(k) \end{aligned} \tag{2.201}$$

where the extended input vector $u_{lift}(k)$ has size mn_s and is defined as

$$\mathbf{u}_{lift}(k) = \left[\tilde{\mathbf{u}}(kn_s)^T \quad \cdots \quad \tilde{\mathbf{u}}(kn_s + n_s - 1)^T\right]^T$$

and the extended output vector $\mathbf{y}_{lift}(k)$ has size pn_s and is defined as

$$\mathbf{y}_{lift}(k) = \left[\begin{array}{ccc} \tilde{\mathbf{y}}(kn_s)^T & \cdots & \tilde{\mathbf{y}}(kn_s + n_s - 1)^T \end{array}\right]^T$$

The time invariant system matrices F, G, H, and E have dimensions, respectively, of n by n, n by mn_s, pn_s by n, and pn_s by mn_s and are given by [140, 141]

$$F = A(n_s - 1)A(n_s - 2)\cdots A(0) \tag{2.202}$$

$$G = \left[\Psi(n_s, 1)B(0) \quad \Psi(n_s, 2)B(1) \ \cdots \ \Psi(n_s, n_s)B(n_s - 1)\right] \tag{2.203}$$

$$H = \left[C(0)^T \quad \Psi(1,0)^T C(1)^T \cdots \ \Psi(n_s - 1, 0)^T C(n_s - 1)^T\right]^T \tag{2.204}$$

$$E = \{(E_{ij})\}, \quad i, j = 1, 2, \ldots n_s \tag{2.205}$$

$$\text{with } E_{ij} = \begin{cases} 0 & i < j \\ D(i-1) & i = j \\ C(i-1)\Psi(i-1, j)B(j-1) & i > j \end{cases} \tag{2.206}$$

It should be noted that the matrix F is the Floquet Transition matrix of the discrete-time periodic system, Eq. (2.199), therefore the constant-coefficient lifted system of Eq. (2.201) has exactly the same stability characteristics as the time-periodic system. This Floquet

Transition Matrix is also the same as that of the original continuous system, and therefore continuous and discrete systems also have the same stability characteristics [140, 141].

2.10.2 Lifted form of the HHC loop

Time lifting can be directly applied to the coupled helicopter/HHC system, Eqs. (2.195)-(2.198). The corresponding lifted form is given by:

$$\tilde{\mathbf{x}}(k+1) = F\tilde{\mathbf{x}}(k) + G\mathbf{u}_{lift}(k) \tag{2.207}$$

$$\mathbf{y}_{lift}(k) = H\tilde{\mathbf{x}}(k) + E\mathbf{u}_{lift}(k) \tag{2.208}$$

The input vector $\mathbf{u}_{lift}(k)$ is given by

$$\mathbf{u}_{lift}(k) = \begin{bmatrix} I \\ I \\ \vdots \\ I \end{bmatrix} \tilde{\mathbf{u}}_{HHC}(k) \tag{2.209}$$

where the mn_s by m matrix that relates $\mathbf{u}_{lift}(k)$ and $\tilde{\mathbf{u}}_{HHC}(k)$ is obtained by assembling n_s identity matrices because the HHC input vector $\tilde{\mathbf{u}}_{HHC}(k)$ is held constant over all the n_s samples that make up one rotor revolution.

Similarly, once the lifted output vector $\mathbf{y}_{lift}$ has been obtained as the output of the lifted system, Eqs. (2.207)-(2.208), the actual discrete output vector $\tilde{\mathbf{y}}_{HHC}(k)$ can be recovered by observing that it is the output of the Fourier coefficients extractor, which is only evaluated once per revolution, i.e., at times $\eta = 0, n_s, 2n_s, \ldots$. Therefore

$$\tilde{\mathbf{y}}_{HHC}(k) = [I \quad 0]\, \mathbf{y}_{lift}(k) \tag{2.210}$$

where $\mathbf{y}_{HHC}(k)$ has size p and $\mathbf{y}_{lift}(k)$ has size pn_s. On the basis of Eqs. (2.209) and (2.210), and recalling the state space form for the discrete HHC controller, Eqs. (2.183)-(2.184)

the overall closed loop system can be constructed as follows:

$$\tilde{\mathbf{x}}(k+1) = F\tilde{\mathbf{x}}(k) + G\begin{bmatrix} I \\ I \\ \vdots \\ I \end{bmatrix}\tilde{C}_C\mathbf{x}_C(k) \tag{2.211}$$

$$\tilde{\mathbf{x}}_C(k+1) = \tilde{B}_C\begin{bmatrix} I & 0 \end{bmatrix}H\tilde{\mathbf{x}}(k) + \left(\tilde{A}_C + \tilde{B}_C\begin{bmatrix} I & 0 \end{bmatrix}E\begin{bmatrix} I \\ I \\ \vdots \\ I \end{bmatrix}\tilde{C}_C\right)\tilde{\mathbf{x}}_C(k) \tag{2.212}$$

This closed loop helicopter/HHC system is now linear time-invariant, with discrete-time k and state variables $\tilde{x}_Z$, $\tilde{x}_H$, $\tilde{x}_F$, and $\tilde{x}_C$. Therefore, the closed loop stability analysis can be carried out by checking the eigenvalues of the closed loop system.

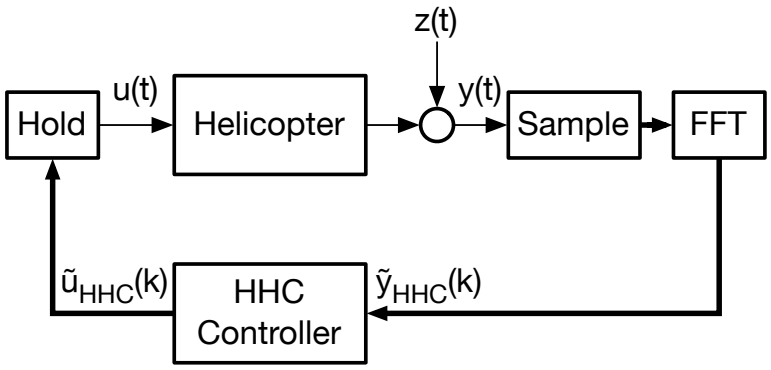

Figure 2.2: Closed loop HHC algorithm block diagram implementation

Chapter 3

Characterization of LQR Controller Gains

3.1 Magnitude of T-matrix based feedback gain

The dicrete-time control law in Eq. (2.126) has been defined on the basis of an optimal LQR control inspired feedback gain matrix $\mathbf{K} = (\mathbf{T}^T Q \mathbf{T} + R)^{-1} \mathbf{T}^T Q$. Equivalent approximate time-continuous controllers, defined by the state matrices in Eqs. (2.132) and (2.133), have been designed to enforce the feedback control law

$$\boldsymbol{u} = -\mathbf{K} \cdot \boldsymbol{y}_N \tag{3.1}$$

where vector $\boldsymbol{y}_N$ contains the N/rev Fourier coefficients of the measured outputs, and vector $\boldsymbol{u}$ contains the higher harmonic control inputs defined also by their Fourier coefficients.

The properties of the LQR implementation of the feedback control law can be characterized qualitatively in terms of the control effort parameter r. Maximum control effort is achieved when $r = 0$. This comes as a consequence of the lack of restrictions placed on the control inputs in the cost function minimization process. In particular if $r = 0$, the feedback control gain matrix resolves again to the ideal case $\mathbf{K} = \mathbf{T}^{-1}$. This situation was briefly discussed in Section 2.6.1 for the SISO HHC algorithm, along with conditions for the deadbeat control of higher harmonic vibrations. On the other end of the spectrum, as

$r \to \infty$, the weighing constants enforce $\|\mathbf{K}\| \to 0$, or equivalently $\mathbf{K} \to \mathbf{0}$, in an attempt to achieve the vibration reduction with minimum control input.

Although this analysis portrays a qualitatively functional description of the feedback control law operational principles, it is however instructive to carry this analysis further, in an attempt to minimally quantify the magnitude of the feedback gains as a function of the control effort parameter r. In this way it can be possible to establish a more precise portrait of how the control effort parameter may potentially affect the stability of the closed loop system. To this effect consider the Euclidean norm of the control vector $\boldsymbol{u}$ in Eq. (3.1), and recall that

$$\check{\sigma}(\mathbf{K}) \cdot \|\boldsymbol{y}_N\| \leq \|\boldsymbol{u}\| \leq \hat{\sigma}(\mathbf{K}) \cdot \|\boldsymbol{y}_N\|, \tag{3.2}$$

where $\check{\sigma}(\mathbf{K})$ and $\hat{\sigma}(\mathbf{K})$ denote the minimum and maximum singular values of the feedback gain matrix $\mathbf{K}$, respectively. The lower bound is non-zero, provided $\mathbf{K}$ is full column rank. The double inequality implies that the magnitude of the feedback gain $\|\boldsymbol{u}\|/\|\boldsymbol{y}_N\|$ is bounded from below by the least or minimum singular value of matrix $\mathbf{K}$, and from above by the maximum singular value.

3.1.1 SISO control characterization

The SISO case yields a simple but illustrative analytic result worth exploring. A time-continuous representation of the SISO version of the HHC algorithm was introduced in Section 2.6.1. The block diagram for this controller is shown in Fig. 2.1. Note that this controller has fundamentally been designed to implement the SISO control law

$$\boldsymbol{u}_N = -K_{N,N} \cdot \boldsymbol{y}_N \tag{3.3}$$

where $K_{N,N} = (T_{N,N}^T Q T_{N,N} + R)^{-1} T_{N,N}^T Q$.

From the discussion presented in Sec. 2.7.2 it can be shown that the SISO T-matrix can be expected to posses the special form

$$T_{N,N} = \begin{bmatrix} \alpha & \beta \\ -\beta & \alpha \end{bmatrix}. \tag{3.4}$$

A similar representation of the T-matrix on the basis of a LTI approximation of the helicopter transfer function was presented in Ref. [58], and also in Ref. [103]. Under this assumption it can be shown that

$$T_{N,N}^T = (\det T_{N,N})\, T_{N,N}^{-1} \tag{3.5}$$

Furthermore, given the special structure of the SISO transfer matrix $T_{N,N}$ in Eq. (3.4), and invoking the assumption that Q and R are proportional to the identity matrix, it is possible to show that feedback gain matrix $K_{N,N}$ is proportional to $T_{N,N}^{-1}$

$$K_{N,N} = \frac{\det T_{N,N}\; q}{\det T_{N,N}\; q + r} T_{N,N}^{-1} \tag{3.6}$$

and with $q = 1.0$ the expression for $K_{N,N}$ becomes

$$K_{N,N} = \frac{\det T_{N,N}}{\det T_{N,N} + r} T_{N,N}^{-1}. \tag{3.7}$$

Again, if $r = 0$ then feedback gain matrix $K_{N,N}$ reduces to the expected result $K_{N,N} = T_{N,N}^{-1}$. If $r > 0$, then $K_{N,N}$ becomes proportional to $T_{N,N}^{-1}$ to the scalar factor of $\det T_{N,N} / (\det T_{N,N} + r)$. Therefore $\|K_{N,N}\| \to 0$ as $r \to \infty$ again. Furthermore, from Eq. (3.7) it can be shown that both of the singular values of matrix $K_{N,N}$ are identical and equal to

$$\hat{\sigma}(K_{N,N}) = \check{\sigma}(K_{N,N}) = \frac{\sqrt{\det T_{N,N}}}{\det T_{N,N} + r}, \tag{3.8}$$

which directly implies that the feedback gain relating the amplitudes of the higher harmonic N/rev input and the measured N/rev vibration output is determined uniquely such that

$$\|\boldsymbol{u}_N\| = \frac{\sqrt{\det T_{N,N}}}{\det T_{N,N} + r} \cdot \|\boldsymbol{y}_N\| \tag{3.9}$$

where the magnitude of the feedback gain is given by Eq. (3.8). Let $\gamma(r)$ be defined as the magnitude of the feedback gain as a function or r. Then

$$\gamma(r) = \frac{\sqrt{\det T_{N,N}}}{\det T_{N,N} + r} \tag{3.10}$$

Sensitivity of the feedback gain magnitude to the control effort parameter r, over any given interval of r, is fundamentally determined by the value of the determinant of the matrix $T_{N,N}$. Consider the nondimensional feedback gain ratio

$$\hat{\gamma}(r) = \frac{\gamma(r)}{\gamma(0)} = \frac{1}{1 + \dfrac{r}{\det T_{N,N}}}. \tag{3.11}$$

Clearly, the larger that $\det T_{N,N}$ becomes, then the less sensitive to variations of the control effort parameter r is the feedback control gain likely to be, since variations of r will necessarily result in smaller variations of the ratio $r/\det T_{N,N}$ for larger values of $\det T_{N,N}$. Moreover, from the first derivative of the nondimensional gain it is evident that, for a given value of the determinant $\det T_{N,N}$, the feedback gain magnitude is more sensitive to variations of r over the lower range of the function domain. In other words, the control is more sensitive to variations of r when r is close to zero. As it translates to the helicopter dynamics, it is reasonable to expect stronger variations of the stability coefficients, if any, when r is nearest to zero.

Figure 3.1 shows the nondimensional feedback gain magnitude ratio, plotted as a function of the control effort ratio $r/\det T_{N,N}$. The same conditions established in Fig. 3.1

are alternatively portrayed in Fig. 3.2 by plotting the nondimensional feedback gain as a function of the control effort parameter r, for multiple values of the transfer matrix $T_{N,N}$ determinant. This family of curves observed in Fig. 3.2 clearly shows how the magnitude drop-off point shifts to higher values of r, for increasingly larger values of the $T_{N,N}$ matrix determinant. This drop-off point marks the maximum limit of r up to which the feedback gain may be considered to correspond to a high control effort. Beyond this point, the feedback gain magnitude quickly diminishes, defining the low control effort operating condition. If the value of $\det T_{N,N}$ is too low, small variations of r measured from zero may result in potentially significant feedback gain reductions which may in turn translate to the helicopter closed loop dynamics.

Consider a constant value of r. Clearly, if the determinant $\det T_{N,N}$ is made increasingly smaller, then a larger drop-off in the feedback gain magnitude can be expected, with respect to whatever the initial value is. Take $r = 10$, for example. The magnitude of the feedback gain for $r = 10$ drops to about 95% of its initial value for $\det T_{N,N} \approx 200$. It drops to 80% for $\det T_{N,N} = 40$, and to 75% for $\det T_{N,N} = 30$. Even greater drop-offs result from lower values of the determinant $\det T_{N,N}$. For $r = 1.0$, the same drop-offs of 95%, 80% and 75% are expected for values of $\det T_{N,N}$ 10 times lower, i.e., for values of 20, 4 and 3, respectively.

A similar analysis can also be established for the SISO problem when the input and the output are at different frequencies, because matrix $T_{N,M}$ possesses the same symmetry characteristics established in Eq. (3.4) for $T_{N,N}$, such that $T_{N,M}^{T} = (\det T_{N,M})\, T_{N,M}^{-1}$.

In practice, the computation of the T-matrix involves a level of numerical approximation, in particular the truncation of higher harmonics in the series expansion of the

helicopter state matrices (Sec. 2.7.3). Computed in this fashion, matrices $T_{N,N}$ and $T_{N,M}$ may differ substantially from the form in Eq. (3.4), resulting in numerical discrepancies in the singular values. Numerical differences between the maximum and minimum singular values can be large enough, however, that for all practical purposes, it may not be possible to restrict the magnitude of the feedback gain to a narrow band, as expected theoretically. Note that this uncertainty in the modeling of helicopter dynamics may in fact a fundamental be cause of instability or reduced robustness of the controller.

3.1.2 MIMO control characterization

The analytical discussion of the MIMO problem is not as simple as that for the SISO example discussed above, since in general the simple property established in Eq. (3.5) for the SISO transfer matrices cannot be extended to the MIMO transfer matrix $\mathbf{T}$. Equation (3.5) is still fundamental, however, in establishing a useful expression for the transpose of matrix $\mathbf{T}$. Let $\mathbf{T}$ be reorganized into the block-matrix form

$$\mathbf{T} = \begin{bmatrix} T_{3,1} & T_{4,1} & T_{5,1} \\ T_{3,2} & T_{4,2} & T_{5,2} \\ T_{3,3} & T_{4,3} & T_{5,3} \end{bmatrix}, \tag{3.12}$$

where $T_{i,j}$ is shorthand notation for the SISO transfer matrix relating the i-th harmonic input to the N/rev harmonic of the ouput channel j. Showing that $\mathbf{T}^T$ is given by

$$\mathbf{T}^T = \begin{bmatrix} (\det T_{3,1})\, T_{3,1}^{-1} & (\det T_{3,2})\, T_{3,2}^{-1} & (\det T_{3,3})\, T_{3,3}^{-1} \\ (\det T_{4,1})\, T_{4,1}^{-1} & (\det T_{4,2})\, T_{4,2}^{-1} & (\det T_{4,3})\, T_{4,3}^{-1} \\ (\det T_{5,1})\, T_{5,1}^{-1} & (\det T_{5,2})\, T_{5,2}^{-1} & (\det T_{5,3})\, T_{5,3}^{-1} \end{bmatrix} \tag{3.13}$$

is completely trivial, given that Eq. (3.5) holds true for each of the SISO matrix blocks in matrix $\mathbf{T}$. Therefore, matrix $\mathbf{T}^T$ is, in a sense, representative of the helicopter dynamics inverse T-matrix relation. As a matter of fact, it establishes an uncoupled SISO relationship

between each of the input and output variables. Let $\mathbf{K}$ take the form

$$\mathbf{K} = \begin{bmatrix} K_{3,1} & K_{3,2} & K_{3,3} \\ K_{4,1} & K_{4,2} & K_{4,3} \\ K_{5,1} & K_{5,2} & K_{5,3} \end{bmatrix} \tag{3.14}$$

where the submatrices $K_{i,j}$ correspond to the feedback gain for the i-th frequency harmonic and the j-th output channel.

Although it is not possible to extend the simple analytical result obtained in Sec. 3.1.1 for the SISO controller to the MIMO problem, it can be shown on the basis of Eq. (3.13) that if Q and R are proportional to the identity matrix, the individual transfer matrices $K_{i,j}$ that compose $\mathbf{K}$ can be expressed as nonlinear combinations of the $T_{i,j}$ matrices and their inverses $T_{i,j}^{-1}$. As such, matrices $K_{i,j}$ will theoretically have the general form

$$K_{i,j} = \begin{bmatrix} \gamma_{i,j} & \delta_{i,j} \\ -\delta_{i,j} & \gamma_{i,j} \end{bmatrix}. \tag{3.15}$$

The analytical expression for $\mathbf{K}$ is fairly convoluted, and is therefore not worthwhile showing here. Instead the magnitude bounds of the feedback gains are determined numerically from the singular value decomposition of the MIMO feedback gain matrix $\mathbf{K}$. Equation (3.15) is significant because it establishes a condition for the identity of the singular values for the SISO transfer matrices similar to Eq. (3.8).

3.2 Numerical evaluation of controller gains

The vector of N/rev Fourier coefficients of the measured vibration outputs in the simulation model is defined as

$$\boldsymbol{y}_N^T = \begin{bmatrix} (\dot{w})_{Nc} & (\dot{p})_{Nc} & (\dot{q})_{Nc} & (\dot{w})_{Ns} & (\dot{p})_{Ns} & (\dot{q})_{Ns} \end{bmatrix} \tag{3.16}$$

where $(\cdot)_{Nc}$ and $(\cdot)_{Ns}$ denote, respectively, the cosine and sine components of the N/rev harmonics for output accelerations $\dot{w}$, $\dot{p}$, and $\dot{q}$; and the vector of control inputs is

$$\boldsymbol{u}^T = \begin{bmatrix} \theta_{3c} & \theta_{3s} & \theta_{4c} & \theta_{4s} & \theta_{5c} & \theta_{5s} \end{bmatrix} \tag{3.17}$$

When analyzing vector norms, units must be consistent. It should be noted that vertical acceleration $\dot{w}$ is expressed in terms of [ft/s^2] while $\dot{p}$ and $\dot{q}$ have units corresponding to angular accelerations, i.e., [rad/s^2]. Therefore, feedback gains need to be scaled appropriately as follows

$$\boldsymbol{u} = -\mathbf{K}U^{-1} \cdot U\boldsymbol{y}_N \tag{3.18}$$

$$= -\hat{\mathbf{K}} \cdot \hat{\boldsymbol{y}}_N \tag{3.19}$$

where U is a dimensioning matrix ensuring the units of $\hat{\boldsymbol{y}}_N$ are consistent. Length is non-dimensionalized with respect to the main rotor radius R, thus heave acceleration components $(\dot{w})_{Nc}$ and $(\dot{w})_{Ns}$ in vector $\boldsymbol{y}_N$ are factored by the ratio $1/R$. Accordingly, vector $\boldsymbol{y}_N$ defined in Eq. (3.16) is redefined as

$$\hat{\boldsymbol{y}}_N^T = \begin{bmatrix} \dfrac{(\dot{w})_{Nc}}{R} & (\dot{p})_{Nc} & (\dot{q})_{Nc} & \dfrac{(\dot{w})_{Ns}}{R} & (\dot{p})_{Ns} & (\dot{q})_{Ns} \end{bmatrix} \tag{3.20}$$

Alternatively, it could also be possible to completely non-dimensionalize the vector by defining $R\Omega^2$ and Ω^2 as dimensionalization parameters, such that vector $\hat{\boldsymbol{y}}_N$ can be defined as

$$\hat{\boldsymbol{y}}_N^T = \begin{bmatrix} \dfrac{(\dot{w})_{Nc}}{R\Omega^2} & \dfrac{(\dot{p})_{Nc}}{\Omega^2} & \dfrac{(\dot{q})_{Nc}}{\Omega^2} & \dfrac{(\dot{w})_{Ns}}{R\Omega^2} & \dfrac{(\dot{p})_{Ns}}{\Omega^2} & \dfrac{(\dot{q})_{Ns}}{\Omega^2} \end{bmatrix} \tag{3.21}$$

Figures 3.3 and 3.4 show the singular values of the MIMO HHC feedback gain matrix for $V = 80$ kn and $V = 140$ kn, respectively. Both cases are characterized by a

monotonically decreasing maximum singular value that converges to 0 as $r \to \infty$. This general behavior is clearly expected from the previous discussion regarding the nature of the LQR feedback control law in Eq. (2.126).

The minimum singular value in both cases results in a negligible lower bound. Consequently, the magnitude of the feedback control gain is loosely restricted within a very wide bounding envelope, specially over the low range of the control effort parameter r.

The singular value decomposition of the feedback matrix for $r = 1.0$, and forward flight speed $V = 80$ kn, is dominated by a large maximum singular value in the order of 21 deg $\cdot$ sec^2, and a nearly negligible minimum singular value. The maximum singular value quickly drops to about 7.0–7.5 deg sec^2 (down from close to 21 deg sec^2) for r in the order of 20–30. This sudden variation in $\hat{\sigma}(\mathbf{K})$ implies there is a potential high sensitivity of the feedback gain with respect to r, over this range.

The high control effort (i.e., low r) gain bounds are noticeably lower for $V = 140$ kn. The maximum singular value at $r = 1.0$ is of the order of 9.2 deg sec^2, while the mimimum singular value is close to 0.4 deg sec^2; roughly a 22–24 to 1 ratio between the upper and lower bounds.

The large difference between the maximum and minimum implies the MIMO feedback gain is not tightly bound, specially for low values of r. The existence of these bounds is for the most part an unavoidable consequence of the mathematical conditions involved in the MIMO matrix relation. However, the amplitude of this uncertainty band may be the result of multiple different factors, chief among them, the numerical uncertainty or error in the computation of $\mathbf{T}$. In as much as the magnitude of the feedback gains has a potentially negative impact on the stability margins of the helicopter, the high upper

bound justifies the higher potential for instability for low values of r over high values of r. Figure 3.5 compares the upper feedback gain bounds as functions of the control effort parameter r, for $V = 80$ kn and $V = 140$ kn, as determined by the maximum singular values of $\hat{\mathbf{K}}$. Both cases show drops to about 50% or less of their initial values for r under 100. For $V = 80$ kn, the maximum singular value drops to 50% at about $r = 10$, and to about 33% at $r = 100$. The sharp decrease in the maximum singular values over such a short control effort range could potentially signal high sensitivity to r of the closed loop control system, in terms of stability. Clearly there is a significant drop-off in the maximum magnitude of the feedback gain, in a manner consistent with the simplified analysis presented in Sec. 3.1.1.

The singular values of the MIMO feedback gain matrix offer insight into the global bounding limits of the feedback gain. It is instructive, nonetheless, to break this down further into individual control frequencies. To this effect the norms of submatrices in $\mathbf{K}$ (or $\hat{\mathbf{K}}$) corresponding to the 3, 4, and 5/rev higher control harmonics are considered individually. Recall the partition of the MIMO feedback gain matrix into multiple SISO feedback gain submatrices defined in Eq. (3.14), and repeated here for convenience,

$$\mathbf{K} = \begin{bmatrix} K_{3,1} & K_{3,2} & K_{3,3} \\ K_{4,1} & K_{4,2} & K_{4,3} \\ K_{5,1} & K_{5,2} & K_{5,3} \end{bmatrix} \tag{3.22}$$

where the submatrices $K_{i,j}$ correspond to the feedback gain for the i-th frequency harmonic and the j-th output channel. Note that as a consequence of numerical error in the computation of the helicopter T-matrix, the submatrices $K_{i,j}$ do not necessarily satisfy

Eq. 3.15. Feedback gain matrices for the individual input harmonics are then defined by

$$\mathbf{K}_3 = \begin{bmatrix} K_{3,1} & K_{3,2} & K_{3,3} \end{bmatrix} \tag{3.23}$$

$$\mathbf{K}_4 = \begin{bmatrix} K_{4,1} & K_{4,2} & K_{4,3} \end{bmatrix} \tag{3.24}$$

and

$$\mathbf{K}_5 = \begin{bmatrix} K_{5,1} & K_{5,2} & K_{5,3} \end{bmatrix} \tag{3.25}$$

such that $\mathbf{K}_3$, $\mathbf{K}_4$ and $\mathbf{K}_5$ relate the vector $\hat{\boldsymbol{y}}_N$ to the individual 3, 4 and 5/rev control input frequencies, respectively. These matrices are not full column rank, so it is not possible to establish a non-zero lower bound based on Eq. (3.2).

Figure 3.6 shows that for very low values of r (i.e., high control effort), maximum feedback gains for the 3 and 5/rev harmonic inputs at $V = 80$ kn are 2–3 times larger than the 4/rev feedback gain. Furthermore, the upper bounds for these inputs remain above the maximum 4/rev feedback gain for $r < 20$. Beyond $r = 1000$ they quickly go to zero, or at the very least become small enough to be considered negligible, specially when compared to the 4/rev maximum feedback gain.

In the $V = 140$ kn case, 3/rev control input is minimal, even for low values of r. Figure 3.7 shows 3/rev control is restricted by a substantially lower bound. The ratio of the maximum 4/rev to 3/rev gains is about 4 to 1 for most of r. On the other hand, the maximum feedback gain corresponding to the 5/rev input shows a behavior that is more familiar to that displayed by feedback gain corresponding to the helicopter T-matrix model for $V = 80$ kn, with the maximum bound dropping about 75% of its initial value at $r = 1.0$ between $r \approx 10$ and 200.

As implemented, for low r, the LQR control law relies more heavily on 3/rev or 5/rev control to enforce minimization of the $\boldsymbol{y}_N^T \boldsymbol{y}_N$ component of cost function J. For higher values of r, 3/rev and 5/rev control input is brought down to near zero, while 4/rev control frequency is retained as the more dominant input.

Figures 3.8–3.13 show the results of the singular value decomposition of the SISO feedback matrices $K_{i,j}$ corresponding to the three higher harmonic control frequencies (i.e., 3, 4 and 5/rev) and three output channels (i.e, $\dot{w}$, $\dot{p}$ and $\dot{q}$) for $V = 80$ kn and $V = 140$ kn. Feedback gain singular value decomposition results for $V = 80$ kn in Figs. 3.8–3.10 indicate a large uncertainty band

The singular values decomposition results for $V = 140$ kn are restricted to much narrower bands

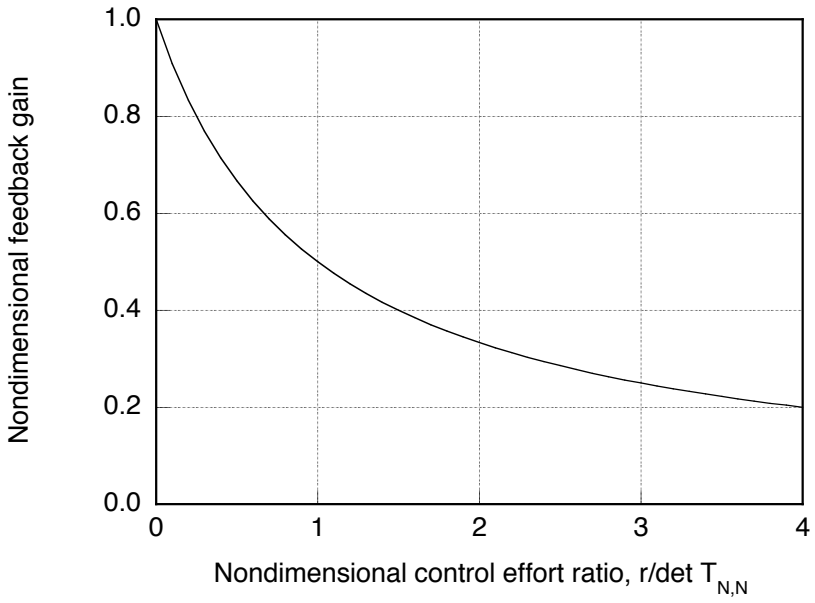

Figure 3.1: SISO nondimensional feedback gain

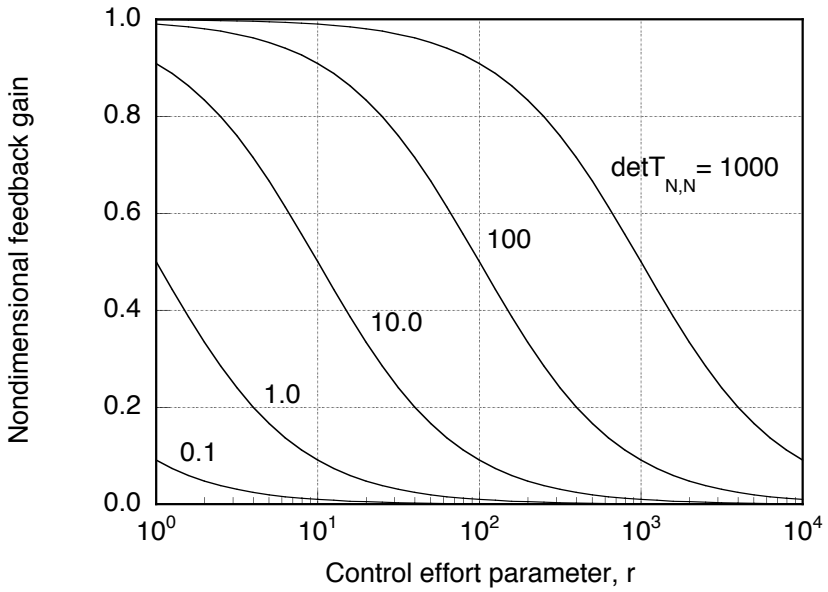

Figure 3.2: SISO feedback gains.

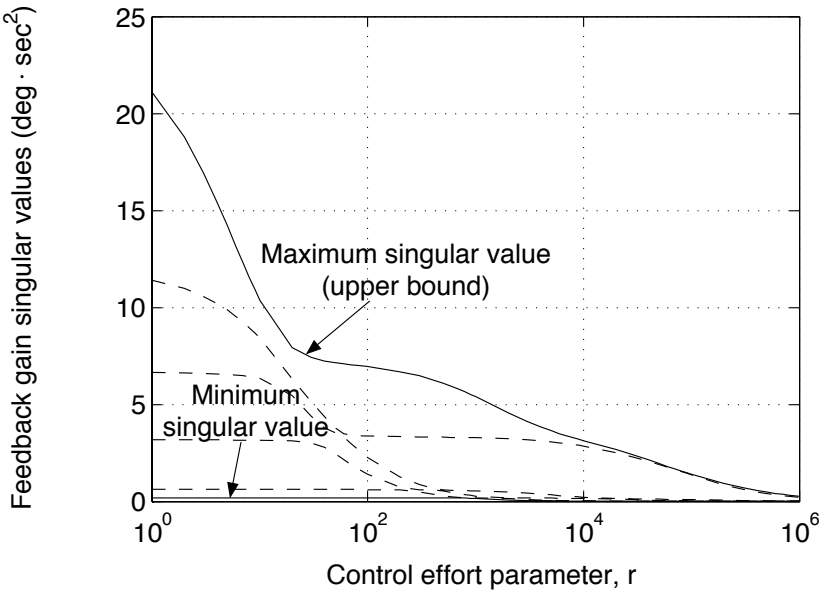

Figure 3.3: Singular values of the feedback gain matrix **K** for $V = 80$ kn ($\mu \approx 0.19$).

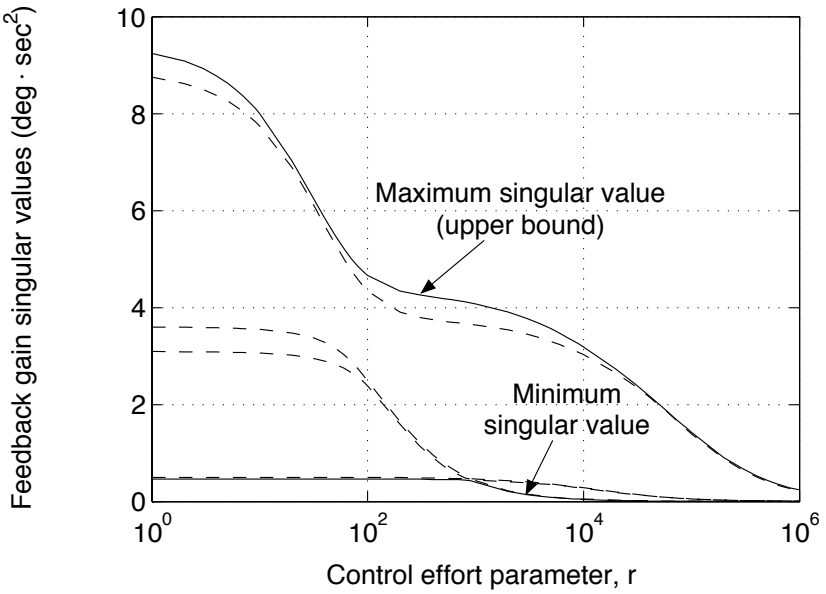

Figure 3.4: Singular values of the feedback gain matrix **K** for $V = 140$ kn ($\mu \approx 0.33$).

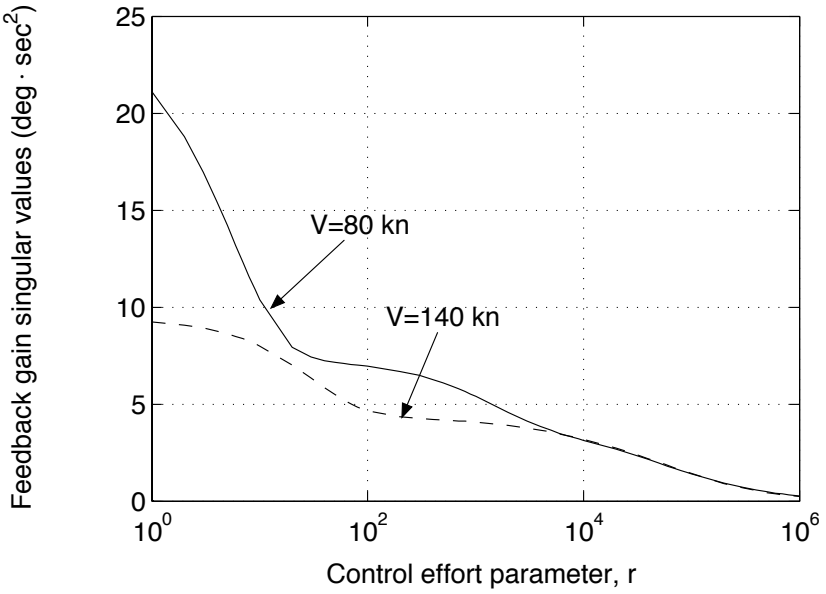

Figure 3.5: Maximum singular values of the feedback gain matrix $\mathbf{K}$ for $V = 80$ kn ($\mu \approx 0.19$) and $V = 140$ kn ($\mu \approx 0.33$).

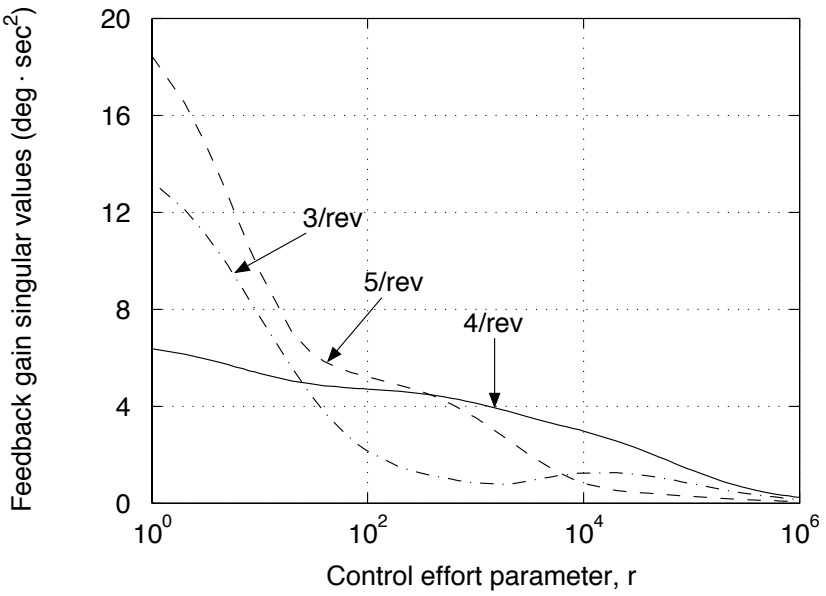

Figure 3.6: Maximum singular values of individual control feedback gain matrices for $V = 80$ kn ($\mu \approx 0.19$)

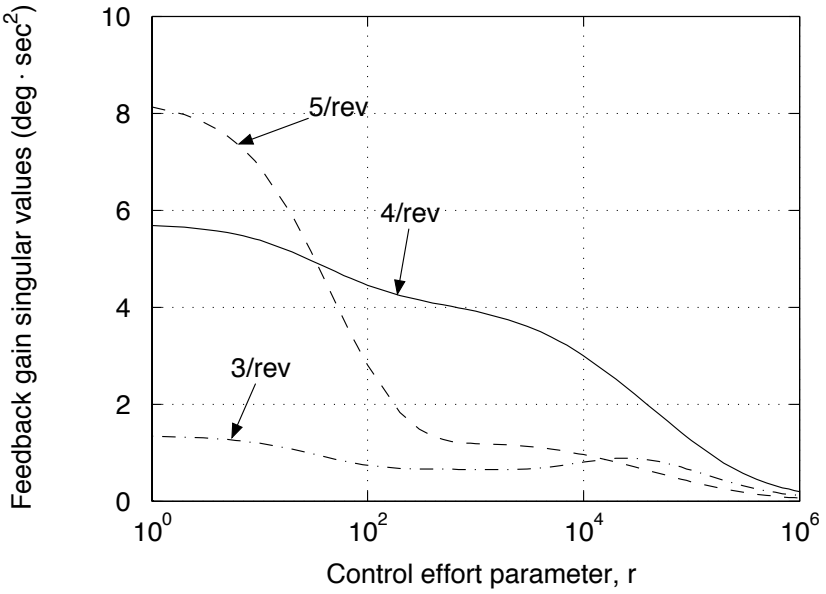

Figure 3.7: Maximum singular values of individual control feedback gain matrices for $V = 140$ kn ($\mu \approx 0.33$).

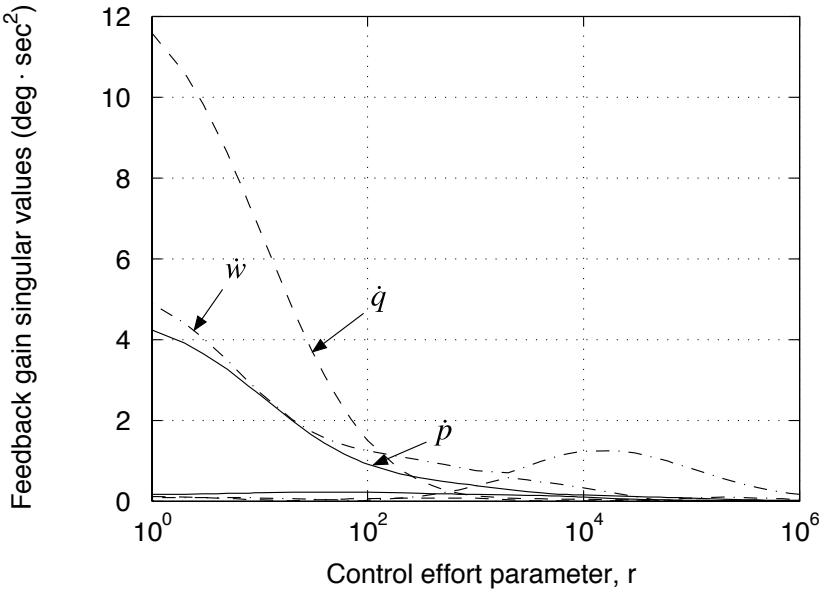

Figure 3.8: Singular values of 3/rev SISO feedback gain sub-matrices for $V = 80$ kn ($\mu \approx 0.19$)

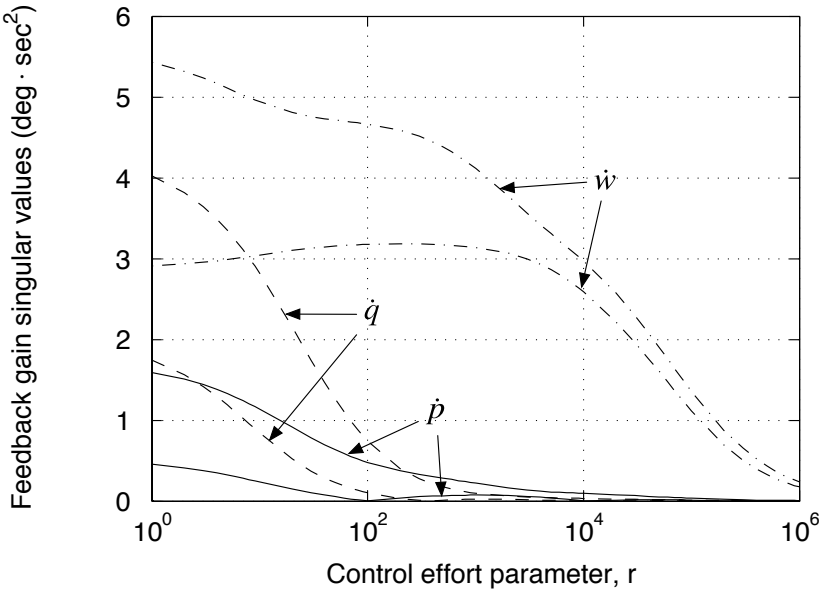

Figure 3.9: Singular values of 4/rev SISO feedback gain sub-matrices for $V = 80$ kn ($\mu \approx 0.19$)

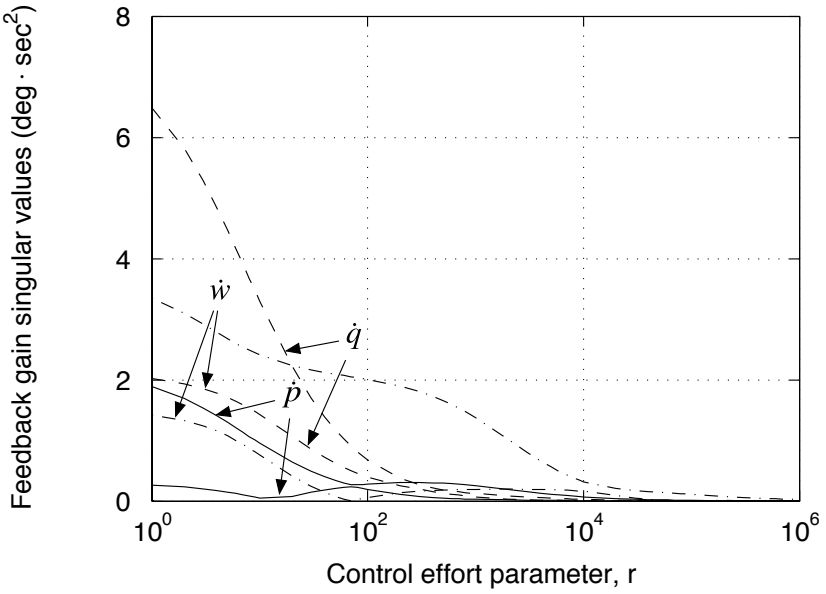

Figure 3.10: Singular values of 5/rev SISO feedback gain sub-matrices for $V = 80$ kn ($\mu \approx 0.19$)

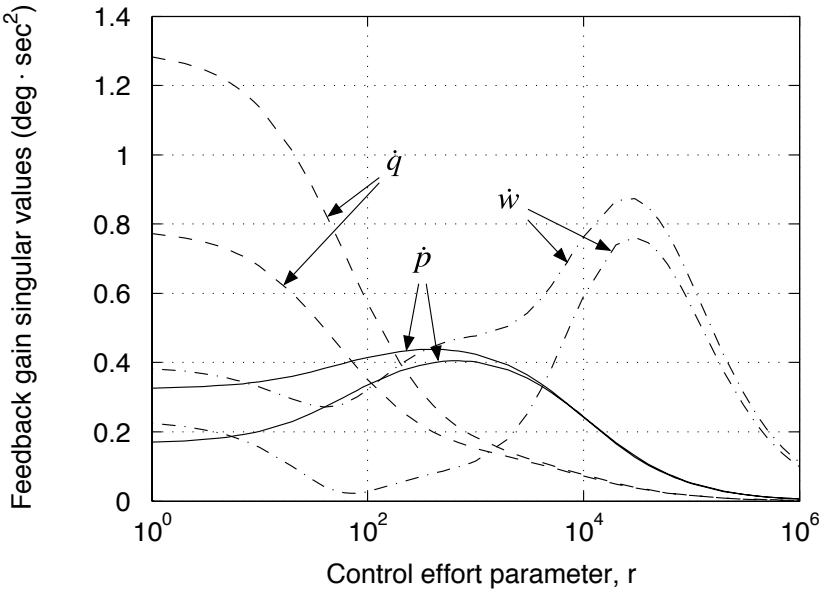

Figure 3.11: Singular values of 3/rev SISO feedback gain sub-matrices for $V = 140$ kn ($\mu \approx 0.33$)

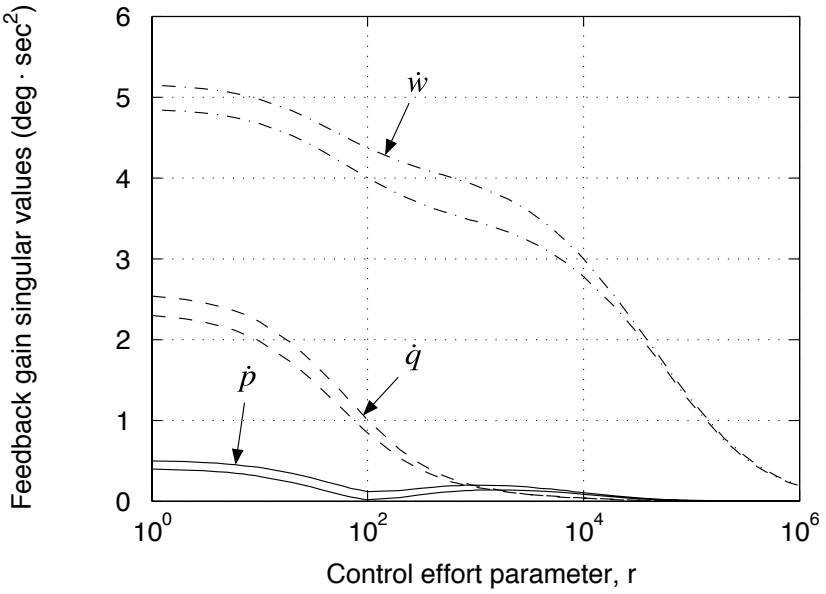

Figure 3.12: Singular values of 4/rev SISO feedback gain sub-matrices for $V = 140$ kn ($\mu \approx 0.33$)

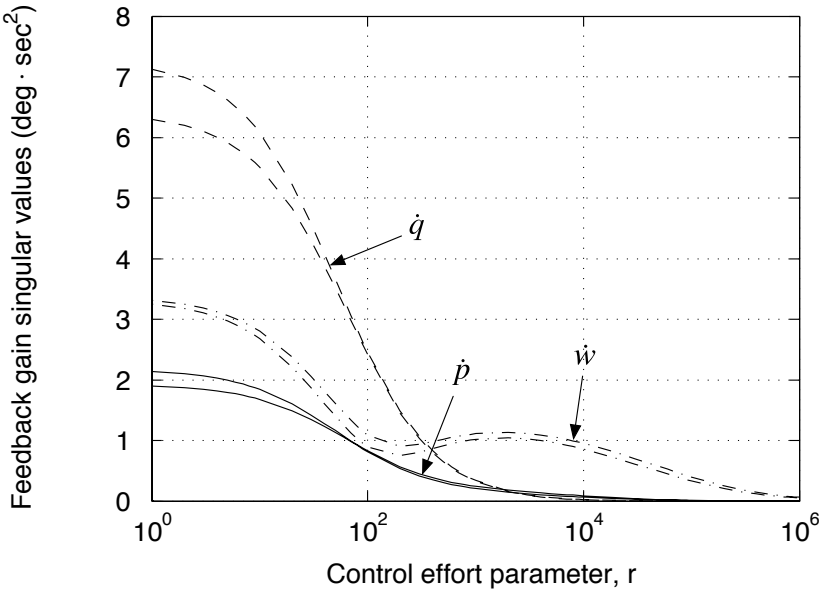

Figure 3.13: Singular values of 5/rev SISO feedback gain sub-matrices for $V = 140$ kn ($\mu \approx 0.33$)

Chapter 4

Continuous-Time HHC Stability Analysis

4.1 Overview

This Chapter presents closed-loop stability and response results for a coupled helicopter/HHC system. The stability results are obtained from a linearized periodic model of the helicopter or its constant coefficient approximation. The closed-loop response results are obtained from the full nonlinear simulation model of the coupled helicopter-HHC system. The primary meaning of the words closed loop is that the HHC vibration control loops are closed. Although a small amount of feedback was added to the model to stabilize the flight dynamic modes, the flight control system model is not realistic enough to enable reliable studies of HHC/flight control system interaction.

The helicopter configuration used for the present study is similar to the Eurocopter BO-105, with a thrust coefficient $C_T/\sigma = 0.07$. Five blade modes are used in the modal coordinate transformation, namely the fundamental flap, lag, and torsion, along with the second flap and lag modes. Blade mode natural frequencies are summarized in Table 4.1.

Because the basic aerodynamic model used in this study consists of a simple linear inflow approximation with quasisteady aerodynamics, and because fuselage flexibility has been neglected, vibratory loads and c.g. accelerations, and consequently also HHC inputs,

tend to be underestimated. Therefore, their absolute values can be considered representative only in a qualitative sense. This is true even if linear unsteady aerodynamics are used instead of the basic quasisteady aerodynamics model, although vibratory loads and c.g. accelerations are substantially improved. Comparisons through both aerodynamic models show, however, the overall simulation model is likely reasonable for stability studies and for a general assessment of the design and closed loop analysis methodology.

The HHC vibration control system has been designed to target the 4/rev harmonic of three (3) helicopter c.g. acceleration components, mainly, the vertical or heave acceleration $\dot{w}$ (i.e., along the z-body axis), and the pitch and roll accelerations $\dot{q}$ and $\dot{p}$, respectively.

For all of the vibratory response results, the helicopter is first trimmed in steady, straight flight at the desired velocity with the HHC system off. Then, the nonlinear simulation begins with the pilot controls largely fixed at their trim values and only a small amount of feedback added to the pilot controls to stabilize the flight dynamic modes. The time integration is allowed to run for a couple of seconds of simulation time to allow the helicopter to converge to a steady state solution before turning the HHC on, in case there exist small discrepancies between the steady solution predicted by the trim solution and the actual steady state solution of the nonlinear system of equations. In the results presented here, time $t = 0$ always marks the instant when the HHC is turned on, however.

The Q and R matrices in Eq. (2.107) have been defined as $Q = I_{6,6}$ and $R = rI_{6,6}$, respectively, where $I_{6,6}$ is an identity matrix with six rows and columns, and r is a parameter that varies from $r = 0$ (no restriction on control effort) to $r = 1000$. A low feedback gain control scheme has been considered for this preliminary analysis by letting

κ in Eq. (2.138) to be $T/2 \approx 0.07$, in order to avoid the closed loop system from becoming unstable for low values of r, and thus permitting a clear evaluation of HHC performance. In the simulation model, these weighing matrices are multiplying the 4/rev components of the heave acceleration, and the roll and pitch accelerations, which have units of ft/sec^2 and rad/sec^2, respectively. Defining the cost index J as nondimensional vibration index, the elements of Q multiplying linear accelerations are assumed to have sec^4/ft^2 units, and similarly, those multiplying angular accelerations have sec^4/rad^2 units. In a similar fashion, r is assumed to have units of 1/rad^2, since higher harmonic control inputs are defined in radians. If the inputs were defined in degrees, the values of r would need to be scaled by a factor of $(\pi/180)^2$ in order to maintain an equivalent cost index J. With such a scale factor values the values of r would range from $r = 0$ to $r = 0.3$.

More meaningful definitions could be established, e.g., vibration cost index $J_Q = \mathbf{y}_N^T \, Q \, \mathbf{y}_N$ could be defined to represent the intrusion index defined in ADS-27. However, the definition chosen for this study is perfectly adequate for stability studies, and can be employed without loss of generality in the assessment of the design and closed loop analysis methodology. Furthermore, the diagonal form of the chosen matrices lead to some insightful and straightforward analytical simplifications discussed below.

Results for a more detailed stability analysis are then presented. Both, this low gain control approach, as well as a high feedback gain configuration with $\kappa = 1.0$ are investigated in this analysis. The higher feedback gain results in instabilities for low values of the parameter r, such that it becomes necessary to place stronger restrictions on the control effort. Consequently, the maximum value of r used in the study is extended to $r = 10^6$.

4.2 HHC performance

4.2.1 Low feedback gain controller

Figure 4.1(a) shows the peak-to-peak magnitude of the 4/rev component of the vertical acceleration at the c.g., for a speed of $V = 80$ kn, corresponding to $\mu = 0.19$. The figure shows four curves, one each for values of $r = 0$, 10, 100 and 1000, corresponding to increasing restrictions on the control effort. Figure 4.1(b) shows the corresponding phase angles. The high frequency oscillations visible in the curves of this, and of many subsequent figures, are largely an artifact of the numerical procedure used to extract the 4/rev magnitude and phase from the time histories of the accelerations. Clearly, the HHC system is very effective and reduces the 4/rev vertical acceleration to a small fraction of its trim value in just a few seconds. The vibration attenuation is also very clear for the c.g. roll acceleration $\dot{p}$ and pitch acceleration $\dot{q}$. The magnitudes of the 4/rev accelerations of both $\dot{p}$ and $\dot{q}$, as well as the corresponding phases, are shown in Figs. 4.3 and 4.5. Both $\dot{p}$ and $\dot{q}$ are reduced to about 30% or less of their trim values in no more than 6–7 s.

Figures 4.9 and 4.10 show the magnitude of the 3, 4, and 5/rev components of the HHC input for the cases $r = 0$ and 1000 and the corresponding phase angles. Comparing the two sets of results, it can be seen that the controls reach their steady-state values much more quickly for the case $r = 0$ than for $r = 1000$. In the latter case, the steady-state values of θ_3 and θ_5 have not been reached at the end of the 7 s of simulation.

The action of the HHC system, and the consequent vibration reduction, occurs within times of the order of 5–7 s or equivalently, of about 1 rad/s. These are also typical timescales for flight control systems and overlap typical piloting frequencies. Therefore,

the results shown earlier indicate the possibility of interaction with the stability and control characteristics of the helicopter.

Figures 4.2, 4.4 and 4.6 show the 4/rev c.g. acceleration components at a speed of $V = 140$ kn, corresponding to an advance ratio $\mu = 0.33$. The magnitude of the vertical acceleration and the corresponding phase angles are shown in Fig. 4.2(a) and 4.2(b). The HHC is extremely effective and reduces the magnitude of the 4/rev accelerations to almost zero within about 7 sec. Attenuations of up to 80% of the 4/rev component of the roll acceleration $\dot{p}$ can be seen in Fig. 4.4 for all values of the control effort parameter r. Figure 4.6 shows that the pitch acceleration $\dot{q}$ is not only, not attenuated by the HHC system, but actually increased to almost twice the baseline value for $r = 1000$ during the first 8 sec of simulation. For the lowest restrictions on the control effort (i.e., $r = 0$ and $r = 10$), however, vibration reductions of up to 80% are observed within the first 7–8 sec.

The combined effect of the 4/rev acceleration components is reflected in the optimal cost index J_Q shown in Figs. 4.7, for an advance ratio $\mu = 0.19$, and 4.8, for $\mu = 0.33$. Only the vibration component of the cost index is shown. Because the chosen weighing coefficients are unitary, the vertical acceleration tends to represent a larger portion of the cost index, due to its higher baseline magnitude relative to the angular accelerations. The cost index for advance ratio $\mu = 0.33$ is particularly influenced by the vertical acceleration. Consequently, the controller directs most of the control effort to reduce the vertical acceleration, in detriment of pitch accelerations, as seen in Fig. 4.6.

The magnitudes of the corresponding values of the 3, 4 and 5/rev inputs are shown in Figs. 4.11 and 4.12 for the cases of $r = 0$ and $r = 1000$, respectively. The steady-state values of each control are reached in about 7–8 sec; therefore the timescale of action

of the controller is approximately the same as in the 80 kn case. Differently from the 80 kn case, with the exception of the 5/rev input, the control time histories for $r = 0$ and $r = 1000$ are very similar. A possible reason for this is that the numerical "size" of the T matrix increases significantly as a function of airspeed; this makes the controller gain less and less sensitive to changes in r as seen in Fig. 3.5.

Finally, Fig. 4.19 shows one result for $V = 170$ kn, corresponding to $\mu = 0.4$. Figure 4.19 shows the baseline and HHC-on magnitudes and phase angles of the 4/rev component of the vertical acceleration with no restrictions placed on the controls (i.e., $r = 0$). Again, the HHC is very effective at attenuating vibrations, and the attenuation occurs on the same timescales as for the speeds already shown. Additional results were obtained for this speed, showing the overall trends are the same as those seen for the $V = 80$ and $V = 140$ kn cases. Figure 4.20 shows the magnitudes and phase angles of the 4/rev component of the roll acceleration $\dot{p}$. Both the baseline trim result and the vibration with the HHC turned on are shown. The corresponding results for the pitch acceleration $\dot{q}$ are shown in Fig. 4.21.

4.2.2 Nominal feedback gain controller

Results for a reduced feedback gain design have been presented up to this point. The possibility of interaction with the stability and control characteristics of the helicopter has been raised based on the vibration attenuation timescales of the HHC. With this in mind, results for a higher feedback gain controller will now be presented in an attempt to provide a more complete picture of the effect of feedback gains on HHC performance and

stability.

Figures 4.25 and 4.26 show the optimal cost index associated with the vibration with different combinations of κ and r, for advance ratios $\mu = .188$ and $\mu = .33$, respectively. Maximum control effort for the low feedback gain configuration is represented by $r = 0$ and $\kappa \approx 0.07$. Two configurations are shown for the nominal control design. Minimum control effort for $\kappa = 1.0$, is achieved by placing a large restriction on the controls with $r = 10^5$. For advance ratio $\mu = .188$, the value for $r = 2 \cdot 10^4$ marks one of the lowest restrictions that can be placed on the controls before the system becomes unstable. The same is true for $r = 10^4$ in Fig. 4.26 for $\mu = 0.33$. Vibration attenuation performance measured by the optimal cost index for $r = 0$ ($\kappa \approx 0.07$), and $r = 2 \cdot 10^4$ ($\kappa = 1.0$) in Fig. 4.25 are comparable in overall reduction effectiveness. Both cases achieve near perfect attenuation of the cost index within the first 4 seconds, although the nominal controller with $\kappa = 1.0$ is slightly faster. Attenuation is significantly degraded for the nominal controller when larger restrictions are placed on the controller effort. Results for $\mu = 0.33$ in Fig. 4.26 show, however, that the controller designed for this flight condition can enforce much faster vibration attenuation rates than those achieved with the reduced gain design, with attenuation for $\kappa = 1.0$ achieved within 0.5–1 sec.

Figures 4.27–4.32 show the corresponding amplitudes of the HHC inputs for $V = 80$ kn and $V = 140$ kn. Amplitudes of the 3, 4 and 5/rev controller blade pitch harmonics for advance ratio $\mu = .19$ are shown in Figs. 4.27, 4.29 and 4.31, for $r = 2 \cdot 10^4$, $r = 4 \cdot 10^4$, $r = 5 \cdot 10^4$ and $r = 10^5$. In general, simulation results indicate that controller reaches the same steady state value, independently of the controller effort restrictions. However, convergence is faster when restrictions on the controller effort are made less stringent.

The corresponding values for an advance ratio $\mu = .33$ are shown in Figs. 4.28, 4.30 and 4.32 for effort parameter values $r = 10^4$, $r = 4 \cdot 10^4$ and $r = 10^5$. As is the case for $\mu = .19$, for $\mu = .33$ controller also responds faster for lower values of r. The controller responds faster for $\mu = .33$ than for $\mu = .19$, however, achieving its steady state condition within 1–4 sec of the HHC being turned on. Controller performance for $\mu = .19$ is less evident, with the closed loop only achieving its steady condition within 4–8 sec after it is turned on.

4.3 Unsteady aerodynamics

Figures 4.33 through 4.35 compare the unsteady and quasisteady blade sectional aerodynamic loads at 75% of the blade span for the $V = 140$ kn case, without HHC. Figure 4.33(b) shows that the unsteady peak-to-peak amplitude of the sectional lift is approximately 40% larger that the quasisteady aerodynamics value. There is a minor 10 deg phase delay between the maximum and minimum peaks. The pitching moment coefficient in Fig. 4.34(a) shows a large 2/rev nosedown value peaking between $\psi = 90$ and $\psi = 180$ deg, and about $\psi = 300$ deg, which results in a $C_M M^2$ value of -0.006 right around $\psi = 100$ deg, as shown in Fig. 4.34(b), compared to the quasisteady $C_M M^2 \approx -0.0045$ at about $\psi = 90$ deg. The unsteady non-dimensional moment represents a 33% increase over the quasisteady value. The unsteady drag coefficient in Fig. 4.35 shows a large 2/rev peak value at $\psi = 0$ and $\psi = 180$ deg. The larger amplitude of the unsteady pitching moment, compared with the quasisteady value, results in slightly larger amplitude blade torsional oscillations, as shown in Figure 4.36(a).

With unsteady aerodynamics, swashplate cyclic pitch is more heavily biased towards longitudinal pitch, in order to maintain the straight and level steady flight condition. Therefore, with unsteady aerodynamics, $\theta_{1c} = 1.17$ deg and $\theta_{1s} = -4.63$ deg, whereas, $\theta_{1c} = 1.76$ deg and $\theta_{1s} = -3.73$ deg, with quasisteady aerodynamics. Consequently, unsteady aerodynamics results in larger geometric pitch angles on the retreating blade, as shown in Figure 4.36(b).

Figure 4.37 shows a markedly higher peak on the overall aerodynamic angle of attack on the retreating side at $\psi = 210$ deg. The peak angle of attack is 8 deg, small enough so the linear unsteady aerodynamics model is adequate for HHC analysis in this flight condition. Stall on the inboard sections of the retreating blade is not captured by the unsteady aerodynamics model, however.

Figures 4.38 through 4.40 show the sectional two-dimensional aerodynamic coefficients and non-dimensional loads at the 75% of the blade span, as a function of the angle of attack of the point on the blade. As shown in Fig. 4.38, unsteady aerodynamics has a negligible impact on the phase angle between the maximum angle of attack and lift coefficient peaks, when compared to quasisteady aerodynamics. The larger amplitude of the angle of attack results in the higher lift coefficient peak at $\psi = 210$ deg in Fig. 4.33(a). The effects of angle of attack on the unsteady aerodynamics are more evident in the pitching moment, shown in Fig. 4.39, and drag shown in Fig. 4.40.

The overall impact of unsteady aerodynamics on the baseline vibration levels, compared with quasisteady aerodynamics is shown in Fig. 4.41. Figure 4.41 plots the square root of cost index J_Q and the individual components corresponding to the vertical (i.e., heave), roll and pitch accelerations. Angular accelerations at the center of gravity, $\dot{p}$ and

$\dot{q}$, are the most largely affected by the sectional, two-dimensional unsteady aerodynamics, probably as a result of the much larger pitching moment and drag oscillations. The 4/rev vertical acceleration is about 29% higher, roll and pitch are, however, 12 and 25 times larger than the quasisteady value, respectively.

Figures 4.42, 4.43 and 4.44 show the 4/rev z-body axis and angular acceleration components for three values of control effort, mainly, $r = 10^4$, $4 \cdot 10^4$ and 10^5. The peak-to-peak amplitude of the vertical acceleration and the corresponding phase angles are shown in Figs. 4.42(a) and 4.42(b). Unsteady aerodynamics has no significant bearing on the time scales of vibration attenuation. HHC remains extremely effective and reduces the magnitude of the 4/rev accelerations to under 10% within about 6 s, for $r = 10^5$. With higher control effort settings, vibration attenuation times can be reduced to within 3.5 sec ($r = 4 \cdot 10^4$) and 2 sec ($r = 10^4$). Near-perfect attenuation of the roll acceleration $\dot{p}$ can be seen in Fig. 4.43. Figure 4.44 shows that the pitch acceleration $\dot{q}$ is also very well attenuated by the HHC system, although maximum vibration reductions are only within 70–90%. The cost functional shown in Fig. 4.45 is dictated mostly by the vertical c.g. and roll accelerations, given the weighing coefficients used. This is reflected by the similar vibration attenuation timescales.

Figures 4.46, 4.47 and 4.48 show the values of the corresponding 3, 4 and 5/rev control inputs. The impact of the larger baseline 4/rev vibrations is reflected in the larger steady state values of the HHC inputs, compared to the results with quasisteady aerodynamics. However, closed loop reponse timescales are very similar in the two cases. So, because the natural transient response of the closed loop helicopter-HHC system after the HHC is turned on is not markedly different, it is assumed that unsteady aerodynamics do

not play a significant role on the closed loop stability evaluations. It remains to be seen whether this assumption is true or not.

4.4 Stability analysis

It is also interesting to consider the closed loop eigenvalues of the system. The computation of the closed loop state matrix A_e was achieved by directly assembling the matrix for the augmented system starting from a linearized set of equations for the plant. Alternatively, A_e can be computed by linearizing the augmented, closed loop nonlinear set of equations directly. The two approaches yielded comparable results.

4.4.1 Formulation of the coupled helicopter/HHC model

The compensator will be designed along the lines of Ref. [67]. Denote with $A(\psi)$, $B(\psi)$, $C(\psi)$, and $D(\psi)$ the matrices for the LTP state space model of the helicopter, for the selected input/output pair. Similarly, denote with $A_c(\psi)$, $B_c(\psi)$, $C_c(\psi)$ the compensator's state space model. The closed-loop LTP state matrix $A_e(\psi)$ is given by

$$A_e(\psi) = \begin{bmatrix} A(\psi) & B(\psi)C_c \\ B_c(\psi)C(\psi) & A_c + B_c(\psi)D(\psi)C_c \end{bmatrix} \tag{4.1}$$

The closed-loop stability of the helicopter with HHC is then given by the characteristic exponents of $A_e(\psi)$, and will be studied as a function of the design parameters Q and R.

4.4.2 Periodic HHC stability

Stability results of the low gain feedback control configuration with $\kappa \approx 0.07$ are now considered. Figure 4.49 shows the real part of the least damped closed-loop eigenvalues

for $V = 80$ kn as functions of the control effort parameter r. These eigenvalues are the Floquet exponents of the LTP closed loop system of equations corresponding to a combination of aircraft modes (i.e., yaw damping, phugoid, Dutch roll and heave modes) and rotor lag modes (i.e., second lag), as well as controller eigenvalues. For the most part, aircraft modes are found to be insensitive to the feedback gains of this HHC configuration. The same cannot be said about the second lag mode, which actually finds its stability slightly reinforced for $r < 200$. This unintended advantage is of minor consequence and will not be discussed further.

In general, for the highest control effort (i.e., tuning parameter $r = 0.0$), controller eigenvalues tend to be more highly damped, and as r increases they tend to converge or come closer to zero (i.e., the imaginary axis). Moreover, the real part of the controller exponents is strongly related to the quickness of control response shown in Figs. 4.9 and 4.10. For $r = 0$, the absolute value of the real part of controller exponents is found within the interval 0.4–0.8 rad/sec, which loosely corresponds to settling times in the order of 5–10 seconds. As r reaches 200, the real part of two of the controller exponents has nearly converged to zero, and the real part of the remaining four exponents are found to be within -0.4–0.5 rad/sec, which would indicate response times of 8–10 seconds for the controller dynamics. Further increments on the controller constraints result in negliglible changes in the damping of controller exponents.

The effect of the parameter r on the rotor dynamics has also been computed. Figure 4.50 shows the real part of the Floquet exponents corresponding to the fundamental flap and lag modes as well as the second lag and second flap modes as functions of r for $V = 80$ kn. The eigenvalues are largely insensitive to the controller effort parameter r,

with the largest variations occurring for $r < 100$. This clearly reinforces the expected result that low feedback control gains should guarantee quasisteady closed loop dynamics.

Stability results for the nominal control design (i.e., $\kappa = 1.0$) paint a dramatically different picture, although very similar qualitative conclusions can be established from them. The first difference to stand out, in contrast with the low gain control design obtained with $\kappa \approx 0.07$, is the manifestation of instability for low control constraint settings (i.e, low r). Figure 4.51 shows the real part of selected closed loop system eigenvalues at $V = 80$ kn, mainly, controller and unstable eigenvalues. The figure shows one of the rotor modes becoming marginally stable for a value of r in between 10^4 and $2 \cdot 10^4$ (i.e., approximately $1.5 \cdot 10^4$).

Exponents for the closed loop system relate very well to the open loop plant exponents for large values of r, where closed loop dynamics can be considered quasisteady, and are thus identified accordingly. Due to the coupled nature of blade flap, lag and torsion modes, identification is not as straightforward for decreasing values of the controller restriction parameter r, as the controller exerts a stronger influence on the helicopter's natural modes. Under such high gain conditions the flap modes can become lag modes, and viceversa.

There are three controller modes shown in the plot with distinctly different real parts. These are complex conjugate pairs, for a total of six eigenvalues. Because these eigenvalues are actually the characteristic exponents of the periodic system, natural modes are periodic and contain all the harmonics of the fundamental frequency. Also, the solution for the imaginary part of the exponents is not unique and is repeated every $\pm\Omega/2$. However, since for the most part the time response of the controller does not exhibit high

frequency content, the lowest frequency exponents are assumed to be the most important. As shown in Fig. 4.52, all three fundamental modes converge to zero for increasingly large controller effort restrictions. Remaining solutions, as well as their conjugate pairs must converge to the points $\pm j\Omega/2$ on the imaginary axis.

The values of the real parts of the controller eigenvalues for $r = 2 \cdot 10^4$ are 5.2, 1.1 rad/sec, approximately, and a third value which is very close to zero. With the exception of this last eigenvalue, these values correspond to settling times of the order of 0.8 and 3.6 sec, respectively. The latter of the two matches the HHC controller settling times observed from the responses in Figs. 4.27, 4.29 and 4.31 for this controller effort. Furthermore, the imaginary part for the second of these exponents (i.e., labeled HHC 2 in Fig. 4.52) is close to 1.38 rad/sec, resulting in the 2.3 sec peak times observed of the 5/rev controller response in Figure 4.31. Similarly, the peak times suggested by the imaginary part of the HHC 2 mode (i.e., damped frequencies) for values of $r = 4 \cdot 10^4$, $r = 5 \cdot 10^4$ and $r = 10^5$ correlate very well with the response histories in Figure 4.31. For $r = 4 \cdot 10^4$, the damped frequency is 0.776 rad/sec, resulting in a peak time $t_p = 4.0$ sec. Damped frequencies for $r = 5 \cdot 10^4$ and 10^5 are 0.62 and 0.27 rad/sec, respectively, which result in peak times of 5.1 and 11.6 sec. The same degree of correlation between the eigenvalues and the HHC controller response times for the 3 and 4/rev inputs is not observed, although the same trend is kept, with peak times for the 3/rev increasing along with the increasing restrictions on the control effort parameter. Certainly none of the controller eigenvalues explain these peak times, so they must to be strongly inluenced either by the rotor or the fuselage dynamics. These timescales are more closely associated with the Dutch roll mode ($c_{DR} = -0.43 \pm j(2.38 \pm \Omega/2)$ rad/sec). They could also suggest a coupling

with rotor blade 2nd lag modes, which would make sense, given the strong relationship demonstrated by the destabilizing effect on the blade lag mode shown in Figure 4.51. As for the 4/rev blade pitch controls, two observations can be made: first, although the plots show two predominant asymptotic settling rates over the 7 seconds span of the simulation, overall settling times are in order with the time constants determined by the real part of the eigenvalues; and second, the control values for $r = 2 \cdot 10^4$ shows a high frequency 4 Hz (i.e., 0.57/rev) oscillation. Independently of the cause for this dynamic behaviour, the present results confirm, however, that closed loop HHC should not be studied in isolation of the helicopter dynamics, or at least the rotor dynamics, by assuming them to be quasisteady.

Similar results have been obtained for the low and nominal feedback gain HHC controllers at $V = 140$ kn. Figure 4.53 shows the real part of the least damped closed-loop Floquet exponents as functions of the control effort parameter r. Not unexpectedly, based on the previous results, aircraft modes at $V = 140$ kn are found to be insensitive to the feedback gains of this low gain HHC configuration. The same is true for the second lag modes, for the most part. As for the other rotor modes, Figure 4.54 shows the real part of the Floquet exponents corresponding to the fundamental flap and lag modes as well as the second lag and second flap modes, as functions of r. Clearly, higher constraints need to be placed on the controls in order to guarantee quasisteady closed loop dynamics, compared to the values required by the controller at $V = 80$ kn. Whereas at $V = 80$ kn it is sufficient to set the control effort parameter to $r = 100$, at $V = 140$ kn the value of r needs be above 400.

Again, the real part of the controller exponents correlates strongly to the quickness

of the controller response shown in Figs. 4.11 and 4.12. For $r = 0$, the absolute value of the real part of the six controller exponents is found within the interval 0.5–0.6 rad/sec, and these values correspond to the 7–8 seconds settling times observed in the controller response. As r reaches 400, the real part of two controller exponents has nearly converged to zero. Differently from the $V = 80$kn case, the other four controller exponents are found to be largely unmodified by r. Again, further increasing the controller constraints results in negliglible changes in the damping of controller exponents, which justifies the small changes observed in the response times for $V = 140$ kn.

Finally, the real part of the eigenvalues for the nominal gain controller for $V = 140$ are presented in Fig. 4.55 as functions of the control effort parameter r. Results are qualitatively very similar to those shown in Fig. 4.51 for the $V = 80$ kn case. The absolute value of the real parts of the more highly damped controller modes for $r = 10^4$, are about 7.5 and 4.5 rad/sec. These values correspond to response settling times in the order of 0.5–0.9 sec, which correspond to the settling time values observed in Figs. 4.28, 4.29 and 4.31. Similarly, 4.6 and 1.6 rad/sec damping of the eigenvalues, for $r = 4 \cdot 10^4$, result in time constants of 0.22 and 0.61 sec, and 0.9–2.4 sec settling times, which are in very good agreement with those observed for the time histories of the controller responses. The 4 sec settling times seen in the control inputs for $r = 10^5$ are also in good agreement with the 1.42–5.63 sec settling times established by the damping values of the controller exponents.

Additionally, results shown in Fig. 4.51 regarding the closed loop stability of the coupled, helicopter-HHC system indicate that helicopter dynamics can become unstable, in the same way they did for the $V = 80$ kn case, if HHC control constraints are loosened

excessively, such that feedback gains are large enough that they result in the erosion of existing stability margins for the helicopter. In the $V = 140$ kn case, however, HHC can be configured to higher control efforts, compared to the $V = 80$ kn case. Whereas the onset of instability for the $V = 80$ kn case occurred for $r \approx 1.5 \cdot 10^4$, control constraints for $V = 140$ can be reduced twicefold, up to about $r \approx 7,000$, before the marginal stability point is reached. Although the feedback gains associated with the T matrix for $V = 80$ kn tend to be higher than those for $V = 140$ kn for lower values of r as shown in Fig. 3.5, for the values in question this is not the case. Differences between the "size" of the feedback gains are only noticeable for values r lower than 5,000. Therefore, the earlier onset of instability in the $V = 80$ kn case, compared to the case for $V = 140$ kn, is probably due to lower stability margins of the helicopter itself at this flight condition.

4.5 LTI approximation

4.5.1 Closed loop formulation

LTI stability calculations are based on the eigenvalues of the constant coefficient approximation of matrix $A_e(\psi)$ given in Eq. 4.1. The underlying assumption in this approach is that periodic dynamics of the closed loop system are not important, compared to the constant component. The constant coefficient approximation of $A_e(\psi)$ is defined as

$$\overline{A}_e = \frac{1}{2\pi} \int_0^{2\pi} A_e(\psi)\, d\psi \tag{4.2}$$

or, equivalently,

$$\overline{A}_e = \begin{bmatrix} A_0 & B_0 C_c \\ [B_c(\psi)C(\psi)]_0 & [B_c(\psi)D(\psi)]_0\, C_c \end{bmatrix} \tag{4.3}$$

where $[\,\cdot\,]_0$ denotes the time average values of the individual sub-matrices. Since linearized equations of the helicopter are expressed as a Fourier series expansion, $\overline{A}_e$ can be simplified as

$$\overline{A}_e = \begin{bmatrix} A_0 & B_0 C_c \\ \frac{1}{2}\mathbf{K}\begin{bmatrix} C_{Nc} \\ C_{Ns} \end{bmatrix} & \frac{1}{2}\mathbf{K}\begin{bmatrix} D_{Nc} \\ D_{Ns} \end{bmatrix} C_c \end{bmatrix} \tag{4.4}$$

where C_{Nc}, C_{Ns}, D_{Nc} and D_{Ns} are the cosine and sine Fourier coefficient matrices for the helicopter. Hence, the current representation of the closed loop helicopter-HHC system matrix preserves, through the matrices C_{Nc}, C_{Ns}, D_{Nc} and D_{Ns}, some of the periodic dynamics of the helicopter.

4.5.2 Stability results

The LTI poles were considered for completeness purposes. The root locus of the HHC closed loop system poles, and selected helicopter open loop poles are shown in Figs. 4.60, 4.62 and 4.64. Not unexpectedly does the system show better stability properties at high speed (140 and 170 knots), since the norm of the feedback gain for $V = 80$ is approximately twice as large as shown in Fig. 3.5, for low values of the control constraints. While all the cases remain unstable for all values of r, the relative "strength" of the instabilities does diminish for high r.

Although the stability issues are not fully addressed, it is clear that the position of the poles is in fact linked to the vibration reduction performance. In general, for the highest control effort (tuning parameter $r = 0.0$) controller poles tend to be farther away from the origin, and as r increases they come closer to it. This is clearly not unexpected, since as $|\mathbf{K}| \to 0$ in Eq. 4.4 for larger values of r, the closed loop state matrix $\overline{A}_e$ becomes

increasingly null rank, i.e., as the bottom rows of $\overline{A}_e$ become increasingly small (becoming zero in the limit as $r \to \infty$) the associated eigenvalues also vanish. This obviously relates to the expected result that best performance at high speed should be achieved for low r, especially for $r = 0.0$.

Figures 4.60, 4.62 and 4.64 also show that closed loop poles associated with the controller display increasingly larger imaginary parts. In particular, one HHC complex conjugate pole pair at 170 knots for $r = 1.0$ is shown to be initially stable, although lightly damped, and to have a natural frequency of 1.4 rad/sec (see Figure 4.65). This frequency is comparable to the phugoid mode frequency, and results show a strong interaction between the phugoid mode and the HHC system dynamics.

Figures 4.61, 4.66 and 4.66 show the real part of the least damped closed loop system poles. While helicopter dynamics remain largely unaffected for the lower speeds, this is not the case for $V = 170$ kn, where the controller is found to modify the damping characteristics of phugoid and Dutch roll modes. The stronger interaction at 170 knots is not unexpected, due to the relative larger "size" of the C_{Nc}, C_{Ns}, D_{Nc} and D_{Ns} matrices in Eq. 4.4, which are indicative of the increased periodicity of the system at high speed. Therefore, results suggest that increased periodicity may potentially play a significant role in FCS/HHC interactions.

Table 4.1: BO-105 FEM blade mode frequencies

Mode number	Mode	Frequency (/rev)
1	1st lag	0.7316
2	1st flap	1.1253
3	1st torsion	3.1806
4	2nd lag	3.4141
5	2nd flap	4.4860

Table 4.2: BO-105 main rotor configuration

Parameter	Value
Thrust coefficient	0.0049
Main rotor radius (ft)	16.12
Blade chord (ft)	0.89
Precone (deg)	2.5
Number of blades	4
Solidity	0.07
Rotor speed (rad/s)	44.4
Linear blade twist (deg)	-6.2
Airfoil section	NACA 23012

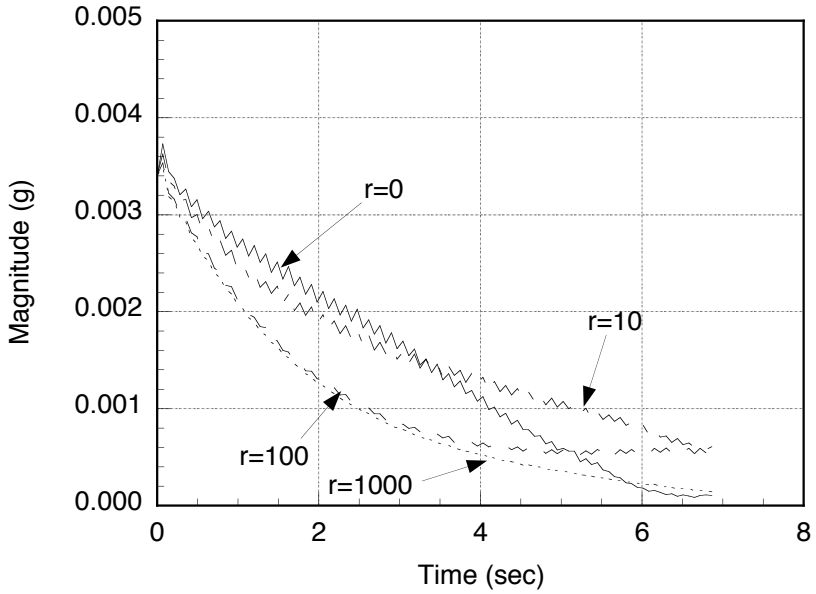

(a) Peak-to-peak

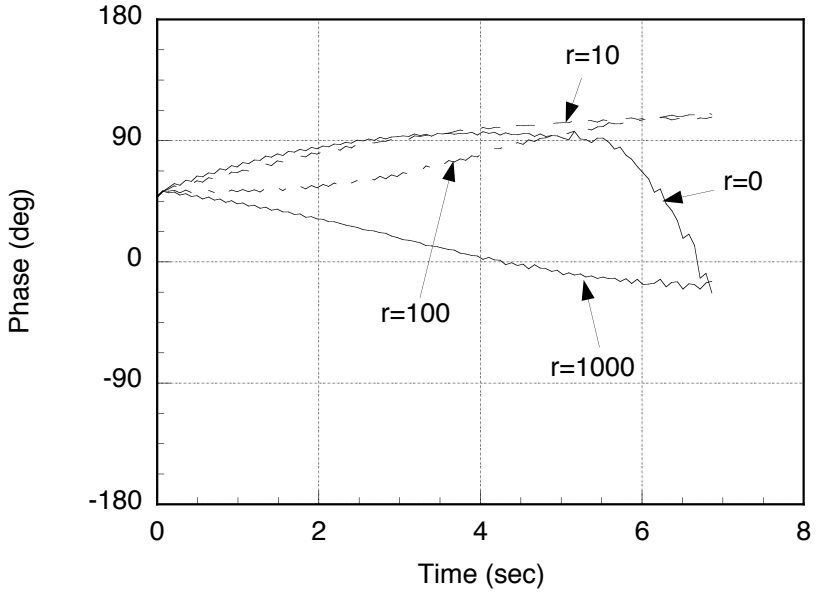

(b) Phase

Figure 4.1: 4/rev vertical accelerations at helicopter CG in g for 80 kn ($\mu = 0.188$).

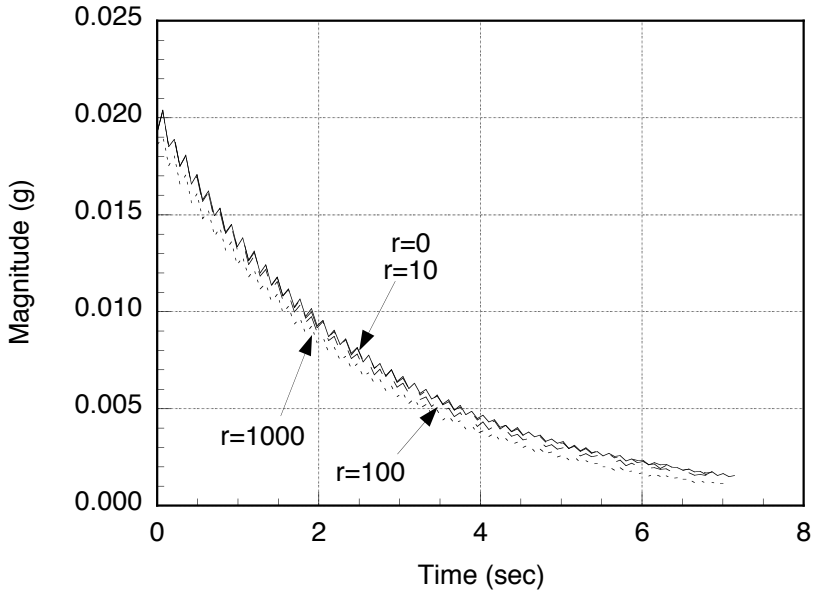

(a) Peak-to-peak

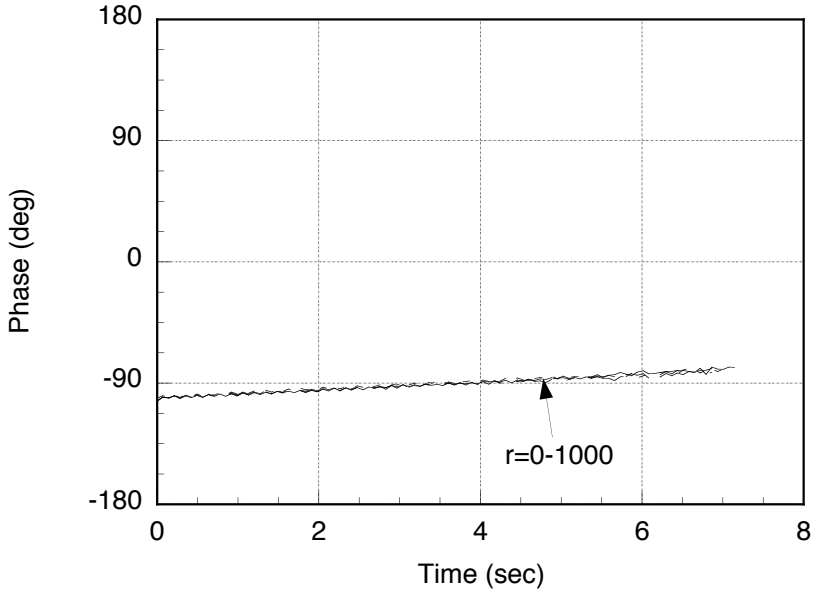

(b) Phase

Figure 4.2: 4/rev vertical accelerations at helicopter CG in g for 140 kn (μ = 0.330).

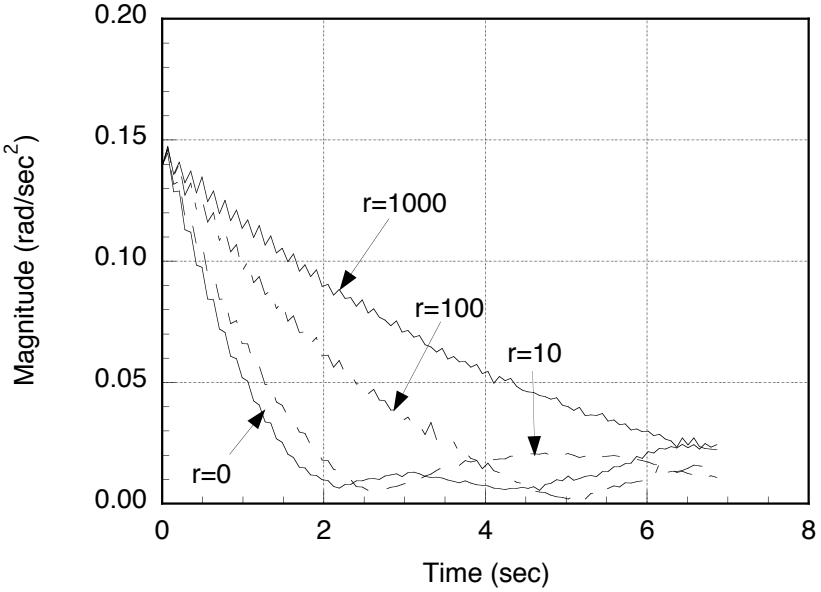

(a) Peak-to-peak

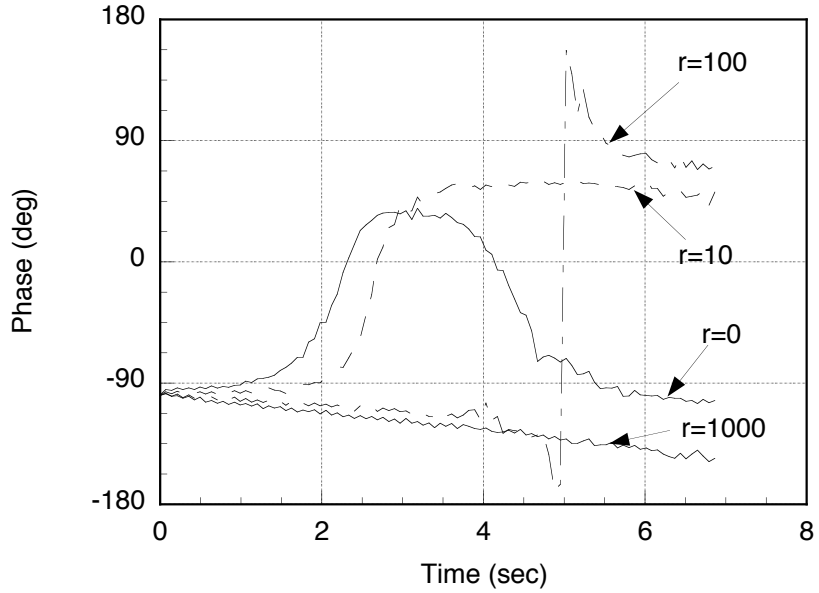

(b) Phase

Figure 4.3: 4/rev roll accelerations of helicopter for 80 kn (μ = 0.188).

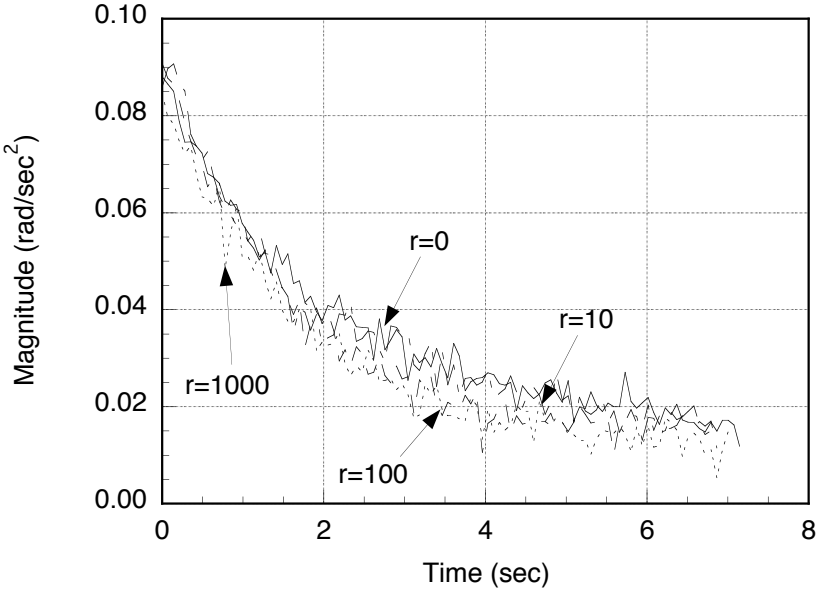

(a) Peak-to-peak

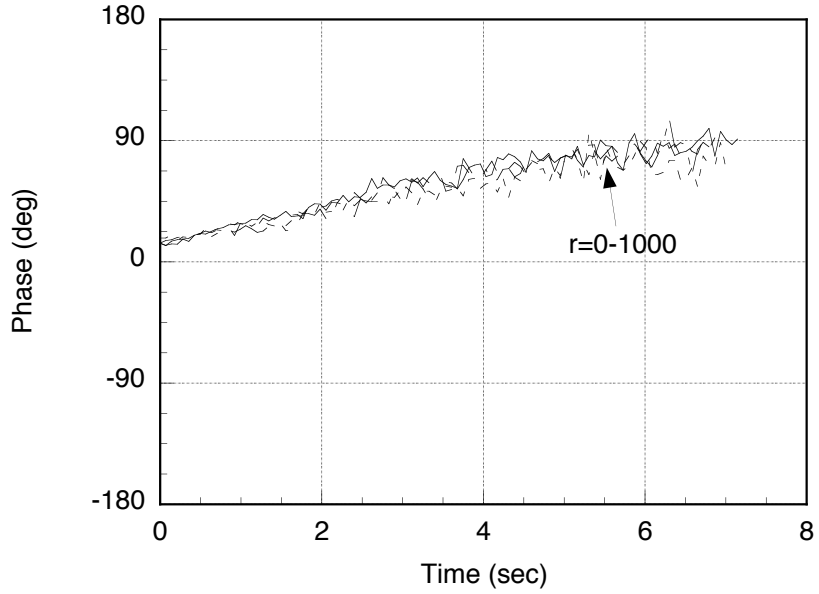

(b) Phase

Figure 4.4: 4/rev roll accelerations of helicopter for 140 kn (μ = 0.330).

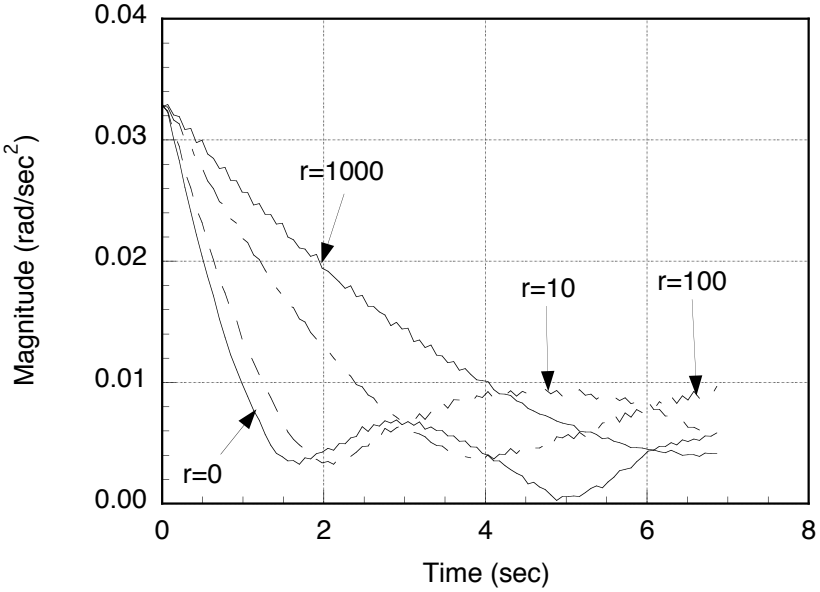

(a) Peak-to-peak

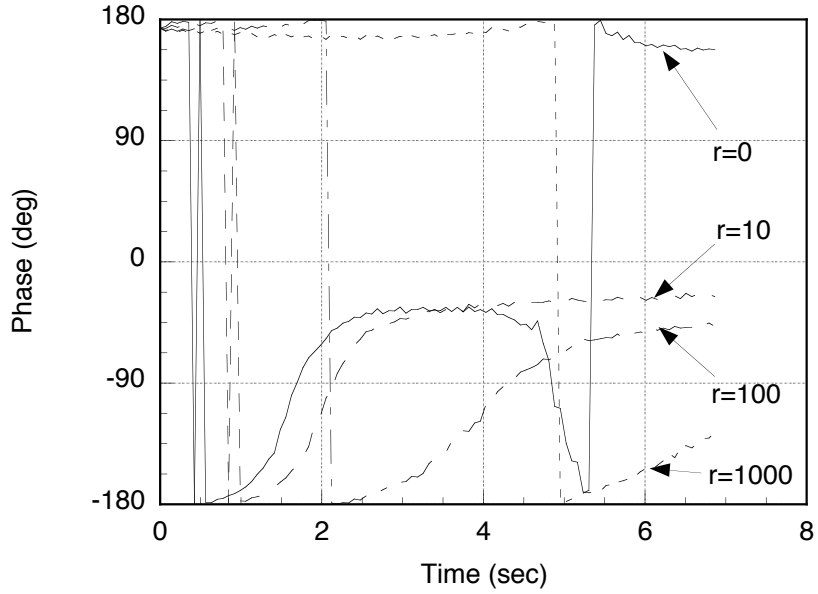

(b) Phase

Figure 4.5: 4/rev pitch accelerations of helicopter for 80 kn (μ = 0.188).

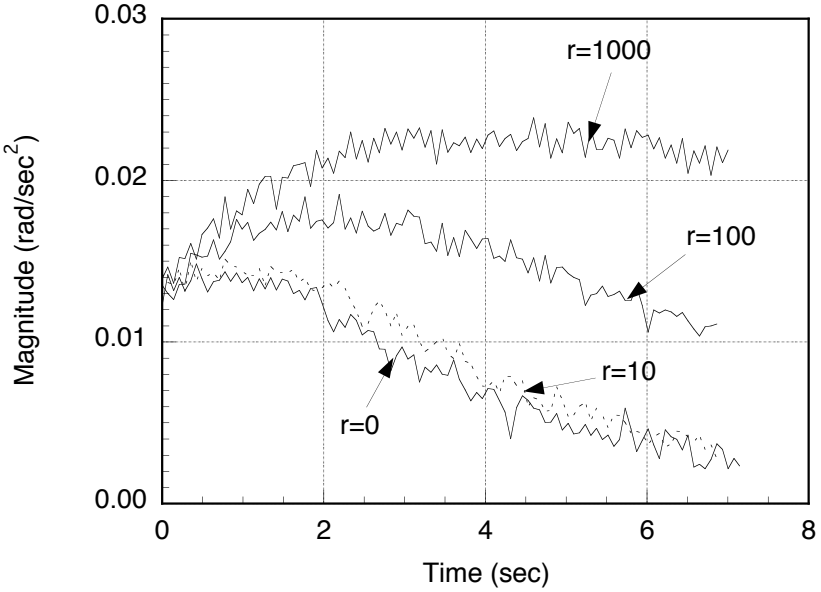

(a) Peak-to-peak

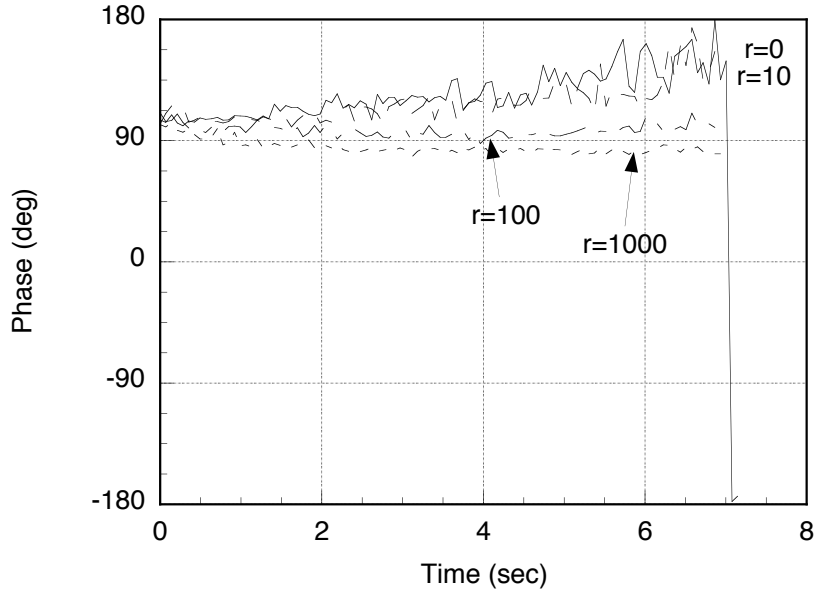

(b) Phase

Figure 4.6: 4/rev pitch accelerations of helicopter for 140 kn (μ = 0.330).

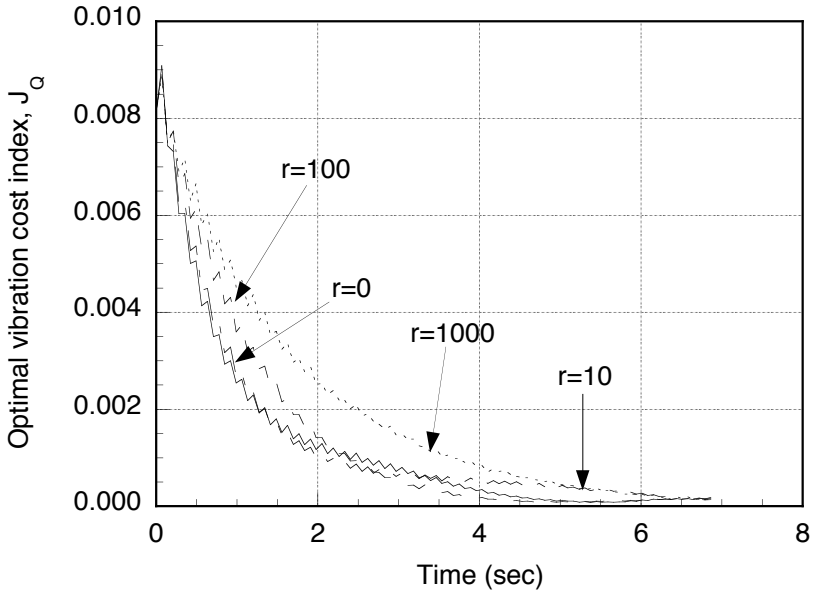

Figure 4.7: Optimal vibration cost index with low gain controller for 80 kn.

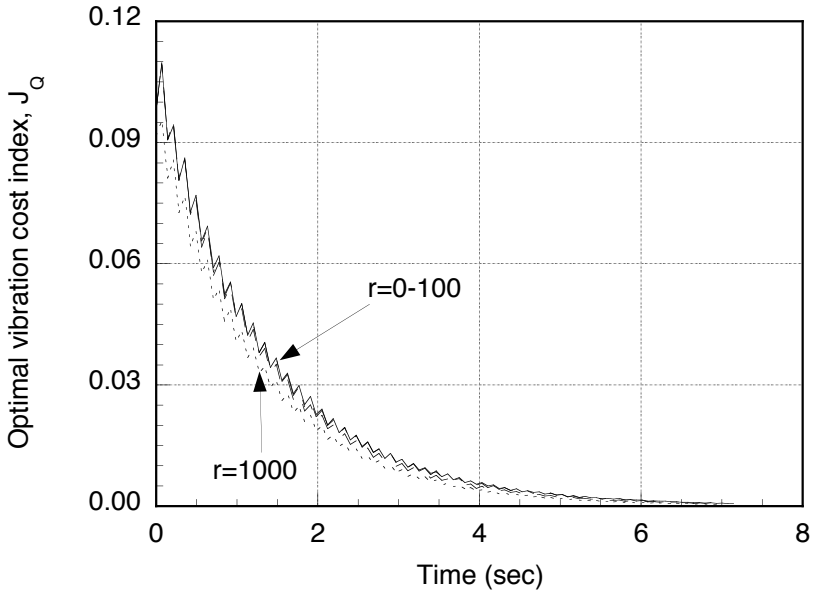

Figure 4.8: Optimal vibration cost index with low gain controller for 140 kn.

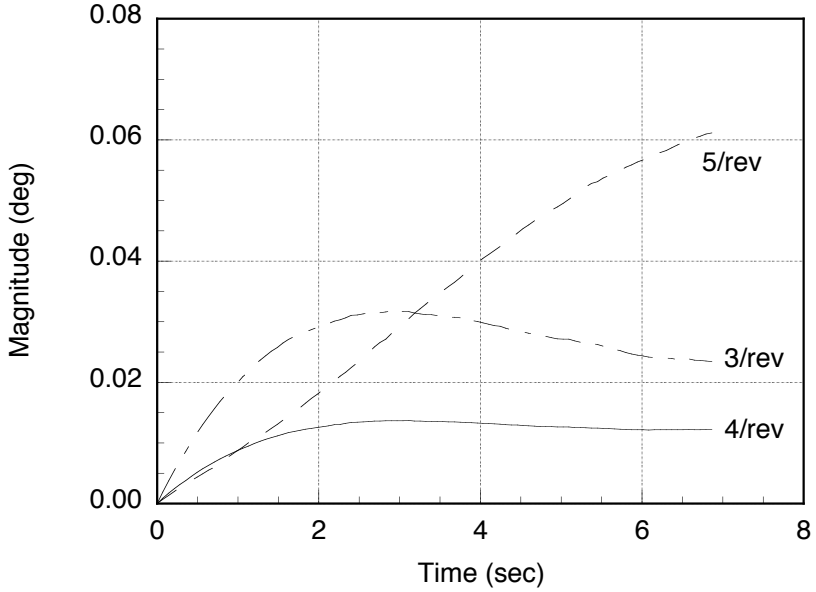

(a) Amplitude

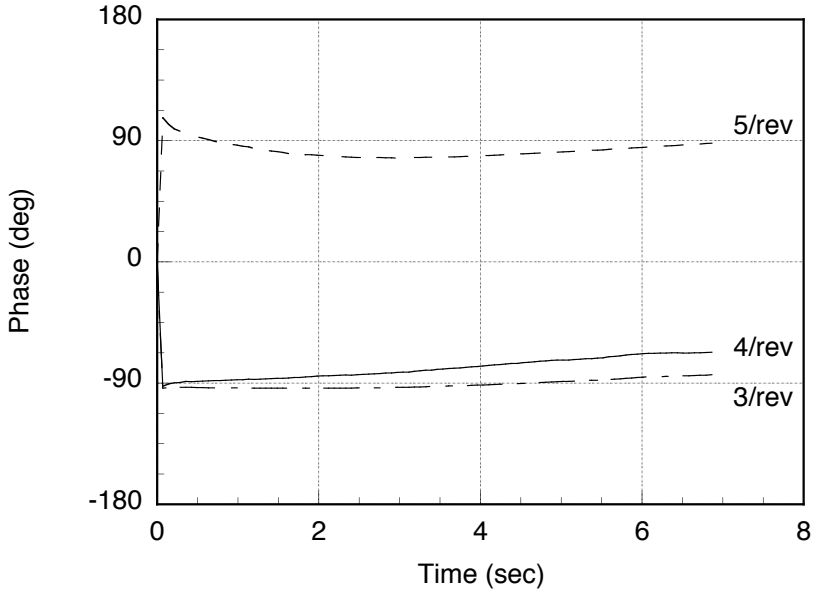

(b) Phase

Figure 4.9: IBC/HHC control inputs, 80 kn ($\mu \approx 0.188$) and r=0.0.

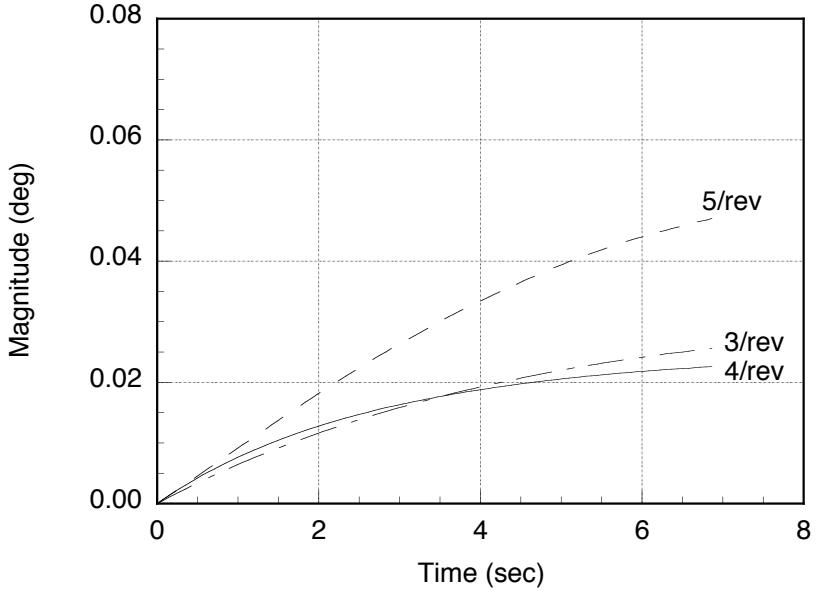

(a) Amplitude

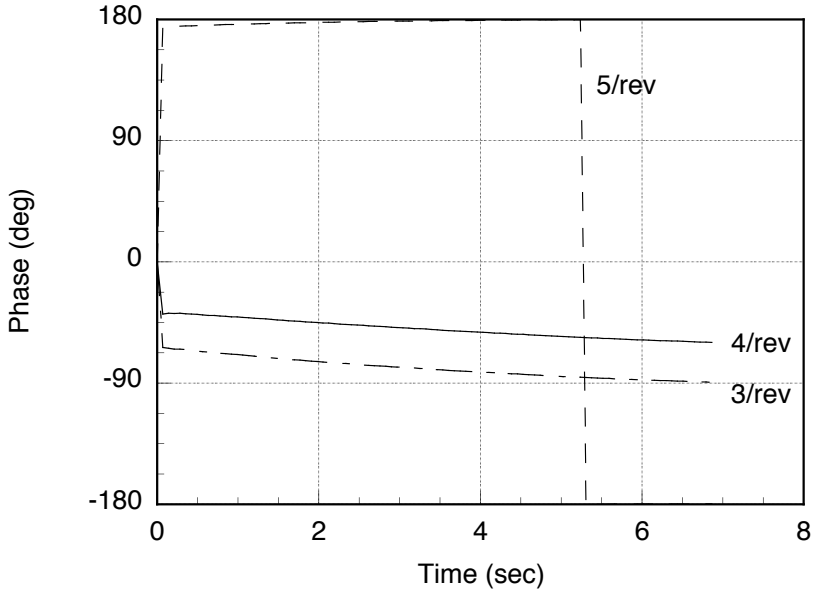

(b) Phase

Figure 4.10: IBC/HHC control inputs, 80 kn ($\mu \approx 0.188$) and r=1000.0.

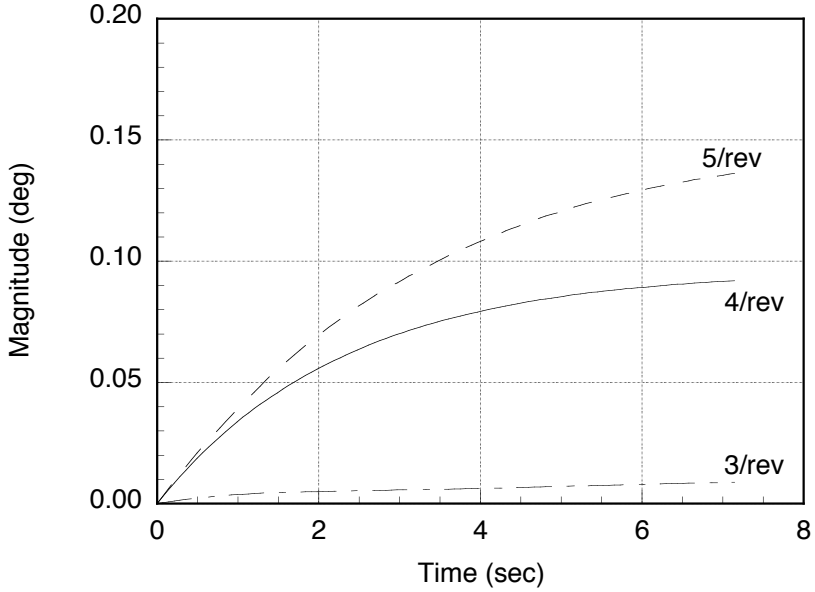

(a) Amplitude

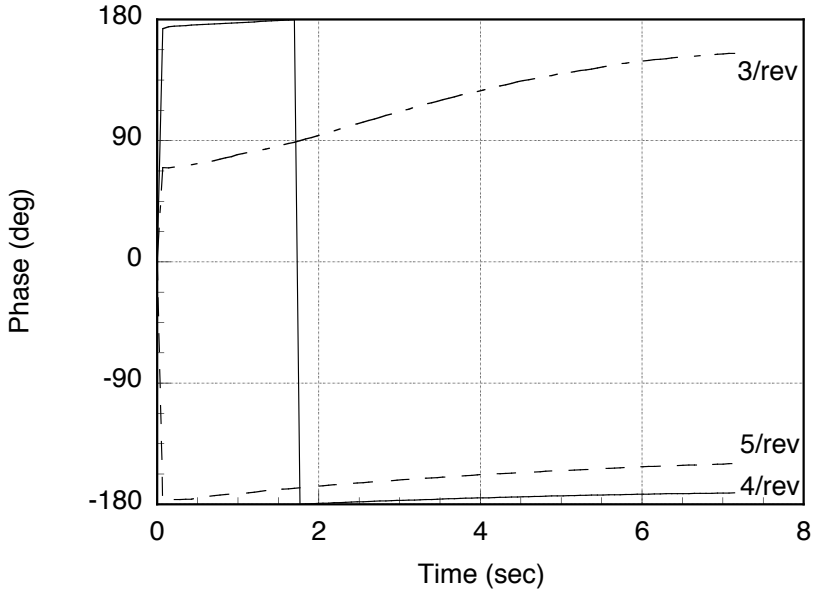

(b) Phase

Figure 4.11: IBC/HHC control inputs, 140 kn ($\mu \approx 0.330$) and r=0.0.

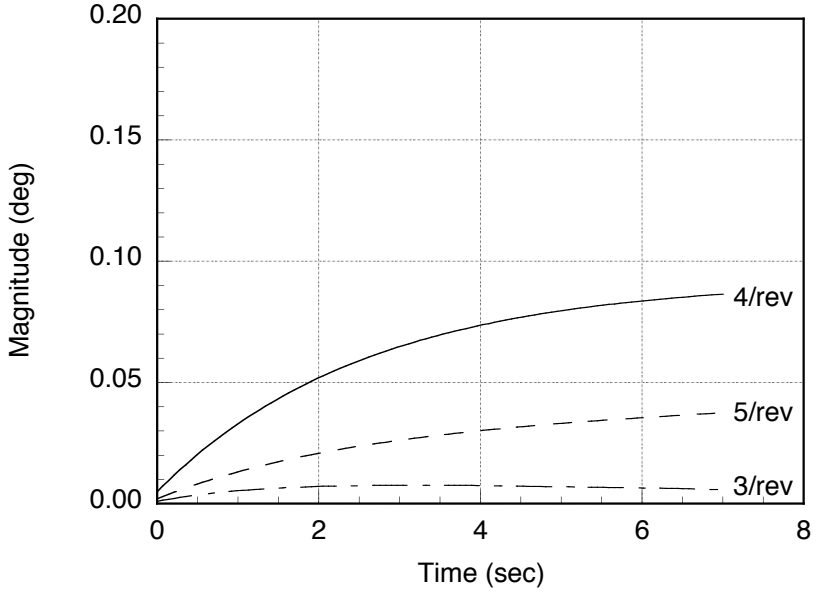

(a) Amplitude

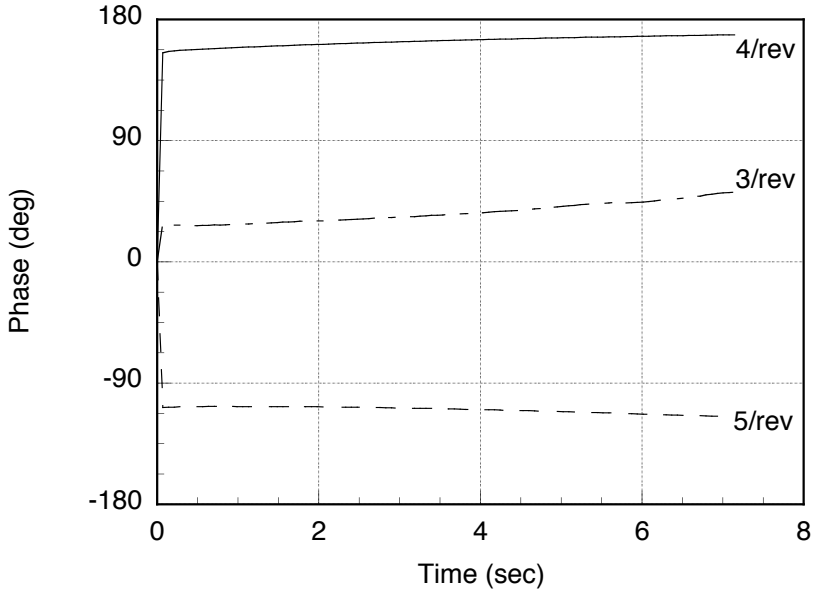

(b) Phase

Figure 4.12: IBC/HHC control inputs, 140 kn ($\mu \approx 0.330$) and r=1000.0.

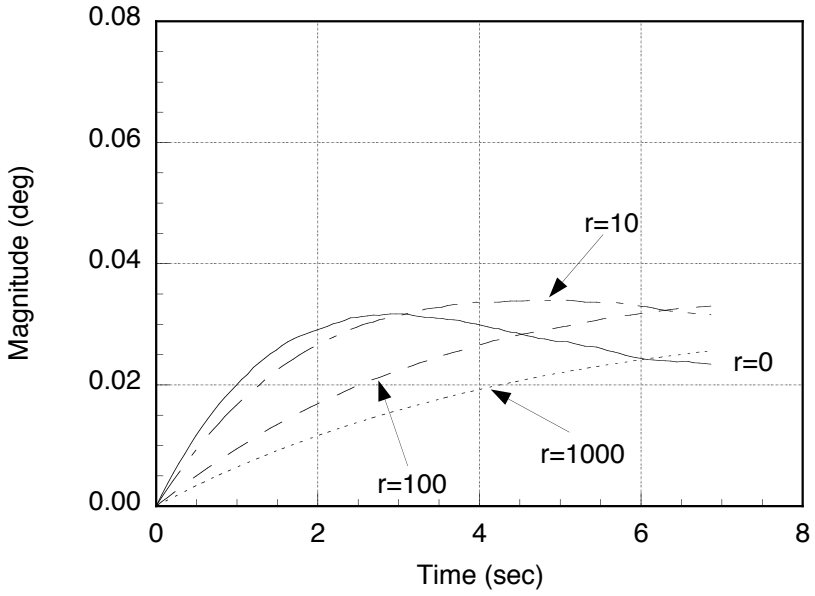

Figure 4.13: 3/rev blade pitch IBC/HHC input amplitude, 80 kn.

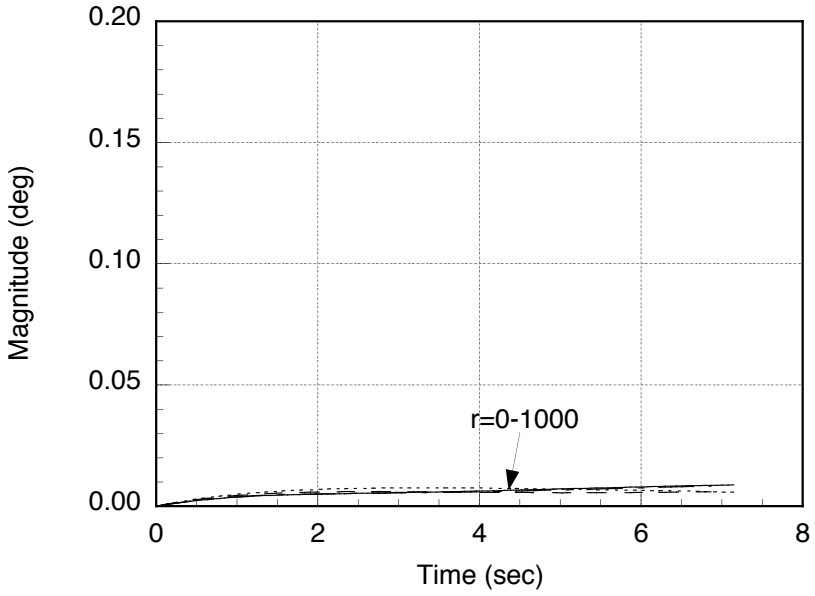

Figure 4.14: 3/rev blade pitch IBC/HHC input amplitude, 140 kn.

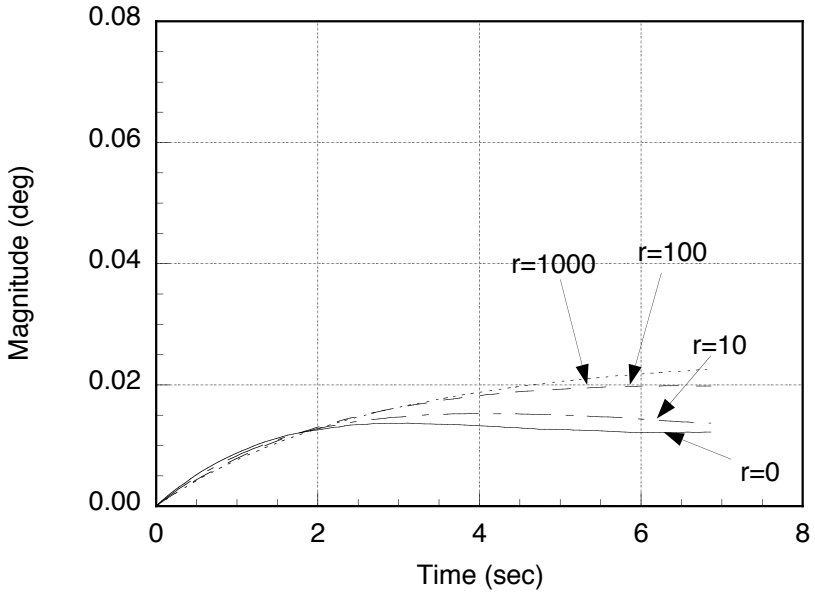

Figure 4.15: 4/rev blade pitch IBC/HHC input amplitude, 80 kn.

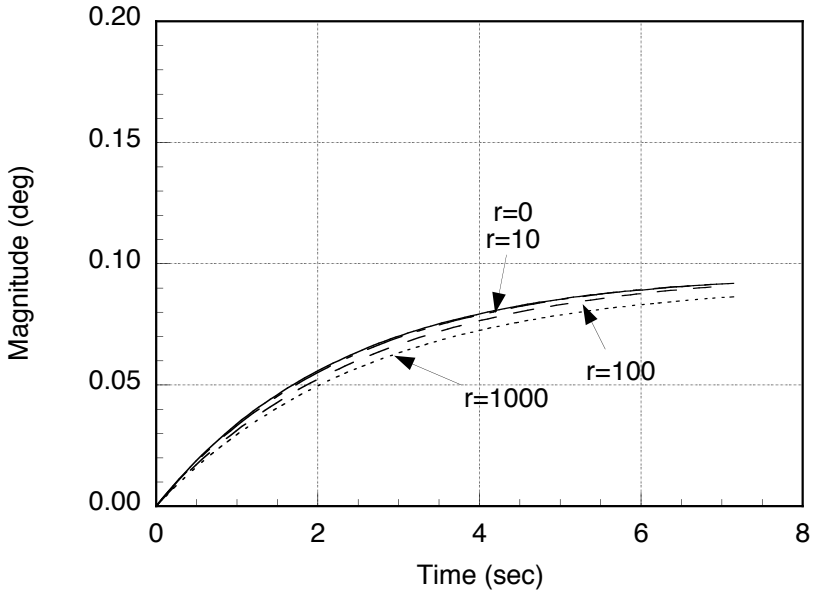

Figure 4.16: 4/rev blade pitch IBC/HHC input amplitude, 140 kn.

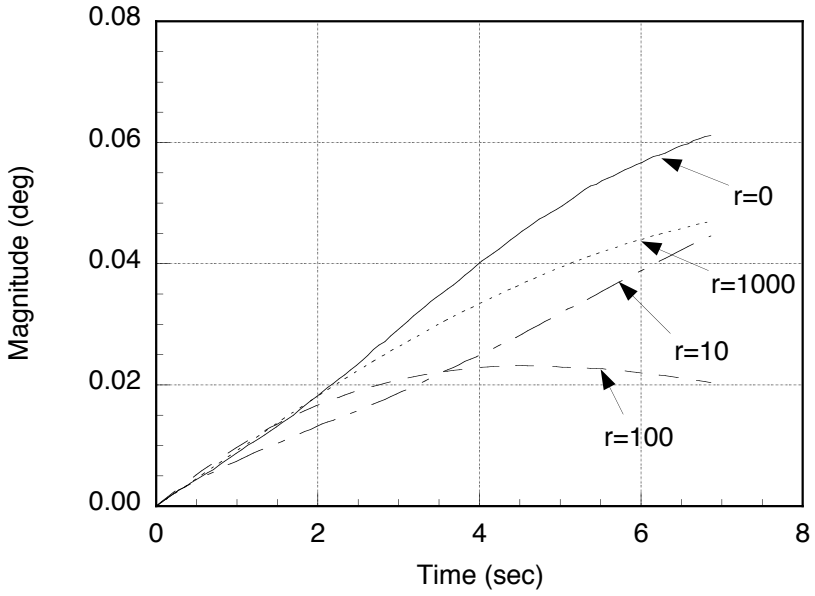

Figure 4.17: 5/rev blade pitch IBC/HHC input amplitude, 80 kn.

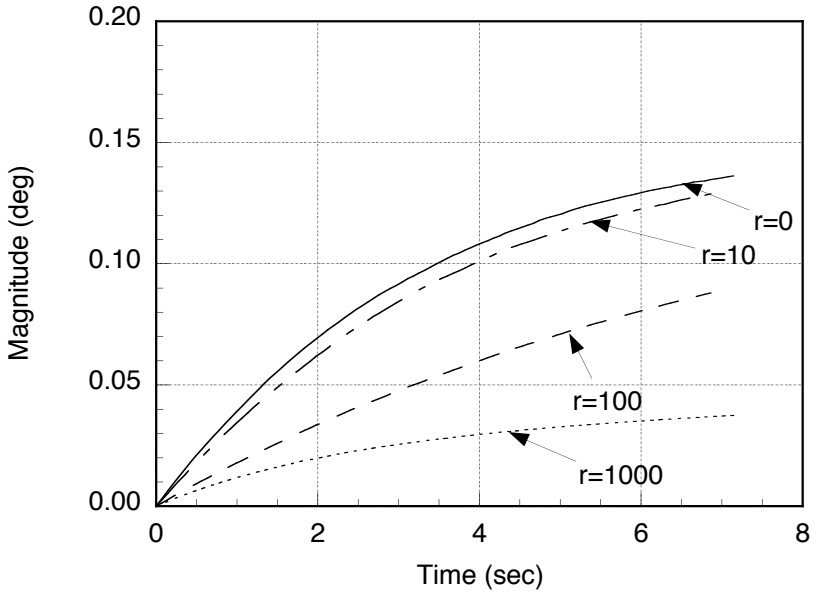

Figure 4.18: 5/rev blade pitch IBC/HHC input amplitude, 140 kn.

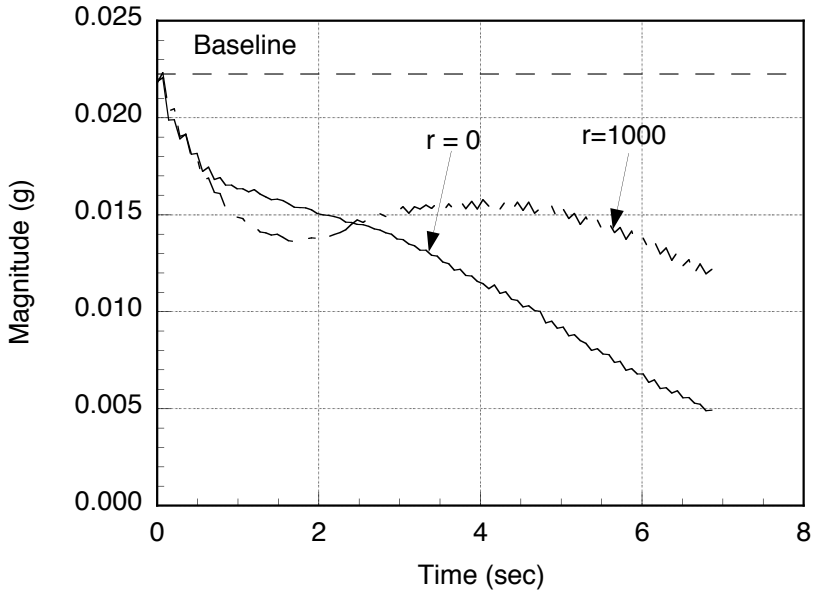

(a) Peak-to-peak

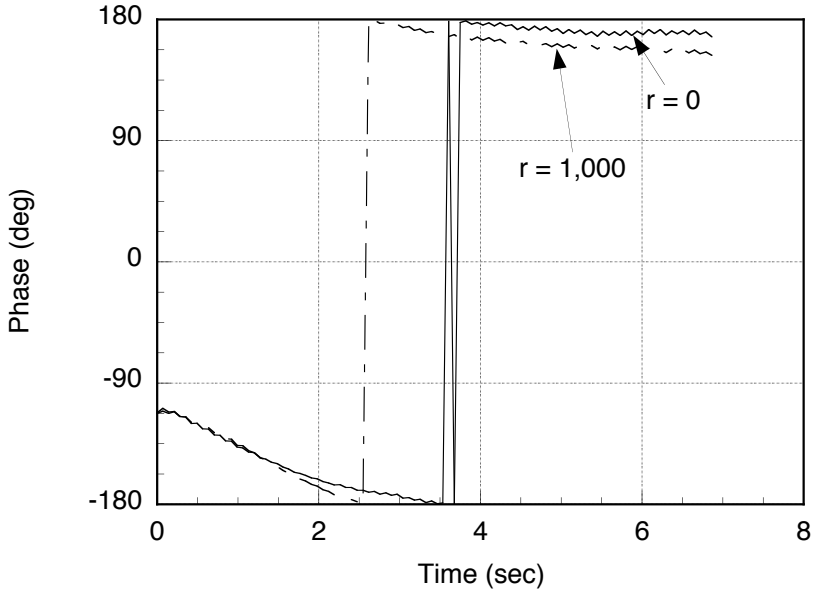

(b) Phase

Figure 4.19: 4/rev vertical accelerations of helicopter for 170 kn (μ = 0.4).

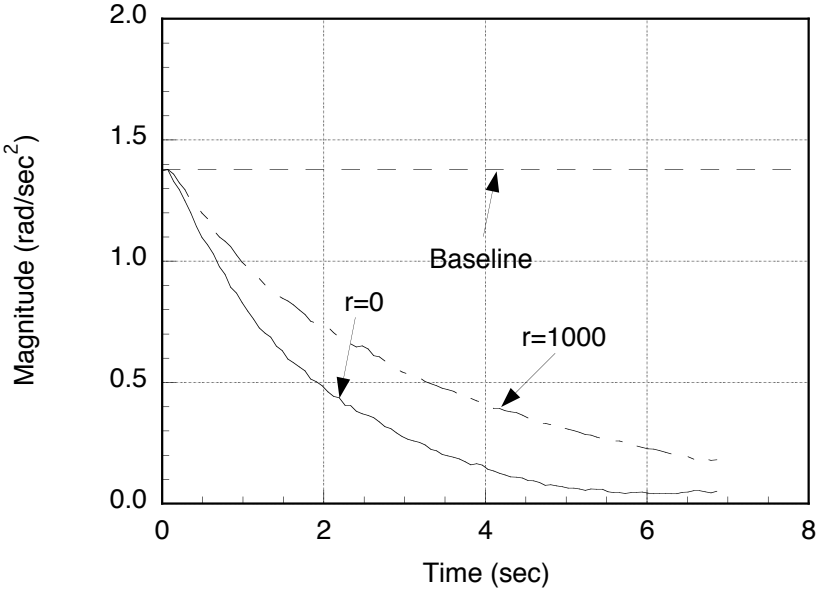

(a) Peak-to-peak

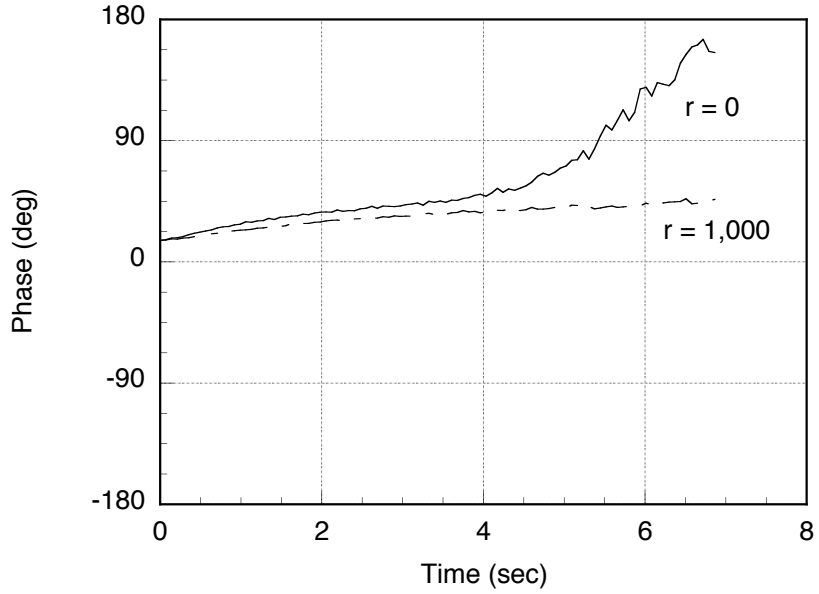

(b) Phase

Figure 4.20: 4/rev roll accelerations of helicopter for 170 kn (μ = 0.4).

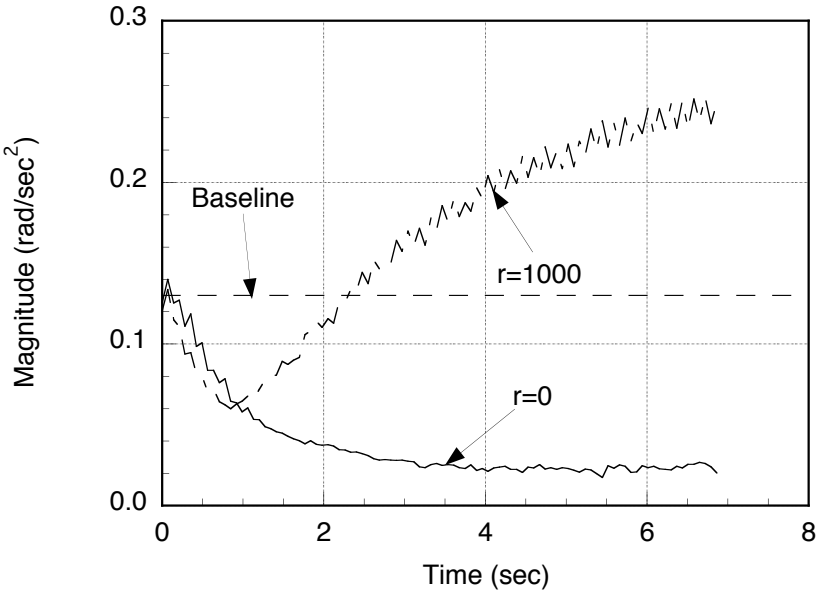

(a) Peak-to-peak

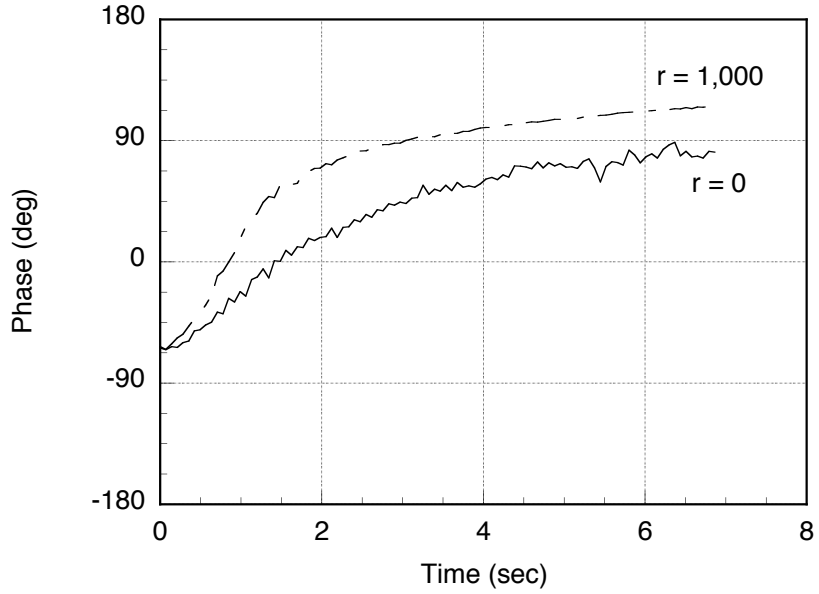

(b) Phase

Figure 4.21: 4/rev pitch accelerations of helicopter for 170 kn (μ = 0.4).

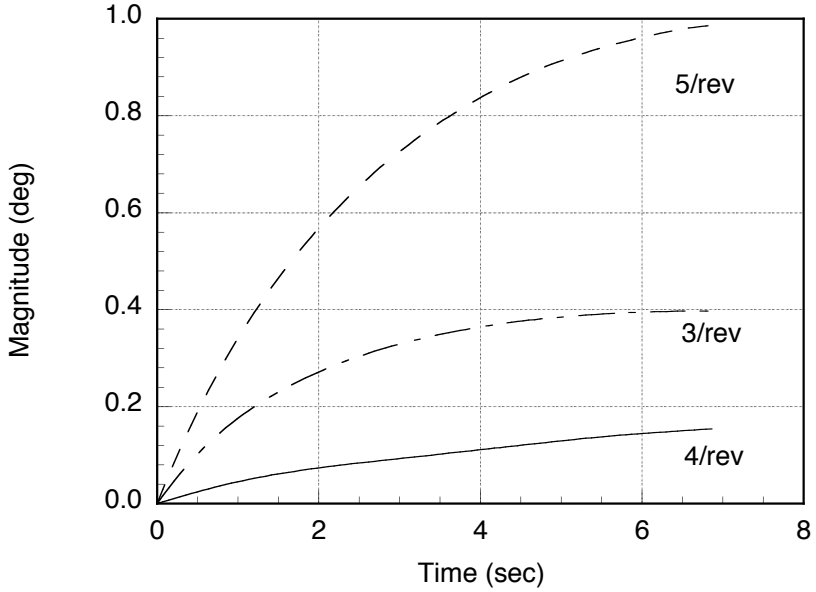

(a) Amplitude

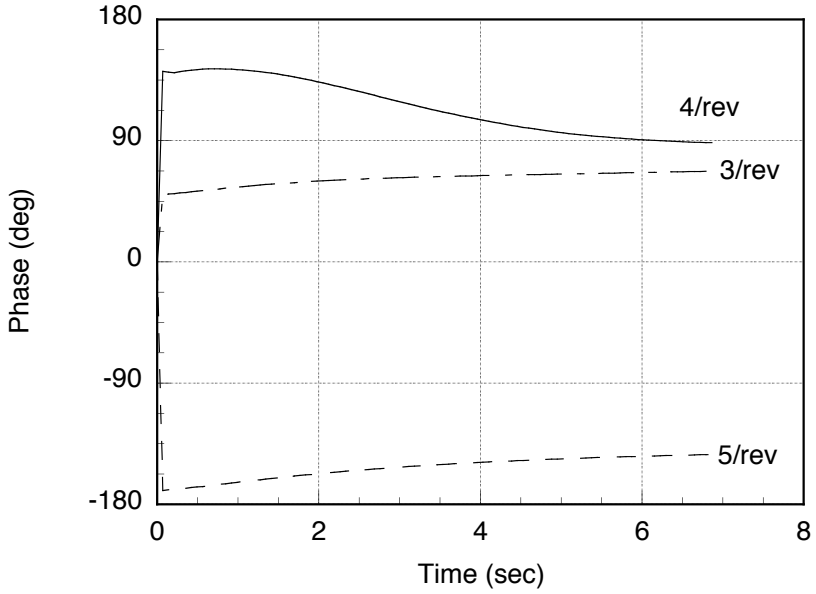

(b) Phase

Figure 4.22: IBC/HHC control inputs, 170 kn ($\mu \approx 0.4$) and r=0.0.

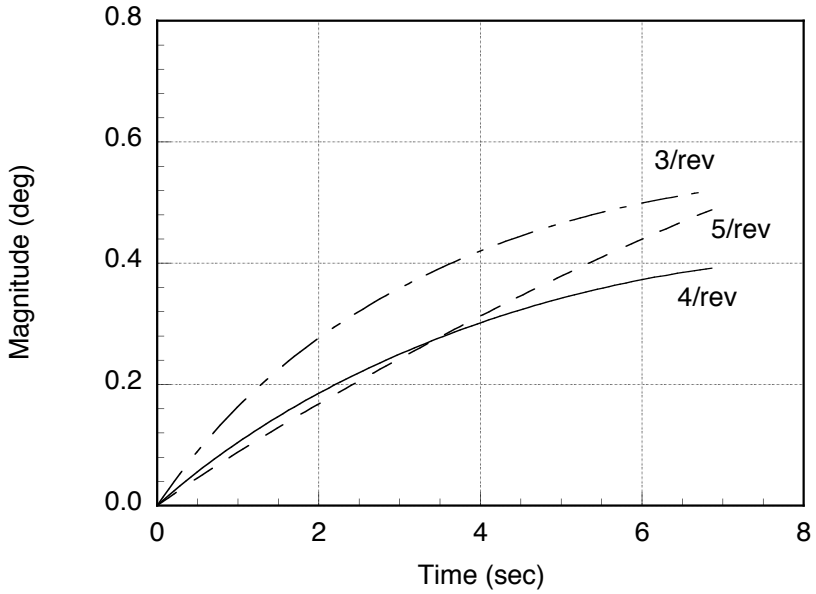

(a) Amplitude

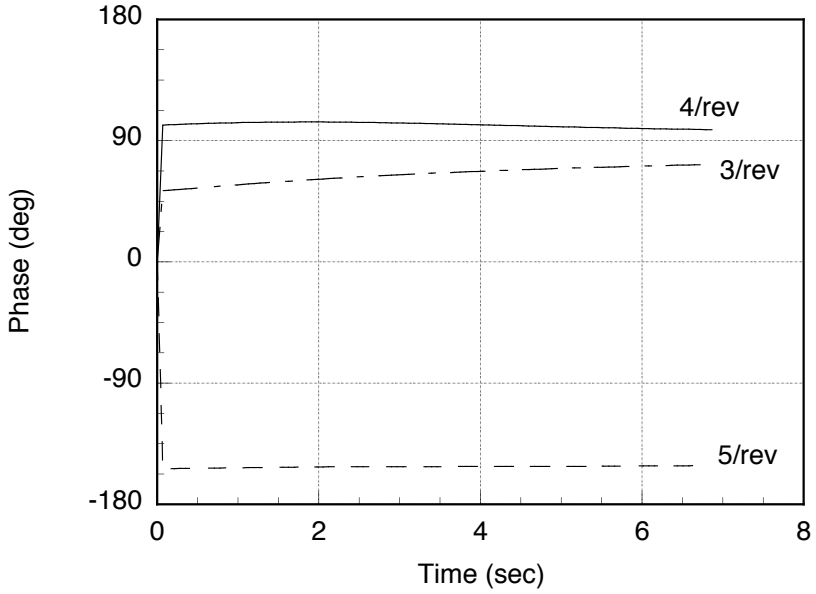

(b) Phase

Figure 4.23: IBC/HHC control inputs, 170 kn ($\mu \approx 0.4$) and r=1,000.0.

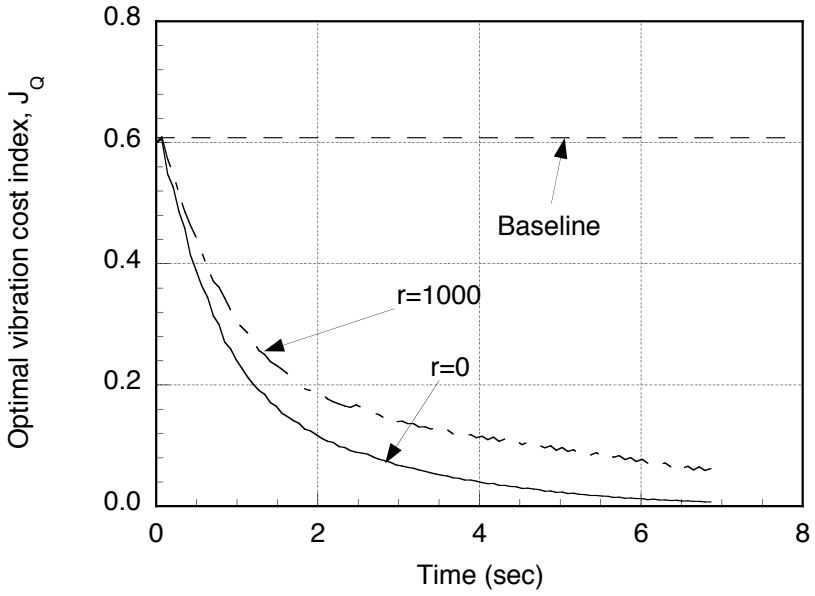

Figure 4.24: Optimal vibration cost index for $V = 170$ kn ($\mu = 0.4$)

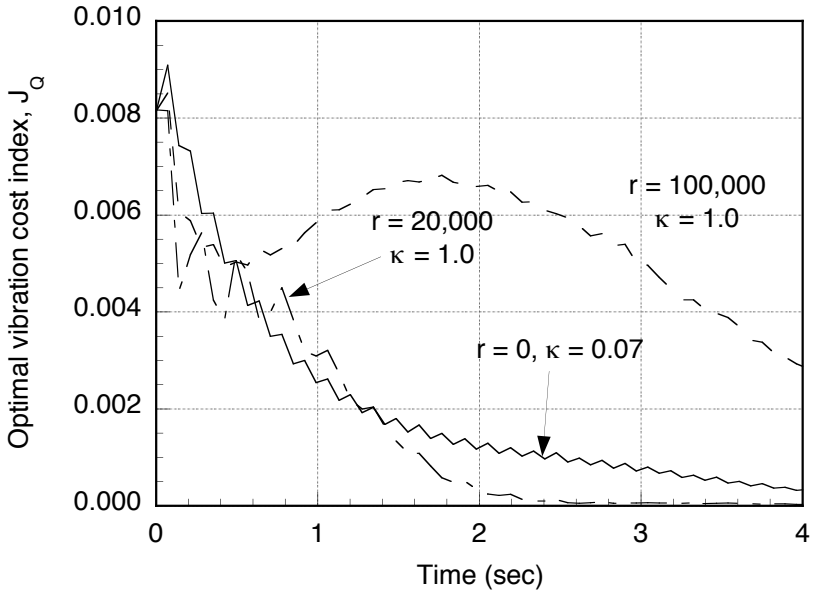

Figure 4.25: Optimal vibration cost index with different feedback gain configurations for $V = 80$ kn ($\mu = 0.188$)

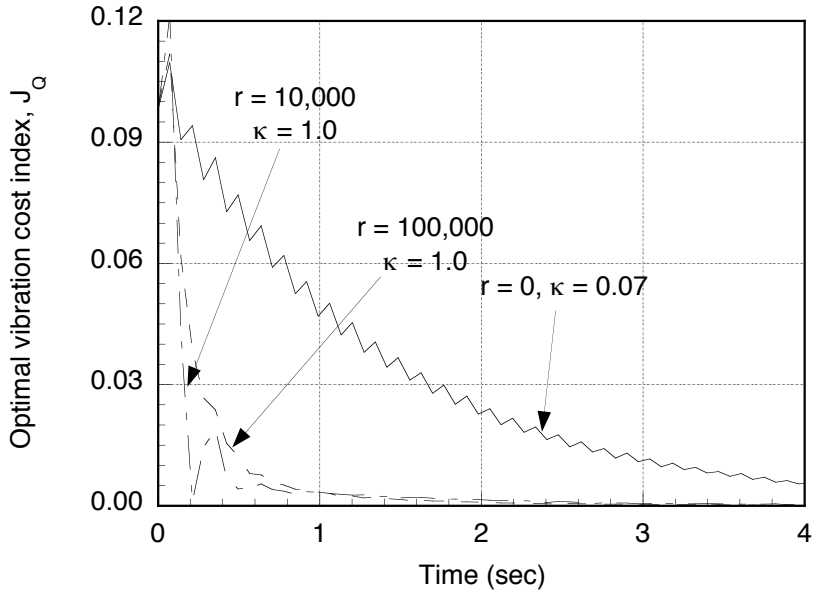

Figure 4.26: Optimal vibration cost index with different feedback gain configurations for $V = 140$ kn ($\mu = 0.33$)

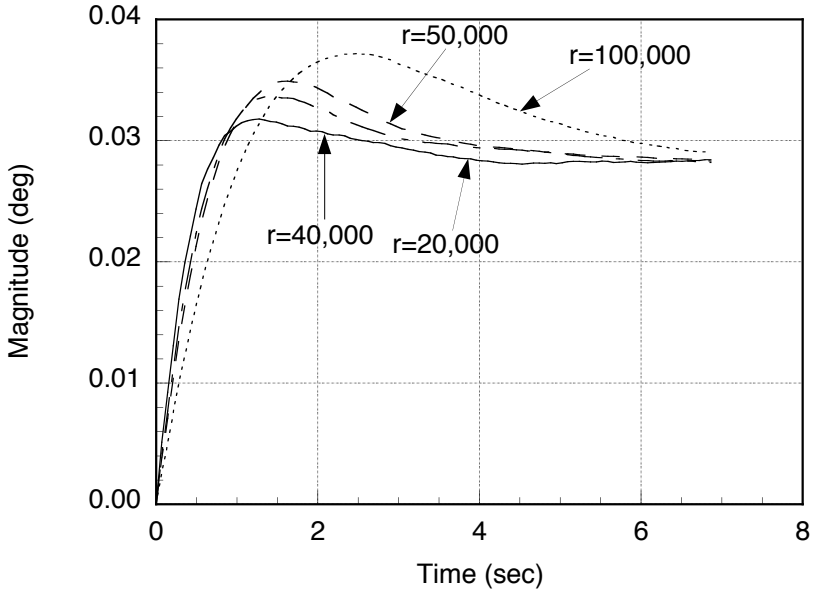

Figure 4.27: 3/rev blade pitch IBC/HHC input amplitude for $\kappa = 1.0$, $V = 80$ kn ($\mu = 0.19$)

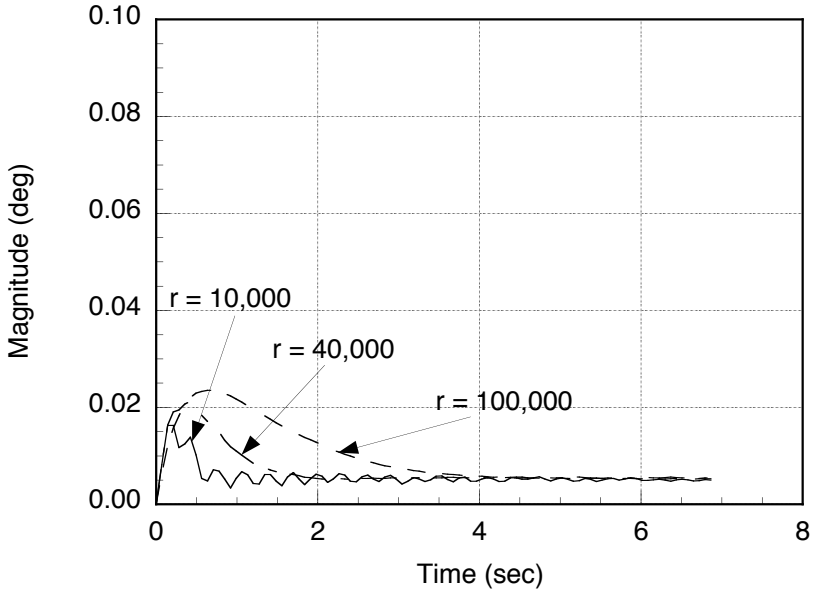

Figure 4.28: 3/rev blade pitch IBC/HHC input amplitude for $\kappa = 1.0$, $V = 140$ kn ($\mu = 0.33$)

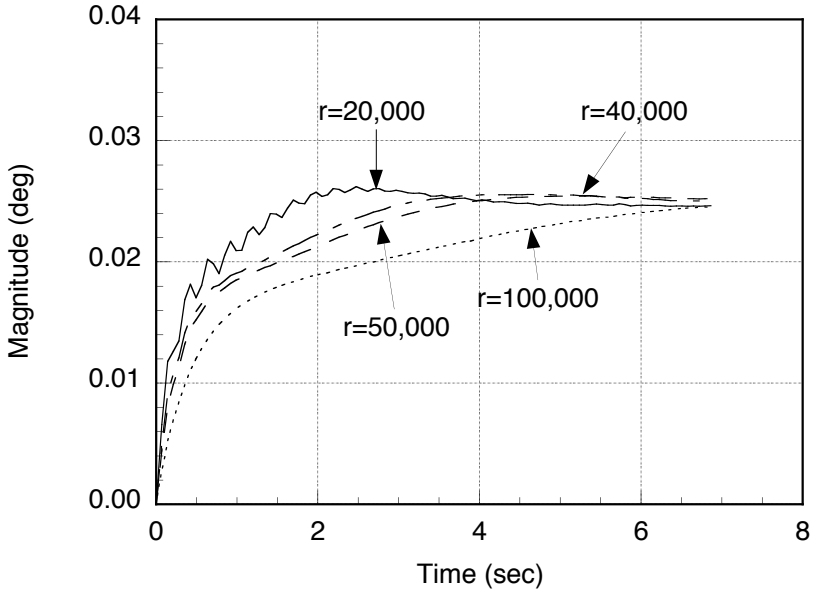

Figure 4.29: 4/rev blade pitch IBC/HHC input amplitude for $\kappa = 1.0$, $V = 80$ kn ($\mu = 0.19$)

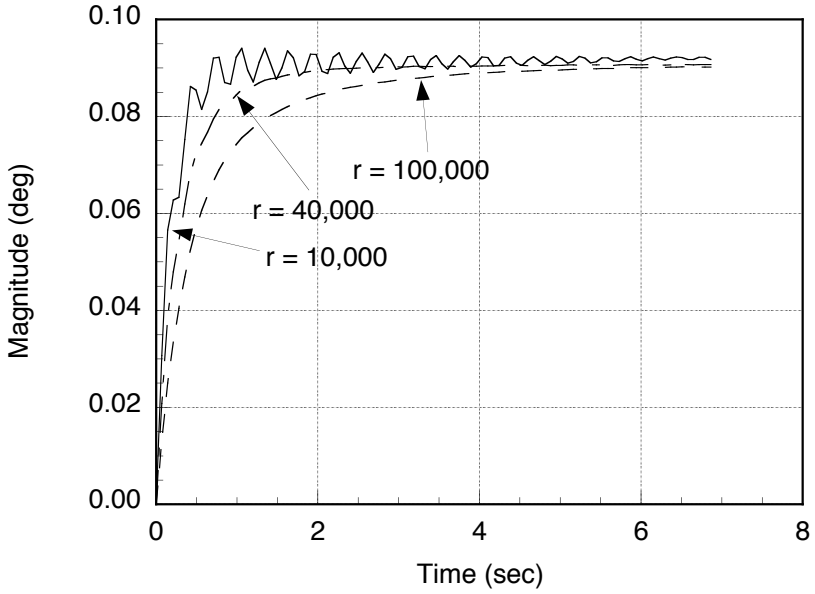

Figure 4.30: 4/rev blade pitch IBC/HHC input amplitude for $\kappa = 1.0$, $V = 140$ kn ($\mu = 0.33$)

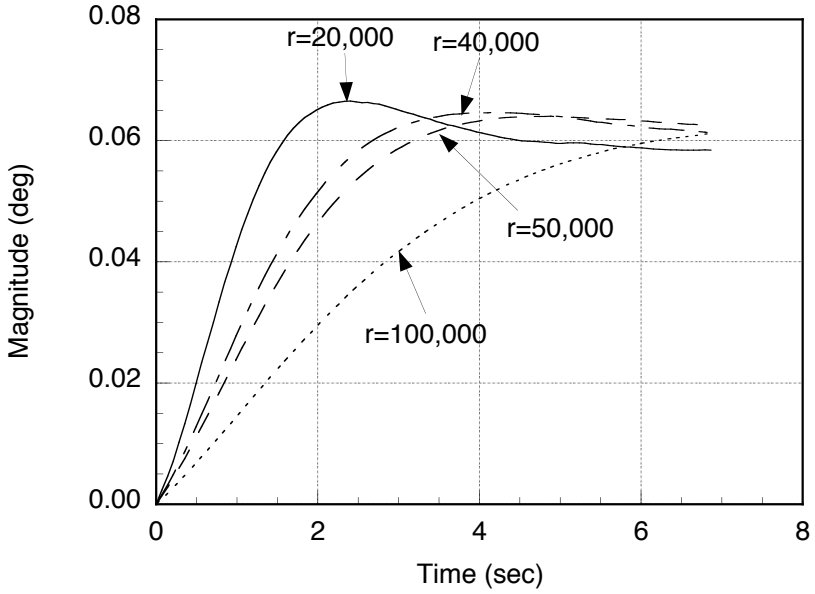

Figure 4.31: 5/rev blade pitch IBC/HHC input amplitude for $\kappa = 1.0$, $V = 80$ kn ($\mu = 0.19$)

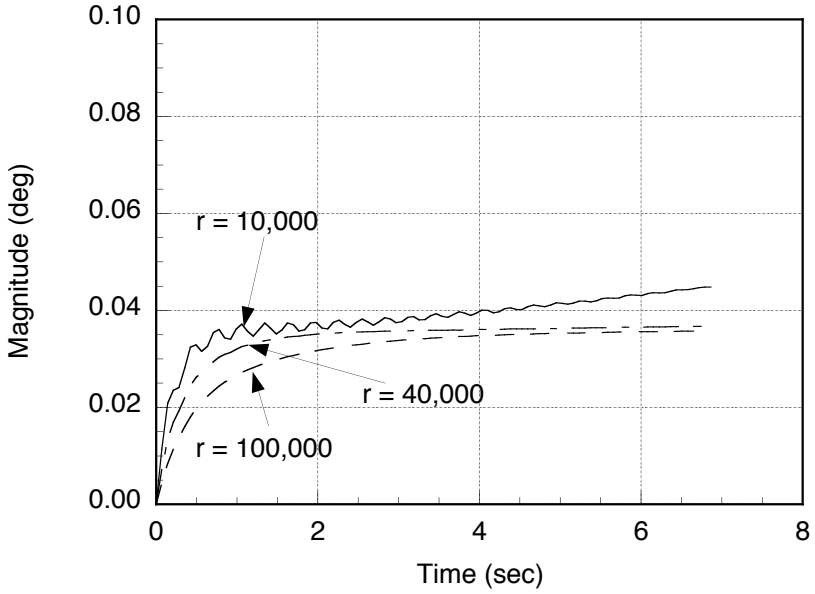

Figure 4.32: 5/rev blade pitch IBC/HHC input amplitude for $\kappa = 1.0$, $V = 140$ kn ($\mu = 0.33$)

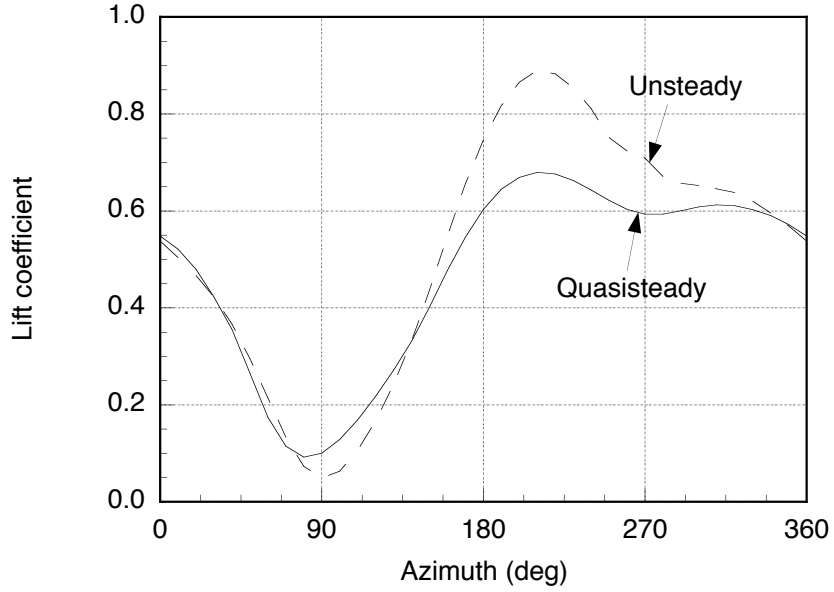

(a) Lift coefficient

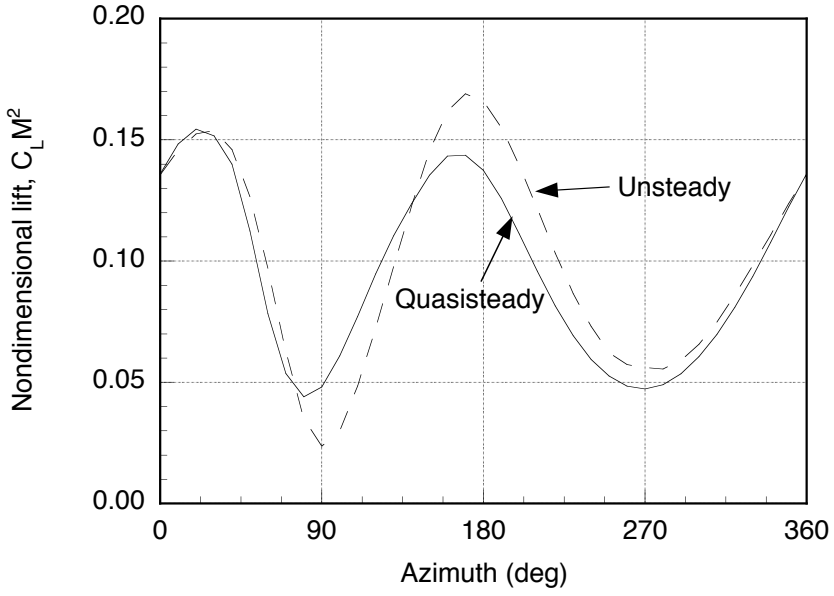

(b) Non-dimensional lift

Figure 4.33: Unsteady vs. quasisteady lift coefficients at 75% blade span vs. azimuth ($\mu = 0.33$).

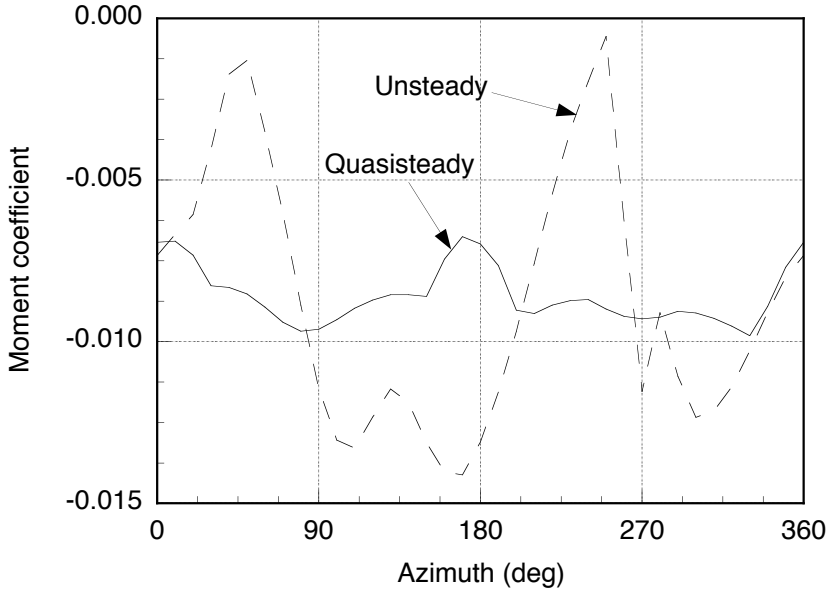

(a) Pitching moment coefficient

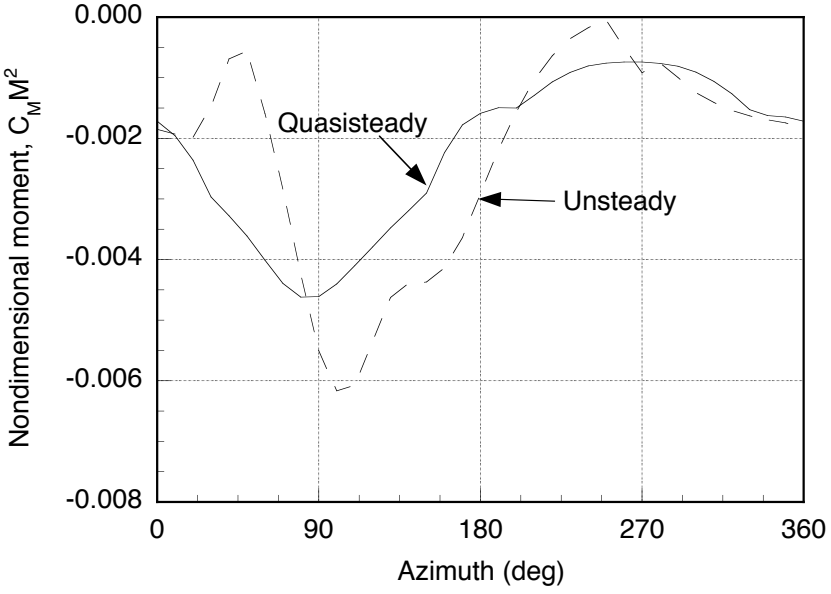

(b) Non-dimensional moment

Figure 4.34: Unsteady vs. quasisteady moment coefficients at 75% blade span vs. azimuth ($\mu = 0.33$).

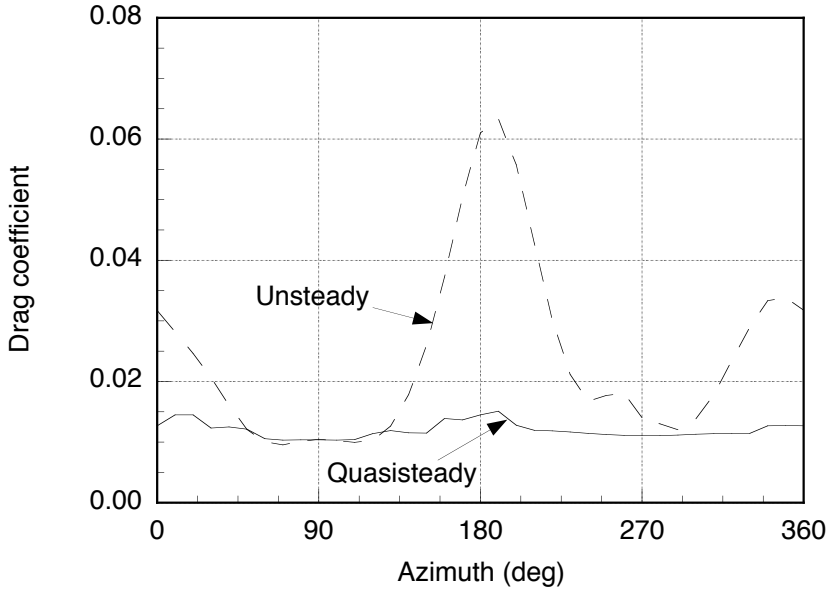

(a) Drag coefficient

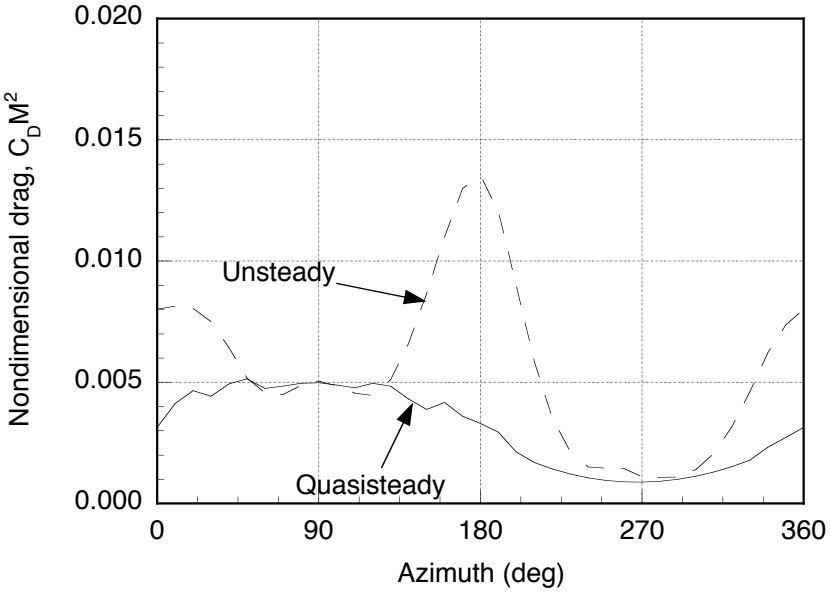

(b) Non-dimensional drag

Figure 4.35: Unsteady vs. quasisteady drag coefficients at 75% blade span vs. azimuth ($\mu = 0.33$).

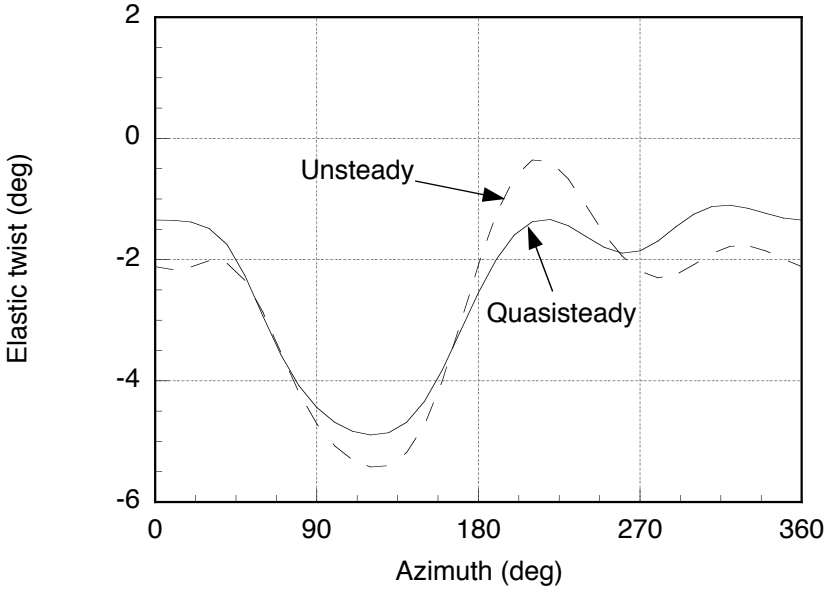

(a) Elastic twist

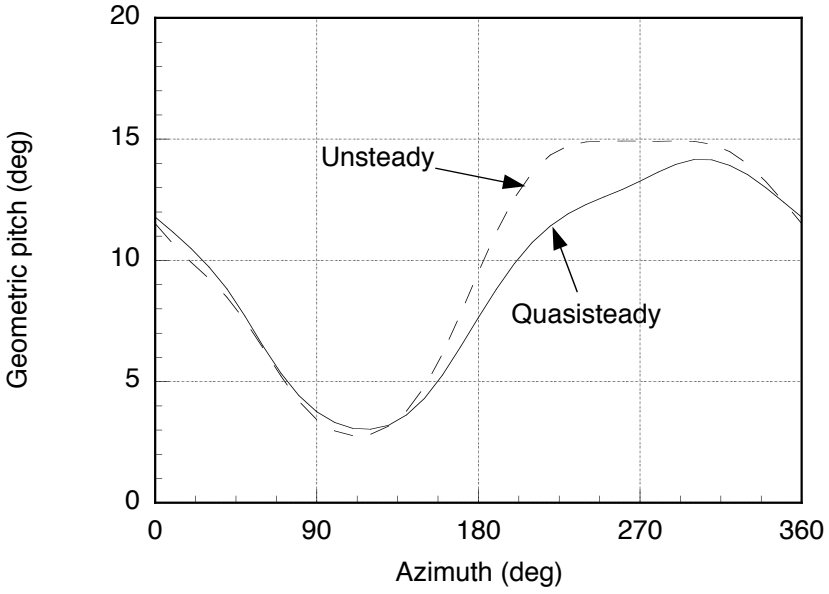

(b) Geometric pitch

Figure 4.36: Geometric blade section pitch at 75% blade span for unsteady and quasisteady aerodynamics (μ = 0.33).

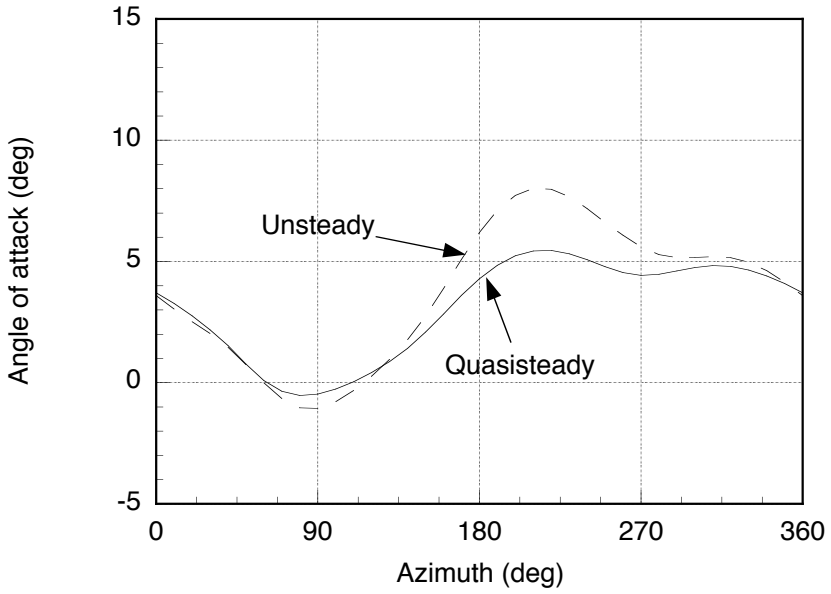

Figure 4.37: Angle of attack at 75% blade span for unsteady and quasisteady aerodynamics ($\mu = 0.33$).

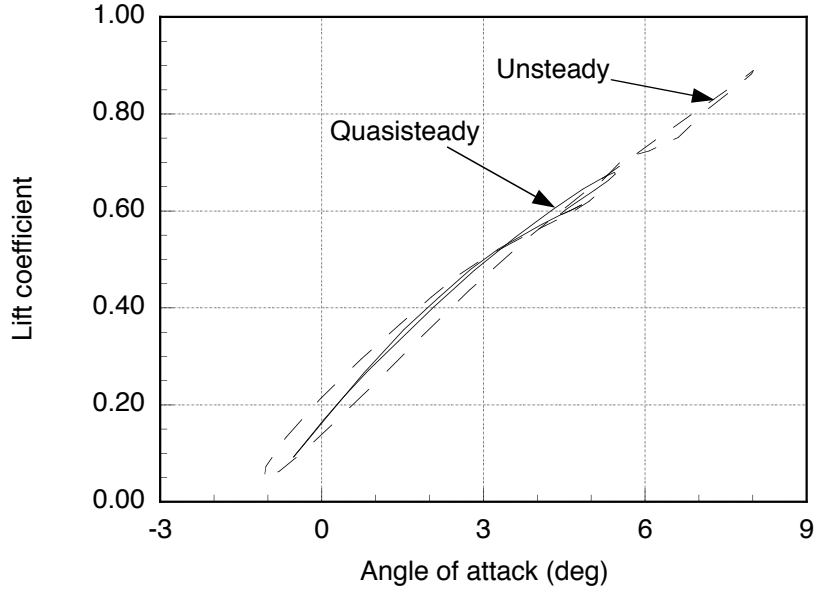

(a) Lift coefficient

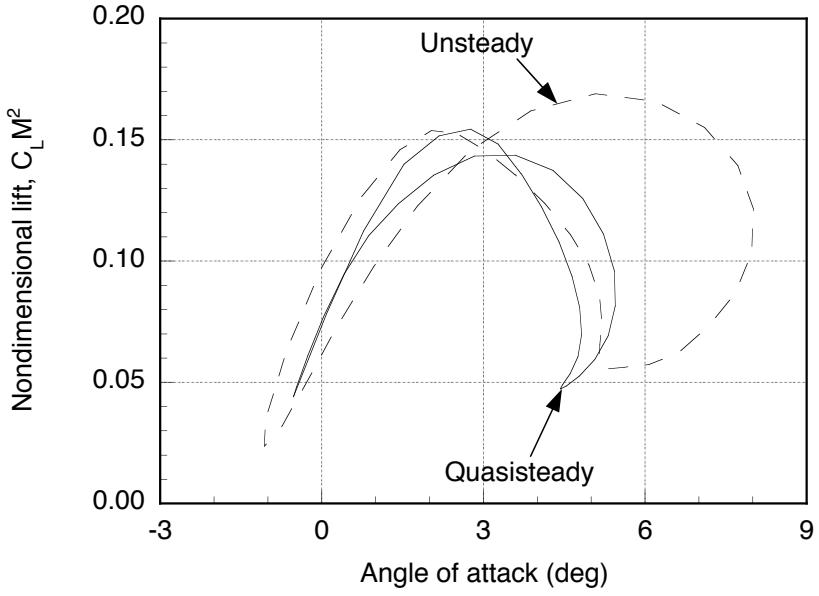

(b) Non-dimensional lift

Figure 4.38: Unsteady vs. quasisteady lift coefficients at 75% blade span vs. angle of attack ($\mu = 0.33$).

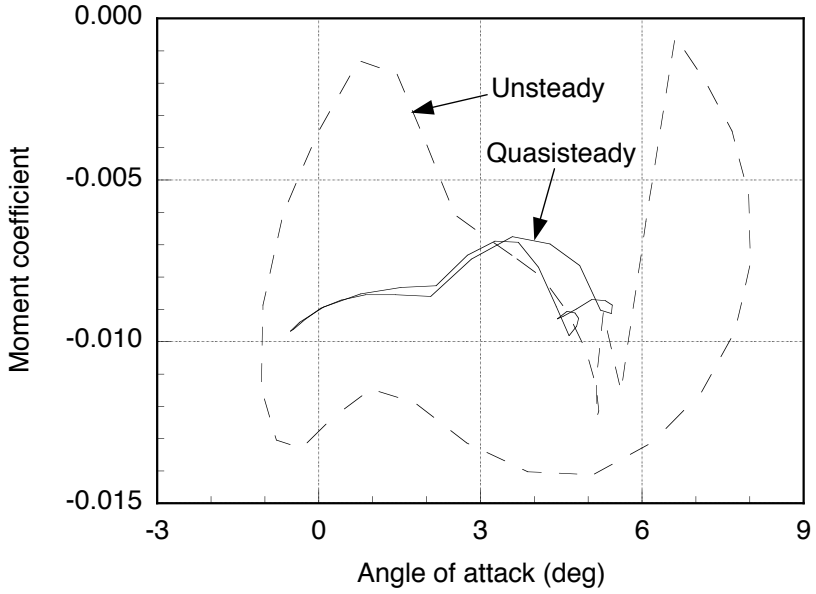

(a) Pitching moment coefficient

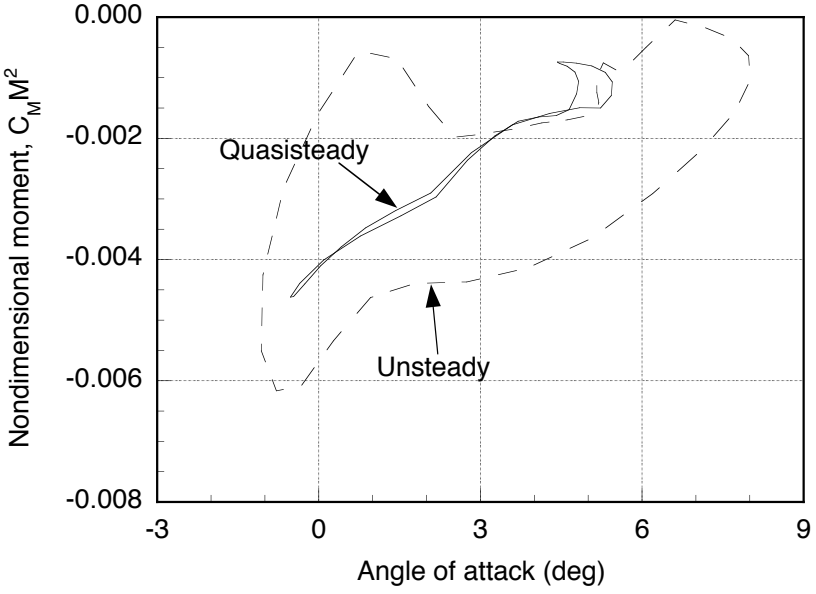

(b) Non-dimensional moment

Figure 4.39: Unsteady vs. quasisteady moment coefficients at 75% blade span vs. angle of attack (μ = 0.33).

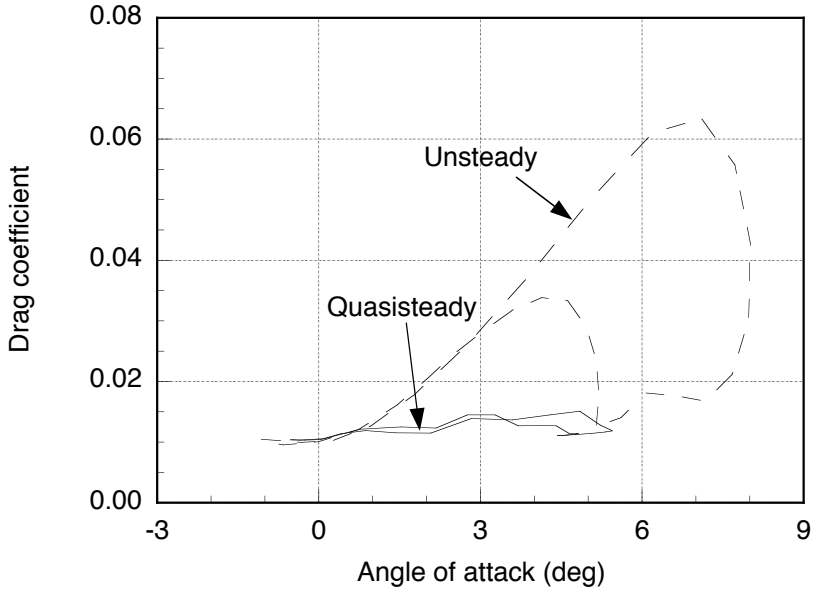

(a) Drag coefficient

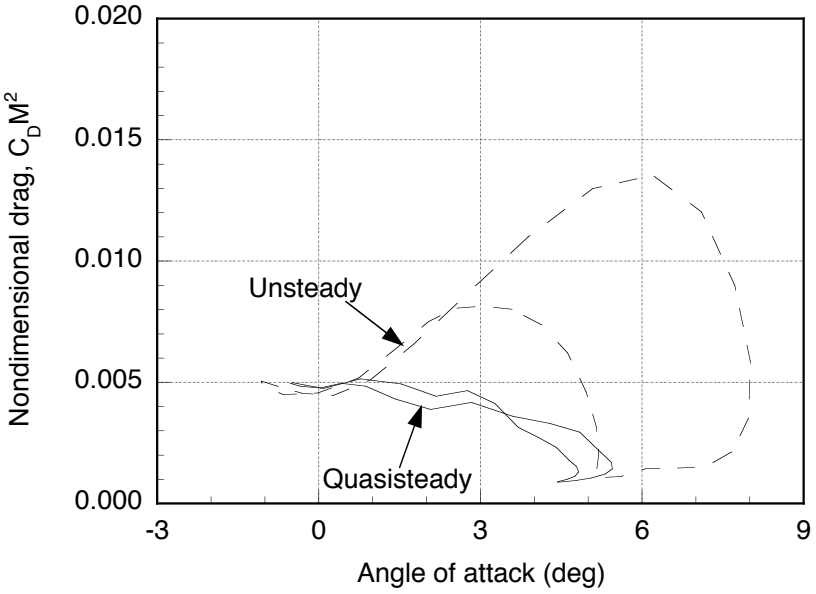

(b) Non-dimensional drag

Figure 4.40: Unsteady vs. quasisteady drag coefficients at 75% blade span vs. angle of attack ($\mu = 0.33$).

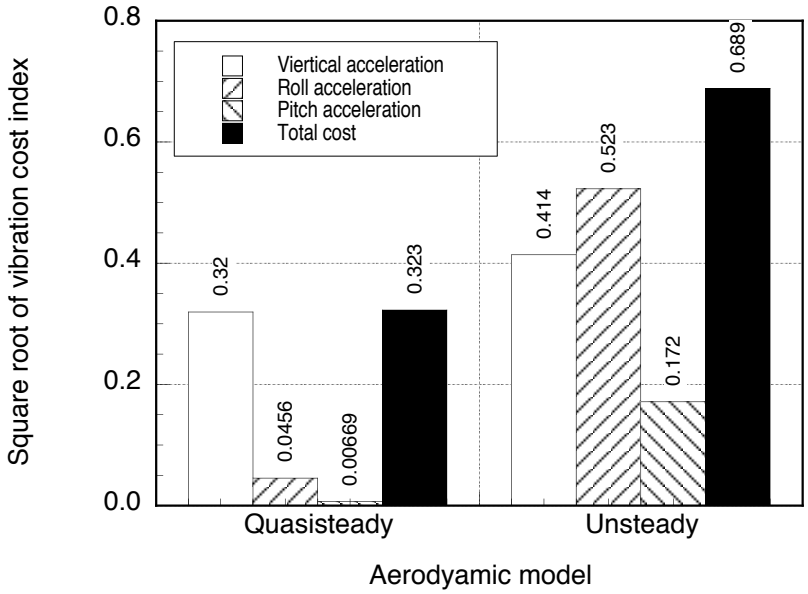

Figure 4.41: Square root of baseline vibration cost index for unsteady and quasisteady aerodynamics ($\mu = 0.33$).

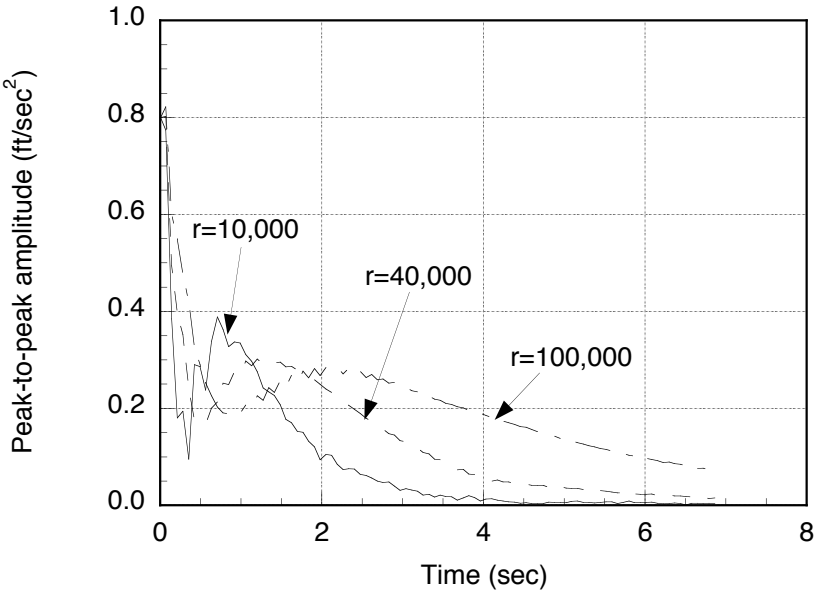

(a) Peak-to-peak

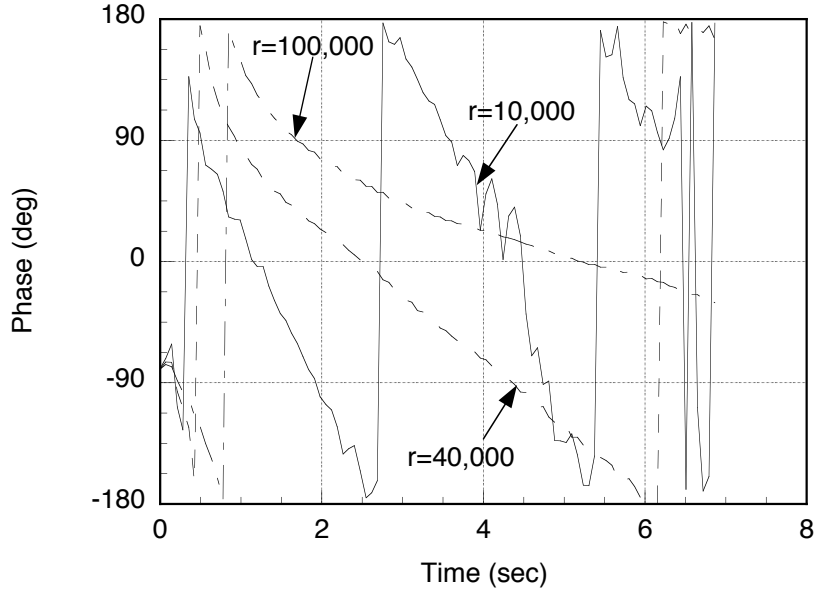

(b) Phase

Figure 4.42: 4/rev fuselage vertical accelerations at helicopter CG with unsteady aerodynamics (μ = 0.33).

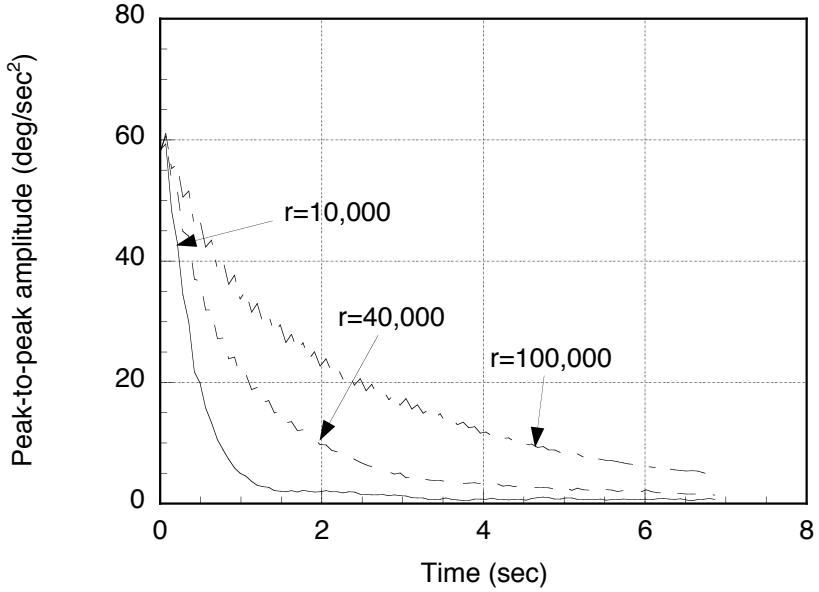

(a) Peak-to-peak

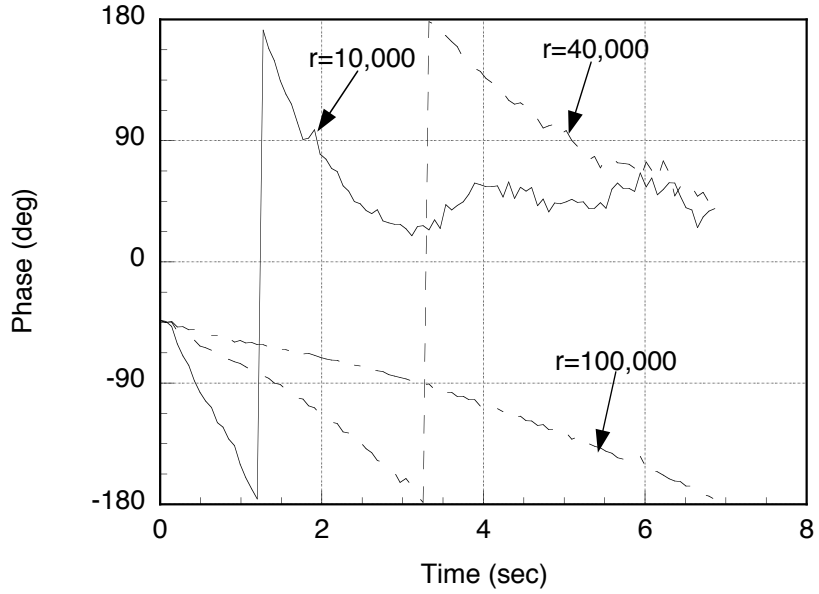

(b) Phase

Figure 4.43: 4/rev fuselage roll accelerations with unsteady aerodynamics (μ = 0.33).

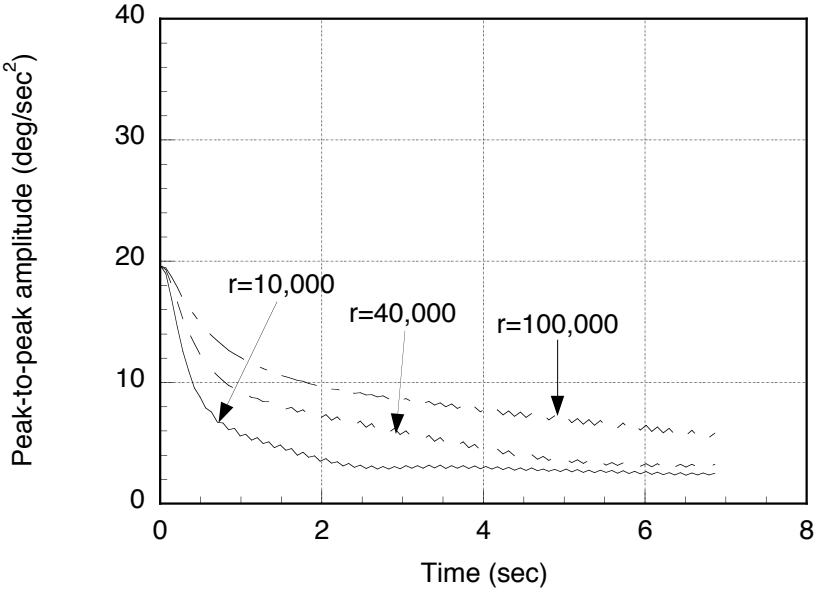

(a) Peak-to-peak

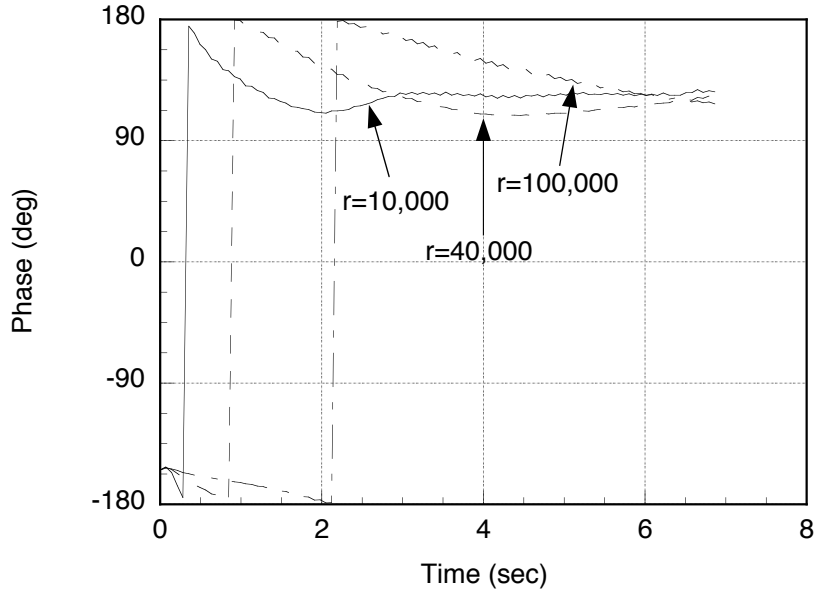

(b) Phase

Figure 4.44: 4/rev fuselage pitch accelerations with unsteady aerodynamics (μ = 0.33).

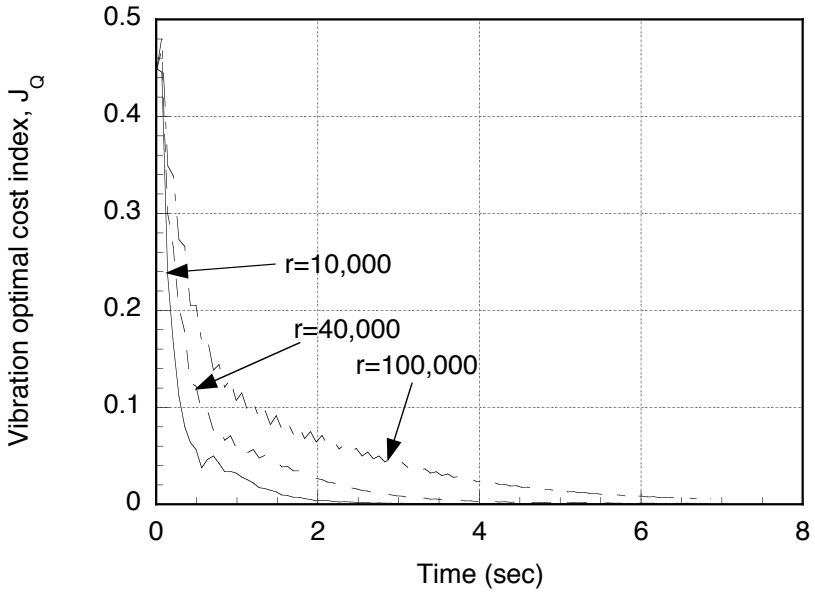

Figure 4.45: Optimal vibration cost index for different control effort parameters (μ = 0.33).

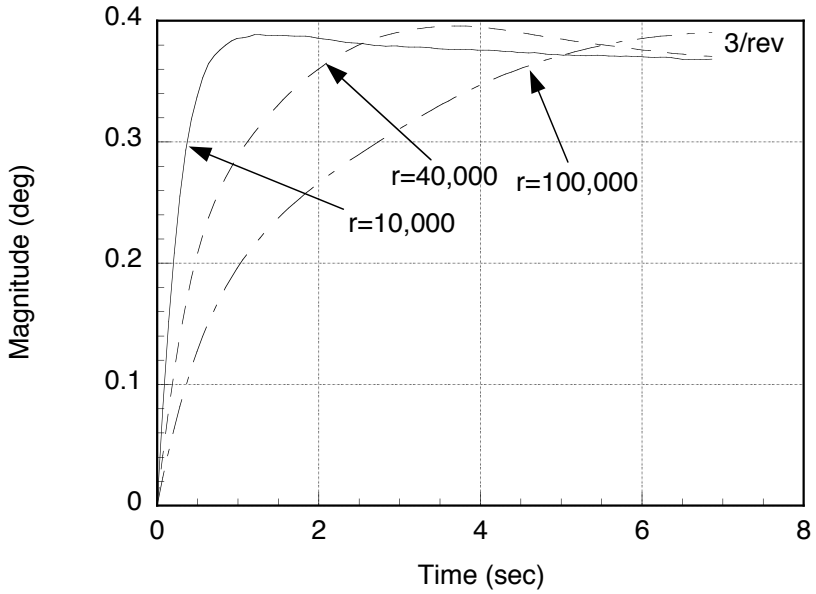

(a) Amplitude

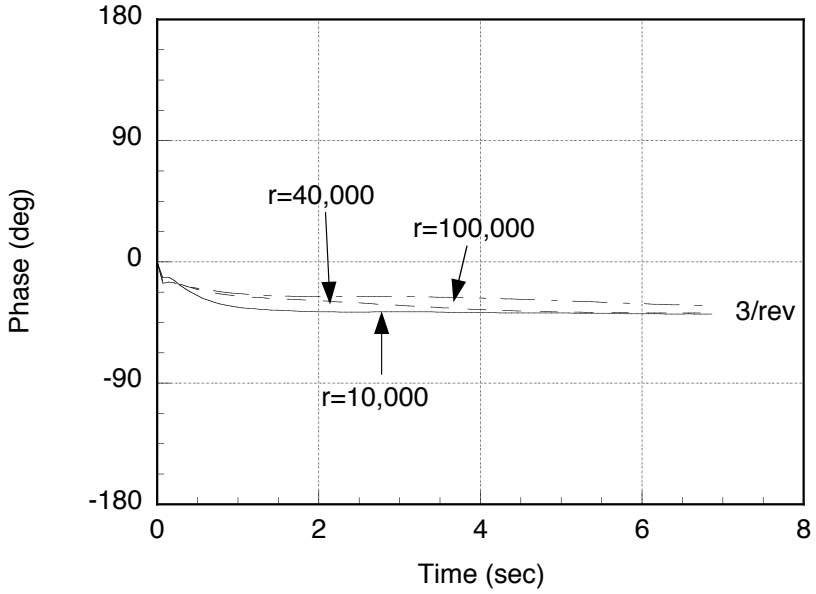

(b) Phase

Figure 4.46: 3/rev blade pitch IBC/HHC input for unsteady aerodynamics, 140 kn.

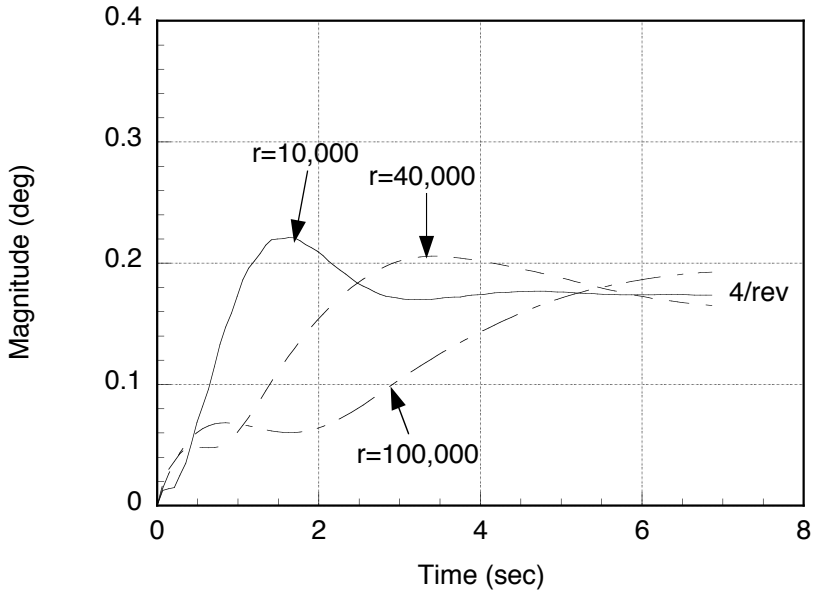

(a) Amplitude

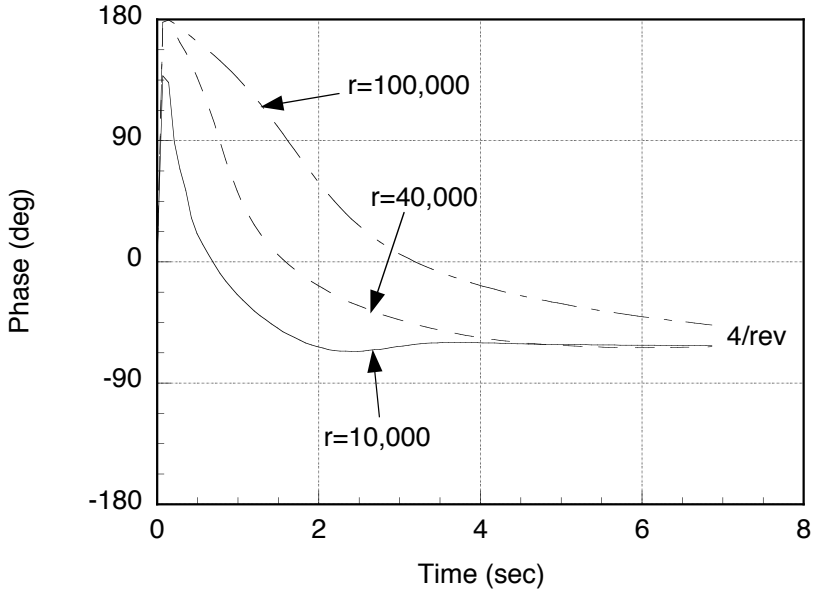

(b) Phase

Figure 4.47: 4/rev blade pitch IBC/HHC input for unsteady aerodynamics, 140 kn.

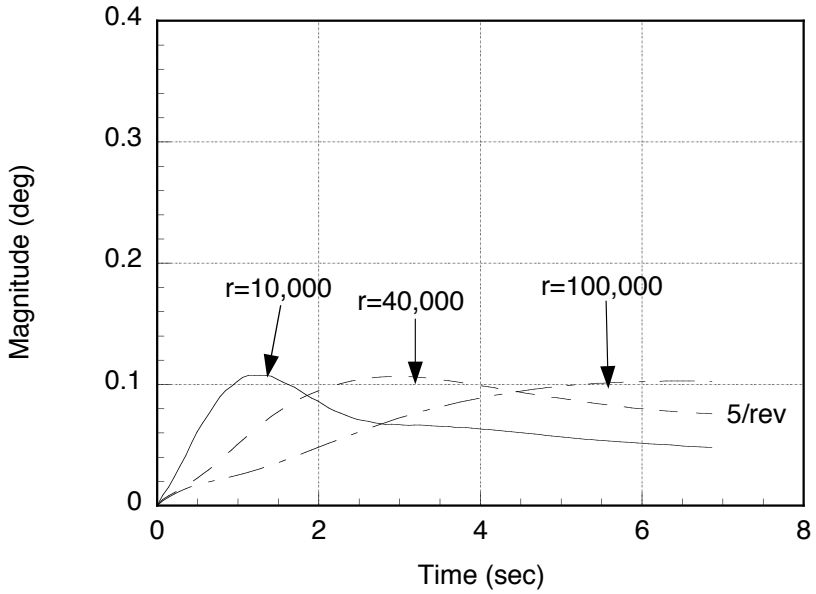

(a) Amplitude

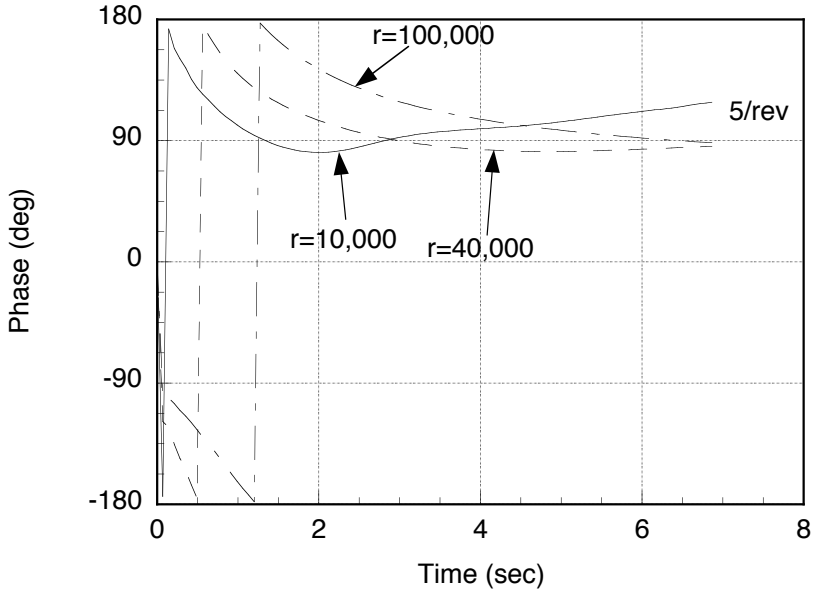

(b) Phase

Figure 4.48: 5/rev blade pitch IBC/HHC input for unsteady aerodynamics, 140 kn.

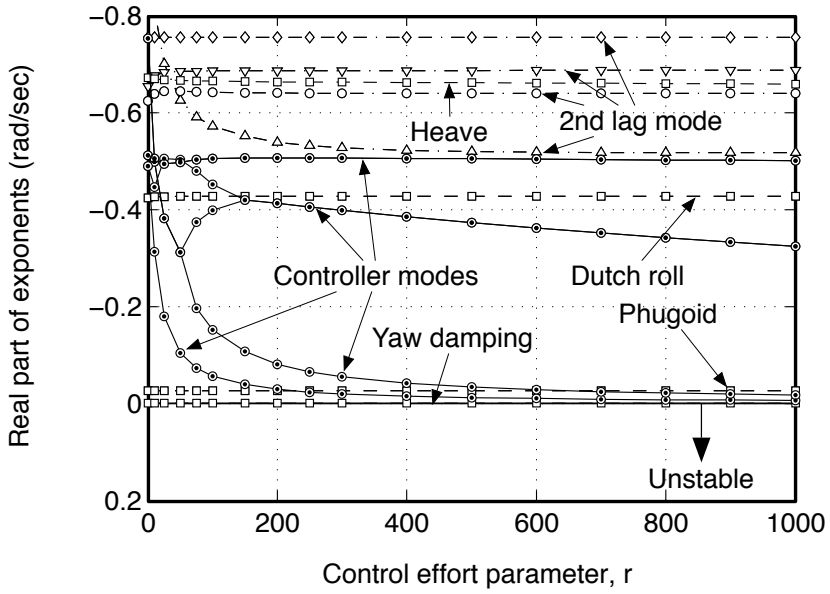

Figure 4.49: Real parts of selected low damping closed-loop stability eigenvalues for $V = 80$ kn ($\mu = 0.188$) and low feedback gain $\kappa \approx 0.07$, as a function of controller tuning parameter r

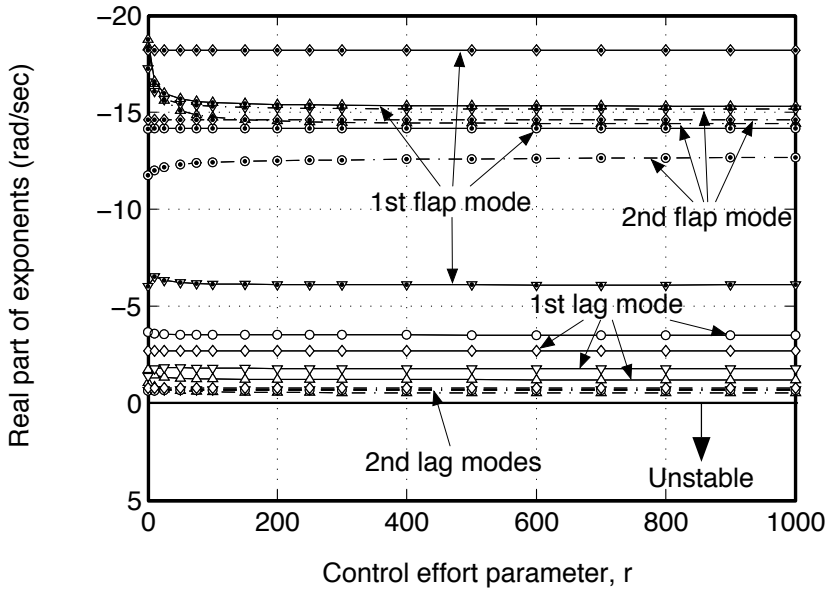

Figure 4.50: Real parts of selected rotor closed-loop stability eigenvalues for $V = 80$ kn ($\mu = 0.188$) and low feedback gain $\kappa \approx 0.07$, as a function of controller tuning parameter r

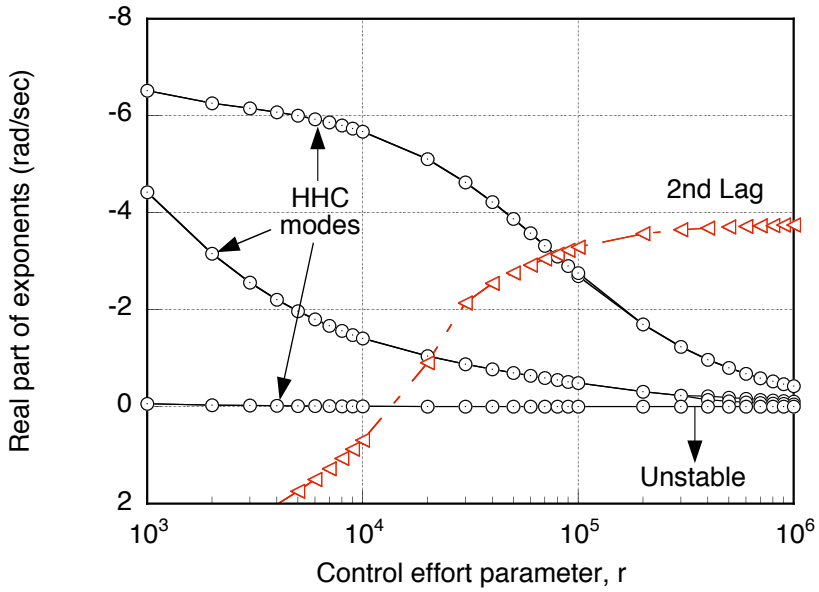

Figure 4.51: Real parts of selected closed-loop stability eigenvalues for $V = 80$ kn ($\mu = 0.188$) and high feedback gain $\kappa = 1.0$, as a function of controller tuning parameter r

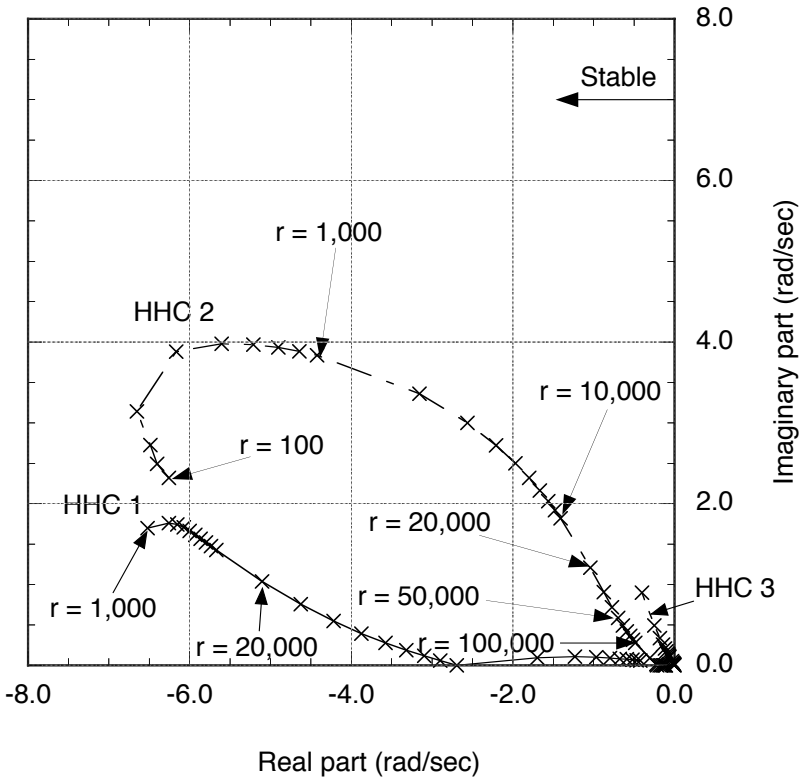

Figure 4.52: Root-locus plot of the fundamental HHC controller eigenvalues at $V = 80$ kn ($\mu \approx 0.188$).

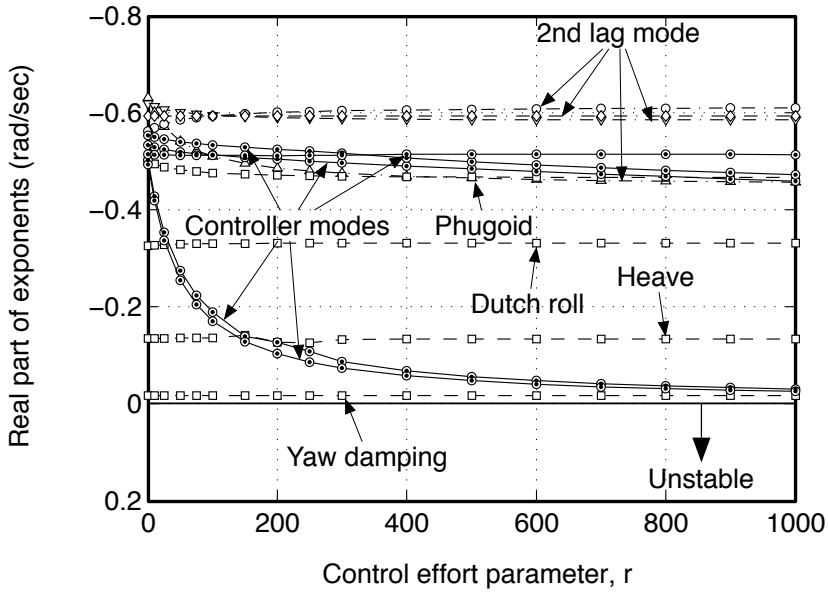

Figure 4.53: Real parts of selected low damping closed-loop stability eigenvalues for $V = 140$ kn ($\mu = 0.33$) and low feedback gain $\kappa \approx 0.07$, as a function of controller tuning parameter r

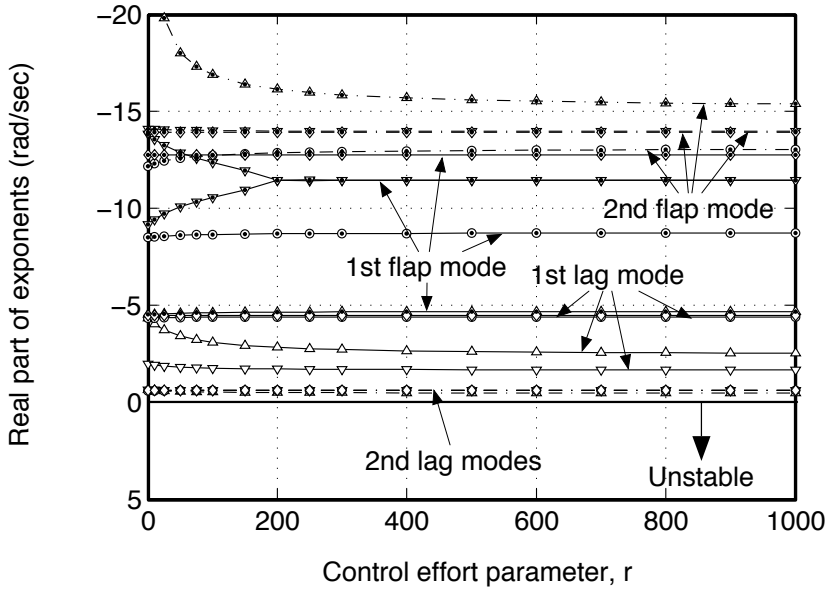

Figure 4.54: Real parts of selected rotor closed-loop stability eigenvalues for $V = 140$ kn ($\mu = 0.33$) and low feedback gain $\kappa \approx 0.07$, as a function of controller tuning parameter r

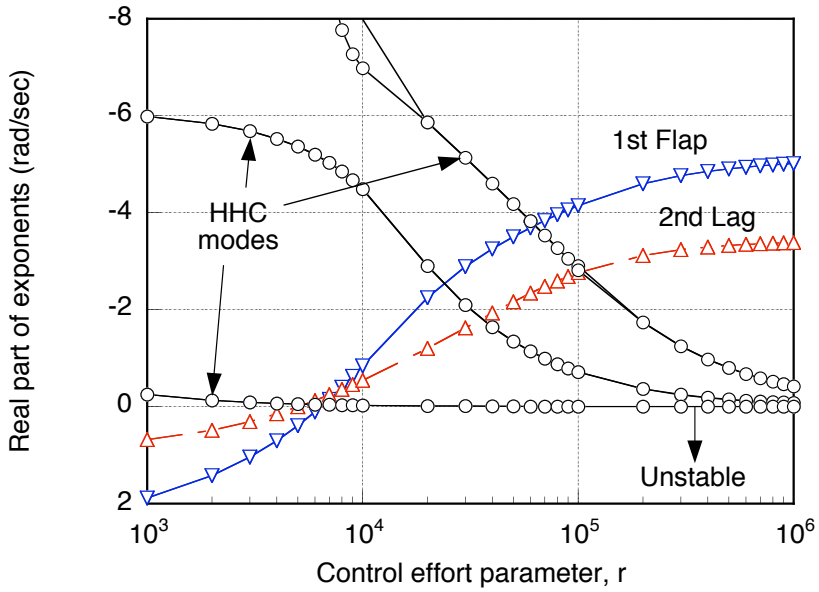

Figure 4.55: Real parts of selected closed-loop stability eigenvalues for $V = 140$ kn ($\mu = 0.33$) and high feedback gain $\kappa = 1.0$, as a function of controller tuning parameter r

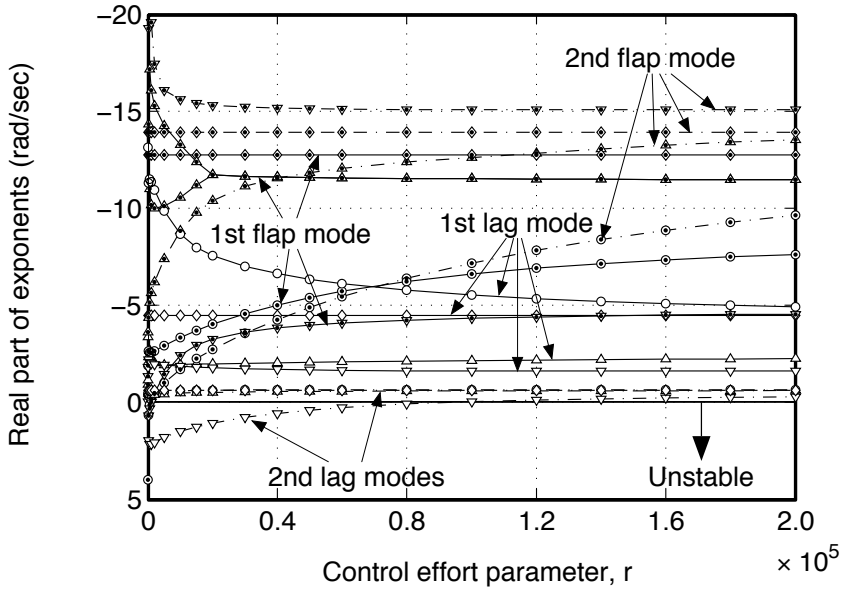

Figure 4.56: Real parts of selected rotor closed-loop stability eigenvalues for $V = 140$ kn ($\mu = 0.33$) and high feedback gain $\kappa = 1.0$, as a function of controller tuning parameter r

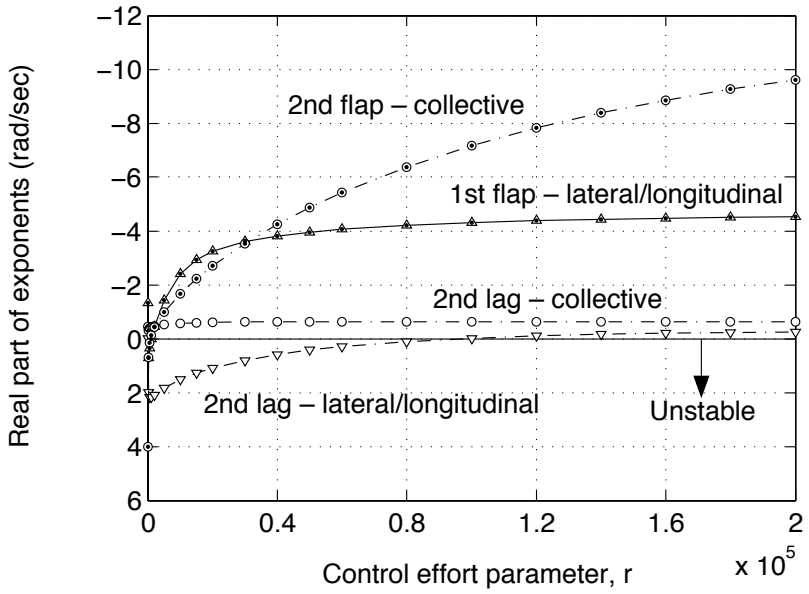

Figure 4.57: Real parts of unstable rotor closed-loop stability eigenvalues for $V = 140$ kn ($\mu = 0.33$) and high feedback gain $\kappa = 1.0$, as a function of controller tuning parameter r (high r).

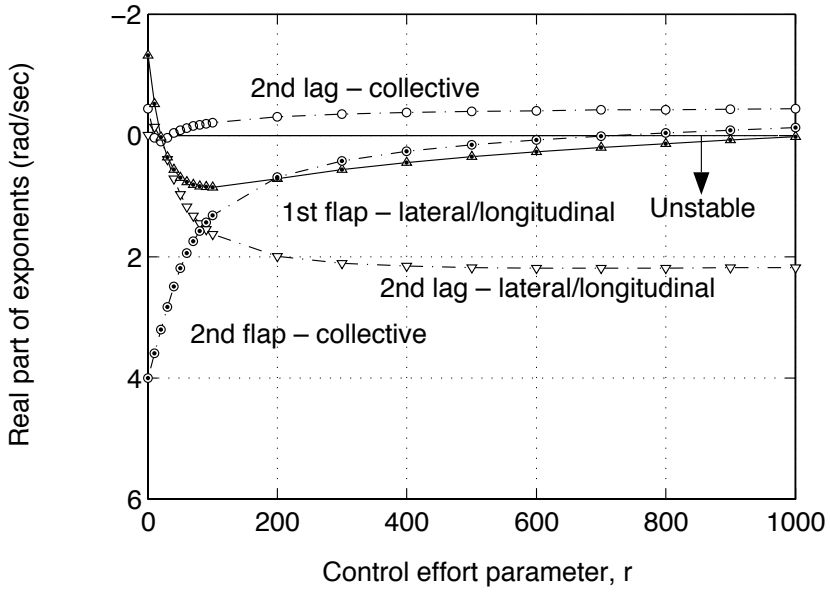

Figure 4.58: Real parts of unstable rotor closed-loop stability eigenvalues for $V = 140$ kn ($\mu = 0.33$) and high feedback gain $\kappa = 1.0$, as a function of controller tuning parameter r (low r).

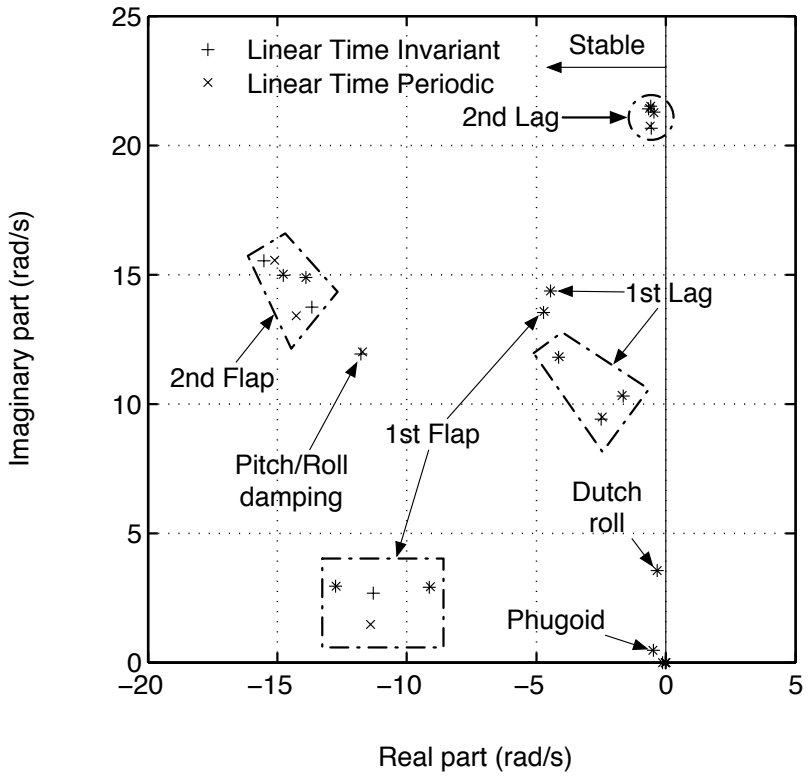

Figure 4.59: Selected open-loop system LTI and LTP eigenvalues at $V = 140$ kn ($\mu \approx 0.33$).

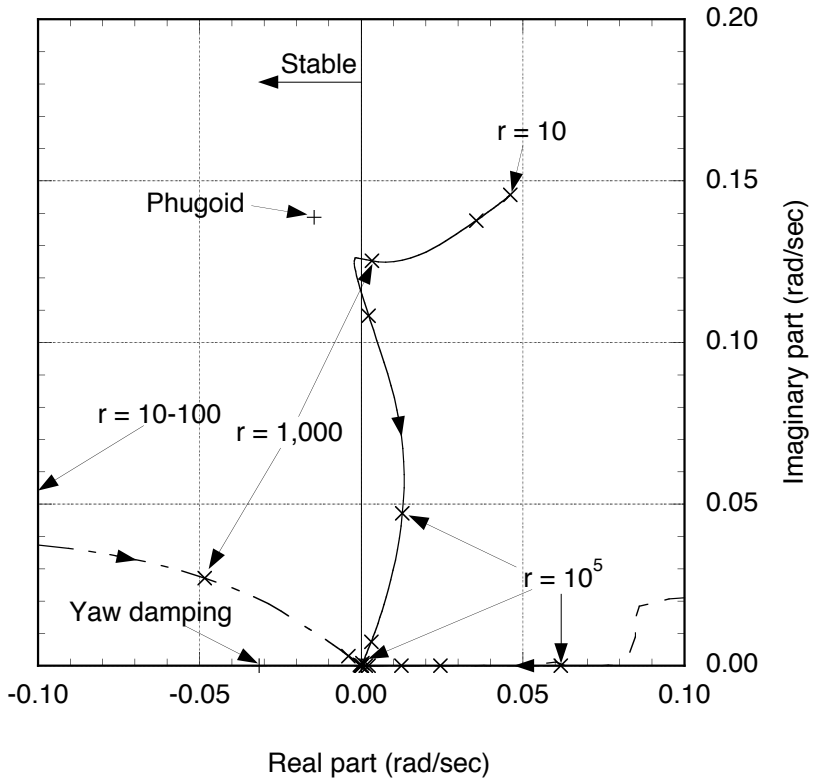

Figure 4.60: Root-locus of LTI closed-loop system controller poles, 80 kn.

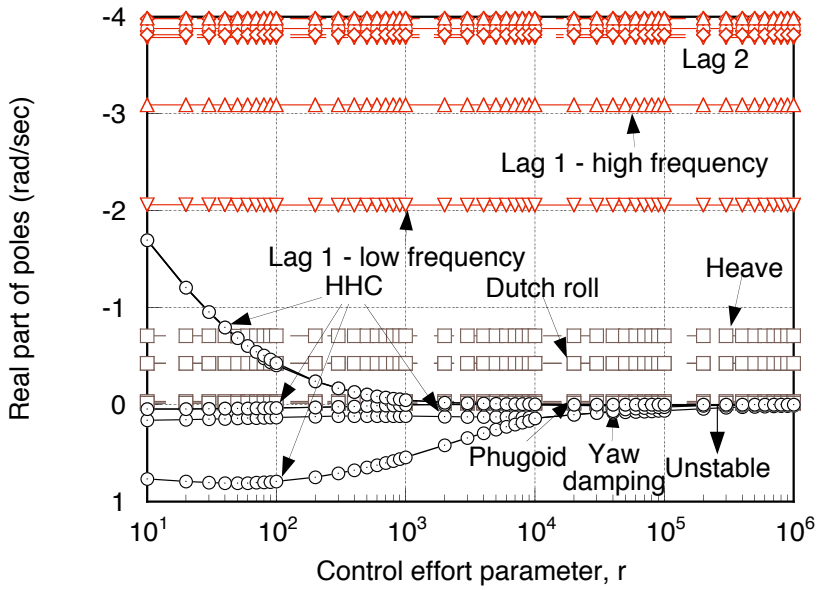

Figure 4.61: Real parts of selected closed-loop poles for $V = 80$ kn ($\mu = 0.188$) and high feedback gain $\kappa = 1.0$, as a function of controller tuning parameter r

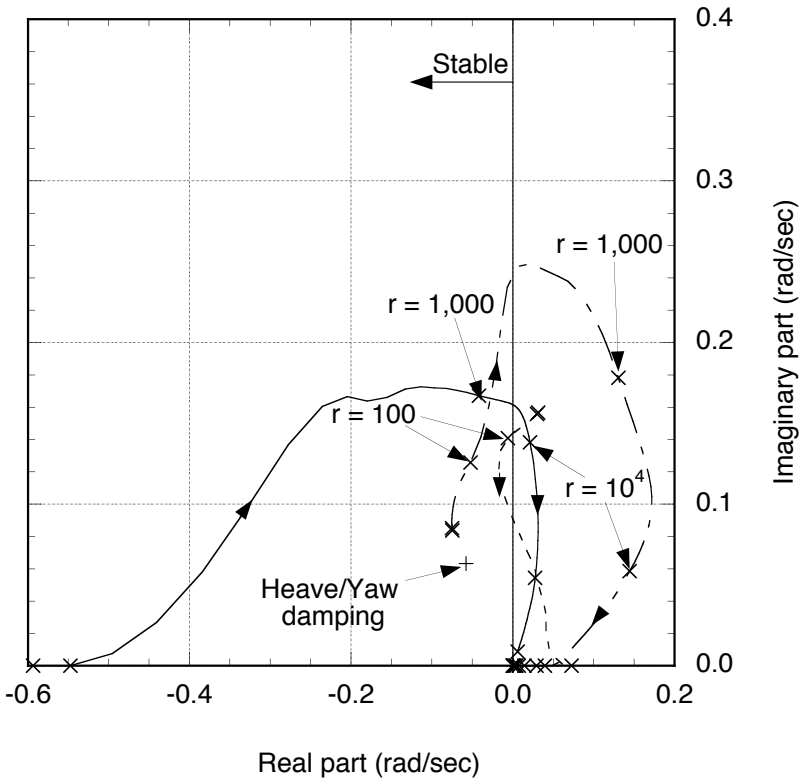

Figure 4.62: Root-locus of LTI closed-loop system controller poles, 140 kn.

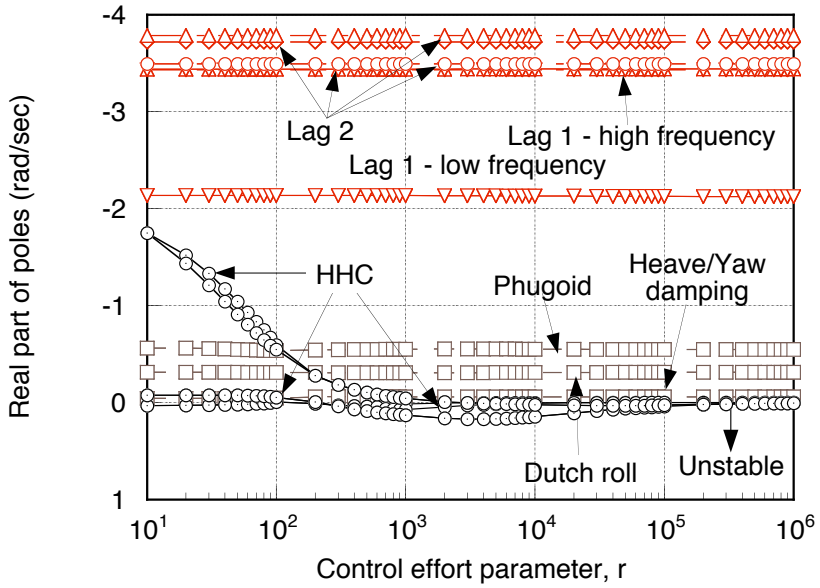

Figure 4.63: Real parts of selected closed-loop poles for $V = 140$ kn ($\mu = 0.33$) and high feedback gain $\kappa = 1.0$, as a function of controller tuning parameter r

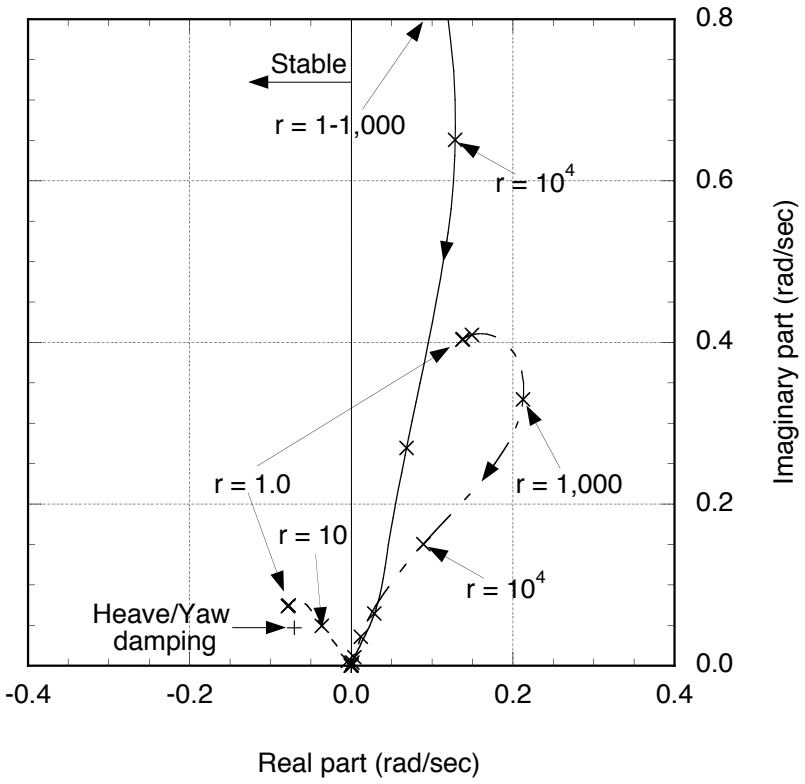

Figure 4.64: Root-locus of LTI closed-loop system controller poles, 170 kn.

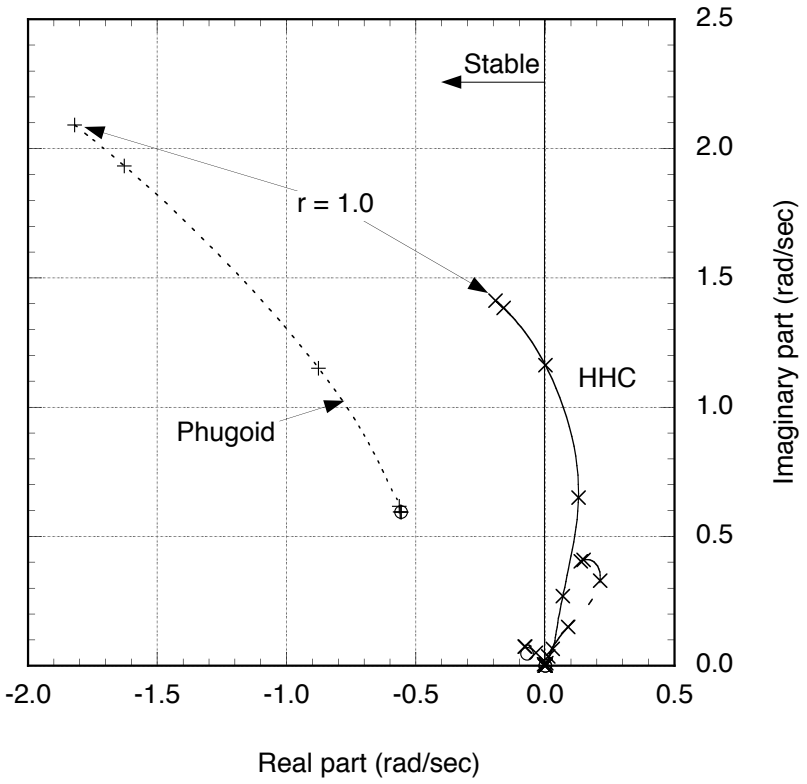

Figure 4.65: LTI Root-locus of closed-loop system phugoid and controller poles, 170 kn.

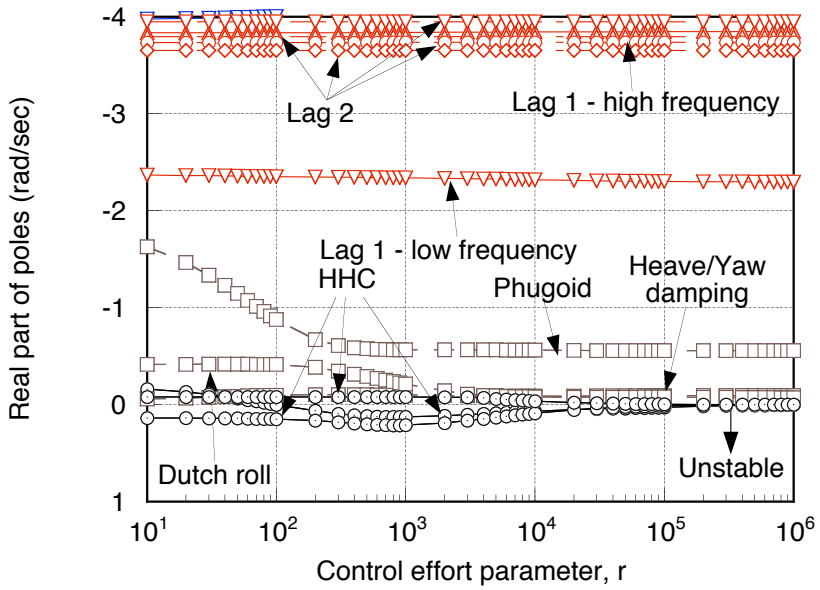

Figure 4.66: Real parts of selected closed-loop poles for $V = 170$ kn ($\mu = 0.4$) and high feedback gain $\kappa = 1.0$, as a function of controller tuning parameter r

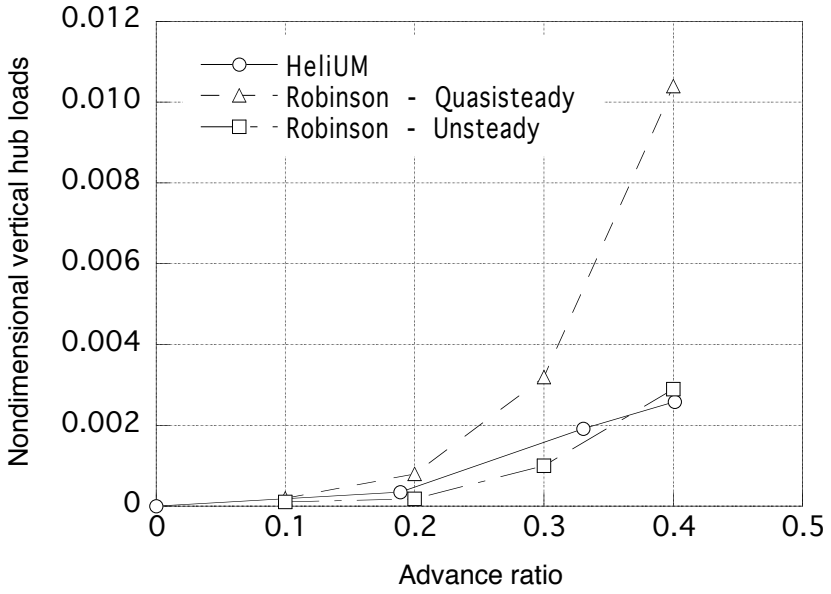

Figure 4.67: Variation of peak-to-peak vertical loads, soft-in-plane.

Chapter 5

Discrete-Time, Closed-Loop Aeromechanical Stability

5.1 Overview

This Chapter presents closed-loop aeromechanical stability and response results for a coupled, helicopter-HHC system. The stability results and the linearized time histories are obtained from the linearized, time-lifted model of Eqs. (2.211) and (2.212). The closed-loop response results are obtained from the full nonlinear simulation of the coupled helicopter-HHC system.

As discussed in 4.1, because the aerodynamic model consists of a simple linear inflow with quasi-steady aerodynamics, vibratory loads and CG accelerations, and consequently also HHC inputs, tend to be underestimated. Therefore, their absolute values can be considered representative only in a qualitative sense. However, it was established that the overall simulation model is likely reasonable for stability studies, and for a general assessment of the design and closed-loop analysis methodology. The use of linearized helicopter models with the linear unsteady aerodynamics model in state space form is intentionally avoided, given the size of the resulting linear system. The unsteady aerodynamics model requires a total minimum of 160 states, compared to 55 states which define the other helicopter dynamics. Such a large number of states, places practical, if

not theoretical, limitations on the stability analysis of discrete-time, periodic systems via the time lifting technique.

The controller has been implemented in discrete time using a "fast" sampling rate of $n_s = 36$ samples per rotor revolution. The weighting matrices Q and R which define the HHC quadratic performance index, Eq. (2.100), have been chosen to be proportional to the identity matrix, i.e., $Q = I$ and $R = rI$, and the effect of different choices for the value of parameter r has been investigated. Also, two different proportional scaling factors for the feedback gain matrix have been investigated, essentially defining a low gain controller and a nominal, or baseline, design, respectively.

5.2 Low feedback gain controller

Figures 5.1 and 5.2 show the amplitude of the 3, 4 and 5/rev controller inputs for $V = 80$ kn, and control effort restrictions $r = 0$ and $r = 1,000$, respectively. Results for $r = 1,000$, in Fig. 5.2, show the controller response times for the discrete and contiunous controllers to be nearly identical. Therefore, under these control effort settings, both models can be considered to be equivalent. The same is not true for $r = 0$ (i.e., completely unrestricted control effort), as shown in Fig. 5.1. Controller response times for the continuous implementation are much slower in this case. The discrete case displays a slightly larger overshoot peak. It should be noted, however, than neither the continuous nor the discrete HHC models have achieved their steady state value within the first 7 seconds after being turned on.

Results for $V = 140$ kn, and for the same controller restriction settings, are shown

in Figs. 5.3 and 5.4. As was the case for $V = 80$ kn, the discrete and continuous versions of the controller for $V = 140$ kn display nearly identical response times for $r = 1,000$, and even for $r = 0$. Again, general controller response times for the low gain feedback designs, with $\kappa \approx -.07$, are shown to be over 7 seconds.

Selected closed loop stability eigenvalues for a small gain feedback controller ($\kappa \approx 0.07$) are shown in Fig. 5.5 as a function of r. The real parts of the eigenvalues are plotted as a function of r. These are the eigenvalues of the discrete system, converted to continuous form. A combination of aircraft, rotor and controller eigenvalues are shown. Qualitatively, these results are similar to those of the approximate continuous-time HHC model of Chapter 3.

Figure 5.6 shows the real part of closed loop stability eigenvalues associated with the rotor dynamics. Eigenvalues corresponding to the fundamental flap and lag are shown, along with the second flap and second lag blade mode eigenvalues. In particular, stability margins associated with the flap and torsion modes are eroded for $r < 500$, although not sufficiently enough for the eigenvalues to become unstable. The fact that the closed loop controller appears to have such a strong effect on the flap and torsion modes, particularly the erosion of flap stability, is intriguing and should be more carefully investigated. This erosion of the stability margins was not captured by the approximate continuous HHC model, which instead predicted closed loop eigenvalues to be invariant for $r > 100$ as shown in Fig. 4.50. This is indication that neglecting the discrete nature of the HHC loop elements is potentially unconservative, and should be avoided even for small feedback gains.

The real part of the least damped closed loop stability eigenvalues for $V = 140$ kn

and $\kappa \approx 0.07$ are shown in Fig. 5.7 as a function of r. As was the case for $V = 80$ kn, the real part of the closed loop eigenvalues associated with rotor dynamics are shown in Fig. 5.8.

Vibration reduction performance for these controller configurations is measured by the cost indices in Figs. 5.9 and 5.10 for $V = 80$ kn and $V = 140$ kn, respectively. From these results it can be established that both, continuous and discrete HHC implementations, possess nearly identical vibration performance properties for the given values of r. Vibration reduction performance is improved slightly with $r = 0$ for $V = 80$ kn, compared to that obtained with $r = 1000$. Attenuation values for $V = 140$ kn show no distinct advantages of choosing $r = 0$ over $r = 1000$.

5.3 Results for nominal gain design

Figure 5.11 shows the closed-loop, vertical acceleration response $\dot{w}$ for three different values of the tuning parameter r, namely $r = 2 \cdot 10^4$ (top plot), $r = 5 \cdot 10^4$ (center plot), and $r = 10^5$ (bottom plot), corresponding to increasing restrictions on the control effort or, equivalently, to decreasing gain. Note that the scales on the vertical axis are different for the top plot. For the value $r = 2 \cdot 10^4$ the response loosely resembles a limit cycle, but the values of the accelerations are of up to $\pm 1g$, and therefore unacceptably high. For this value of r the linearized analysis predicts an instability. For the value $r = 5 \cdot 10^4$ the response is stable, but the magnitude of the response decreases slowly. The linearized analysis indicates the system is near a point of marginal stability. Finally, for $r = 10^5$, the response becomes stable and the HHC is very effective in suppressing $\dot{w}$. This is

also predicted by the linearized analysis. The behavior of roll and pitch accelerations is qualitatively very similar to that of $\dot{w}$, and it will not be shown here.

Figure 5.12 shows the time history of the response of just the 4/rev harmonic of $\dot{w}$. The three curves show, respectively, the baseline response with the HHC system turned off, the response predicted by the nonlinear simulation model, and that predicted by the linearized, time periodic model used to design the HHC system. Apart from a small initial transient, caused by a small initial mismatch between the trimmed and the time-marching solution, the baseline 4/rev response rapidly converges to a constant, nonzero steady value. The nonlinear closed-loop response exhibits a brief but strong transient, during which the acceleration increases by almost three times the baseline value. The transient lasts for less than 2 seconds, after which the 4/rev response is rapidly reduced to almost zero. This strong transient is not present in the 4/rev $\dot{p}$ and $\dot{q}$ responses, not shown in the figure, which start being attenuated as soon as the HHC is turned on. The figure also shows that the 4/rev responses predicted by the LTP and by the nonlinear model are nearly identical. This indicates that, for the type of mathematical model used in this study, and for the flight condition considered, (i) the effect of nonlinearities on the 4/rev $\dot{w}$ response is small, and the response is adequately captured by a linearized model as long as the periodicity is retained (the same conclusions hold for $\dot{p}$ and $\dot{q}$), and (ii) the LTP model is sufficiently accurate for the HHC design.

Similar results were presented in Chapter 4 for the same flight condition and helicopter configuration, but with the HHC closed loop modeled as entirely continuous, and the harmonic analysis, the computation delay, and the zero-order-hold not modeled at all. The response was stable for values of the tuning parameter r above a point in between

10^4 and $2 \cdot 10^4$, and the HHC would effectively suppress vibrations in six seconds or less. Comparing these results with those shown in Fig. 5.11, it is clear that the allowable gains of the HHC system must be lower because of the reduction in phase margin brought about by the delays in the HHC loop.

The magnitude of the 3, 4 and 5/rev control harmonics for $r = 8 \cdot 10^4$ are plotted in Fig. 5.13 as a function of time. The controls for both the rigorous discrete model and the approximate continuous model are shown in the figure. Except for minor transient differences over the first couple of revolutions, discrete and continuous controls tend to the same magnitude value, and are nearly dynamically equivalent. The magnitudes of the 3, 4 and 5/rev harmonics of both controllers reach essentially the respective steady state values in about 5–6 seconds. Similar agreement between the phases of the discrete and continuous model can be seen in Fig. 5.14. Except for the first 1–2 rotor revolutions (slightly more for the 4/rev control), discrete and continuous phases are almost identical.

Lessening the constraints placed on the controller, however, presents a much different picture. Figures 5.15 and 5.16 show the magnitude and phase angles in degrees of the 3, 4 and 5/rev control harmonics for a control effort constraint determined by $r = 5 \cdot 10^4$. While the magnitude of the controls for the continuous and discrete HHC models possess the same mean value, and converge to the same steady state values, the transient behaviour is significantly different. The discrete response contains a large high frequency oscillatory component at 1.5 Hz (0.21/rev). The same behavior is observed in the values of the HHC input phase angles.

Further decreasing the restrictions on the controller blade pitch harmonics eventually results in the system becoming unstable for values of r slightly below $5 \cdot 10^4$. The

real part of selected closed loop system stability eigenvalues for the nominal feedback gain configuration ($\kappa = 1.0$) as a function of r are shown in Fig. 5.17. The plot shows the closed loop system becomes unstable for $r < 5 \cdot 10^4$.

This plot is similar to Fig. 4.51. Although instabilities were also captured by the approximate continuous model, physical mechanisms involved in the two cases are different, as evidenced by the differences in the closed loop characteristic exponents for the discrete HHC model, compared to the continuous case, and should be explored in the future. The onset of instability was not captured for such high values of the control constraint parameter r by the approximate continuous HHC model, which instead predicted closed loop stability for values of $r \gtrsim 1.5 \cdot 10^4$. This further demonstrates the significance of neglecting the discrete nature of the HHC loop, and reinforces the message that this should be avoided.

Figure 5.18 shows the closed-loop, vertical acceleration response $\dot{w}$ for three different values of the tuning parameter r, namely $r = 10^4$ (top plot), $r = 4 \cdot 10^4$ (center plot), and $r = 10^5$ (bottom plot). The scale on the vertical axis of the top plot is different from those of the other two. As in the 80 kn case, for the value $r = 10^4$ the acceleration response is very high and erratic, with peaks well over $1g$ in absolute value, and loosely resembling a limit cycle. For this value of r the linearized analysis predicts an instability. For the value $r = 5 \cdot 10^4$ the response is stable, and slowly decreases in magnitude. Finally, for $r = 10^5$, the response is stable and the vibrations are reduced very quickly, in less than 2 seconds from the application of HHC. The linearized analysis also indicates that these last two cases are stable. The behavior of roll and pitch accelerations is qualitatively very similar to that of $\dot{w}$, and it will not be shown here. Figure 5.19 shows the closed-loop, ver-

tical acceleration response $\dot{w}$ based on a linearized helicopter model, for the same values of the tuning parameter.

Figure 5.20 is similar to Fig. 5.12, but refers to $V = 140$ kn. As in Fig. 5.12, after a small initial transient, the baseline 4/rev response rapidly converges to a constant, nonzero steady value. The nonlinear closed-loop response no longer exhibits the strong transient observed at $V = 80$ kn, and the 4/rev response is substantially reduced after just one second. The same happens for the $\dot{p}$ and $\dot{q}$ 4/rev responses, not shown in the figure. As in the $V = 80$ kn case, the 4/rev responses predicted by the LTP and by the nonlinear model are nearly identical, and the same conclusions on the effect of nonlinearities and the adequacy of the LTP model for design purposes apply.

The magnitude of the 3/, 4/, and 5/rev harmonics for $r = 10^5$ are plotted in Fig. 5.21 as a function of time. The controls for both the discrete and the continuous model are shown in the figure. As in the $V = 80$ kn case, discrete and continuous controls tend to the same steady state magnitude value, although the initial transients are slightly different and the magnitudes of the discrete controls present a slight overshoot, compared to those of the continuous controls, before settling at their steady values. The magnitudes of all the harmonics of the discrete and continuous controllers reach their respective steady state values after about 2-4 seconds.

An almost perfect agreement between the phases of the discrete and continuous model can be seen in Fig. 5.22. Except for the first few rotor revolutions, discrete and continuous 4 and 5/rev phases are almost identical. Discrepancies in the 3/rev phase angle are not considered to be significant, considering the small amplitude of the 3/rev input, relative to the amplitude of the 4 and 5/rev controls shown in Fig. 5.21.

The near perfect agreement between the values of the HHC inputs for both, the discrete and continuous controller models serves to establish an equivalence criterion between the two cases, for this particular value of r. Equivalence can only be guaranteed when large restrictions are placed on the control input harmonics. Figures 5.23 and 5.24 show the amplitudes and phases of the discrete and continuous model controls for a less stringent restriction on the control effort with $r = 4 \cdot 10^4$. Although both controllers result in the same mean value of the control harmonics, the discrete-time version is subject to a quite different transient response, than the continuous-time model. HHC inputs display the same 1.5 Hz (0.21/rev) oscillatory behavior observed for the controller at $V = 80$ kn.

The closed loop system at $V = 140$ kn becomes unstable for $r \lesssim 3.7 \cdot 10^4$ in the same fashion that the system at $V = 80$ kn did. Results for the case at $V = 140$ kn are qualitatively very similar to the stability values shown in Fig. 5.17 for $V = 80$ kn, and the same conclusions on the effects of the discrete nature of the HHC can be reached.

Figure 5.25 shows the real parts of selected discrete-time, closed-loop characteristic exponents for $V = 140$ kn ($\mu = 0.33$), and nominal feedback gain $\kappa = 1.0$, as a function of the controller effort setting r. Exponents for modes identified as the HHC, fundamental blade flapwise bending, and blade torsion modes are shown, with the flap mode becoming unstable for r between $3 \cdot 10^4$ and $4 \cdot 10^4$.

Compared with results obtained, for the same flight condition but with a continuous HHC model, the allowable gains are lower. In Chapter 3, the closed loop system was studied for values of r ranging from 10^3 to 10^6, and it was shown it becomes unstable at much lower values of r. Results shown in Fig. 4.55 show the system becomes unstable for $r \lesssim 7 \cdot 10^3$.

5.4 Other considerations

The results presented in this section underscore the importance of a correct modeling of "real life" effects such as discrete sampling, computations, and control updates, even for the simplified, fixed T-matrix scheme used in this study. Several additional effects were neglected, and should be included or more carefully analyzed in future research. First, in the scheme of Fig. 1.1, it was assumed that the transient following each HHC update would take one quarter of a rotor revolution to die out. Simulation results not presented here indicate that a more realistic figure is 1-2 rotor revolutions for well-damped rotors with mechanical lag dampers, and up to 4-6 revolutions for lowly damped hingeless rotors. Second, the HHC update at each rotor revolution was simulated as a pure step. While rotating system HHC actuators are very fast, they cannot generate such steps, and therefore they add their own delay. Third, perfect measurements were assumed, whereas real sensors introduce their own dynamics in the loop. Finally, practical digital harmonic analyses will require the use of windows, which may introduce further delays and spurious dynamics. All these effects must be taken into account to obtain realistic predictions of the maximum performance achievable by an HHC system.

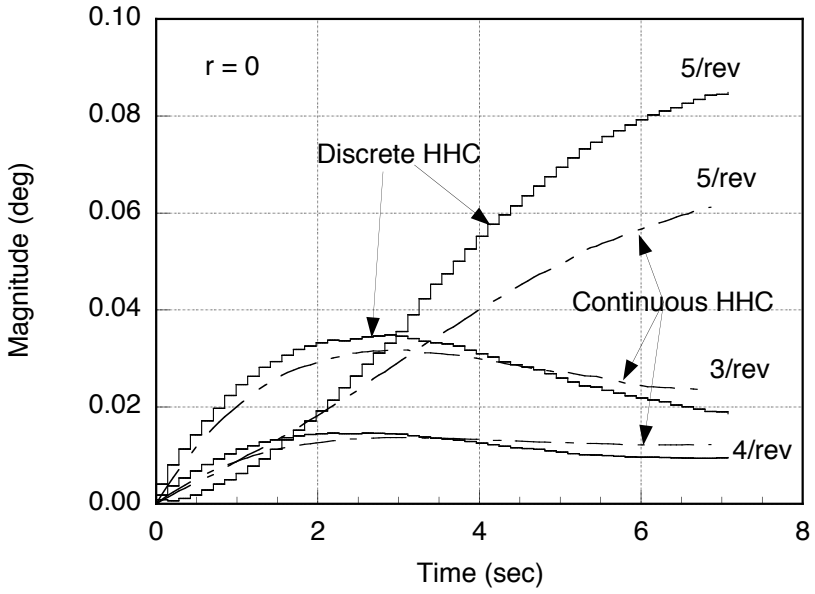

Figure 5.1: HHC control input magnitude in degrees for continuous and discrete models with $r = 0$, $V = 80$ kn ($\mu = 0.188$)

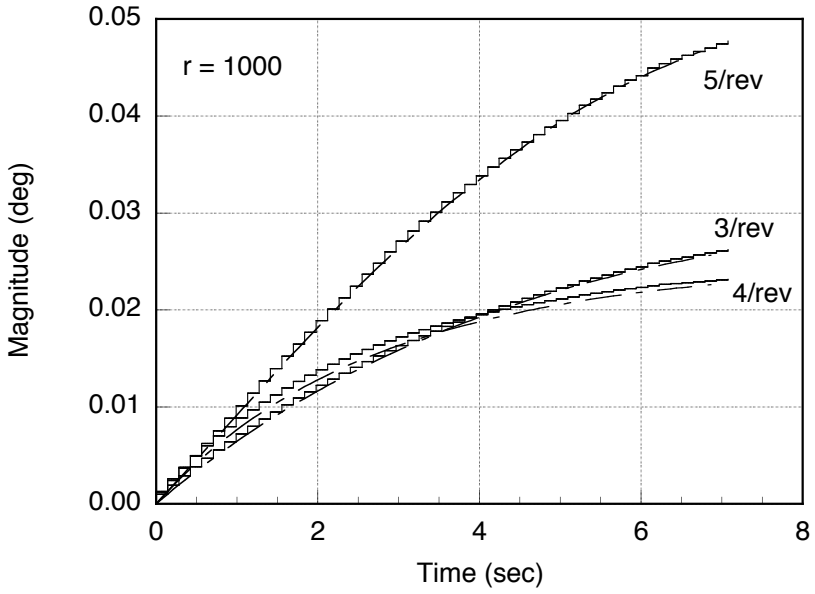

Figure 5.2: HHC control input magnitude in degrees for continuous and discrete models with $r = 1,000$, $V = 80$ kn ($\mu = 0.188$)

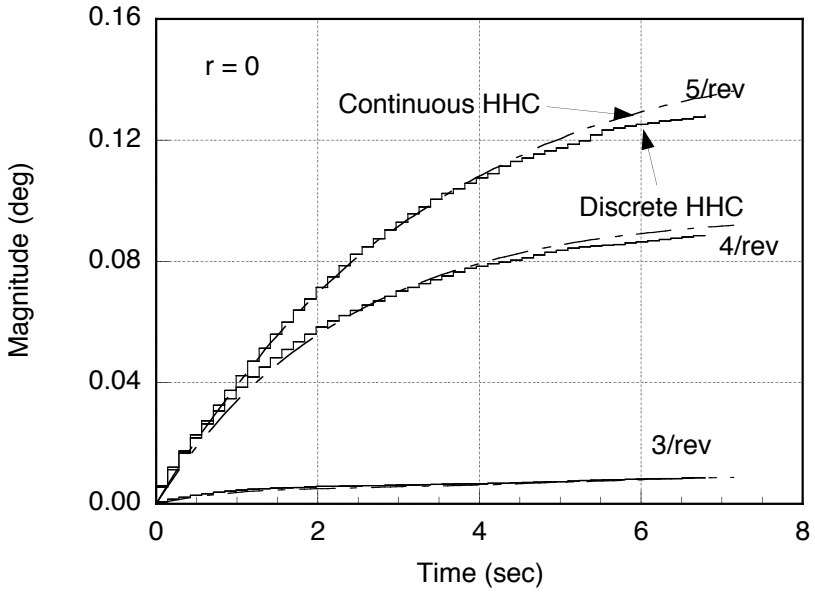

Figure 5.3: HHC control input magnitude in degrees for continuous and discrete models with $r = 0$, $V = 140$ kn ($\mu = 0.33$)

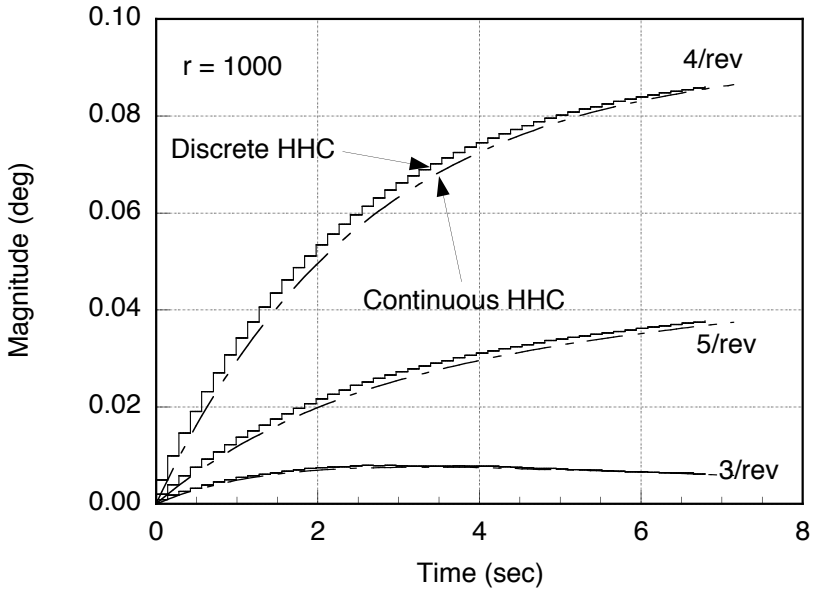

Figure 5.4: HHC control input magnitude in degrees for continuous and discrete models with $r = 1,000$, $V = 140$ kn ($\mu = 0.33$)

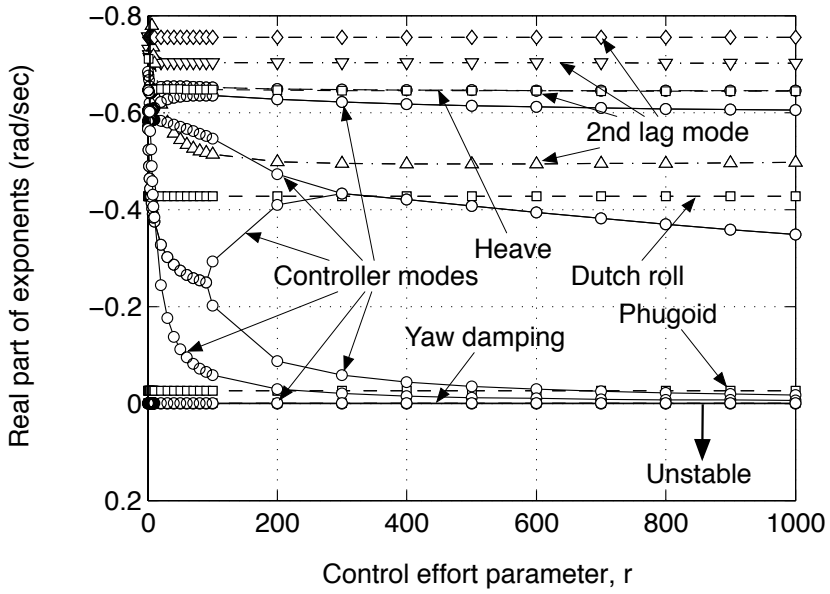

Figure 5.5: Real parts of selected low damping closed-loop stability eigenvalues for V = 80 kn ($\mu = 0.188$) and low feedback gain $\kappa \approx 0.07$, as a function of controller tuning parameter r

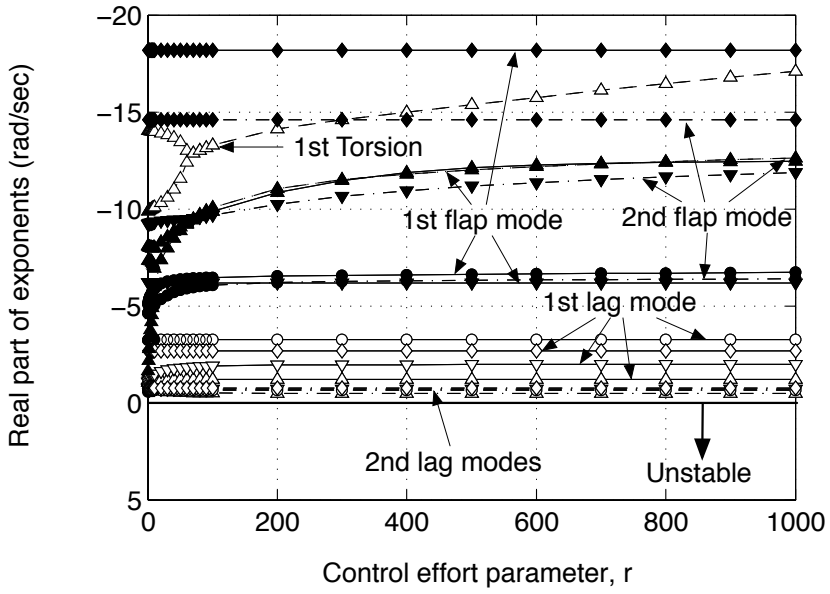

Figure 5.6: Real parts of selected rotor closed-loop stability eigenvalues for $V = 80$ kn ($\mu = 0.188$) and low feedback gain $\kappa \approx 0.07$, as a function of controller tuning parameter r

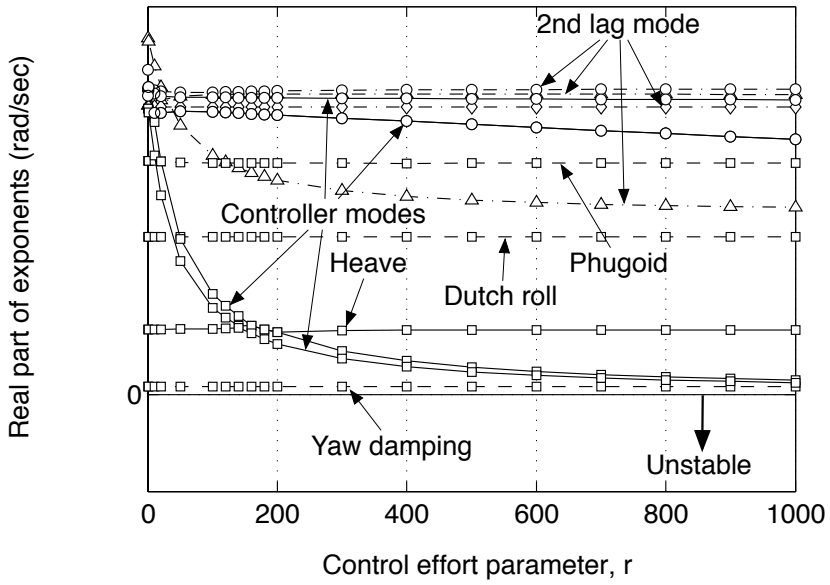

Figure 5.7: Real parts of selected low damping closed-loop stability eigenvalues for V = 140 kn ($\mu = 0.33$) and low feedback gain $\kappa \approx 0.07$, as a function of controller tuning parameter r

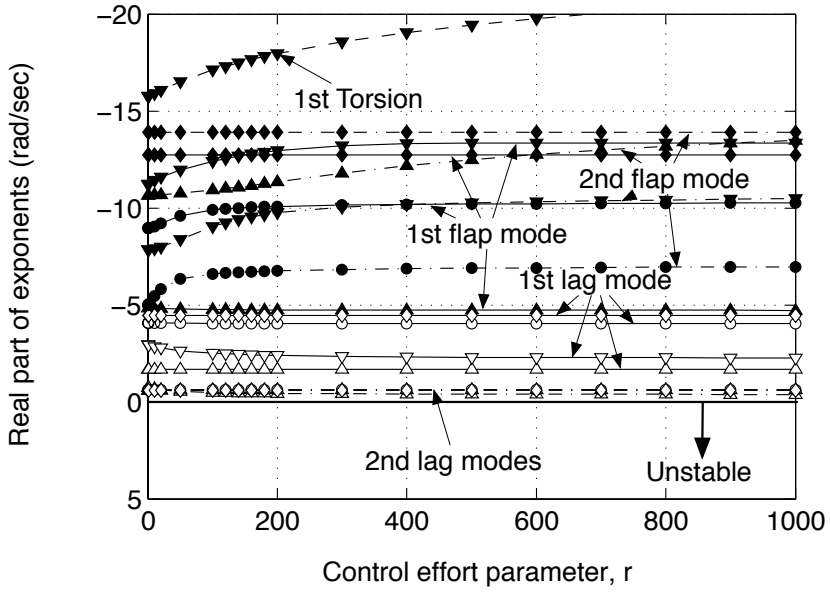

Figure 5.8: Real parts of selected rotor closed-loop stability eigenvalues for $V = 140$ kn ($\mu = 0.33$) and low feedback gain $\kappa \approx 0.07$, as a function of controller tuning parameter r

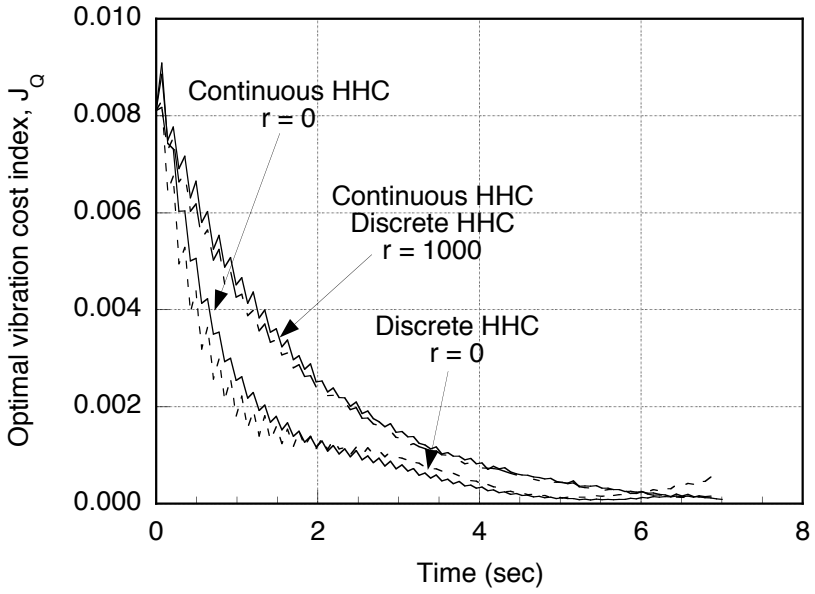

Figure 5.9: Optimal vibration cost index for low feedback gain continuous and discrete HHC controllers with different control effort settings, V = 80 kn (μ = 0.188)

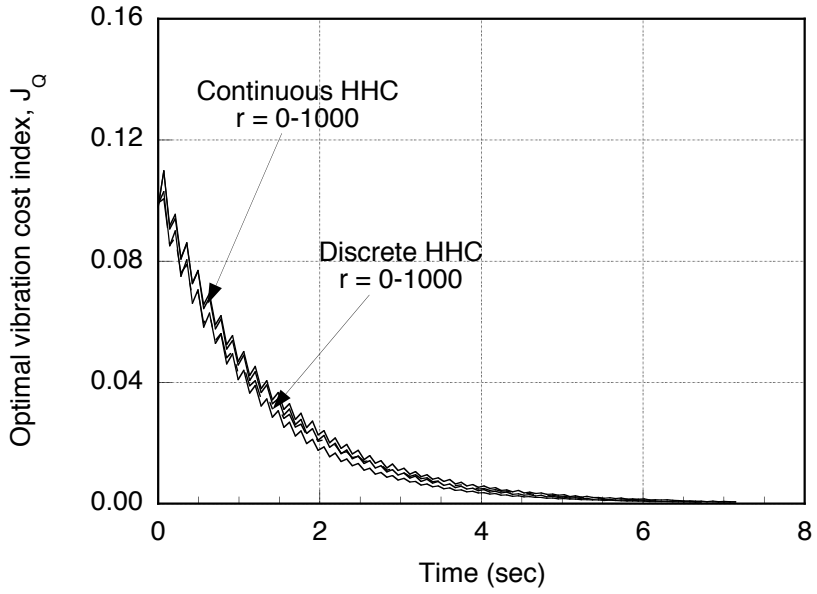

Figure 5.10: Optimal vibration cost index for low feedback gain continuous and discrete HHC controllers with different control effort settings, V = 140 kn (μ = 0.33)

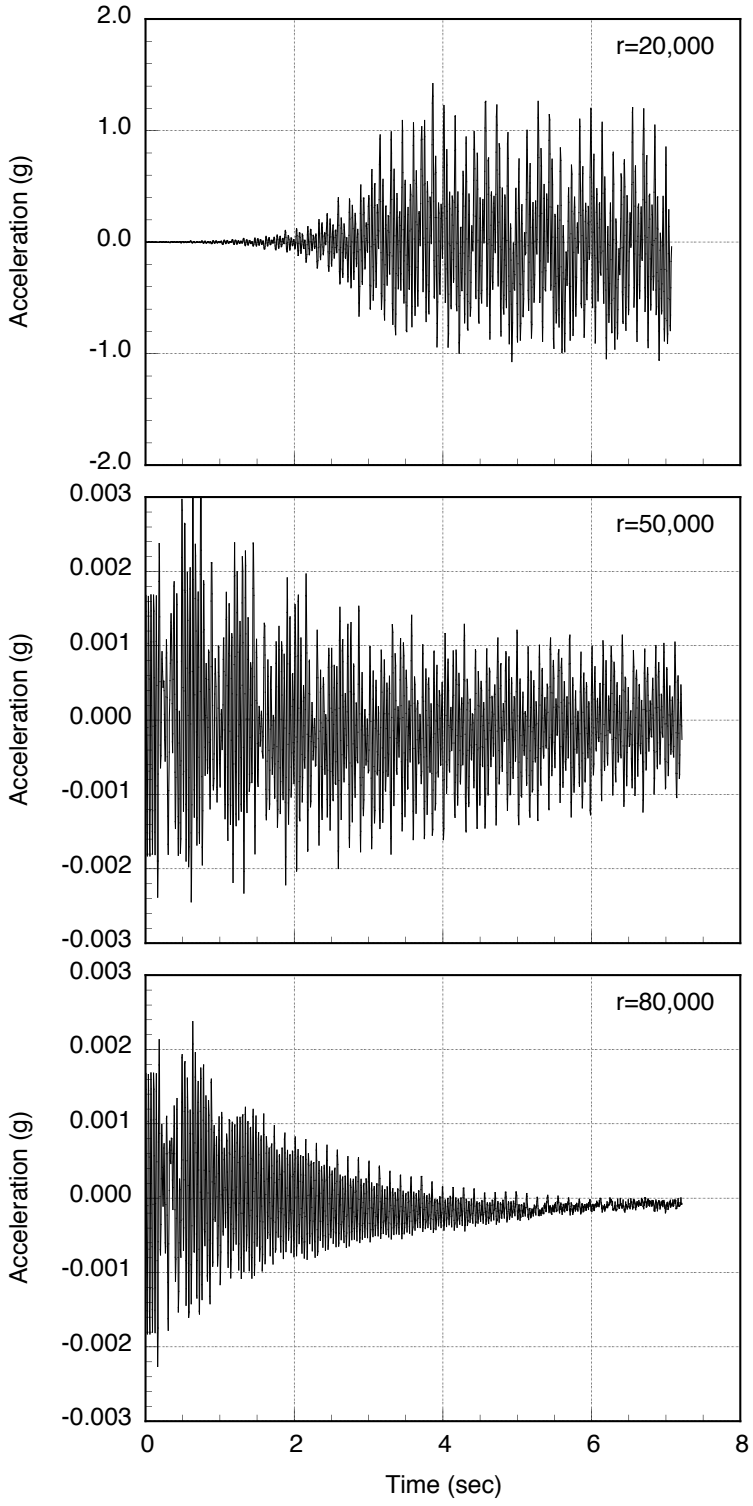

Figure 5.11: Vertical accelerations $\dot{w}$ at the helicopter center of mass for $V = 80$ kn ($\mu = 0.188$) and tuning parameter $r = 2 \times 10^4$ (top), $r = 5 \times 10^4$ (center), and $r = 8 \times 10^4$ (bottom)

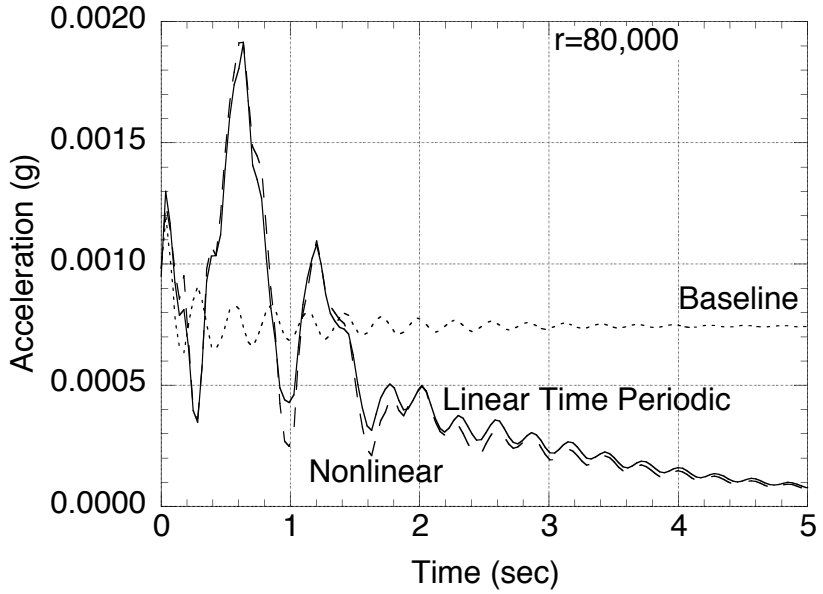

Figure 5.12: Closed-loop 4/rev vertical acceleration response $\dot{w}$ at the helicopter center of mass for $V = 80$ kn ($\mu = 0.188$); baseline open-loop response, and prediction with linear and nonlinear simulation models.

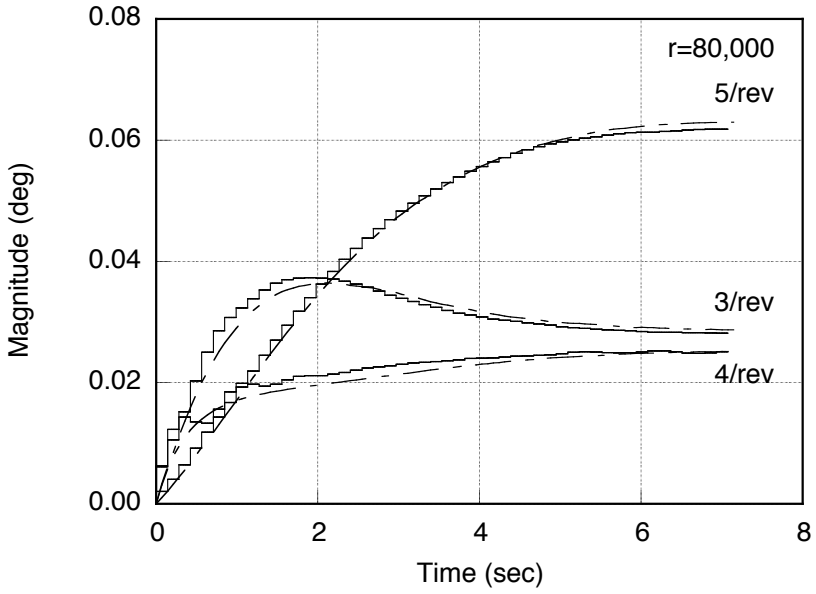

Figure 5.13: HHC control input magnitude in degrees for continuous and discrete models with $r = 8 \cdot 10^4$, $V = 80$ kn ($\mu = 0.188$)

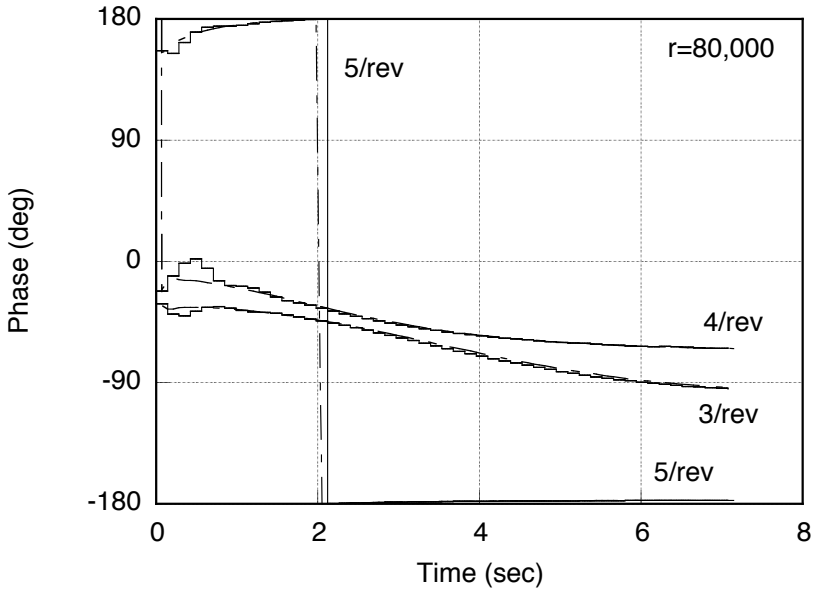

Figure 5.14: HHC control input phase in degrees for continuous and discrete models with $r = 8 \cdot 10^4$, $V = 80$ kn ($\mu = 0.188$)

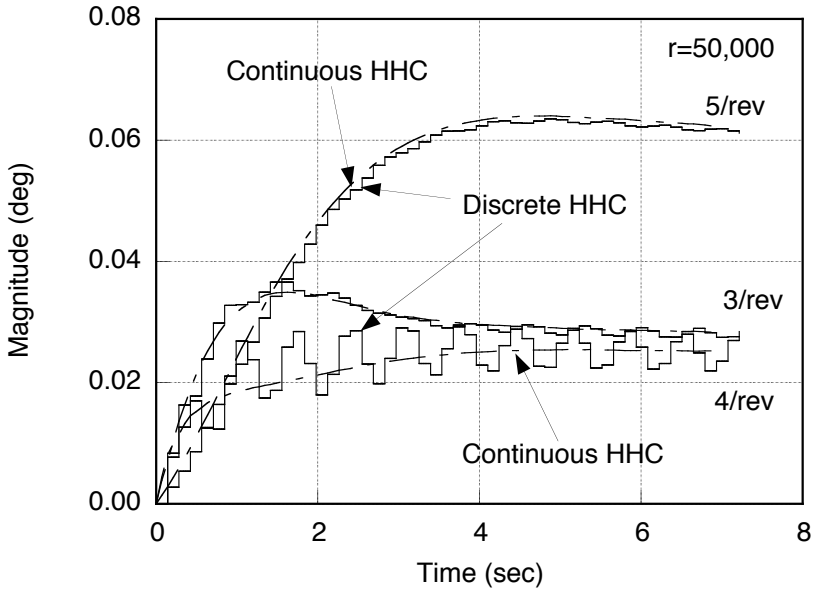

Figure 5.15: HHC control input magnitude in degrees for continuous and discrete models with $r = 5 \cdot 10^4$, $V = 80$ kn ($\mu = 0.188$)

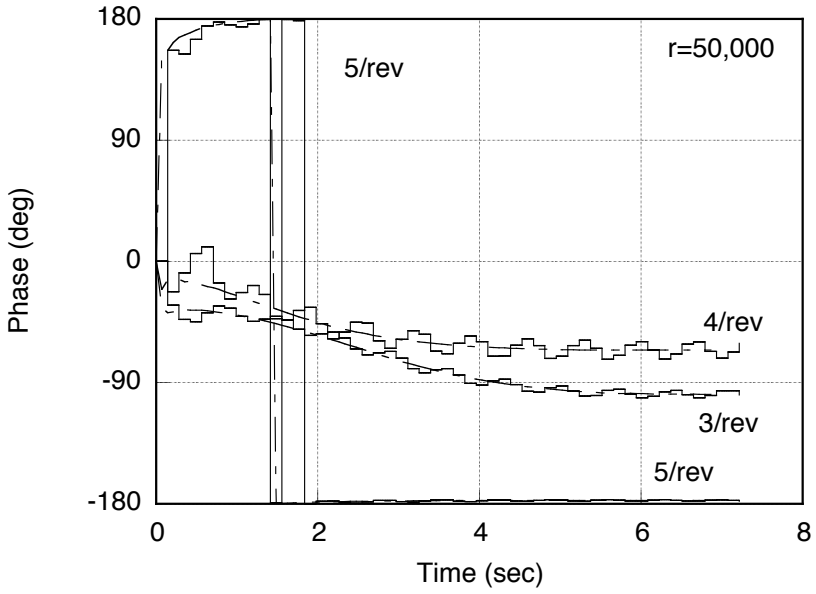

Figure 5.16: HHC control input phase in degrees for continuous and discrete models with $r = 5 \cdot 10^4$, $V = 80$ kn ($\mu = 0.188$)

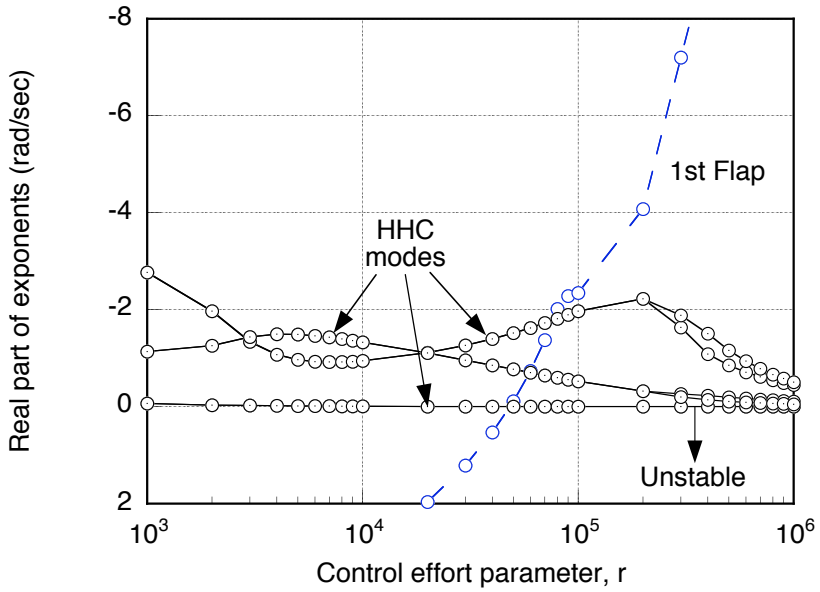

Figure 5.17: Real parts of selected closed-loop stability eigenvalues for $V = 80$ kn ($\mu = 0.188$) and a high feedback gain $\kappa = 1.0$, as a function of controller tuning parameter r

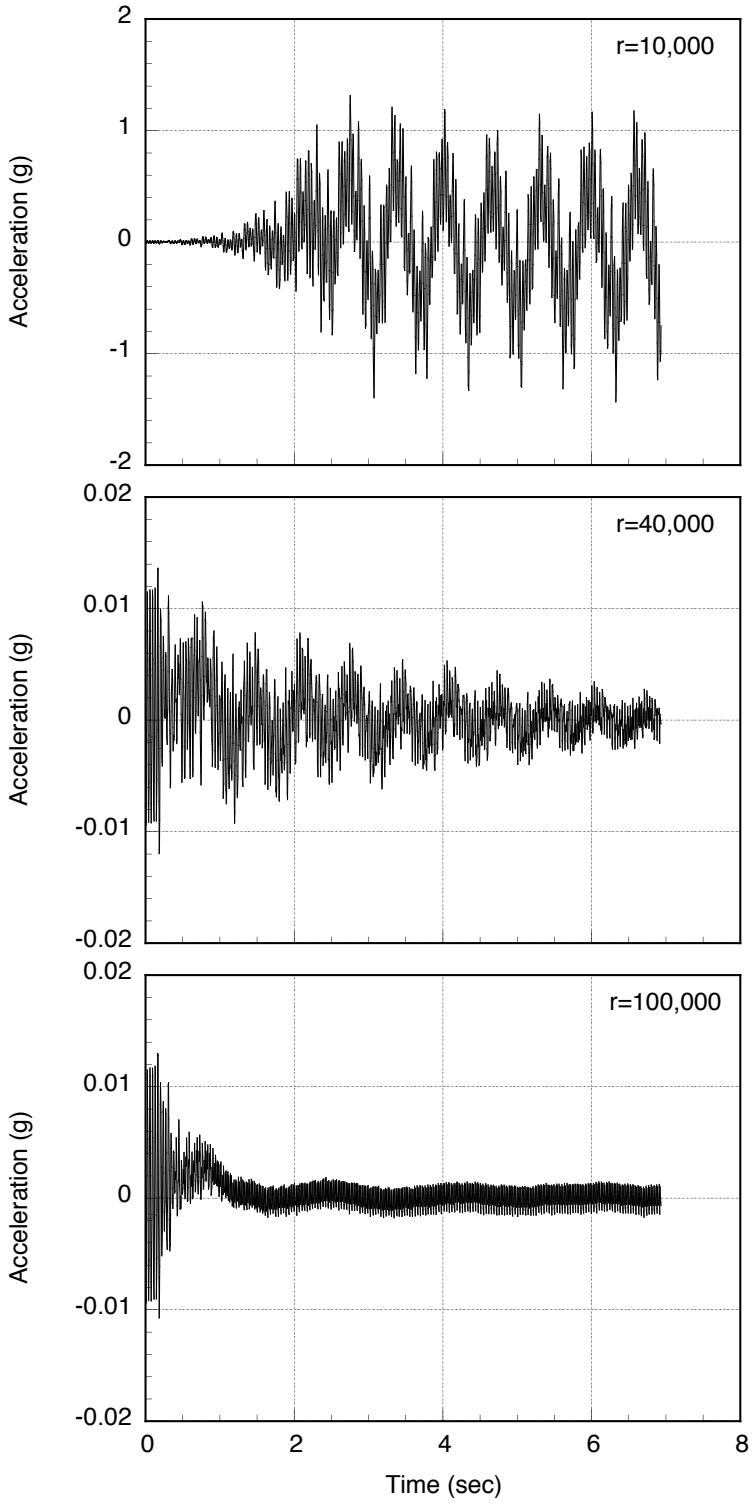

Figure 5.18: Vertical accelerations $\dot{w}$ at the helicopter center of mass for $V = 140$ kn ($\mu = 0.33$) and tuning parameter $r = 10^4$ (top),$r = 3.8 \times 10^4$ (center), and $r = 10^5$ (bottom)

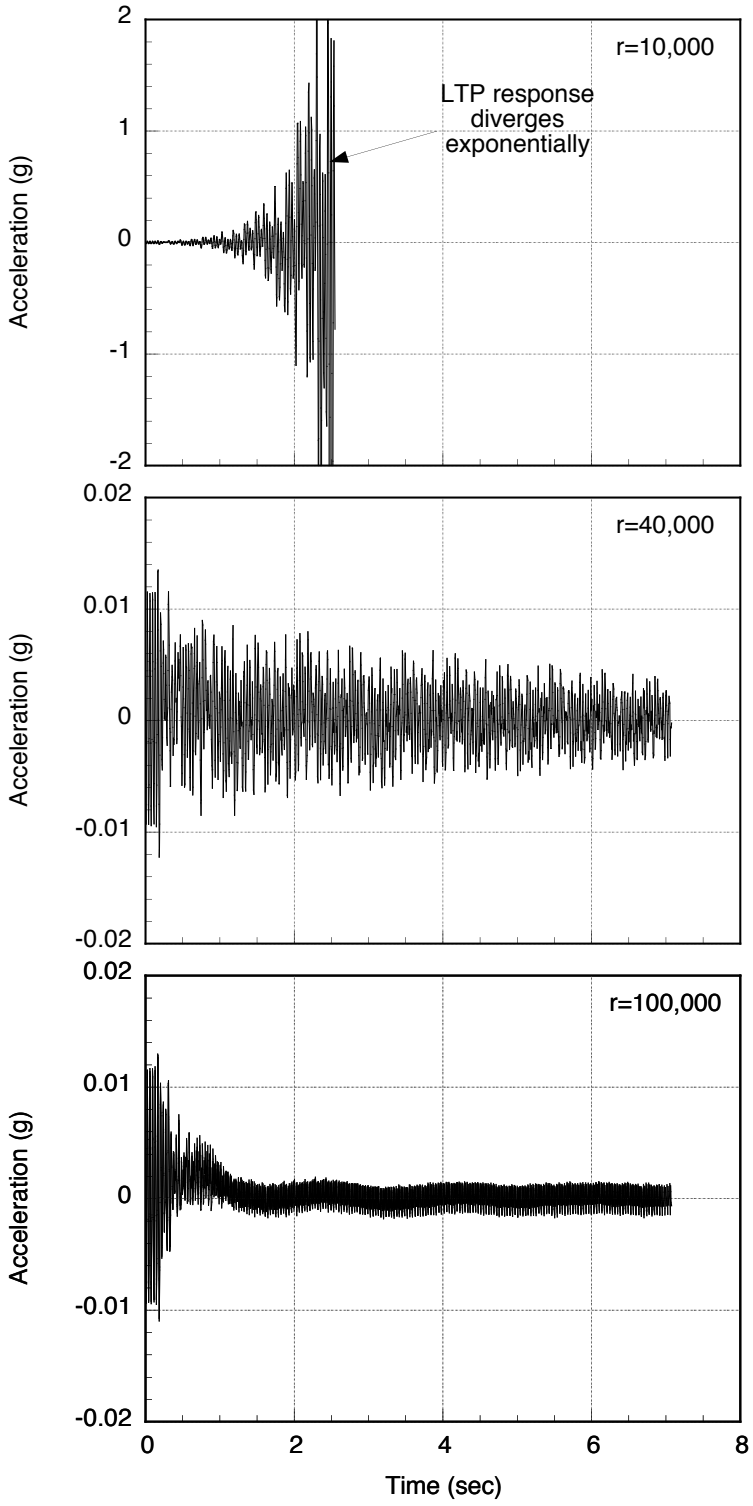

Figure 5.19: Vertical accelerations $\dot{w}$ at the helicopter center of mass for $V = 140$ kn ($\mu = 0.33$) and tuning parameter $r = 10^4$ (top),$r = 5 \times 10^4$ (center), and $r = 10^5$ (bottom)

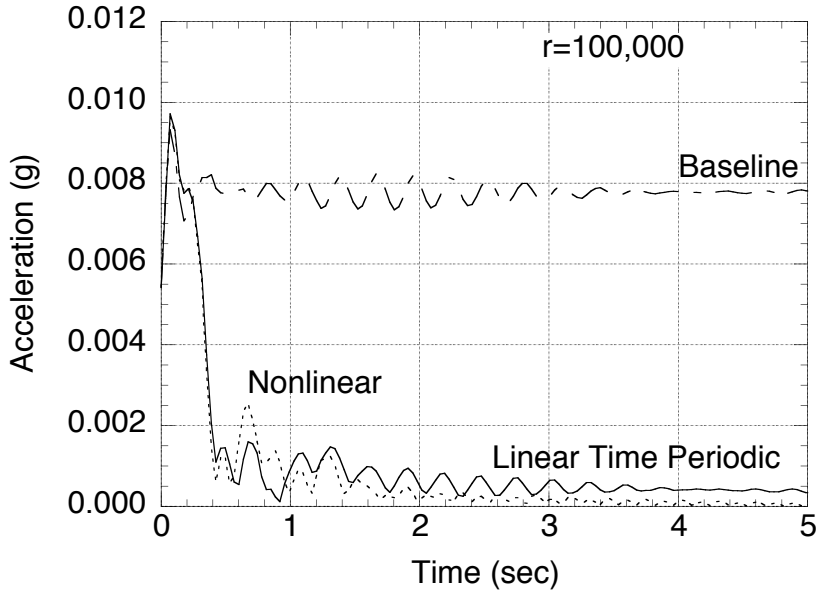

Figure 5.20: Closed-loop 4/rev vertical acceleration response $\dot{w}$ at the helicopter center of mass for $V = 140$ kn ($\mu = 0.33$); baseline open-loop response, and prediction with linear and nonlinear simulation models.

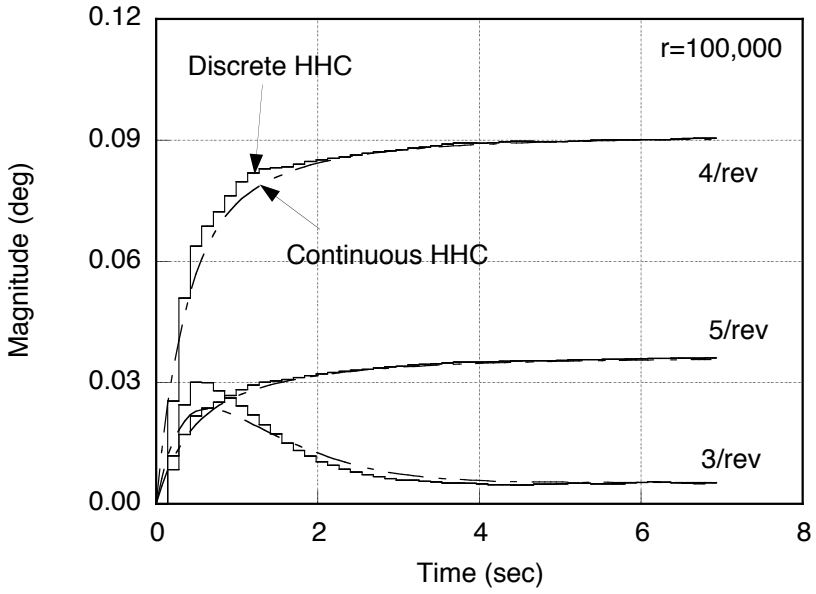

Figure 5.21: HHC control input magnitude in degrees for continuous and discrete models with $r = 10^5$, $V = 140$ kn ($\mu = 0.33$)

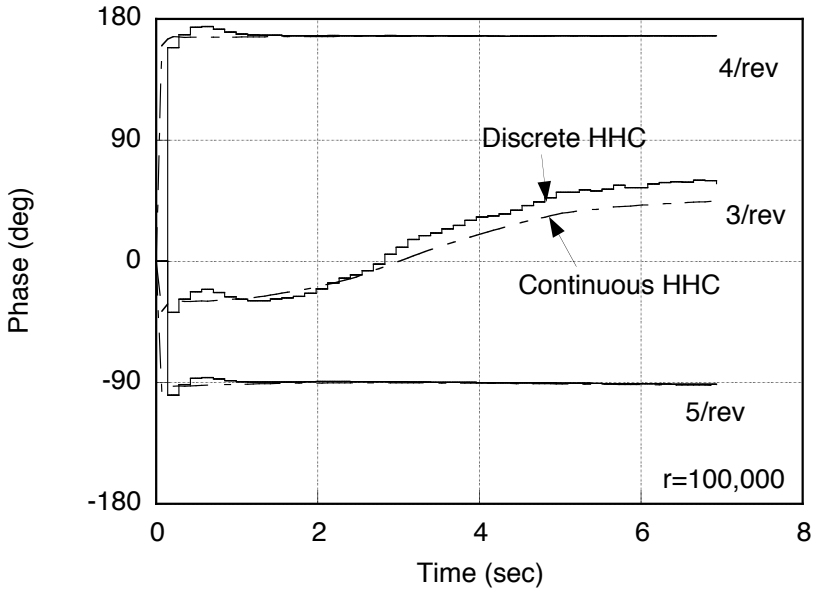

Figure 5.22: HHC control input phase in degrees for continuous and discrete models with $r = 10^5$, $V = 140$ kn ($\mu = 0.33$)

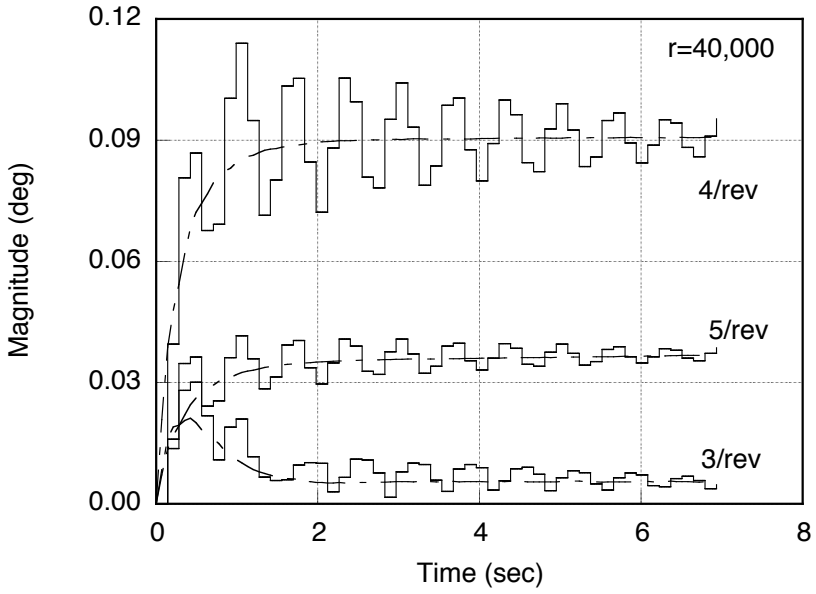

Figure 5.23: HHC control input magnitude in degrees for continuous and discrete models with $r = 4 \cdot 10^4$, $V = 140$ kn ($\mu = 0.33$)

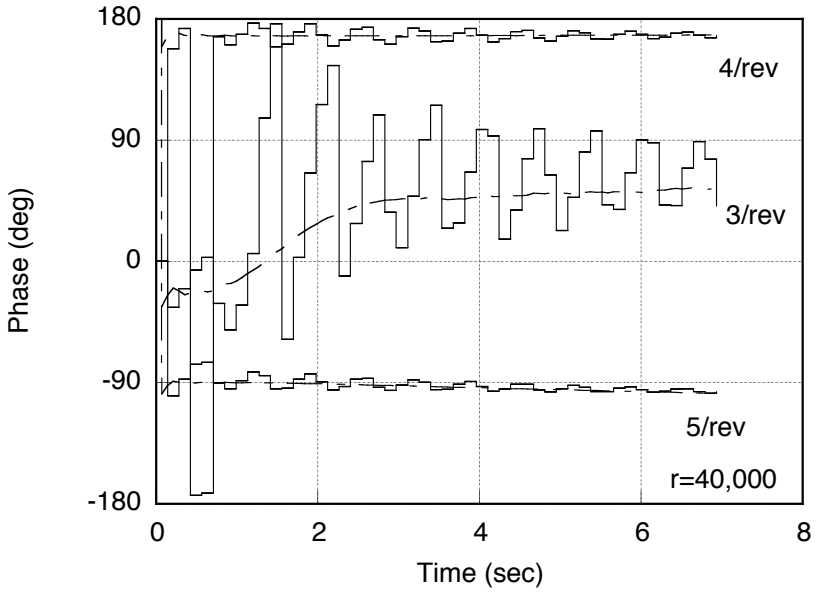

Figure 5.24: HHC control input phase in degrees for continuous and discrete models with $r = 4 \cdot 10^4$, $V = 140$ kn ($\mu = 0.33$)

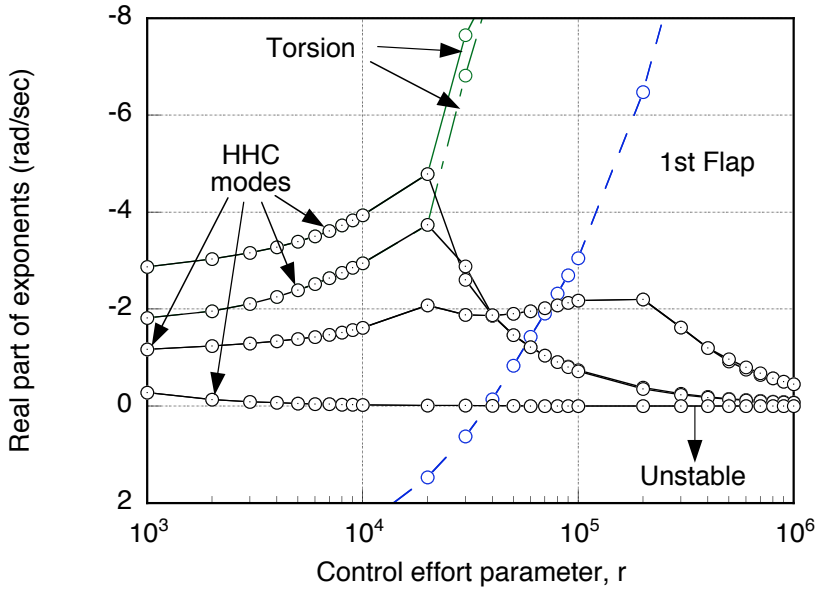

Figure 5.25: Real parts of selected discrete-time, closed-loop characteristic exponents for $V = 140$ kn ($\mu = 0.33$) and nominal feedback gain $\kappa = 1.0$, as a function of controller tuning parameter r

Chapter 6

Summary and Conclusions

This study presented an aeromechanical closed loop stability and response analysis of a hingeless rotor helicopter with a Higher Harmonic Control (HHC) system for vibration reduction. The analysis fully included the rigid body dynamics of the helicopter and the flexibility of the rotor blades. It was assumed that the gain matrix T was fixed and computed off-line. The discrete elements of the HHC control loop were rigorously modeled, including the presence of two different time scales in the loop. By also formulating the coupled rotor-fuselage dynamics in discrete form, the entire coupled helicopter-HHC system could be rigorously modeled as a discrete system. Finally, the effect of the periodicity of the equations of motion was rigorously taken into account by converting the system with periodic coefficients into an equivalent system with constant coefficients and identical stability properties using a time lifting technique.

Before studying the effects of the discrete elements in the loop, however, an approximate continuous modeling of the Higher Harmonic Control system for the control of vibrations in helicopters was formulated in a state space framework. The extension of this state space representation to the case of control inputs acting at a frequency different from that of the disturbance has been analyzed in the framework of periodic systems

theory. The development of the state-space formulation for a multi-input/multi-output (MIMO) Higher Harmonic Control (HHC) system was presented in this study. The first step in this formulation was the state space derivation of a continuous-time form of a single-input/single-output HHC compensator with input and output at the same rotor harmonic; this approach was then extended to the case of different harmonics in input and output, which resulted in a periodic single-input/single-output HHC compensator; and finally, this result was generalized for the derivation of the MIMO state space form of the HHC controller.

The study presented the results of a numerical investigation of stability and performance properties of a closed loop HHC system, implemented in the rotating system, based on a simulation model of the coupled rotor-fuselage dynamics of a four-bladed hingeless rotor helicopter. Stability was quantified through the Floquet chracteristic exponents of the closed loop systems, which are formulated from linearized time periodic helicopter models extracted numerically from a nonlinear mathematical model. Performance of the HHC system and validation of the stability results is done in the time-domain by computation of the dynamic time history of the closed loop responses for both linear and nonlinear helicopter models.

The aforementioned computational helicopter model is found to lead to deficient vibratory hub load predictions, due to oversimplifications made in the aerodynamics modeling. The conclusions reached in this study must be considered in light of the natural limitations or simplifications of the computational helicopter model at hand. This exemplifies the fundamental tradeoff between the desire to accurately model nature, and the availability of mathematical models suitable for control design or analysis.

6.1 Conclusions

Simulation results show that both, the periodicity of helicopter dynamics, as well as the discrete time nature of the controller, play significant roles in determining the closed loop characteristics of the control system, especially for high bandwidth, or high feedback gain, control system designs which would invalidate the normal quasisteady assumption found in the literature. In light of the simulation and stability results presented in this study the following conclusions are put forward:

The first and most important conclusion of the present study is that discrete elements in the HHC loop must be modeled in any HHC stability analysis, in particular the control updating frequency, which is found to have the strongest impact on stability. Not doing so is unconservative and can potentially result in erroneous predictions of the stability of the coupled helicopter-HHC closed loop system, as well as of the HHC vibration attenuation performance. For the helicopter configuration and HHC structure used in this study, there exists a significant band of control effort settings in which the closed loop, coupled helicopter-HHC system with an approximate continuous modeling of the HHC system remains stable, whereas the more rigorous discrete analysis shows that closed loop instabilities can occur. The HHC gains must be reduced to account for the loss of gain margin brought about by the discrete elements.

The previous conclusion is predicated on the assumption that periodic dynamics inherent in the closed loop helicopter-HHC system are correctly taken into account in the stability analysis. The HHC problem is intrinsically time periodic if the HHC inputs include frequencies other than the frequency one wishes to attenuate. This is true even

if the rest of the model is assumed to be time invariant. In these cases, the closed loop stability results obtained using constant coefficient approximations are incorrect even at the lower values of the advance ratio μ, where the constant coefficient approximation of the open loop dynamics is accurate.

Based on the results presented in this dissertation, the following conclusions of the study can also be established:

1. The fixed gain HHC controller is very effective in reducing the combined effect of the desired components of the 4/rev accelerations at the center of gravity, at least at its design condition. Overall percentage reductions of the optimal cost function J indicated in the simulations are in excess of 90–94%. The minimization of the cost index J does not guarantee all the components of the 4/rev accelerations are reduced for every control design. However, because the simplifications in the model lead to the underestimation of these vibratory components, the absolute values of the reduction and the control inputs might not be fully reliable.

2. The attenuation of vibration, as measured by the optimal cost index J, occurs within 1–7 sec after the HHC system is turned on, depending on the amount of control effort applied. These time-scales indicate that closed loop bandwidth ranges from values well below 1 up to 6 rad/sec. The lowest of these values overlap with the frequency band in which flight control systems and human pilots tend to operate. This is mainly the case for the lowest control effort settings, for which vibration attenuation takes place within 4–7 sec after the HHC is turned on. The time constants associated with these settling times are roughly equivalent to closed loop

bandwidths of up to 1 rad/sec, which are well within the bandwidth of flight control systems and human pilots. Therefore, the interactions and potential adverse effects on the stability and other control characteristics of the helicopter should be explored.

3. Adequate vibration attenuation is achieved by means of a LQR control framework designed on the basis of an approximate estimate of the T-matrix. This shows that accurate knowledge of $\mathbf{T}^{-1}$ is not strictly necessary, although performance does improve when the feedback gain is closer to the ideal case (i.e. $\mathbf{K} = \mathbf{T}^{-1}$). Relience on a constant T-matrix is one of the key limitations of this research, although it is fully justifiable as a first step toward a rigorous treatment of the problem, due to the lack of a suitable theory to deal with an adaptive (and therefore essentially nonlinear) T-matrix.

4. When feedback gains are sufficiently small, as is the case for low control effort HHC designs, closed loop helicopter stability exponents of discrete and continuous sytems remain in good agreement with the open loop values, so that closed loop dynamics can be considered quasisteady. Therefore discrete and continuous systems are both stable, and predicted steady state values of HHC input harmonics are in good agreement, although the initial transient behavior can be different. These differences become progressively less marked for lower control effort settings (i.e., $r \to \infty$), or low feedback gain designs ($\kappa = T/2$).

5. A linearized model of the helicopter dynamics is adequate for HHC design, as long as the periodicity of the system is correctly taken into account, i.e., periodicity is

more important than nonlinearity, at least for the mathematical model used in this study.

6. Unsteady aerodynamics has a minor impact on the closed loop HHC vibration attenuation performance for the model used in this study, due to the small amplitudes of the HHC input harmonics which result from the low vibration levels predicted by the mathematical model. Under these conditions, linearized models of the helicopter on the basis of quasisteady aerodynamics are adequate for HHC design. However, this assertion should be reevaluated when better predictions of the vibratory components are available.

6.2 Future work

The research presented in this investigation points out to the importance of accounting for the time-periodic dynamics in the loop and the discrete-time elements of the HHC system in the analysis of closed loop HHC stability, in particular when controller conditions are such that the quasisteady assumption is not satisfied. There are some areas, however, in which the present analysis was limited by modeling constraints of the analytical simulation program. This section suggests possible research efforts which could serve to fill in some of the gaps left in this investigation.

1. Improve the vibratory hub load level prediction capability of the mathematical model. If possible, support this effort through validation with wind tunnel data or flight test data.

2. Improve the modeling of aerodynamic loads through the incorporation of non-uniform inflow or time-marching free wake models, and dynamic stall models. Dynamic stall has been shown to be a primary cause of vibration in helicopters, particularly at high advance ratio flight, and becomes significant in maneuvers or flight conditions where portions of the blade are subject to stalling.

3. Extend this investigation to include the impact of dynamic stall on stability and performance of the closed loop, coupled helicopter-HHC system. The latter is significant because HHC can potentially increase stall regions on the rotor disk, especially at the onset of closed loop instability, where large amplitude higher harmonic blade pitch oscillations are expected. Additionally, dynamic blade stall invalidates the linearity assumption of the HHC input-output relation, and can, consequently, have a real impact on the stability boundaries of the closed loop, coupled helicopter-HHC system.

4. Investigate the robustness of HHC in more aggressive maneuvers, as well as the potential impact of FCS/HHC interactions on the closed loop stability of the coupled helicopter-HHC systems.

Bibliography

[1] Albers, J. A., "NASA Rotorcraft Technology for the 21st Century," Proceedings of the AIAA/AHS/ASEE Aircraft Design, Systems and Operations Conference, Seattle, WA, July 31-Aug. 2 1989.

[2] Coy, J. J., "A Vision for the Role of Vertical Flight in the Next 100 Years," Proceedings of the AIAA/ICAS International Air and Space Symposium and Exposition: The Next 100 Years, Dayton, OH, July 14-17 2003.

[3] Coy, J. J., "Rotorcraft Vision," AHS/AIAA/SAE/RaeS International Powered Lift Conference, Arlington, VA, Oct. 30–Nov. 1 2000.

[4] Furusawa, M., and Fujigaki, T., "Research and Development Activities for 'Ninja' in the Air," Proceedings of the AIAA/ICAS International Air and Space Symposium and Exposition: The Next 100 Years, Dayton, OH, July 14-17 2003.

[5] Bousman, W. G., "Putting the Aero Back Into Aeroelasticity," Eighth ARO Workshop on Aeroelasticity of Rotorcraft Systems, University Park, PA, October 18-20 1999.

[6] Arnold, U. T., "Definitely the Harder Way to Get Airborne," Proceedings of the AIAA/ICAS International Air and Space Symposium and Exposition: The Next 100 Years, Dayton, OH, July 14-17 2003.

[7] Leatherwood, J. D., Dempsey, T. K., and Clevenson, S. A., "A Design Tool for Estimating Passenger Ride Discomfort Within Complex Ride Environments," *Human Factors*, Vol. 22, No. 3, June 1980, pp. 291–312.

[8] Leatherwood, J. D., "Combined Effect of Noise and Vibration on Passenger Acceptance," NASA TM-86284, August 1984.

[9] Leatherwood, J. D., Clevenson, S. A., and Stephens, D. G., "The Development of Interior Noise and Vibration Criteria," NASA TM-102736, October 1990.

[10] Mansfield, N. J., and Griffin, M. J., "Effect of Magnitude of Vertical Whole-Body Vibration on Absorbed Power for the Seated Human Body," *Journal of Sound and Vibration*, Vol. 215, No. 4, August 1998, pp. 813–825.

[11] Breen, D. L., and Butler, B. P., "A Comparison of Two Whole-Body Vibration Standards as Applied to Rotary-Wing Aircraft: ISO (International Standards Organization) 2631 vs ADS (Aeronautical Design Standards) 27," Army Aeromedical Research Lab, Fort Rucker, AL, July 1988.

[12] Crews, S. T., "Rotorcraft Vibration Criteria – A New Perspective," Proceedings of the American Helicopter Society 43rd Annual Forum, Saint Louis, MO, May 18-20 1987, Vol. 2, pp. 991–998.

[13] Mueller, A. W., Conner, D. A., Rutledge, C. K., and Wilson, M. R., "Full Scale Flight Acoustic Results for the UH-60A Airloads Aircraft," American Helicopter Society Vertical Lift Aircraft Design Conference, San Francisco, CA, January 18-20 1995, pp. 5.1–1 to 5.1–25.

[14] Millott, T. A., Welsh, W. A., Yoerkie, C. A., Jr., MacMartin, D. G., and Davis, M. W., "Flight Test of Active Gear-Mesh Noise Control on the S-76 Aircraft," Proceedings of the American Helicopter Society 54th Annual Forum, Washington, DC, May 20-22 1998.

[15] Yu, Y. H., "Rotor Blade-Vortex Interaction Noise," *Progress in Aerospace Sciences*, Vol. 36, No. 2, February 2000, pp. 97–115.

[16] Johnson, W., Yamauchi, G. K., and Watts, M. E., "NASA Heavy Lift Rotorcraft Systems Investigation," NASA TP–2005-213467, December 2005.

[17] Jackson, P., Munson, K., and Peacock, L.,, Eds. *Jane's All the World's Aircraft, 2004-2005*, 95 sub ed., Jane's Information Group, June 2004.

[18] Schwarz, K., "Mil MI-26: The Russian Giant," *Flug Revue*, July 1998.

[19] Friedmann, P. P., and Millott, T. A., "Vibration Reduction in Rotorcraft Using Active Control—A Comparison of Various Approaches," *Journal of Guidance, Control, and Dynamics*, Vol. 18, No. 4, July-August 1995, pp. 664–673.

[20] Friedmann, P. P., "Rotary-Wing Aeroelasticity: Current Status and Future Trends," *AIAA Journal*, Vol. 42, No. 10, October 2004, pp. 1953–1972.

[21] Teves, D., Niesl, G., Blaas, A., and Jacklin, S., "The Role of Active Control in Future Rotorcraft," Proceedings of the 21st European Rotorcraft Forum, Saint Petersburg, Russia, September 1995.

[22] Anusonti-Inthra, P., and Gandhi, F., "Optimal Control of Helicopter Vibration through Cyclic Variations in Blade Root Stiffness," *Smart Materials and Structures*, Vol. 10, No. 1, February 2001, pp. 86–95.

[23] Ormiston, R. A., "Aeroelastic Considerations for Rotorcraft Primary Control with On-Blade Elevons," Proceedings of the American Helicopter Society 57th Annual Forum, Washington, DC, May 9-11, 2001.

[24] Shen, J., Yang, M., and Chopra, I., "Swashplateless Helicopter Rotor with Trailing-Edge Flaps for Flight and Vibration Control," *Journal of Aircraft*, Vol. 43, No. 2, March-April 2006, pp. 346–352.

[25] Shen, J., Yang, M., and Chopra, I., "Swashplateless Helicopter Rotor System with Active Trailing-Edge Flaps for Primary and Vibration Controls," Proceedings of the 45th AIAA/ASME/ASCE/AHS/ASC Structures, Structural Dynamics and Materials Conference, Palm Springs, CA, April 19-22, 2004.

[26] Shen, J., and Chopra, I., "Swashplateless Helicopter Rotor with Trailing-Edge Flaps," *Journal of Aircraft*, Vol. 41, No. 2, March-April 2004, pp. 208–214.

[27] Shen, J., and Chopra, I., "Aeroelastic Modeling of Trailing-Edge Flap Helicopter Rotors Including Actuator Dynamics," *Journal of Aircraft*, Vol. 41, No. 6, Nov.–Dec. 2004, pp. 1465–1472.

[28] Shen, J., *Comprehensive aeroelasatic analysis of helicopter rotor with trailing-edge flap for primary control and vibration control.* PhD thesis, University of Maryland, College Park, MD, 2003.

[29] Shen, J., Chopra, I., and Johnson, W., "Performance of Swashplateless Ultralight Helicopter Rotor with Trailing-Edge Flaps for Primary Flight Control," Proceedings of the American Helicopter Society 59th Annual Forum, Phoenix, AZ, May 25-27, 2003.

[30] Malpica, C., and Celi, R., "Simulation-Based Bandwidth Analysis of a Swashplateless Rotor Helicopter," Proceedings of the 63rd Annual Forum of the American Helicopter Society, Virginia Beach, VA, May 1-3 2007.

[31] Johnson, W., *Helicopter theory* Princeton University Press, 1980.

[32] Splettstoesser, W. R., Kube, R., Wagner, W., Seelhorst, U., Boutier, A., Micheli, F., Mercker, E., and Pengel, K., "Key Results from a Higher Harmonic Control Aeroacoustic Rotor Test (HART) in the German-Dutch Wind Tunnel," *Journal of the American Helicopter Society*, Vol. 42, No. 1, Jan. 1997, pp. 58–78.

[33] Kube, R., Splettstoesser, W. R., Wagner, W., Seelhorst, U., Yu, Y. H., Tung, C., Beaumier, P., Prieur, J., Rahier, G., Spiegel, P., Boutier, A., Brooks, T. F., Burley, C. L., Boyd, D. D., Jr, Mercker, E., and Pengel, K., "HHC Aeroacoustic Rotor Tests in the German-Dutch Wind Tunnel: Improving Physical Understanding and Prediction Codes," *Aerospace Science and Technology*, Vol. 2, No. 3, March-April 1998, pp. 177–190.

[34] Yu, Y. H., Tung, C., van der Wall, B. G., Pausder, H.-J., Burley, C., Brooks, T., Beaumier, P., Delrieux, Y., Mercker, E., and Pengel, K., "The HART-II Test: Rotor Wakes and Aeroacoustics with Higher-Harmonic Pitch Control (HHC) Inputs - The Joint German/French/Dutch/US Project -," Proceedings of the 58th Annual Forum of the American Helicopter Society, Montreal, Canada, June 11-13 2002.

[35] Splettstoesser, W. R., Schultz, K.-J., van der Wall, B., Buchholz, H., Gembler, W., and Niesl, G., "Helicopter Noise Reduction by Individual Blade Control [IBC] -Selected Flight Test and Simulation Results-," Deutsches Zentrum für Luft-und Raumfahrt (DLR), Braunschweig, Germany, June 2001.

[36] Booth, E. R., Jr., and Wilbur, M. L., "Acoustic Aspects of Active-Twist Rotor Control," Proceedings of the 58th Annual Forum of the American Helicopter Society, Montreal, Canada, June 11-13 2002.

[37] Mueller, M., Arnold, U. T., and Morbitzer, D., "On the Importance and Effectiveness of 2/rev IBC for Noise, Vibration and Pitch Link Load Reduction," Proceedings of the 25th European Rotorcraft Forum, Rome, Italy, Sept. 14-16 1999, pp. G4.1–G4.12.

[38] Nguyen, K., Betzina, M., and Kitaplioglu, C., "Full-Scale Demonstration of Higher Harmonic Control for Noise and Vibration Reduction on the XV-15 Rotor," Proceedings of the 56th Annual Forum of the American Helicopter Society, Virginia Beach, VA, May 2-4 2000, pp. 751–763.

[39] Nguyen, K., and Chopra, I., "Effects of Higher Harmonic Control on Rotor Performance and Control Loads," *Journal of Aircraft*, Vol. 29, No. 3, May-June 1992, pp. 336–342.

[40] Kessler, C., Fuerst, D., and Arnold, U. T., "Open Loop Flight Test Results and Closed Loop Status of the IBC System on the CH-53G Helicopter," Proceedings of the American Helicopter Society 59th Annual Forum, Phoenix, AZ, May 6-8 2003.

[41] Arnold, U. T., and Fuerst, D., "Closed Loop IBC Results from CH-53G Flight Tests," *Aerospace Science and Technology*, Vol. 9, No. 5, July 2005 2005, pp. 421–435.

[42] Liu, L., Friedmann, P. P., and Patt, D., "Simultaneous Vibration and Noise Reduction in Rotorcraft – Practical Implementation Issues," Proceedings of the 46th AIAA/ASME/ASCE/AHS/ASC Structures, Structural Dynamics and Materials Conference, Austin, TX, April 18-21, 2005.

[43] Sim, B. W., "Suppressing In-Plane, Low Frequency Helicopter Harmonic Noise with Active Controls," Proceedings of the AHS Specialists' Conference on Aeromechanics, San Francisco, CA, January 23–25 2008.

[44] Kelly, M. E., Duraisamy, K., and Brown, R. E., "Predicting Blade Vortex Interaction, Airloads and Acoustics using the Vorticity Transport Model," Proceedings of the AHS Specialists' Conference on Aeromechanics, San Francisco, CA, January 23–25 2008.

[45] Kube, R., Achache, M., Niesl, G., and Splettstoesser, W. R., "A Closed-Loop Controller for BVI Impulsive Noise Reduction by Higher Harmonic Control," Proceedings of the 48th Annual Forum of the American Helicopter Society, Washington, DC, 1992.

[46] Kube, R., "Simultaneous Vibration and BVI Noise Feedback for Closed Loop Higher Harmonic Control: Influence of Rotor Dynamics on Controller Design," Proceedings of the 19th European Rotorcraft Forum, Cernobbio, Italy, Sept. 14-16 1993.

[47] Gopalan, G., and Schmitz, F. H., "Understanding Far Field Near-In-Plane High Speed Harmonic Helicopter Rotor Noise in Hover: Governing Parameters and Active Acoustic Control Possibilities," Proceedings of the AHS Specialists' Conference on Aeromechanics, San Francisco, CA, January 23–25 2008.

[48] Bebesel, M., Roth, D., and Pongratz, K., "Reduction of BVI Noise on the Ground - In Flight Evaluation of Closed-Loop Controller," Proceedings of the 28th European Rotorcraft Forum, Bristol, England, Sept. 2002, pp. 19.1–19.9.

[49] Dieterich, O., Enenkl, B., and Roth, D., "Trailing Edge Flaps for Active Rotor Control Aeroelastic Characteristics of the ADASYS Rotor System," Proceedings of the American Helicopter Society 62nd Annual Forum, Phoenix, AZ, May 9-11 2006.

[50] Patt, D., Liu, L., and Friedmann, P. P., "Helicopter Noise Reduction by Actively Controlled Flaps," Proceedings of the 11th AIAA/CEAS Aeroacoustics Conference, Monterey, CA, May 23-25, 2005.

[51] Kube, R., and Klöppel, V., "On the Role of Prediction Tools for Adaptive Rotor System Developments," *Smart Materials and Structures*, Vol. 10, No. 1, February 2001, pp. 137–144.

[52] Welsh, W. A., "Evolution of Active Vibration Control Technology," Proceedings of the AHS 4th Decennium Specialist's Conference on Aeromechanics, San Francisco, CA, January 2004.

[53] Johnson, W., "Self-Tuning Regulators for Multicyclic Control of Helicopter Vibration," NASA TP-1996, March 1982.

[54] Goodman, R. K., and Millott, T. A., "Design, Development, and Flight Testing of the Active Vibration Control System for the Sikorsky S-92," Proceedings of the American Helicopter Society 56th Annual Forum, Virginia Beach, VA, May 2000.

[55] Shaw, J., *Higher harmonic blade pitch control: a system for helicopter vibration reduction.* PhD thesis, Massachusets Institute of Technology, June 1980.

[56] Shaw, J., and Albion, N., "Active Control of the Helicopter Rotor for Vibration Reduction," *Journal of the American Helicopter Society*, Vol. 26, 1981.

[57] Shaw, J., Albion, N., Hanker, E. J., and Teal, R. S., "Higher Harmonic Control: Wind Tunnel Demonstration of Fully Effective Vibratory Hub Force Suppression," Proceedings of the 41st Annual Forum of the American Helicopter Society, Ft. Worth, TX, May 15–17 1985.

[58] Hall, S. R., and Wereley, N. M., "Linear Control Issues in the Higher Harmonic Control of Helicopter Vibrations," Proceedings of the American Helicopter Society 45th Annual Forum, Boston, MA, May 22-24 1989, pp. 955–971.

[59] McCloud, J. L., III, and Kretz, M., "Multicyclic Jet-Flap Control for Alleviation of Helicopter Blade Stresses and Fuselage Vibration," Rotorcraft Dynamics, NASA SP-352, 1974, pp. 233–238.

[60] Shaw, J., and Albion, N., "Active Control of the Helicopter Rotor for Vibration Reduction," Proceedings of the American Helicopter Society 36th Annual Forum, Washington, DC, May 1980.

[61] McHugh, F. J., and Shaw, J., "Helicopter Vibration Reduction with Higher Harmonic Blade Pitch," *Journal of the American Helicopter Society*, Vol. 23, No. 4, October 1978, pp. 26–35.

[62] Taylor, R. B., Farrar, F. A., and Miao, W., "An Active Control System for Helicopter Vibration Reduction by Higher Harmonic Pitch," Proceedings of the 36th Annual Forum of the American Helicopter Society, Washington, DC, May 13–15 1980.

[63] Molusis, J. A., "The Importance of Nonlinearity on the Higher Harmonic Control of Helicopter Vibration," Proceedings of the 39th Annual Forum of the American Helicopter Society, Saint Louis, MO, May 9–11 1983.

[64] Hammond, C. E., "Wind Tunnel Results Showing Rotor Vibratory Loads Reduction Using Higher Harmonic Blade Pitch," Proceedings of the 36th Annual Forum of the American Helicopter Society, Washington, DC, May 13–15 1980.

[65] Molusis, J. A., Hammond, C. E., and Cline, J. H., "A Unified Approach to the Optimal Design of Adaptive and Gain Scheduled Controllers to Achieve Minimum Helicopter Rotor Vibration," Proceedings of the 37th Annual Forum of the American Helicopter Society, New Orleans, LA, May 17–20 1981.

[66] Chopra, I., and McCloud, J. L., III, "A Numerical Simulation Study of Open-Loop, Closed-Loop, and Adaptive Multicyclic Control Systems," *Journal of the American Helicopter Society*, Vol. 28, No. 1, January 1983, pp. 63–77.

[67] Wereley, N., and Hall, S. R., "Frequency Response of Linear Time Periodic Systems," Proceedings of the 29th IEEE Conference on Decision and Control, Honolulu, HI, December 5-7 1990, Vol. 6, pp. 3650–3655.

[68] Wereley, N. M., and Hall, S. R., "Linear Time Periodic Systems: Transfer Functions, Poles, Transmission Zeros and Directional Properties," Proceedings of 1991 American Control Conference, Boston, MA, 1991.

[69] Hwang, S. H., and Wereley, N. M., "Frequency Domain System Identification of Helicopter Blades with Trailing Edge Flaps," Proceedings of the AIAA/ASME/AHS Adaptive Structures Forum, Salt Lake City, UT, April 18-19 1996, pp. 46–61.

[70] Siddiqi, A., and Hall, S. R., "Identification of the Harmonic Transfer Functions of a Helicopter Rotor," Massachusetts Institute of Technology AMSL Report #01-01, Cambridge, MA, 2001.

[71] Shin, S. J., Cesnik, C. E. S., and Hall, S. R., "System Identification Technique for Active Helicopter Rotors," *Journal of Intelligent Material Systems and Structures*, Vol. 16, No. 11-12, 2005, pp. 1025–1038.

[72] Chopra, I., and McCloud, J. L., III, "Considerations of Open-Loop, Closed-Loop, and Adaptive Multicyclic Control Systems," Proceedings of the American Helicopter Society Northeast Region National Specialists' Meeting on Helicopter Vibration Technology for the Jet Smooth Rid, Hartford, CT, Nov. 2-4 1981.

[73] Jacklin, S. A., "Comparison of Five System Identification Algorithms for Rotorcraft Higher Harmonic Control," NASA TP-1998-207687, May 1998.

[74] Chandrasekar, J., Liu, L., Patt, D., Friedmann, P. P., and Bernstein, D. S., "Adaptive Harmonic Steady State Control for Disturbance Rejection," Proceedings of the 2004 American Control Conference, Boston, MA, June 30 – July 2 2004, pp. 1247–1252.

[75] Patt, D., Liu, L., Chandrasekar, J., Bernstein, D. S., and Friedmann, P. P., "Higher-Harmonic-Control Algorithm for Helicopter Vibration Reduction Revisited," *Journal of Guidance, Control, and Dynamics*, Vol. 28, No. 5, September-October 2005, pp. 918–930.

[76] Gupta, N. K., and Du Val, R. W., "A New Approach for Active Control of Rotorcraft Vibration," *Journal of Guidance*, Vol. 5, No. 2, March-April 1982, pp. 143–150.

[77] Ham, N. D., "A Simple System for Helicopter Individual-Blade-Control Using Modal Decomposition," *Vertica*, Vol. 4, 1980, pp. 23–28.

[78] Ham, N. D., and McKillip, R. M., Jr., "A Simple System for Helicopter Individual-Blade-Control and Its Application to Gust Alleviation," Proceedings of the 36th Annual Forum of the American Helicopter Society, Washington, DC, May 1980.

[79] McKillip, R. M., Jr., "Periodic Control of the Individual-Blade-Control Rotor," *Vertica*, Vol. 9, No. 2, 1985, pp. 199–225.

[80] Ham, N. D., "Helicopter Individual-Blade-Control Research at MIT 1977–1985," *Vertica*, Vol. 11, No. 1/2, 1987, pp. 109–122.

[81] McKillip, R. M., Jr., "Kinematic Observers for Active Control of Helicopter Vibration," *Vertica*, Vol. 12, No. 1/2, 1988, pp. 1–11.

[82] Ham, N. D., and McKillip, R. M., Jr., "Research on Measurement and Control of Helicopter Rotor Response Using Blade-Mounted Accelerometers 1990–91," Proceedings of the 17th European Rotorcraft Forum, Berlin, Germany, Sept. 24–26 1991.

[83] Ham, N. D., and McKillip, R. M., Jr., "Research on Measurement and Control of Helicopter Rotor Response Using Blade-Mounted Accelerometers 1991–92," Proceedings of the 18th European Rotorcraft Forum, Avignon, France, Sept. 15–18 1992.

[84] Spencer, M. G., Sanner, R. M., and Chopra, I., "Adaptive Neurocontrol of Simulated Rotor Vibrations Using Trailing Edge Flaps," *Journal of Intelligent Material Systems and Structures*, Vol. 10, No. 11, November 1999, pp. 855–871.

[85] Arcara, P., Bittanti, S., and Lovera, M., "Active Control of VIbrations in Helicopters by Periodic Optimal Control," Proceedings of the 1997 IEEE International Conference on Control Applications, Hartford, CT, October 5-7 1997, pp. 730–735.

[86] Arcara, P., Bittanti, S., and Lovera, M., "Periodic Control of Helicopter Rotors for Attenuation of Vibrations in Forward Flight," *IEEE Transactions on Control Systems Technology*, Vol. 8, No. 6, November 2000, pp. 883–894.

[87] Bittanti, S., and Colaneri, P., "Periodic control," In *Wiley Encyclopedia of Electrical and Electronic Engineering*, J. G. Webster, Ed. John Wiley and Sons, 1999.

[88] Bittanti, S., and Cuzzola, F. A., "Generalized Active Control of Vibrations in Helicopters," *Journal of Guidance, Control and Dynamics*, Vol. 25, No. 2, March-April 2002, pp. 340–351.

[89] Bittanti, S., and Cuzzola, F. A., "Periodic Active Control of Vibrations in Helicopters: a Gain-Scheduled Multi-Objective Approach," *Control Engineering Practice*, Vol. 10, No. 10, March-April 2002, pp. 1043–1057.

[90] Mannchen, T., and Well, K. H., "Helicopter Vibration Reduction Using Periodic Robust Control," Proceedings of the AIAA Guidance, Navigation and Control Conference & Exhibit, August 6-9 2001.

[91] Mannchen, T., and Well, K. H., "Helicopter Vibration Reduction and Damping Enhancement Using Individual Blade Control," *Journal of Guidance, Control, and Dynamics*, Vol. 27, No. 5, September–October 2004, pp. 760–766.

[92] Shin, S., Cesnik, C. E. S., and Hall, S. R., "Closed-Loop Control Test of the NASA/Army/MIT Active Twist Rotor for Vibration Reduction," *Journal of the American Helicopter Society*, Vol. 50, No. 2, April 2005, pp. 178–194.

[93] Millott, T. A., and Friedmann, P. P., "Vibration Reduction in Hingeless Rotors Using an Actively Controlled Trailing Edge Flap: Implementation and Time Domain Simulation," Proceedings of the 35th AIAA/ASME/ASCE/AHS/ASC Structures, Structural Dynamics, and Materials Conference, 1994.

[94] Friedmann, P. P., Venkatesan, C., and Papavassiliou, I., "Nonlinear Coupled Rotor-Fuselage Helicopter Vibration Studies with Higher Harmonic Control," Proceedings of the 46th Annual Forum of the American Helicopter Society, Washington, DC, May 21–23 1990.

[95] Papavassiliou, I., Friedmann, P. P., and Venkatesan, C., "Coupled Rotor-Flexible Fuselage Vibration Reduction Using Open Loop Higher Harmonic Control," Proceedings of the 32nd AIAA/ASME/ASCE/AHS/ASC Structures, Structural Dynamics, and Materials Conference, Baltimore, MD, April 8–10 1991.

[96] Cheng, R. P., Tischler, M., and Celi, R., "A High-Order, Time Invariant Linearized Model for Application to HHC/AFCS Interaction Studies," Proceedings of the 59th Annual Forum of the American Helicopter Society, Phoenix, AZ, June 2003.

[97] Polychroniadis, M., and Achache, M., "Higher Harmonic Control Flight Tests of an Experimental System on a SA 349 Research Gazelle," Proceedings of the 42nd Annual Forum of the American Helicopter Society, Washington, DC, June 2–5 1986.

[98] Hammond, C. E., "Wind Tunnel Results Showing Rotor Vibratory Loads Reduction Using Higher Harmonic Blade Pitch," *Journal of the American Helicopter Society*, Vol. 28, No. 1, January 1983, pp. 10–15.

[99] Wood, E. R., Powers, R. W., and Hammond, C. E., "On Methods for Application of Harmonic Control," *Vertica*, Vol. 4, No. 1, 1980, pp. 43–60.

[100] Wood, E. R., Powers, R. W., Cline, J. H., and Hammond, C. E., "On Developing and Flight Testing a Higher Harmonic Control System," Proceedings of the 39th Annual Forum of the American Helicopter Society, St. Louis, MO, May 9–11 1983.

[101] Wood, E. R., Powers, R. W., Cline, J. H., and Hammond, C. E., "On Developing and Flight Testing a Higher Harmonic Control System Higher Harmonic Control System," *Journal of the American Helicopter Society*, Vol. 30, No. 1, January 1985, pp. 3–20.

[102] Jacklin, S. A., Blaas, A., Teves, D., and Kube, R., "Reduction of Helicopter BVI Noise, Vibration, and Power Consumption Through Individual Blade Control," Proceedings of the 51st Annual Forum of the American Helicopter Society, Fort Worth, TX, May 9–11 1995.

[103] Hall, S. R., and Wereley, N. M., "Performance of Higher Harmonic Control Algorithms fot Helicopter Vibration Reduction," *Journal of Guidance, Control, and Dynamics*, Vol. 16, No. 4, July-August 1993, pp. 793–797.

[104] Robinson, L. H., and Friedmann, P. P., "Aeroelastic Simulation of Higher Harmonic Control," NASA CR-4623, August 1994.

[105] Millott, T. A., and Friedmann, P. P., "Vibration Reduction in Helicopter Rotors Using an Actively Controlled Partial Span Trailing Edge Flap Located on the Blade," NASA NASA-CR-4611, June 1994.

[106] Nguyen, K. Q., *Higher harmonic control analysis for vibration reduction of helicopter rotor systems* PhD thesis, University of Maryland, College Park, MD, 1989.

[107] Nguyen, K., and Chopra, I., "Application of Higher Harmonic Control (HHC) to Hingeless Rotor Systems," Proceedings of the 30th ASME/ASCE/AHS/ASC Structures, Structural Dynamics and Materials Conference, Mobile, AL, April 3-5 1989.

[108] Milgram, J., and Chopra, I., "Helicopter Vibration Reduction with Trailing-Edge Flaps," Proceedings of the 36th AIAA/ASME/ASCE/AHS/ASC Structures, Structural Dynamics and Materials Conference, New Orleans, LA, April 10–12, 1995.

[109] Milgram, J., *A comprehensive aeroelastic analysis of helicopter main rotors with trailing-edge flaps for vibration reduction.* PhD thesis, University of Maryland, College Park, MD, 1997.

[110] Roget, B., and Chopra, I., "Robust Individual Blade Control Algorithm for a Dissimilar Rotor Robust Individual Blade Control Algorithm for a Dissimilar Rotor," *Journal of Guidance, Control, and Dynamics*, Vol. 25, No. 5, September–October 2002, pp. 915–923.

[111] Leishman, J. G., and Beddoes, T. S., "A Generalised Model for Airfoil Unsteady Aerodynamic Behaviour and Dynamic Stall Using the Indicial Method," Proceedings of the American Helicopter Society 42nd Annual Forum, Washington, DC, June 2-4, 1986, Vol. I, pp. 243–265.

[112] Nguyen, K. Q., "Higher Harmonic Control Analysis for Vibration Reduction of Helicopter Rotor Systems," NASA 103855, October 1994.

[113] Depailler, G., and Friedmann, P. P., "Reductions of Vibrations Due to Dynamic Stall in Helicopters Using an Actively Controlled Flap," Proceedings of the 43rd AIAA/ASME/ASCE/AHS/ASC Structures, Structural Dynamics and Materials Conference, Denver, CO, April 2002, no. No. 2002-1431 in AIAA Paper.

[114] Hanagad, S., Meyyappa, M., Sarkar, S., and Craig, J. I., "A Coupled Rotor/Airframe Vibration Model with Higher Harmonic Control Effects," Proceedings of the 42nd Annual Forum of the American Helicopter Society, Washington, DC, June 2–5 1986.

[115] Pearson, J. T., and Goodall, R. M., "Adaptive Schemes for the Active Control of Helicopter Structural Response," *IEEE Transactions on Control Systems Technology*, Vol. 2, No. 2, June 1994, pp. 61–72.

[116] Chiu, T., and Friedmann, P. P., "A Coupled Helicopter Rotor/Fuselage Aeroelastic Response Model for ACSR," Proceedings of the 36th AIAA/ASME/ASCE/AHS/ASC Structures, Structural Dynamics and Materials Conference, New Orleans, LA, April 10–13 1995.

[117] Cribbs, R. C., Friedmann, P. P., and Chiu, T., "Coupled Helicopter Rotor/Flexible Fuselage Aeroelastic Model for Control of Structural Response," *AIAA Journal*, Vol. 38, No. 10, October 2000, pp. 1777–1788.

[118] Chiu, T., and Friedmann, P. P., "ACSR System for Vibration Suppression in Coupled Rotor-Flexible Fuselage Model," Proceedings of the 37th AIAA/ASME/ASCE/AHS/ASC Structures, Structural Dynamics and Materials Conference, Salt Lake City, UT, April 15–17 1996.

[119] Lovera, M., Colaneri, P., Malpica, C., and Celi, R., "Closed-Loop Aeromechanical Stability Analysis for a Hingeless Rotor Helicopter With HHC or IBC," Proceedings of the 29th European Rotorcraft Forum, Friedrichshafen, Germany, September 2003.

[120] Lovera, M., Colaneri, P., Malpica, C., and Celi, R., "Discrete-time, Closed-Loop Aeromechanical Stability Analysis for Helicopters With Higher Harmonic Control," Proceedings of the 60th Annual Forum of the American Helicopter Society, Baltimore, MD, June 7-10 2004.

[121] Lovera, M., Colaneri, P., Malpica, C., and Celi, R., "Closed-Loop Aeromechanical Stability Analysis of Hingeless Rotor Helicopters with Higher Harmonic Control," *Journal of Guidance, Control, and Dynamics*, Vol. 29, No. 1, January–February 2006, pp. 179–189.

[122] Lovera, M., Colaneri, P., Malpica, C., and Celi, R., "Discrete-Time, Closed-Loop Aeromechanical Stability Analysis of Helicopters with Higher Harmonic Control," *Journal of Guidance, Control, and Dynamics*, Vol. 30, No. 5, September-October 2007, pp. 1249–1260.

[123] Theodore, C. R., and Celi, R., "Flight Dynamic Simulation with Refined Aerodynamic and Flexible Blade Modeling," Proceedings of the 56th Annual Forum of the American Helicopter Society, Virginia Beach, VA, 2000.

[124] Theodore, C. R., and Celi, R., "Helicopter Flight Dynamic Simulation with Refined Aerodynamic and Flexible Blade Modeling," *Journal of Aircraft*, Vol. 39, No. 4, July-August 2002, pp. 577–586.

[125] Celi, R., "Helicopter Rotor Blade Aeroelasticity in Forward Flight with an Implicit Structural Formulation," *AIAA Journal*, Vol. 30, No. 9, Sept. 1992, pp. 2274–2282.

[126] Turnour, S. R., and Celi, R., "Modeling of Flexible Rotor Blades for Helicopter Flight Dynamics Applications," *Journal of the American Helicopter Society*, Vol. 41, No. 1, Jan. 1996, pp. 52–66; Correction in Vol. 41, No. 3, Jul 1996, pp. 191–194.

[127] Celi, R., "Implementation of Rotary-Wing Aeromechanical Problems Using Differential-Algebraic Equation Solvers," *Journal of the American Helicopter Society*, Vol. 45, No. 4, October 2000, pp. 253–262.

[128] Howlett, J. J., "UH-60A Black Hawk Engineering Simulation Program - Volume II - Mathematical Model," NASA CR-166309, Dec. 1981.

[129] Turnour, S. R., *Flight dynamics simulation modeling for hingeless and bearingless rotor helicopters* PhD thesis, University of Maryland, College Park, MD, 1996.

[130] Peters, D. A., Boyd, D. D., and He, C. J., "Finite-State Induced-Flow Model for Rotors in Hover and Forward Flight," *Journal of the American Helicopter Society*, Vol. 34, No. 4, Oct. 1989, pp. 5–17.

[131] Peters, D. A., and He, C. J., "Correlation of Measured Induced Velocities with a Finite-State Wake Model," *Journal of the American Helicopter Society*, Vol. 36, No. 3, July 1991, pp. 59–70.

[132] Nguyen, K. Q., and Leishman, J. G., "State-Space Representation of Unsteady Airfoil Behavior," *AIAA Journal*, Vol. 28, No. 5, May 1990, pp. 836–844.

[133] Theodore, C. R., *Helicopter Flight Dynamics Simulation with Refined Aerodynamic Modeling* PhD thesis, University of Maryland, College Park, MD, 2000.

[134] Shamie, J., and Friedmann, P. P., "Effect of Moderate Deflections on the Aeroelastic Stability of a Rotor Blade in Forward Flight," Proceedings of the 3rd Annual European Rotorcraft and Powered Lift Aircraft Forum, Aixen-Provence, France, Sept. 1977.

[135] Chen, R. T. N., and Jeske, J. A., "Kinematic Properties of the Helicopter in Coordinated Turns," NASA TP 1773, April 1981.

[136] Celi, R., "Hingeless Rotor Dynamics in Coordinated Turns," *Journal of the American Helicopter Society*, Vol. 36, No. 4, Oct. 1991, pp. 39–47.

[137] Celi, R., "Hingeless Rotor Dynamics in Coordinated Turns," Proceedings of the 31st AIAA/ASME/ASCE/AHS/ASC Structures, Structural Dynamics and Materials Conference, Long Beach, CA, April 2-4 1990.

[138] D'Angelo, H., *Linear time-varying systems: analysis and synthesis* Allyn and Bacon, 1970.

[139] Zhou, J., and Hagiwara, T., "H_2 and H_∞ Norm Computations of Linear Continuous-time Periodic Systems Via the Skew Analysis of Frequency Response Operators," *Automatica*, Vol. 38, No. 8, 2002, pp. 1381–1387.

[140] Bittanti, S., and Colaneri, P., "Invariant Representations of Discrete-Time Periodic Systems," *Automatica*, Vol. 36, No. 12, December 2000, pp. 1777–1793.

[141] Colaneri, P., Celi, R., and Bittanti, S., "Constant-Coefficient Representations of Periodic-Coefficient Discrete Linear Systems," Proceedings of the AHS 4th Decennium Specialist's Conference on Aeromechanics, Alexandria, VA, January 2004.

[142] Rugh, W. J., *Linear System Theory*, 2nd ed., Prentice-Hall, 1996.

[143] Anonymous "Handling Qualities Requirements for Military Rotorcraft," U.S. Army AMCOM ADS-33E-PRF, March 2000.

[144] Hariharan, N., and Leishman, J. G., "Unsteady Aerodynamics of a Flapped Airfoil in Subsonic Flow by Indicial Concepts," Proceedings of the 36th AIAA/ASME/ASCE/AHS/ASC Structures, Structural Dynamics and Materials Conference, New Orleans, LA, April 10–12, 1995.

[145] Theodorsen, T., and Garrick, I. E., "Nonstationary Flow about a Wing-Aileron-Tab Combination Including Aerodynamic Balance," NACA TR 736, 1942.

[146] Hariharan, N., "Unsteady aerodynamics of a flapped airfoil in subsonic flow using indicial concepts.," Master's thesis, University of Maryland, College Park, MD, 1995.

[147] Bao, J., Allen, K., and Chopra, I., "Design and Test of a Mach Scale Swashplateless Rotor Using Smart Trailing-Edge Flaps," Proceedings of the American Helicopter Society 62nd Annual Forum, Phoenix, AZ, May 9-11, 2006.

[148] Fulton, M. V., "Design of the Active Elevon Rotor for Low Vibration," American Helicopter Society Specialist's Meeting, Atlanta, GA, November 13-15, 2000.

[149] Fulton, M. V., and Ormiston, R. A., "Hover Testing of a Small-Scale Rotor with On-Blade Elevons," *Journal of the American Helicopter Society*, Vol. 46, No. 2, April 2001, pp. 96–106.

[150] Milgram, J., Chopra, I., and Straub, F., "A Comprehensive Rotorcraft Aeroelastic Analysis with Trailing-Edge Flap: Validation with Experimental Data," Proceedings of the American Helicopter Society 52nd Annual Forum, Washington, DC, June 4-6, 1996.